Aldritt Scaria Madathiparambil

Multiscale X-ray tomography for shale microstructure and mechanical behaviour

Doctoral thesis

NTNU
Norwegian University of Science and Technology
Thesis for the Degree of
Philosophiae Doctor
Faculty of Natural Sciences
Department of Physics

NTNU
Norwegian University of
Science and Technology

Aldritt Scaria Madathiparambil

Multiscale X-ray tomography for shale microstructure and mechanical behaviour

Thesis for the Degree of Philosophiae Doctor

Trondheim, January 2024

Norwegian University of Science and Technology
Faculty of Natural Sciences
Department of Physics

NTNU
Norwegian University of
Science and Technology

This thesis is dedicated to my parents, Prof. M.S. Mathew and Betsy Mathew, my wife, Dr. Agnus Mathew, and my daughter, Criselda Elizabeth Madathiparambil.

I also dedicate this thesis to my supervisors, Prof. Dag Werner Breiby, Dr. Basab Chattopadhyay, and Dr. Pierre Cerasi.

Abstract

This thesis is focused on proving a better understanding of shales using X-ray computed tomography-based techniques. Shales, a type of sedimentary rock, have received greater attention during the past decade due to the role their special properties play in oil and natural gas production, production of clays and cements, and issues related to groundwater flow. Studying shale is extremely important not only to provide a better fundamental understanding of its properties, but is crucial for CO_2 sequestration, environmental remediation of polluted aquifers, and preservation of cultural heritage.

Probing porous materials like shale with destructive techniques such as FIB-SEM can disrupt their properties. In contrast, X-ray computed tomography (CT) is a promising non-destructive tool that reconstructs internal three-dimensional information from numerous two-dimensional projections taken at various angles. CT can be conducted with the shale kept in its in situ conditions and offers various contrast mechanisms, including absorption, phase, scattering, and diffraction. These imaging techniques enable the study of different properties in shales and other sedimentary rock systems.

Understanding the mechanical properties of shales is crucial due to their potential use in isolating subsurface activities and predicting their long-term behavior. In the past, several ex-situ X-ray CT experiments have been carried out to investigate shale's mechanical response, requiring post-analysis to comprehend its behavior. However, our understanding of the microscale mechanisms within shale during mechanical testing, leading to structural failure, remains limited. Additionally, we lack insights into the occurrence of strain localization before and after bulk failure in these tests. Therefore, it is crucial to evaluate the primary mechanism responsible for strain localization in shale during macroscopic failure.

The extraction of shale oil and gas creates shale waste, potentially harmful if not managed correctly. Efforts are underway to reuse or recycle it, e.g., in soil stabilization, and reducing landfill use. Investigating the long-term stability of shale waste mixed with cement for soil stabilization is crucial. To assess durability, these materials need cyclic loading tests, revealing strain accumulation and fatigue from seasonal variations.

Abstract

Shale's complex mineral composition, anisotropic behavior, and intricate pore structure present challenges in understanding mineral orientation and distribution, in turn affecting its petrophysical and mechanical properties. To overcome these difficulties, novel non-destructive methods like X-ray diffraction CT (XRD-CT), X-ray diffraction tensorial tomography (XRDTT), and coherent X-ray diffraction imaging (CXDI) are employed in this thesis. These techniques provide unique insights into mineral orientation and the complex internal structures of shale. By combining CXDI, XRD-CT/TT, and attenuation-based contrast CT, a comprehensive analysis reveals the detailed multiscale distribution of shale minerals.

In Paper 1, we explore the mechanical properties of Draupne shale, a caprock in the Norwegian offshore, employing an innovative approach combining 4D X-ray microtomography with a triaxial deformation apparatus. This study adopts a uniform loading pattern to analyze the shale's mechanical behavior and utilizes Digital Volume Correlation (DVC) on experimental data to break down strain into elements such as dilation, compaction, and shear. In Paper 2, we demonstrate the potential of 4D X-ray microtomography coupled with a triaxial deformation apparatus, along with cyclic loading and unloading patterns, to investigate fatigue evolution in cement-shale composites. Employing DVC on the collected data elucidates microstructural mechanisms governing strain propagation and localization during cyclic loading. Paper 3 employs CXDI imaging and wide-angle X-ray diffraction to map the nanoscale morphology and mineral distribution of Pierre shale, often representative of North Sea shales. CXDI provides detailed mapping of nanoscale mineralogy and pore structures with a remarkable 26 nm resolution, showcasing its utility for studying shales and geological formations at the nanoscale. Paper 4 complements Paper 3 by further investigating the mineralogy and 3D orientation of clay minerals in Pierre shales, employing XRD-CT to map mineralogy and clay mineral orientation in 3D and XRDTT to delve into clay mineral orientation, particularly in millimeter-sized samples.

The thesis has shown how the combination of time-resolved *in situ* X-ray CT with digital volume correlation can be used in a novel way to understand the mechanical properties of geological samples. Application of novel X-ray CT techniques to study the complex and hierarchical nature of minerals and microstructure of shales is proposed to help mitigate risks in complex subsurface engineering operations.

Acknowledgement

valuable training. Ole Tore Buset's assistance in sample cell preparations, in-house CT experiments, and the management of the group's server is greatly appreciated.

I am pleased to acknowledge all the members of the X-ray Physics group within the Department of Physics, particularly Kim Robert, Daniyal, Fazel, and Ingvild, for their engaging discussions on X-ray and technological aspects. Special thanks to Kim and Fazel for their review of sections of my thesis. My sincere gratitude goes to my office mate Daniyal for infusing fun and a positive atmosphere into our workspace. Frederico, and Katharina have provided invaluable assistance in answering queries and dispelling doubts.

I wish to express my appreciation to individuals unrelated to my PhD journey at NTNU, including Rajeshkumar, Jibin, Vivek, and Syam, for their mutual support and motivation during challenging times. I must also acknowledge the Malayali community in Trondheim and their families for embracing me and making me feel at home during these years.

Lastly, I extend my gratitude to my father, Prof. M. S. Mathew, my mother, Betsy Mathew and my brothers Mohith Mathew and Abraham Rajath Mathew Betsy Mathew, for their unwavering love, encouragement, and support throughout my PhD journey. I also wish to thank my mother-in-law, Philomena Mathew, my brother-in-law, Don Mathew, and sister-in-law, Sithara, for their steadfast support.

Lastly and most importantly, I want to express my profound gratitude to a truly special person, my wife, Dr. Agnus T Mathew, who shares my field of study and has made this scientific voyage more comfortable and enriching. She has been a wellspring of unwavering love and energy. Her continuous and unwavering love, support, and understanding during the thesis writing phase of my PhD have been pivotal in its timely completion. Her presence has been indispensable, and without her, achieving this milestone would not have been possible. I am indebted to my lovely daughter Criselda Elizabeth Madathiparambil as she has been my source of energy for finishing this PhD.

In conclusion, I extend my heartfelt thanks to all individuals, directly or indirectly, who have extended their helping hands in the realization of this thesis.

Aldritt Scaria Madathiparambil

September 2023, Trondheim.

Preface

This thesis is submitted in partial fulfillment of the requirements for the degree Philosophiae Doctor (PhD) at the Norwegian University of Science and Technology (NTNU) in Trondheim, Norway. The candidate's supervisors are Prof. Dag W. Breiby (Department of Physics, NTNU), Dr. Pierre R. Cerasi (Department of Applied Geosciences, SINTEF Industry), and Assoc. Prof. Basab Chattopadhyay (Department of Physics, NTNU). The project was funded by the Norwegian Research Council through Petromaks2 (#280942 CuttingEdge).

The work was done at NTNU, SINTEF Industry, Trondheim, Norway, and at the European Synchrotron Radiation Facility (ESRF), Grenoble, France. Time-resolved X-ray μCT (4D-CT) using the hard X-ray transparent triaxial deformation apparatus (HADES) experiments were done at the beamline ID19. Coherent X-ray diffraction imaging (CXDI) was done at the beamline ID10. X-ray diffraction computed tomography (XRD-CT) experiment was done at the beamline ID15A.

List of papers

Paper 1

Aldritt Scaria Madathiparambil, Kim Robert Tekseth, Fredrik K. Mürer, Benoît Cordonnier, Nicolaine Agofack, Jessica McBeck, Pierre Cerasi, François Renard, Basab Chattopadhyay, Dag W. Breiby. Time-Resolved in Situ Imaging of Strain Localization in Draupne Shale Under Triaxial Compression. *Phys.Rev. Applied, vol. 20 vol. 20, no. 3, pp. 34046, Sep. 2023.*

Mechanical properties of Draupne shales were studied using Time-resolved micro-computed tomography (4D-μCT) using a triaxial rig under stress conditions similar to those prevailing in geological reservoirs. Detailed mechanical analysis of the tomography datasets using digital volume correlation to identify the in-situ investigations of deformation processes via quantification of shear and volumetric strains within the sample.

The experiment was planned by PC, NA, BC, FR, and DWB. The time-resolved 4D computed tomography (CT) was carried out by BC, PC, NA, and BC. The data was analyzed by ASM with assistance from BC, PC, JM, FR, FKM, KRT, and DWB. The draft was written by ASM and DWB. The manuscript was reviewed by all the authors.

Paper 2

Aldritt Scaria Madathiparambil, Fazel Mirzaei, Kim Robert Tekseth, Benoît Cordonnier, Nicolaine Agofack, Pierre Cerasi, François Renard, Basab Chattopadhyay, Dag W. Breiby. Mechanical response of cement and shale admixtures under cyclic triaxial loading monitored by in-situ synchrotron micro-computed tomography. *Submitted to Cement and Concrete Research.*

Cyclic loading experiments made on Portland G cement mixed with shale particles using a triaxial test apparatus monitored with synchrotron-based X-ray μCT. The temporal variations in the displacement vector field were tracked using digital volume correlation (DVC) on reconstructed tomograms. The experiment provides unmatched insight into the course of fatigue degradation within these composite samples under cyclic loading, explaining the failure process. The sample

failure occurred mostly within the cement matrix after strong compression of the softer shale particles.

A.S. Madathiparambil, N. Agofack, F. Renard, P. Cerasi, and D.W. Breiby conceived and prepared the experiment. A.S. Madathiparambil, F. Mirzaei, K.R. Tekseth, and B. Cordonnier and P. Cerasi conducted the synchrotron experiment. A.S. Madathiparambil analyzed the data with assistance from P. Cerasi, B. Chattopadhyay, and D.W. Breiby. A.S. Madathiparambil and D.W. Breiby wrote the original draft. F. Renard, P. Cerasi, and D.W. Breiby acquired funding and administrated the project. All authors contributed to the discussions and to finalizing the manuscript.

Paper 3

Basab Chattopadhyay, Aldritt S. Madathiparambil, Fredrik K. Mürer, Pierre Cerasi, Yuriy Chushkin, Federico Zontone, Alain Gibaud and Dag W. Breiby, Nanoscale imaging of shale fragments with coherent X-ray diffraction. J. Appl. Crystallogr., vol. 53, no. 6, pp. 1562–1569, 2020.

Micrometer-sized Pierre shale fragments were investigated utilizing a combined coherent diffraction imaging (CDI) and wide-angle X-ray diffraction (XRD) setup. The pore distributions and mineral inclusions were mapped in three dimensions (3D).

The experiment was planned by BC, YC, DWB, and PC. The samples were prepared by BC and PC. The experiment was carried out by BC, FKM, YC, and FZ. The data was analyzed by BC, ASM, FKM, and YC. The draft was written by BC. The manuscript was reviewed by all the authors.

Paper 4

Fredrik K. Mürer, Aldritt Scaria Madathiparambil, Kim Robert Tekseth, Marco Di Michiel, Pierre Cerasi, Basab Chattopadhyay and Dag W. Breiby. Orientational mapping of minerals in Pierre shale using X-ray diffraction tensor tomography. IUCrJ vol. 8, no. 5, pp. 747-756, 2021.

XRDTT was used to investigate a sample of Pierre shale having orientated clay minerals and high-attenuating inclusions. Complementary experiments with attenuation-contrast computed tomography (CT) were performed on the same material.

The experiment was planned by FKM, BC, MDM, and DWB. PC was in charge of sample preparation. The XRD-CT experiments were carried out by FKM, BC, ASM, KRT, and MDM. The attenuation contrast CT experiments were carried out by ASM. The data was evaluated by FKM, BC, ASM, and DWB. The draft was written by FKM and DWB.

Additional publications not included in the thesis

Fredrik K. Mürer, Basab Chattopadhyay, Aldritt Scaria Madathiparambil, Kim Robert Tekseth, Marco Di Michiel, Marianne Liebi, Magnus B. Lilledahl, Kristin Olstad and Dag W. Breiby. Quantifying the hydroxyapatite orientation near the ossification front in a piglet femoral condyle using X-ray diffraction tensor tomography. vol. 11, no. 1, pp. 2144, 2021

X-ray diffraction tensor tomography (XRDTT) and propagation phase-contrast CT were used to examine the HA orientation in a bone and cartilage sample from a piglet's femoral condyle.

The experiment was planned by FKM, DWB, BC, MBL, KO, and MDM. The sample was prepared by FKM, BC, and KO. The synchrotron experiment was carried out by FKM, BC, KRT, ASM, and MDM. FKM examined the data with the use of DWB, BC, MDM, and ML. The manuscript was written by FKM, BC, and DWB. All authors contributed to the final discussions and text finalization.

Acronyms

1D   one-dimensions.

2D   two-dimension.

3D   three-dimension.

CCS   carbon capture and storage.

CG   conjugate gradient.

CT   computed tomography.

CXDI coherent x-ray diffraction imaging.

DVC   digital volume correlation.

EOR   enhanced oil recovery.

ESRF European Synchrotron Radiation Facility.

FBP   filter backprojection.

FDK   Feldkamp-David-Kress.

FIB SEM   focussed ion beam scanning electron microscopy.

FoV   Field of view

FT   Fourier transform.

HADES   hard X-ray transparent triaxial deformation apparatus.

NPD   Norwegian Petroleum Directorate.

ROI   region of interest.

SEM scanning electron microscopy.

TEM transmission electron microscopy.

TOC total organic content.

UCT uniaxial compression test.

XRD-CT x-ray diffraction computed tomography.

XRDTT x-ray diffraction tensorial tomography.

WAXD wide-angle X-ray diffraction.

Contents

Contents

1.   Introduction

Shales are a type of fine-grained sedimentary rocks which have drawn more attention over the past decade because of their special properties as source rock or seal in oil and natural gas production, soil stabilizers, production of clays and cements, and in groundwater flow. Due to the small particle sizes and interstitial pore sizes in shales, the permeability to oil, natural gas, and water flow is extremely low. Hence, shales act as a cap rock for oil and natural gas traps and also as an aquiclude that blocks or limits the flow of groundwater. Clay mineral compositions of shale have the ability to absorb or adsorb large amounts of water, natural gas, ions, or other substances. This property of shale enables selectively and tenaciously holding or releasing fluids or ions. As a result of the capacity to store and retain water, shales are often associated with landslides. Shale may also act as a barrier for permanent plug and abandonment operations in the oil industry[1] and have the potential to seal CO_2 storage reservoirs [2]–[5].

Shales are exposed to significant loading due to both natural geological stresses, such as thermal stresses and high fluid pressure, and industrial stresses like drilling, fracturing, and fluid injection. Hence an integrated characterization of shale properties is critical. However, the extremely fine-grained nature of shales, hierarchical structure, and structural features make precise quantification challenging [6]–[9]. Knowledge of the hierarchical structure of shales is crucial for anticipating their performance in diverse uses, such as containment seals in geological carbon sequestration. Additionally, shales are as stated above, practically impermeable, making it difficult to extract fluid samples from them, which can be used to analyze their properties [10], [11]. Moreover, shales are prone to undergoing deformation and fracturing (e.g., creep deformation and fissility) [12], which can further complicate their mechanical behavior. Some shales are very ductile and prone to creep deformation, while others are very fissile and exhibit brittle fracturing. All of these factors make the study of shales challenging, but also essential for a better understanding of their geological, engineering, and environmental implications.

The macroscopic and microscopic characterization of shale formations has been made easier with the development of advanced imaging and image-based quantification tools [6]. Using traditional 2D imaging techniques the physical and chemical properties can be destructively studied at the pore scale level using techniques like scanning electron microscopy (SEM), focused ion beam (FIB)- SEM, and transmission electron microscopy (TEM) [13], [14]. These techniques are frequently inadequate or imprecise in addressing contemporary challenges, and these can also be a laborious and time-consuming process. In several shale articles, 3D imaging techniques like X-ray computed tomography (X-ray CT) have been employed to offer morphological and topological information on fine-grained components in a non-destructive manner [15], [16].

X-ray computed tomography (X-ray CT) is the process of directing X-rays at samples from multiple orientations and then measuring the decrease in transmitted intensity along a series of linear paths [17]. The decrease in intensity can be expressed as a function of X-ray energy, path length, and the attenuation coefficient of the material [18]. With the help of specialized algorithms, 3D attenuation coefficient distributions are reconstructed for the imaged volume. X-ray CT is employed to image a wide range of materials, including bones, polymers, shales, and other rocks, as well as for medical imaging, all while preserving their microstructures. Studies have demonstrated that CT can be performed in situ and combined with various contrast mechanisms, such as absorption contrast, phase contrast, and diffraction contrast. [19]–[23] .

Different X-ray imaging techniques have been developed over the years that are capable of non-destructively providing the internal structural details of the samples [6]. X-ray tomography is an increasingly used tool in the study of rocks, shales, and cement to understand the pore size and distribution, microstructures, and identify microfractures and deformation bands [6]. Numerous studies have been conducted on porous rocks such as sandstones and shales to understand their mechanical behavior under uniaxial and triaxial loading [24]–[26]. These studies use X-ray images obtained before, after, or during experiments. Earlier materials were deformed outside of the CT instrument in ex-situ testing but advances in CT technology now enable in situ testing [27], [28], where material specimens are deformed within the CT instrument. This technique facilitates the characterization of new mechanisms, such as crack opening, shear banding, and fast transformation [29], [30]. Furthermore, X-ray CT becomes a potent tool for experimental mechanics when combined with imaging analysis techniques. Digital Volume Correlation (DVC) is an image

analysis technique used to capture the deformation of a solid between two captured 3D images. It is an extension of 2D digital image correlation and enables precise measurement of 3D displacement fields using the microstructure of the registered volumes as reference points between successive images [31].

1.1   Aim and structure of the thesis.

The aim of this thesis is to provide a better understanding of the different properties of shales. The physical properties at the pore scale of shale rocks directly influence their mechanical behavior, permeability, and fluid flow characteristics, which are critical in industries like oil and gas extraction, underground storage, and environmental risk assessment. Studying shale physics at the pore scale level is essential for optimizing resource extraction techniques, assessing geological hazards, and driving innovation in energy production and storage technologies. Understanding shale's pore-scale properties is at the core of sustainable and efficient practices in various fields. To do so, we make use of non-destructive imaging and measuring techniques which are able to probe the shale at microscopic level while under changing loads. The goal is to shed light on deformation mechanisms bringing shales and shale mixtures to fracture and loss of load-bearing capacity.

Shale is a sedimentary rock widely distributed across the globe and is frequently relied upon to ensure the isolation of subsurface activities from shallower layers. Thus, studying the mechanical properties of shales is necessary for predicting their behavior over time, such as how they might deform or erode in response to changes in the surrounding environment. Therefore, investigating the mechanical properties of shales is essential for gaining a comprehensive understanding of these rocks and for effectively using them in a variety of applications. Such an understanding may lead to reducing uncertainty on operation limits in the subsurface, commonly known as "de-risking".

Numerous ex-situ X-ray CT experiments have been conducted over time to investigate the mechanical response of shales, involving post-mortem analysis to characterize the behavior of the shales. There is a lack of understanding of the different internal microscale mechanisms during mechanical testing, that leads to structural failure. Studies showing a linear stress-strain behavior in shale have assumed a homogeneous strain distribution. However, there are few insights into how strain localization occurs before and after bulk failure. The dominant strain localization mechanism for shales during macroscopic failure must also be evaluated.

3

The extraction of shale oil and gas generates a residue known as shale waste, which poses a potential environmental threat if not handled correctly [32]. Shale waste typically includes various pollutants and efforts are underway to find ways to reuse or recycle shale waste, such as its utilization in soil stabilization, which could minimize the requirement for shale waste disposal in landfills [33]. Consequently, it becomes essential to investigate the long-term stability of using shale waste with cement for soil stabilization. To comprehensively assess the long-term stability of such materials, they must be subjected to cyclic loading and unloading to fully understand the strain accumulation and development of fatigue. Such cyclic loading occurs for example due to seasonal variations in temperature and water content. We have explored the potential of using continuous X-ray imaging of shale mixed with cement as it provides a much-improved understanding of the deformation in composite materials containing both a brittle (cement) and ductile (clayey shale) component phase.

The complex mineralogy, anisotropic behavior, and complex pore structure make it challenging to study the mineral orientation and distribution in shales. Furthermore, due to its fragile nature, limited availability, and difficulty preserving the original structure during preparation, new methods for non-destructive characterization are required. Hence, we have explored the potential of X-ray diffraction CT (XRD-CT) and X-ray diffraction tensorial tomography (XRDTT) for this purpose. XRD-CT/TT has been demonstrated as a method to study the orientation features of minerals and can provide insights into the complicated structures of shales. Furthermore, coherent X-ray diffraction imaging (CXDI) could provide high-resolution 3D electron-density maps of shale samples with spatial resolutions as precise as 5 nm. This method yields valuable insights into the internal structure and morphology of shale fragments. To comprehensively analyze the multiscale distribution of shale minerals we use CXDI, XRD-CT/TT, and attenuation-based contrast CT to demonstrate the multiscale distribution of shale minerals.

The thesis comprises six chapters, including an introduction (Chapter 1). Chapter 2 summarizes the scientific background relevant to the thesis, including an overview of X-ray imaging techniques and a brief discussion of the various CT techniques used. The strain theory employed in the thesis is also presented. Chapter 3 describes the materials used in the research. Chapter 4 summarizes the key findings of four studies in this thesis, two as main author and two as co-author. Chapter 5 offers concluding remarks on the thesis's findings and provides an outlook on prospects. Chapter

6 details the innovative experimental approaches used in the individual manuscripts and the author's contribution to each manuscript.

In **Paper 1**, the mechanical properties of a sealing caprock in the Norwegian offshore, the Draupne shale, are investigated using a novel experimental technique of 4D X-ray microtomography coupled with a triaxial deformation apparatus. This work used a monotonous or uniform loading pattern to study the mechanical properties of the shale. By utilizing DVC on the experimental data, it is possible to break down the strain into different elements, including dilation, compaction, and shear. In **paper 2**, we demonstrated the potential of the 4D X-ray microtomography coupled with triaxial deformation apparatus and cyclic loading and unloading patterns to study the evolution of fatigue in cement-shale composites. We applied DVC on the captured data to elucidate the microstructural mechanisms of strain propagation and localization during such a cyclic loading scheme. **Paper 3** uses Coherent X-ray diffraction (CXDI) imaging together with wide-angle X-ray diffraction to explore and map an outcrop shale from the USA often used for its representativeness for North Sea shales, Pierre shale's nanometer-scale morphology and mineral distribution. CXDI allowed mapping the detailed information of the nanoscale mineralogy and pore structure in micrometer-sized samples with a resolution of 26 nm. We demonstrate how the combination of CXDI-WAXD can be used to study shales and other geological structures at the nanoscale by using a series of measurements, that can be performed on specimens including cuttings from drillings. **Paper 4** is a complementary work to **paper 3** and explores the mineralogy and 3D orientation of clay minerals in Pierre shales using a combination of different experiments and analyses. Here, XRD-CT is used to map the mineralogy and the orientation of clay minerals in 3D while XRDTT is used to study the clay mineral orientation respectively in millimeter-sized samples.

5

2. Background

This chapter will encapsulate the essential main theory and prepare the reader for the results presented in the papers in the following chapters. A brief introduction to different X-ray techniques is given and in addition the theoretical background for different types of computed tomography (CT), digital volume correlation (DVC) as well as the theory used for the calculation of the strains. The reader is assumed to have some preexisting knowledge in physics to understand this thesis.

2.1. X-ray techniques

X-rays were first studied by William Conrad Röntgen on November 5th, 1895, and he called it X-rays[34]. These photons have energy ranges approximately from 120 eV (electron volts) to 1000 keV, corresponding to wavelength ranges between 10 nm to 1 pm. The X-rays are traditionally divided into two groups depending on their energies. Lower energy X-rays are termed soft X-rays, within the energy range of 0.1- 10 keV [35],[36]. Soft X-rays are easily absorbed by most substances. Higher energy X-rays are termed hard X-rays, and their energies can range from 6 keV up to 1 MeV [35],[36]. Hard X-rays have a lower absorption (lower attenuation) and a higher penetration and are used for the experiments in this thesis.

X-rays can be generated from different sources, the following three devices and methods are the most used namely X-ray tube, rotating anodes, and synchrotrons [17], [33]. In this thesis, the data presented are generated from the synchrotron source. Some of the supporting data for the experiments were made using a Nikon XT H 225 ST CT instrument. X-rays are produced in laboratory sources either by an evacuated tube or a rotating anode. Usually, the filaments act as the cathode and will emit electrons which are accelerated in the field provided across the vacuum to the anode. Commonly used anode materials are copper (Cu), molybdenum (Mo), silver (Ag), and tungsten (W) depending on the required wavelength [17]. When the high energy electrons suddenly decelerate in the heavy metal target, according to Maxwell's equation, they will emit a continuous radiation known as Bremsstrahlung or braking radiation as shown by figure 2.1 [17],

[33]. When the inner shell electrons are knocked out by the incident electrons, an electron from the neighboring shell will drop down to fill the vacancy thereby emitting the difference in energy between the shells. These emissions that are superimposed on the bremsstrahlung are called the characteristic emissions as can be seen in figure 2.1.
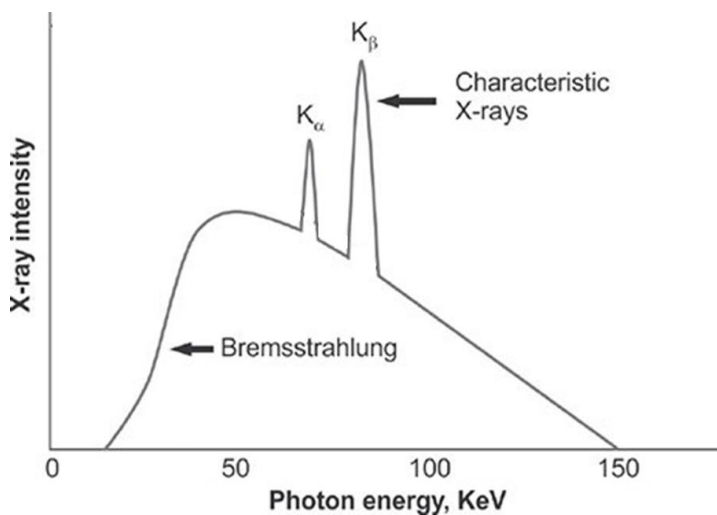
Figure 2.1 Schematic illustration of the emitted spectrum from an X-ray tube. The continuous bremsstrahlung and the superimposed characteristic radiations are shown

A synchrotron is an alternative method to produce X-ray particles where electrons are accelerated in a storage ring to produce X-rays. Compared with the home laboratory sources the main advantage of synchrotron radiation is related to a property called *brilliance* which is defined as [17]

$$Brilliance = \frac{(Number\ of\ photons\ per\ second)}{[\xi[mrad^2\ mm^2](0.1\%\ BW)]}$$

where ξ is the emittance of the source which is the product of the size of the source and BW is the bandwidth [17]. Brilliance takes into account the beam dimension and is maximized by making the size of the beam and the divergence as small as possible and the photon flux as large as possible. In short high brilliance means that a large number of photons are emitted from a small emitting

surfaced source in a narrow cone, and thus a high brilliant source helps to conduct experiments that are otherwise infeasible in the home-laboratory.

2.2. Computed Tomography

Tomography originates from the Greek words 'tomos' and 'graphia', meaning 'slice' and 'writing' [37]. Tomography is the cross-sectional imaging of objects by illuminating any object from different directions. The term computed in CT (computed tomography) implies using numerical methods to produce the images. CT operations are based on X-rays [37]–[39]. X-ray CT technology, which was made by combining computer technology with X-ray technology, was invented in 1972 by British engineer Godfrey N. Hounsfield and American physicist Allan M. Cormack [40]. They were named as "CT's father." Subsequently, Godfrey N. Hounsfield won a Nobel Prize in 1979, due to the success of CT invention [38]. So, the technique of computed tomography (CT) acquires X-ray projections in multiple angles through an object and creates or reconstructs its attenuation characteristics. CT provides the internal 3-dimensional (3D) maps of the object and can be considered as an extended version of the 2-dimensional (2D) radiographic X-ray imaging [37], [39]. With the technological advances of CT, the technique has been increasingly used for the non-destructive visualization and quantification of a vast range of materials, ranging from bones, polymer, and geological samples in three-dimensions and for medical imaging. New developments have made it possible to investigate the pore network properties, micro-textures, fractures, and transport properties at spatial resolutions down to the nanometer level. 4-dimensional time-resolved CT has now recently been used extensively to monitor dynamic processes like mechanical responses and fluid penetration of geomaterials [26][41]. There exist different measurement geometries for CT and in this thesis, the experiments were done using a parallel beam geometry.

The interaction of these X-rays with matter will consequently attenuate X-rays that propagate through a sample[17], [37], [38], [39]. This results in loss of photons from incident flux and the process is called attenuation. This attenuation rate of photons through a differential section in a material can be related to the attenuation coefficient and the position of the photons in the material given by

$$\frac{dI}{dl} = -\mu I \qquad\qquad 2.1$$

where incident X-ray intensity (I), μ is the attenuation coefficient and l is the position of the X-rays through a material. Now integrating equation 2.1, we get the Beer-Lamberts law in the object coordinate system [x, y] and the 1D intensity profile measured along the x-direction is described as:

$$I(x) = I_0 \exp\left[-\int_0^l \mu(x,y)dy\right] \qquad 2.2$$

where $\mu(x,y)$ is the linear attenuation coefficient [37],[38] of the material that depends on the energy of the X-rays. I_0 and I are the incident and the attenuated X-ray photon intensities and the integral in equation 2.2 represents the path of the beam through the sample. The equation 2.2 can be represented as

$$I = I_0 \exp\left[-\sum_i \mu_i X_i\right] \qquad 2.3$$

where, μ_i is the attenuation of the ith phase and X_i is the thickness or path length for each phase [17][39].

Rearranging the equation 2.2 we define the projection p as:

$$p = -\ln\left(\frac{I(x)}{I_0}\right) = \int \mu(x,y)dy \qquad 2.4$$

The algorithms used for the CT image reconstruction are based on the mathematical foundations of the Radon transform and the inverse Radon transform published in 1917 by the Austrian mathematician Johann Radon. The Radon theorem states that image reconstruction is possible from an image distribution function that can be obtained from an infinite set of projections at different angles. The relationship between the slices and projections is described mathematically by the Radon transform [42]–[45]. The Radon transform is the mathematical description of a forward projection operation and gives a mathematical description of the measured intensity on a detector in attenuation contrast CT [37],[39]. For θ, the projection can be related to the object function as

$$p_\theta = \int f(r,s)ds \qquad 2.5$$

$$= \iint_{-\infty}^{+\infty} f(x,y)\delta(x\cos\theta - y\sin\theta - r)dxdy \qquad 2.6$$

where δ is the delta distribution and the polar coordinates are defined as $r = x\cos\theta - y\sin\theta$ and $s = x\sin\theta + y\cos\theta$. On comparing the equations 2.4 and 2.6 we get the following equation.

$$\ln\left(\frac{I(x)}{I_0}\right) = -\iint_{-\infty}^{\infty} \mu(x,y)\delta(x\cos\theta - y\sin\theta - r)dxdy \qquad 2.7$$

Equation 2.7 shows the relation between the measured intensity and attenuation coefficient μ. The set of whole measured projections for different angles θ is called a sinogram. The idea is to determine the object function $f(x, y)$ which involves inverting the Radon function. This process is typically performed using an approximate method and is known as tomography reconstruction. So, we need to use an inverse radon function for the tomographic reconstruction. A *backprojection* of the measured data produces a blurred reconstruction due to the delta distribution in the equations mentioned above [17], [18], [39]. To obtain a good reconstruction, we need to apply a filter followed by the backprojection.

A direct two-dimensional deconvolution is time-consuming as well as inaccurate. A deconvolution in frequency space is multiplication so we can use the Fourier transform to solve the issue. The idea of filtered back projection (FPB) is to calculate the one-dimensional Fourier transform of a line integral, multiply with a filter function correcting for the blur, calculate the one-dimensional inverse Fourier transform, and perform the backprojection [46], [47]. The FBP algorithm is here briefly described for the case of parallel beams as used in scattering CT, whereas clinical and home-laboratory CT typically uses the Feldkamp-David-Kress (FDK) algorithm, a FBP optimized for conical beams [48]. The FBP algorithm relies on the Fourier slice theorem.
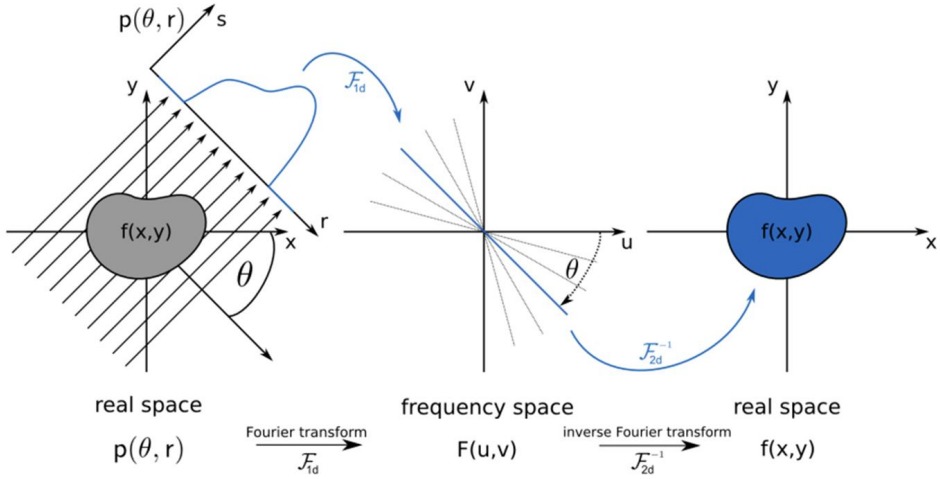
Figure 2.2 Fourier slice theorem. The object function is projected in beam direction forming the line integral *p(θ, r)*. The Fourier slice theorem (or central slice theorem) states that the one-dimensional Fourier transform of a single projection *p(θ, r)* corresponds to a slice of the two-dimensional Fourier transform of the object function under the same angle *θ*. If the two-dimensional Fourier transform is sampled, the object function *f(x, y)* is determined via two-dimensional inverse Fourier transform.

The Fourier slices theorem or central slice theorem states that a one-dimensional Fourier transform of a projection *p (θ, r)* at an angle *θ* is equal to the 2D Fourier transform of a slice of the object *f (x, y)* at the same angle [46]. The 1D FT of *p (θ, r)* is

$$P(\theta, \omega) = F_{1D}\{p(\theta, r)\}$$

$$= \int_{-\infty}^{\infty} p(\theta, r) e^{-2\pi i \omega r} dr \qquad 2.8$$

Combining equations 2.8 and 2.6 we get the following

$$P(\theta, \omega) = \iint_{-\infty}^{\infty} f(x, y) e^{-2\pi i(ux+vy)} dx dy \,|_{u=\omega \cos\theta, v=-\omega \sin\theta,}$$

$$= F_{2D}\{f(x, y)\}(u, v)|_{u=\omega \cos\theta, v=-\omega \sin\theta,}$$

$$= F(u = \omega \cos\theta, v = -\omega \sin\theta) \qquad 2.9$$

where $F(u,v)$ is the 2D Fourier transform for $f(x,y)$ and $u= \omega \cos\theta$ and $v= -\omega \sin\theta$ are the Cartesian Fourier frequencies [17], [18], [37], [39].

In the numerical CT reconstruction, the filtering of each of the projections is done in Fourier space and a detailed sketch describing the CT image reconstruction using FBP is shown in figure 2.3 [47]. Then the backprojection is made to recover the measured object in real space after the filter is applied in the Fourier space.
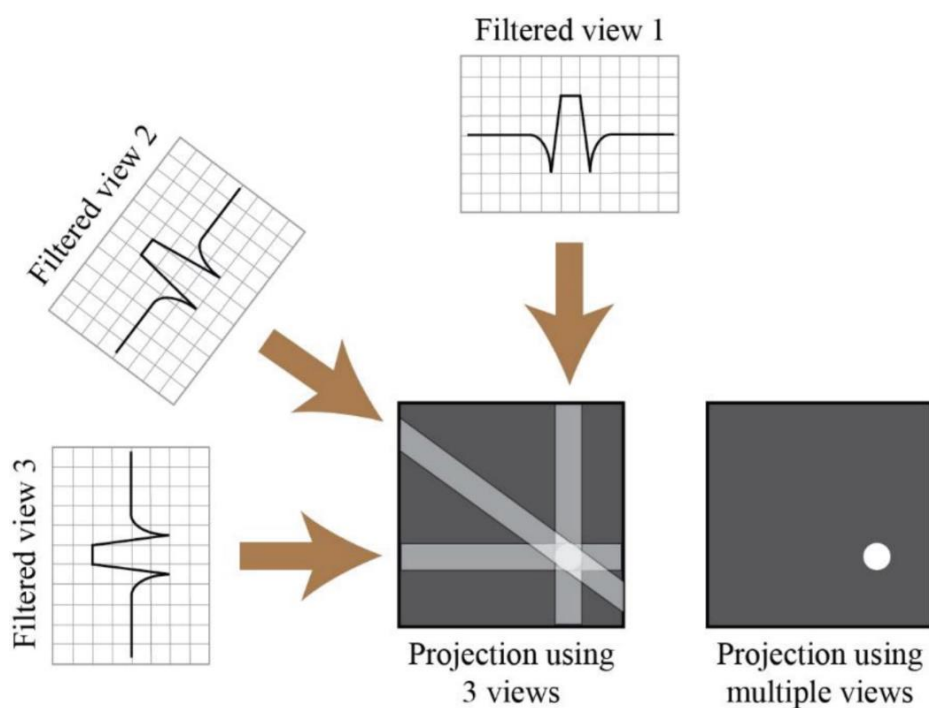
Figure 2.3 Sketch describes the CT image reconstruction process using a backprojection algorithm. Projections obtained for each rotation are filtered and back-projected as shown. The filter helps to remove the blurring resulting from a simple backprojection. Figure adapted from [47].

There are different filters for CT characteristics like noise and spatial resolution like Cosine, Hamming, Hann, or Shepp-Logan filters as indicated by figure 2.4 [48]. The function shown in figure 2.4 can be expressed as

$$f(\omega) = |\omega| \, b(\omega) \qquad\qquad 2.10$$

where $b(\omega)$ varies according to the following filter function

$$b(\omega) = \begin{cases} 1 & \text{Ram} - \text{Lak filter} \\ \text{sinc}\omega & \text{Shepp} - \text{Logan filter} \\ \cos\pi\omega & \text{Cosine filter} \\ \alpha + (1-\alpha)\cos2\pi\omega & \text{Hann}(\alpha = 0.5) \text{ and Hamming } (\alpha = 0.54)\text{filter} \end{cases} \qquad 2.11$$
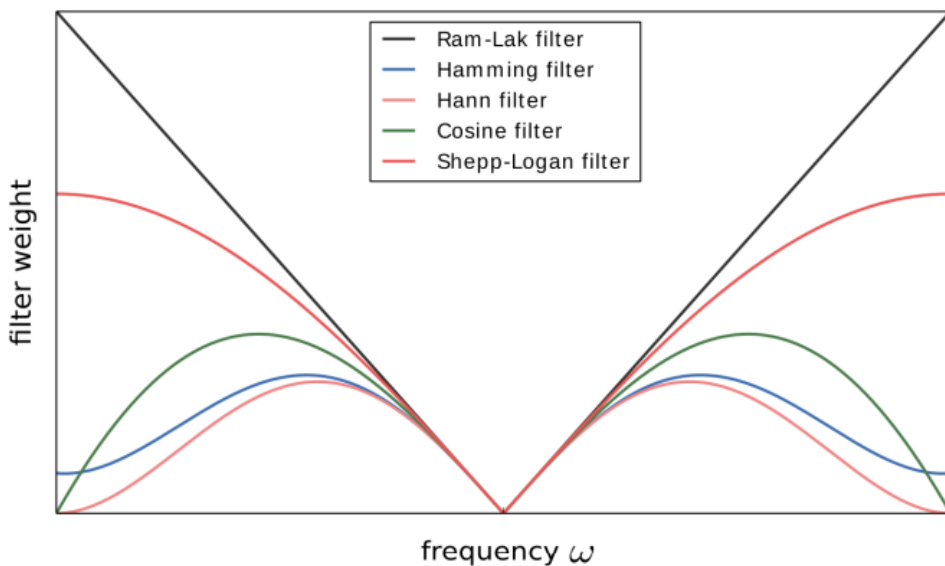
Figure 2.4 Shows the five different FBP filter functions.

2.2.1 X-ray diffraction computed tomography.

X-ray diffraction computed tomography (XRD-CT) is a technique that uses information from the diffracted X-rays rather than the conventional X-ray attenuation used in CT [20],[49]–[51]. In this section, only a brief outline of the technique is made. XRD-CT provides a 3D map where each pixel or voxel contains a distinct diffraction pattern and helps in providing information on the crystalline phases in the samples non-destructively. In XRD-CT, the measured diffracted intensities are used to reconstruct the scattering characteristics of each voxel in the sample volume [20]. The scattered signal from the sample contains the orientation information and hence XRD-CT can also provide a 3D orientation of the structures in the sample [49]–[55]. Using XRD-CT, the scattering patterns from the different components in the sample could be separated and the spatial distribution of each phase can be made with good sensitivity. This technique also reduces the efforts required for the sample preparations (like slicing, and drying) and allows studying the sample without complex environments like vacuum or inert atmospheres.

XRD-CT typically is performed using high-energy synchrotron X-rays due to the high flux at a (close to) monochromatic beam and a small beam spot [33]. Recently XRD-CT has been used for imaging materials with hierarchical features like bone [20], [51], [56],[57] cartilage, muscles [58], fossils [20], catalysts [59], [60], inorganic materials and construction materials [50]. The technique allows retrieving information about the sample features in the nanometer or Angstrom range, hence it has been used for studying hierarchically structured materials like bones, and shales. Even though there are a large number of publications employing the XRD-CT technique, studies have reported that each voxel in the volume of the imaged sample should have a large number of isotropically oriented crystallites or be weakly textured as in bone [20], [50].

Figure 2.5 shows the experimental setup of the XRD-CT. The experimental setup for XRD-CT consists of a monochromatic and collimated synchrotron X-ray. XRD-CT is based on recording diffraction data while translating (along x and y, perpendicular to the incident beam direction) and rotating (ω, around the vertical z-axis) the sample irradiated by the pencil beam [20], [61]. The 2D diffraction patterns are recorded using steps in the horizontal scan (along y), and scans were taken with steps over the rotation angle (ω). The beam has a rectangular shape with dimensions most often in the range of 1-100 μm and the final voxel size of the reconstructed tomograms depends on these dimensions. The resolution of the final reconstructed images is directly determined by the

scanning step size. This is in turn limited by the focusing capability of the beamline and by the scattering properties of the sample. In addition, the resolution also depends on the angular range, number of projections, and reconstruction method.

$N_y \times N_\omega$ 2D diffractograms are recorded during the XRD-CT experiment. These diffractograms are usually corrected for the beam flux and detector gain and then azimuthally integrated to obtain a series of 1D diffraction profiles. Then the regions of interest (ROIs), corresponding to different scattering contributions will be selected to create the sinograms $Sp(y,\omega)$ corresponding to the specific phases. These sinograms are similar to the sinograms of attenuation contrast CT described in the previous section. Tomographic reconstruction is made to reconstruct the cross-sections mapping the spatial distribution of the selected phase from the sinograms [20], [23]. The reconstruction gives the variation of the intensity of any local diffraction as a function of x, y, and z, thus obtaining axial slices of the corresponding phases.
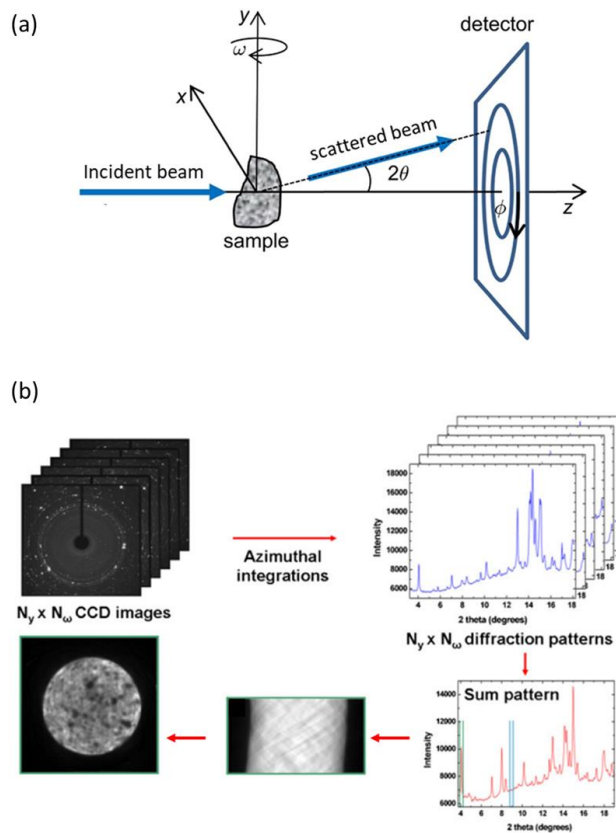
Figure 2.5 (a) Generic sketch of the XRD-CT (adapted from Fredrik et al [4]), where a collimated synchrotron X-ray beam enters the sample, and a fraction of the beam is scattered and exists. (b) The reconstruction scheme of the XRD-CT is illustrated. The 2D diffraction patterns are collected for all the different translations (y) and rotations (ω) of the sample. The obtained patterns are then azimuthally integrated to obtain a set of linear diffraction patterns. The selected peaks on the linear diffraction patterns are used to make the sinograms which is a function of the intensity that depends on y and ω. From these sinograms, the spatial distribution of the selected phases is made. The figure is adapted with permission from [23].

2.2.2 Coherent X-ray Diffraction Imaging

Over the past decade, coherent X-ray diffraction imaging (CXDI) has evolved as an elegant, and reliable imaging approach to obtain the 3-dimensional images of the micrometer-sized samples with a resolution of 20-30 nm. Recently CXDI has been demonstrated on a wide range of samples to understand the structural aspects of coccolithophores [62], polymer microcomposites [63], [64] vaterite-to-calcite phase transitions in microparticles [65]. In CXDI, the image of the object is reconstructed from the far-field diffraction pattern obtained with a highly coherent X-ray beam [66]–[68]. Through CXDI 3D electron density maps of the sample can be obtained with a high resolution [69]. One of the advantages of CXDI is that it can be used in both polycrystalline and amorphous samples, unlike other CT-based scattering techniques [66], [69]. Unlike other X-ray-based CT techniques or other electron microscopy techniques (scanning electron microscopy, transmission electron microscopy) CXDI does not require a vacuum which reduces the challenges with the sample [69]. In this thesis, CXDI was used to study the internal structure and morphology of shale fragments.

Figure 2.6 shows the sketch of the experimental setup of CXDI. Typically, the micro-sized samples are mounted on a membrane under ambient conditions. The membranes are usually made from Si_3N_4 which are transparent to X-rays and the samples are fixed on the surface by capillary forces. A beamstop is used to block the intense direct beam to prevent damage to the detector. The sample to the detector distance is denoted as L, in our case, it was 5.25 m, and a Maxipix detector was used to collect the 2 D scattering patterns [70]. Typically, the sample sizes are between 1-4 µm in diameter and mounted on the membrane and then illuminated by X-rays with high spatial coherence and the speckle patterns are recorded by a detector. The scattering measurements were carried out at projection angles ω with respect to the normal of the membrane surface. At each projection angle, a small angle scattering pattern was collected on the 2D detector using an exposure time of about 2.0 s.
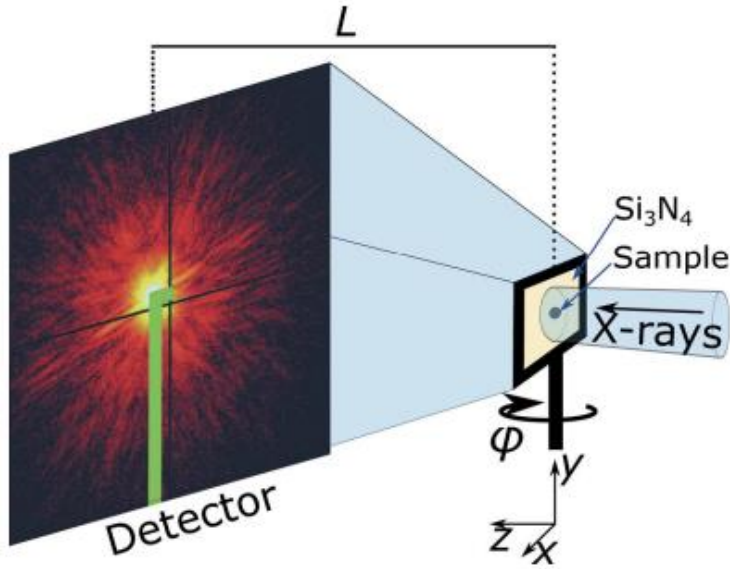
Figure 2.6 The Experimental setup of the CXDI is shown here. The figure is adapted with permission from [64].

To collect the speckle patterns with good visibility, incident X-rays must have almost complete spatial coherence [62], [64]. The transverse coherence length of the beam should be larger than the size of the object; for the speckled diffraction pattern to be recorded by the detector. The measured far-field diffraction intensity (I) is directly proportional to the absolute square of the modulus of the Fourier transform (FT) of the sample electron density $\rho(\mathbf{r})$ [66].

$$I(\mathbf{q}) \propto |F(\mathbf{q})|^2 \qquad\qquad 2.12$$

where q is the scattering vector and F($\mathbf{q}$) is defined as

$$F(\mathbf{q}) = |F(\mathbf{q})| \exp[-i\varphi(\mathbf{q})] = \text{FT} (\rho(\mathbf{r})) \qquad\qquad 2.13$$

The above equation shows that the knowledge of the phase information is necessary for retrieving the image. As we are measuring only the intensity the phase information is lost in the experiment. The lost phase of the scattered field can be reconstructed using iterative numerical algorithms relying on appropriate constraints. Using an iterative phase-recovery algorithm an initial guess of

the phase is used as an input [71]. The algorithm then updates the phase based on a comparison of the forward simulated scattered intensity from the sample model and the measured intensity. An oversampling condition is also required by the reconstruction algorithm, in practice, the detector pixel size should be three times smaller than the speckles in the diffraction pattern.

$$s = \frac{D\lambda}{3p} \qquad\qquad 2.14$$

where D is the sample to detector distance, λ is the wavelength of the X-rays, s is the sample size and p is the detector pixel size. The spatial resolution of the samples is estimated using a phase retrieval transfer function and it depends on the size of the samples. This means that we obtain a weaker signal from smaller samples and hence a poor resolution.

2.3. Strain calculation

Time-resolved X-ray μCT (4D-CT) has opened the possibility of monitoring dynamic processes like the mechanical behavior of geological systems [72]–[75]. The hard X-ray transparent triaxial deformation apparatus (HADES) installed at the ID19 beamline at the European synchrotron radiation facility (ESRF) was used for studies here [76]. It allows us to study the evolution of deformation in rocks at loading conditions similar to conditions found in the earth's crust. This apparatus has a low X-ray attenuation for photon energies > 60 keV and can be used to apply stresses both axially (up to 200 MPa) and radially (up to 100 MPa) at temperatures up to 200°C, while the pore fluid pressure can be varied from 0.1 to 100 MPa [76]. The sample chamber allows cylindrical samples with dimensions of 5 mm diameter and height of 10 mm.

The main body of the triaxial cell is machined from a single piece of titanium with a wall thickness surrounding the sample of 5 mm [26], [30], [77]. The triaxial rig consists of two pumps that control the axial load and confining pressure [76]. It also consists of two pumps that control the pore fluid, a heating system integrated into the rig, and the experiments in this thesis being at room temperature. The rock sample was surrounded by an elastomer, and the confining pressure was applied to the elastomer casing using a silicone jacket [76]. The sample was installed between two stainless steel pistons, with the axial loading imposed by the movable upper piston. The HADES triaxial cell is rotated across 180º to obtain 2D radiographic scans [26], [30] [76],[78]. A total of 2500 2D radiographs are acquired, and the three-dimensional tomogram is reconstructed using a backprojection algorithm described in the previous section, using this set of projections.
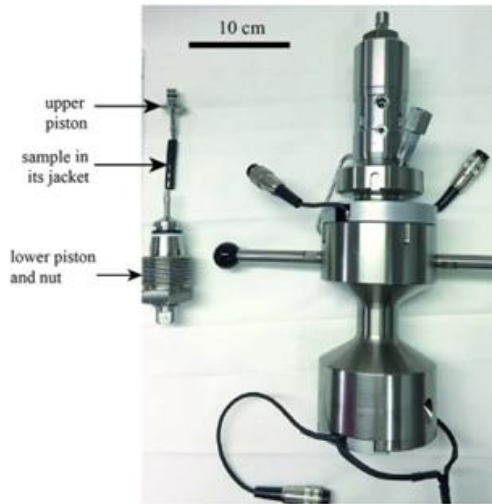
Figure 2.7 Main body of the HADES rig. (*a*) Sample assembly and body of the rig. The figure is used with permission from [76].

2.3.1 Digital Volume Correlation

Digital volume correlation (DVC) is a non-invasive experimental technique used to measure the deformation of materials, biological samples, and medical applications in three dimensions (3D) [78]–[80]. DVC allows for the measurement of displacement fields and strains within a sample, providing valuable insight into the mechanical behavior of the material or tissue under study [81]. The technique involves correlating two or more 3D volumes of a sample, acquired using techniques such as computed tomography (CT) or magnetic resonance imaging (MRI), before and after deformation [82]. The displacement field between the two volumes is then calculated using digital image correlation algorithms [82].

19
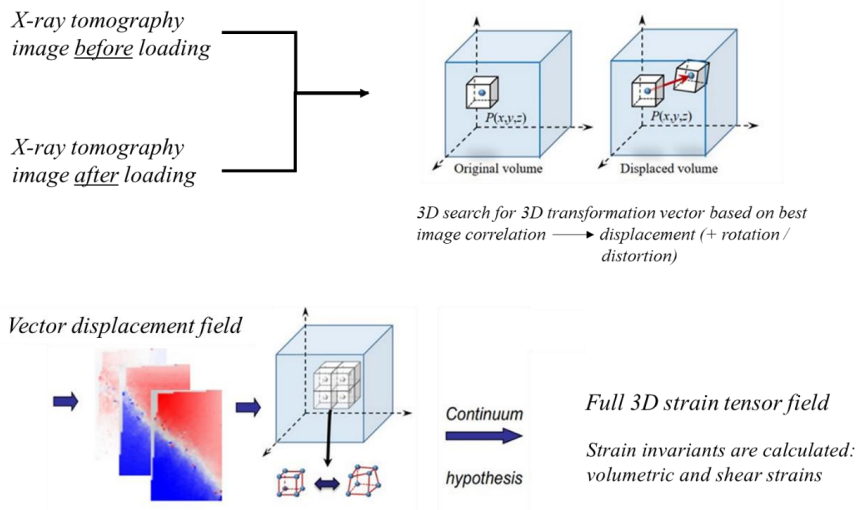
Figure 2.8 Explains the process of digital volume correlation on how the algorithm searches for the displacement fields and how the vector displacement fields, and the strain tensor are obtained.

DVC has been used in a wide range of applications, including studying the deformation of bone under mechanical loading, monitoring the mechanical behavior of materials under stress, and investigating the deformation of soft tissues such as the brain or heart [80]–[85]. Recent developments in DVC have focused on improving the accuracy and speed of the technique, as well as developing new methods for analyzing the large amounts of data generated by DVC experiments. For example, machine learning algorithms have been used to automate the process of image registration and improve the accuracy of the displacement measurements. Overall, DVC is a valuable technique for studying the mechanical behavior of materials and tissues, with a wide range of potential applications in engineering, medicine, and biology.

2.3.2 Theory of strain calculation

DVC was used to obtain the displacement vector between a set of reconstructed 3D tomograms, obtained from triaxial loading at incremental stress steps. This technique, as mentioned earlier, finds out the displacement of voxel **r** from **f** ⟶**g** defined by the field **u(r),** and the images can be correlated as **g (x + u(r)) = f(r)** [82], [86]–[88]. Here for the thesis, Tomowarp2 was used to compute the displacement fields between the pair of 3D tomograms. Then using these displacement fields, the evolving incremental strain distributions between the pair of 3D tomograms are calculated.

Tomograms (3D images) are divided into subvolumes that are distributed over a regular grid that covers the entire sample volume. Subvolumes in one 3D image are mapped onto subvolumes in another image by TomoWarp2, which identifies similar patterns within these subvolumes by translations and rotations [31], [88]–[90]. Division of subvolumes requires a node space and mapping subvolumes requires a correlation window size, which are user-defined input parameters. The search window size determines the maximum detected displacement magnitudes, and so larger changes in the macroscopic axial strain require larger search window sizes. The incremental 2nd rank infinitesimal strain tensor ε can be derived from the incremental displacement fields [91], [92]. The theory used for the calculation of the strains is described in this section.

Consider an elastic material where **u(x)** represents the displacement from the original location of the material at **x**, and the displacement of a nearby point originally at **x + δx** can be written as

$$u_i(\boldsymbol{x} + \boldsymbol{\delta x}) \approx u_i(\boldsymbol{x}) + \frac{\partial u_i(\boldsymbol{x})}{\partial x_j} \delta x_j \qquad 2.15$$
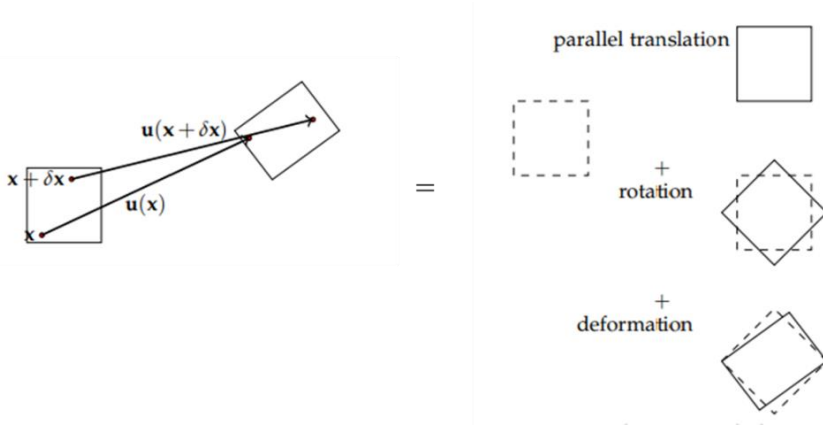
Figure 2.9 The sketch showing the deformation of a body. The body is displaced, rotated, and deformed.

We will now restrict ourselves to a linearized analysis in which the displacement derivates are small, $\left|\frac{\partial u_i}{\partial x_j}\right| \ll 1$. The term $\frac{\partial u_i}{\partial x_j}$ is known as the displacement gradient tensor and is a second-order tensor [94].

$$\frac{\partial u_i}{\partial x_j} = \begin{bmatrix} \dfrac{\partial u_1}{\partial x_1} & \dfrac{\partial u_1}{\partial x_2} & \dfrac{\partial u_1}{\partial x_3} \\[2ex] \dfrac{\partial u_2}{\partial x_1} & \dfrac{\partial u_2}{\partial x_2} & \dfrac{\partial u_2}{\partial x_3} \\[2ex] \dfrac{\partial u_3}{\partial x_1} & \dfrac{\partial u_3}{\partial x_2} & \dfrac{\partial u_3}{\partial x_3} \end{bmatrix} \qquad 2.16$$

$$\begin{bmatrix} \dfrac{\partial u_1}{\partial x_1} & \dfrac{\partial u_1}{\partial x_2} & \dfrac{\partial u_1}{\partial x_3} \\[2ex] \dfrac{\partial u_2}{\partial x_1} & \dfrac{\partial u_2}{\partial x_2} & \dfrac{\partial u_2}{\partial x_3} \\[2ex] \dfrac{\partial u_3}{\partial x_1} & \dfrac{\partial u_3}{\partial x_2} & \dfrac{\partial u_3}{\partial x_3} \end{bmatrix} = \begin{bmatrix} \dfrac{\partial u_1}{\partial x_1} & \dfrac{1}{2}\left[\dfrac{\partial u_1}{\partial x_2}+\dfrac{\partial u_2}{\partial x_1}\right] & \dfrac{1}{2}\left[\dfrac{\partial u_1}{\partial x_3}+\dfrac{\partial u_3}{\partial x_1}\right] \\[2ex] \dfrac{1}{2}\left[\dfrac{\partial u_1}{\partial x_2}+\dfrac{\partial u_2}{\partial x_1}\right] & \dfrac{\partial u_2}{\partial x_2} & \dfrac{1}{2}\left[\dfrac{\partial u_2}{\partial x_3}+\dfrac{\partial u_3}{\partial x_2}\right] \\[2ex] \dfrac{1}{2}\left[\dfrac{\partial u_1}{\partial x_3}+\dfrac{\partial u_3}{\partial x_1}\right] & \dfrac{1}{2}\left[\dfrac{\partial u_2}{\partial x_3}+\dfrac{\partial u_3}{\partial x_2}\right] & \dfrac{\partial u_3}{\partial x_3} \end{bmatrix}$$

$$-\begin{bmatrix} 0 & \frac{1}{2}\left[\frac{\partial u_2}{\partial x_1} - \frac{\partial u_1}{\partial x_2}\right] & \frac{1}{2}\left[\frac{\partial u_3}{\partial x_1} - \frac{\partial u_1}{\partial x_3}\right] \\ -\frac{1}{2}\left[\frac{\partial u_2}{\partial x_1} - \frac{\partial u_1}{\partial x_2}\right] & 0 & \frac{1}{2}\left[\frac{\partial u_3}{\partial x_2} - \frac{\partial u_2}{\partial x_3}\right] \\ -\frac{1}{2}\left[\frac{\partial u_3}{\partial x_1} - \frac{\partial u_1}{\partial x_3}\right] & -\frac{1}{2}\left[\frac{\partial u_3}{\partial x_2} - \frac{\partial u_2}{\partial x_3}\right] & 0 \end{bmatrix} \qquad 2.17$$

The above equation 2.17 can be written as the sum of the infinitesimal strain tensor (ε_{ij}) and the rotation tensor (ω_{ij}). The first part of equation 2.17 is called the strain tensor and is ''symmetric'', and the second part is the rotation tensor which is antisymmetric [91], [92].

$$\varepsilon_{ij} = \frac{1}{2}\left[\frac{\partial u_i}{\partial x_j} + \frac{\partial u_j}{\partial x_i}\right] = \frac{1}{2}\left[u_{ij} + u_{ji}\right] = \begin{bmatrix} \varepsilon_{11} & \varepsilon_{12} & \varepsilon_{13} \\ \varepsilon_{21} & \varepsilon_{22} & \varepsilon_{23} \\ \varepsilon_{31} & \varepsilon_{32} & \varepsilon_{33} \end{bmatrix} \qquad 2.18$$

As the strain tensor ε_{ij} is symmetric the eigenvectors v_1, v_2, and v_3 are the principal directions of the strain. The principal directions are the directions where the shear strain is zero i.e., no shear strain. The eigenvalues λ_1, λ_2, and λ_3 are the principal strains and they give the unit elongations in the principal directions. The eigen values λ_1, λ_2, and λ_3 are called the maximum, medium, and minimum principal strain, respectively [94]. Due to the symmetry condition of the strain tensor, it has only 6 independent components, i.e., $\varepsilon_{12} = \varepsilon_{21}$, $\varepsilon_{13} = \varepsilon_{31}$ and $\varepsilon_{23} = \varepsilon_{32}$ [94].
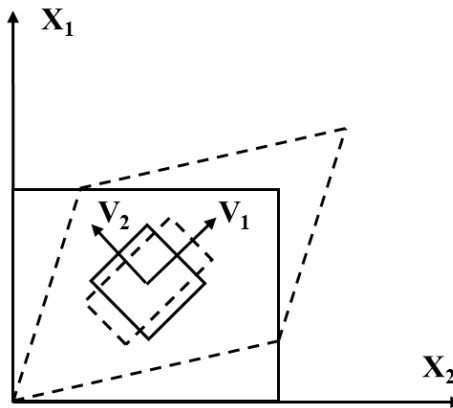

Figure 2.10 The meaning of the principal directions. The solid line represents a body before deformation and the dashed lines represent the body after deformation. This deformation is called

pure shear. The eigenvectors of the corresponding strain tensor at any point are given by v1 and v2. It is to be noted that v1 and v2 are aligned with the central square which is deformed to a rectangle.

The second term of equation 2.17 is called the rotation tensor which is antisymmetric and is defined as

$$\omega_{ij} = \frac{1}{2}\left[\frac{\partial u_i}{\partial x_j} - \frac{\partial u_j}{\partial x_i}\right] = \frac{1}{2}[u_{ij} - u_{ji}] = \begin{bmatrix} 0 & \omega_{12} & \omega_{13} \\ -\omega_{12} & 0 & \omega_{23} \\ -\omega_{13} & -\omega_{23} & 0 \end{bmatrix} \qquad 2.19$$

Hence the equation 2.17 can be rewritten in terms of the equations 2.18 and 2.19 as

$$\nabla \boldsymbol{u} = \frac{\partial u_i}{\partial x_j} = \varepsilon_{ij} + \omega_{ij} \qquad 2.20$$

The strain tensor can additionally be decomposed into a deviatoric part **e** and an isotropic volumetric part, as

$$\mathbf{e} = \boldsymbol{\varepsilon} - \frac{1}{3}\cdot\text{tr}(\boldsymbol{\varepsilon})\mathbf{I}, \qquad 2.21$$

$$e_{ij} = \varepsilon_{ij} - (\varepsilon_{11} + \varepsilon_{22} + \varepsilon_{33})\frac{\delta_{ij}}{3} \qquad 2.22$$

The volumetric strain is defined as the unit change in volume, i.e., the change in volume divided by the original volume. Certain operations on the strain tensor give the same result without regard to which orthonormal coordinate system is used to represent the components of strain. The results of these operations are called strain invariants. The volumetric strain is related to the first invariant (I_1) of the strain tensor or the trace of the tensor.

$$\varepsilon_v = \frac{V_f - V_i}{V_i} = tr(\varepsilon) = \varepsilon_{11} + \varepsilon_{22} + \varepsilon_{33} = I_1 \qquad 2.23$$

where V_i and V_f are the initial and final volumes of the samples respectively.

The chosen coordinate convention is with the z-axis parallel to the cylinder axis, coinciding with the direction of the axial stress. The incremental volumetric strain field ε_v reveals the magnitude of local dilatancy (positive values; $\Delta V/V > 0$) and compaction (negative values) in the sample. The DVC reveals the presence of intermittent compaction and dilation events throughout the sample

and the localization of the pattern can also be studied. The presence of secondary fractures could also be understood using the DVC.

To characterize the incremental shear strain, we calculated the von Mises shear strain from the incremental deviatoric strain. For the sake of completeness, the so-called von Mises equivalent strain is evaluated. This scalar-valued strain variable is used to represent the intensity of shearing deformation. The equivalent shear strain is used to easily illustrate the strain localization process in the tested sample. To describe the evolution of incremental deviatoric strain, we chose to use the von Mises equivalent strain [95]. The equivalent plastic strain conjugate to the von-Mises equivalent stress is calculated from

$$\bar{\varepsilon} = (4/3 \times Y_2)^{1/2}, \qquad\qquad 2.24$$

where,

$$Y_2 = 0.5 \times (e_{11}^2 + e_{22}^2 + e_{33}^2 + 2 \times e_{12}^2 + 2 \times e_{23}^2 + 2 \times e_{13}^2) \qquad\qquad 2.25$$

and e_{ij} are the components of the deviator of plastic strain defined in equation 2.21. In this thesis I have used the above equations to calculate the distribution of the strains to further understand the progressive development of incremental strain localization within the specimen and also the localization of the strain. Using DVC analysis, the three-dimensional small-strain displacement field can be obtained using the in-situ CT data. Based mainly on the calculated volumetric strain and the von Mises equivalent strain, we can understand in detail the evolution of the strain localization.

2.4.   CO₂ Capture and Storage (CCS).

CO_2 capture and storge (CCS) is one of the crucial ways for reducing CO_2 emissions from reaching the atmosphere. According to the UN Intergovernmental Panel on Climate Change CCS is one of the means to limit global warming to 1.5 degrees Celsius [93]. The concept includes separation and capture of carbon dioxide from various onshore industries prior to release into the atmosphere and storing the CO_2 permanently in deep underground formations ~ 1000 – 2000 meters below the seabed [93], [94]. A brief outline of CO_2 storage is presented in this section.

The earth's subsurface is the largest carbon reservoir housing the majority of the planet's carbon in forms like coals, oil, gas, organic-rich shales, and carbonate rocks. For hundreds of millions of years, the Earth's upper crust has naturally served as a geological storage site for CO_2. Carbon dioxide resulting from biological processes, igneous activity, and chemical interactions between rocks and fluids gathers in the natural subsurface environment. It can exist in various forms, such as carbonate minerals, in solution, or as a gaseous or supercritical substance, either alone as pure CO_2 or as part of a gas mixture [93]. As a part of the enhanced oil recovery (EOR), engineered injection of CO_2 into geological subsurface was first undertaken in Texas, USA, in the early1970s [93]. Storage of anthropogenic CO_2 in geological formation was first proposed in the early 1970s but the world's first large-scale storage project was initiated in 1996 by Statoil (Equinor) and its partner at Sleipner Gas Field in the North Sea [93], [95].

CO_2 storage is the ultimate phase of the CCS process, where the captured CO_2 is injected into subsurface formations. Geological storage of CO_2 can be undertaken in a variety of geological settings in sedimentary basins. The usual type of formations includes deep saline aquifers, depleted oil and gas reservoirs, unmineable coal seams, basalt formations, and organic-rich shales [93]. Subsurface geological storage can be achieved in both onshore and offshore locations. Offshore sites can be accessed using pipelines from the shore or offshore platforms. Potential offshore storage sites include the continental shelf and certain deep-marine sedimentary basins. However, most sediments found on the abyssal deep ocean floor are not thick enough or permeable enough to be suitable for geological storage [93], [94]. Figure 2.11 illustrates the varieties of sequestration sites. The diagram illustrates the locations of potential storage sites for CO_2 injection, as well as areas where CO_2 injection is employed to enhance oil and/or methane recovery.
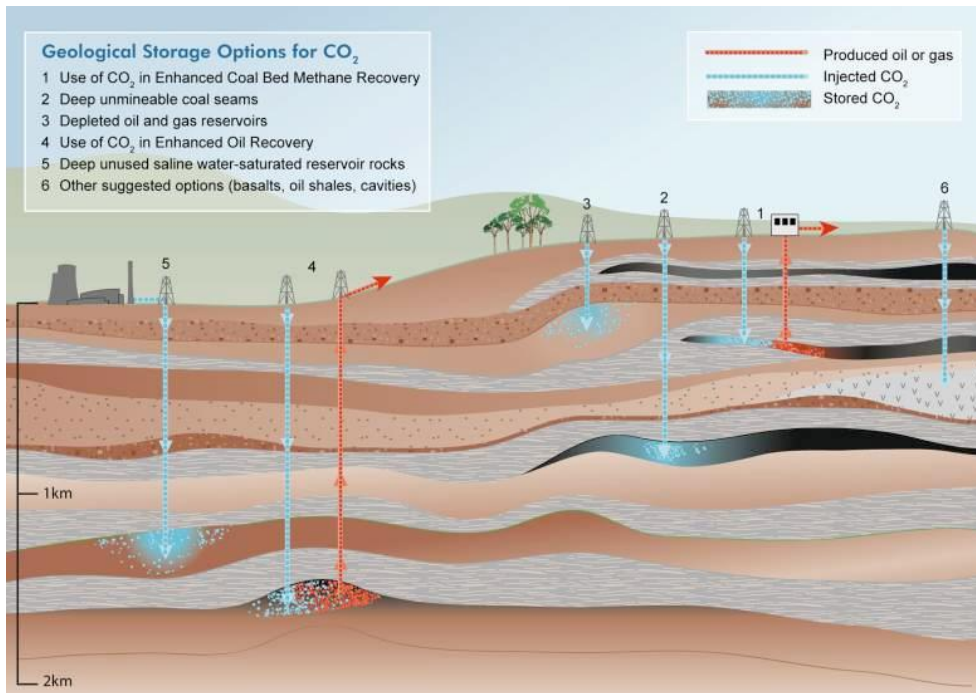
Figure 2.11 Possible sites for geological storage of CO₂ [93].

2.3.3 How is CO$_2$ stored underground?

To geologically store the CO$_2$, it must first be compressed into a state called supercritical state. Supercritical CO$_2$ refers to the CO$_2$ at a critical point which is at a temperature above 31.1°C (88°F) and a pressure over 72.9 atm (about 1,057 psi) [93], [96]. Above the critical point, CO$_2$ has some properties like a gas and some properties like a liquid, which means that it has the density of a liquid and viscosity like a gas. The key advantage of storing CO$_2$ under supercritical conditions is that the required storage volume is much smaller than if the CO$_2$ was stored under "standard" (room) pressure settings. Temperature and pressure naturally increase with depth in the Earth's crust. Depending on the geothermal gradient and at depths of about 800 m or greater, the temperature and pressure cross the critical point of CO$_2$. At the pressures and temperatures, CO$_2$ injected at this depth or deeper will remain in the supercritical state [93], [96].
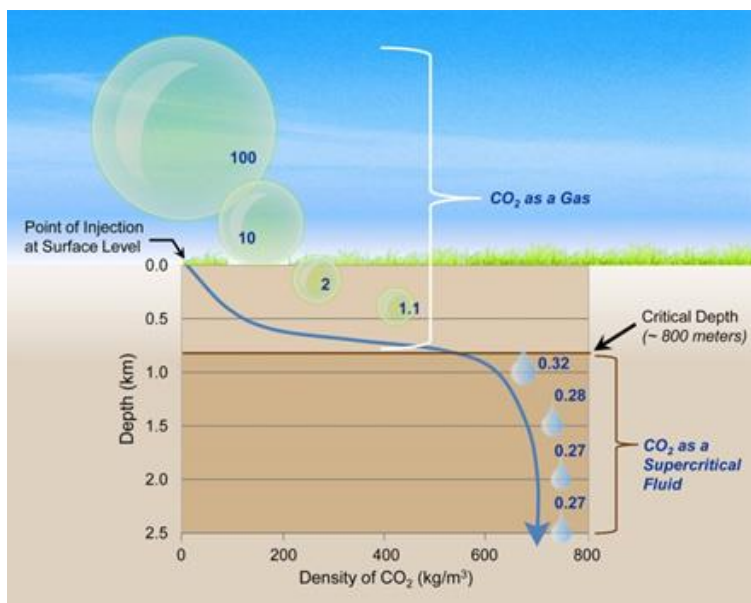
Figure 2.12 The variation of the CO$_2$ density with the depth is shown. The assumed geothermal gradient of 25°C km^{-1} from 15°C at the surface. At depths of ~ 800m depth, the CO$_2$ reached the supercritical state. The bubbles represent the relative volume of CO$_2$ till it reaches 800m. It can be noted from the figure that at depths below 1.5 km, the density and volume are almost constant [95].

2.3.4 Trapping Mechanisms

Trapping of CO_2 is an important aspect of geological storage without which injection of CO_2 into the subsurface would be merely a waste. The effectiveness of geological storage or storage security is a combination of physical and geochemical trapping. The storage sites that prove to be the most efficient are those where CO_2 remains immobile due to being permanently trapped beneath a thick, low-permeability seal, transformed into solid minerals, or adsorbed onto the surfaces of coal micropores. A physical trapping mechanism, as the name implies, relates to the preservation of CO_2 in a way that keeps its chemical properties while undergoing no significant changes. This process usually starts soon after injection and can last for centuries [93]. Chemical entrapment, on the other hand, involves interactions between CO_2 and reservoir fluids, rocks, and minerals, resulting in CO_2 no longer existing as a distinct phase and its chemical characteristics being reconstructed [97], [98]. This chemical transition is a long-term process, and it occurs over a longer time span than physical trapping processes.

The most common types of physical trapping include structural trapping and residual trapping [93], [94]. Structural trapping involves the physical entrapment of CO_2 within the rock and is the first form of trapping that happens immediately when CO_2 is injected. The rock layers and faults within and above such storage formation act as seals thus preventing the moving out of CO_2 from the storage sites. The injected CO_2 becomes supercritical, and it becomes more buoyant than other liquids present in the surrounding pore space. The CO_2 will move through the rocks till it reaches an impermeable seal rock and is trapped. Residual trapping is the process where CO_2 remains trapped in the pore spaces between the rock grains as the plume migrates trough the rock [99].

On the other hand, chemical trapping includes solubility trapping and mineral trapping [93], [94]. In solubility trapping the injected CO_2 will move into the brine present in the pore spaces thereby leading to solubility trapping. In mineral trapping the CO_2 dissolved in the rock's brine water reacts with the minerals present in them which eventually transforms into heavier compounds like calcite, muscovite, or quartz [93], [98]. This is a comparatively slower process and is an irreversible and permanent form of storage. The further details of these processes are beyond the scope of the thesis.

2.3.5 Geological Impacts of CO_2 injection

The ability to securely store CO_2 for long periods of time in depleted oil or gas reservoirs is dependent on the hydraulic integrity of both the geological formations that surround it and the wellbores that traverse it [93], [100], [101]. The geo-mechanical effects of the injection of CO_2 are due to the development of pore pressure together with the effect of cool CO_2 injected into the reservoir rock at a higher temperature. As a result, it causes an initiation of the different stresses, elastic and thermal, that change the pre-injection state of stress in the region. CO_2 injection could cause significant geo-mechanical responses like reactivation of the pre-existing fractures and faults in the reservoir.

The possible leakage channels during CO_2 injection include fault reactivation, caprock failure brought on by induced shear stress, hydraulic fracturing that extends outside of the intended zone, and inadequately sealed casing cement in enlarged, unstable boreholes [100], [101]. Factors controlling these mechanisms include the upper and lower pressure and temperature limits encountered by the reservoir, the orientation and mechanical properties of existing faults, rock mechanical properties, in situ stresses, and reservoir depth and shape. Furthermore, the abrupt displacement along pre-existing faults brought on by the injection of CO_2 might cause the Earth's surface to be raised and cause noticeable seismic activity[93]. Normally, this fault movement begins at the reservoir depth, but the ensuing dynamic rupture may reach beyond the reservoir, possibly jeopardizing the integrity of sealing formations above or even triggering stronger earthquakes along faults that are already under a lot of stress[100], [101].

The geological conditions and the structure of the basin like porosity, permeability, geometry, capacity, mineralogy, etc. play a crucial role in the selection of reservoirs and their caprocks as potential CO_2 storage sites. The injection of CO_2 into the reservoir causes many geochemical reactions which leads to a change in the integrity and trapping potential of the reservoir [93], [98]. The changes involve processes like dissolution of primary minerals and changes in porosity and permeability. The effects of these alterations can be favorable or detrimental. As a result, it is critical to undertake a thorough investigation of the lithology and mineral content before beginning CO_2 injection.

2.3.6 CO₂ storages today
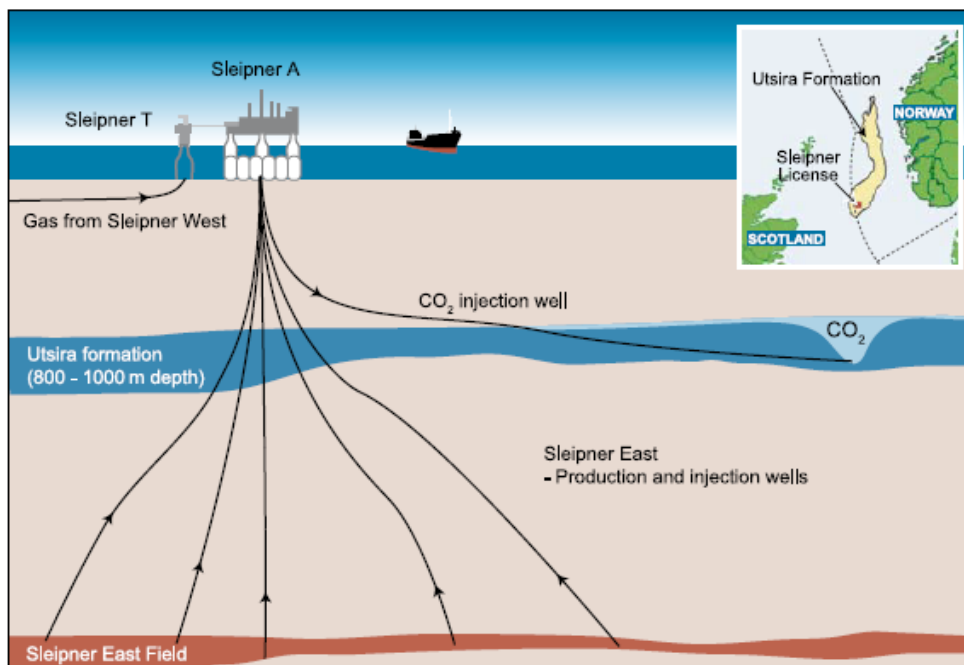
Figure 2.13 Diagram illustrates the Sleipner CO_2 Storage project. The location of Utsira formation (inset) [93].

Carbon dioxide storage is currently happening worldwide. Some of the notable commercial-scale projects are the Sleipner CO_2 Storage site in Norway [93], [102], [103] and the Weyburn-Midale CO_2 Project in Canada [93], [104], [105]. These sites have been used for CO_2 injection for many years and store more than 1 million metric tons of CO_2 per year. These large-scale efforts demonstrate that vast amounts of CO_2 may be safely and permanently stored. Statoil's Sleipner Project is a commercial-scale effort in Norway's North Sea [102]–[104]. It focuses on geological CO_2 storage in a saline formation, where CO_2 (about 9%) from the Sleipner West Gas Field is isolated and injected 800 meters below sea level into a saline formation. To monitor and investigate the CO_2 storage process, the Saline Aquifer CO_2 Storage (SACS) project was formed. 7 million tonnes of CO_2 have been injected since the project's inception in October 1996, with a total storage capacity of 20 million tonnes predicted for the project's lifetime [102], [103]. Seismic surveys have

successfully monitored the injected CO_2, and calculations indicate that long-term leakage risks are reduced due to CO_2 dissolving in the pore water.

The Williston Basin, which stretches from Canada to the United States, is home to the Weyburn CO_2-enhanced oil recovery (CO_2-EOR) project [104], [105]. The CO_2 is obtained from a nearby gasification plant and delivered to Weyburn for usage in the field. Over its 20–25-year lifespan, the facility is planned to store around 20 million tonnes of CO_2. To maximize CO_2 sweep efficiency, the oil field uses standard well designs and a combination of vertical and horizontal wells. Extensive monitoring is in place to detect any potential CO_2 leakage, although there have been no reports of such occurrences yet. A multitude of additional carbon capture and storage (CCS) activities are also underway in various parts of the world to demonstrate the feasibility of geologic storage and technology for future long-term CO_2 storage. More than 200 CO_2 capture and/or storage activities (both ongoing and completed) have been carried out worldwide to date [93].

3.   Materials

This chapter gives a concise overview of the materials investigated in the articles, namely Pierre shale I and Draupne shale. This chapter covers the mineral composition, distribution of organic matter, pore size and connectivity, microstructure, anisotropy characteristics of Pierre shales, and the mechanical properties of Draupne shales.

Two shales were tested: the Draupne shale, taken from a field core in the North Sea, and the Pierre I shale, an outcrop from the Northwest in the USA. As it is rare to obtain intact field cores, especially from the shale layers, suitable for destructive laboratory testing (e.g., for establishing mechanical properties), one looks for analogues from onshore quarries. These analogues can either be outcrops from the same formation, that surface on either side of the North Sea in Norway or in the UK for example, or completely different rock formations displaying approximately the same petrophysical properties and mineralogies. This is the case for the Pierre I shale, which has been widely used for mechanical tests as a proxy for typical North Sea overburden shales, as it exhibits similar clay contents and porosity values. The few field shale cores are then used as calibration points for the tests performed on outcrops such as the Pierre I shale.

3.1   Shales

Shales are the most abundant rocks in sedimentary basins, and unconventional shale gas and shale oil reservoirs are increasingly important in oil and gas production globally [16]. Recently they have played a crucial role in a range of environmental processes, like large-scale permanent storage of CO_2 for the reduction of anthropogenic CO_2 and periodic H_2 storage [16]. Shales are typically made up of clay microparticles and silt size [16], [106]. The shale caprocks are exposed to significant loading due to natural geological stresses such as thermal and high fluid pressure and industrial stresses like drilling, fracturing, and fluid injection [107].

Shales are fine-grained sedimentary rocks that are characterized by their finely laminated structure. The main features of shales are pores, organic matter (OM), fissibility, and minerals. These are the main features that give it its role as a caprock properties like low permeability, high capillary entry

pressure, relatively high porosity but small pore volumes, etc A wide range of techniques has been previously used to characterize the shales. To investigate and understand the 3D microstructure and pore system across four orders of magnitude (10^{-9}-10^{-4} m), we must use multi-scale and multi-modal imaging techniques [108]–[110]. The commonly used techniques are optical microscopy (OM), SEM, TEM, X-ray scattering, and X-ray CT. Imaging techniques like scanning electron microscopy (SEM), sometimes combined with focused ion beam milling (FIB-SEM), can acquire high-resolution images and chemical information through spectroscopy [16] [111], [112] X-ray diffraction (XRD) is also extensively used for mineral identification [8]. During the last decade, X-ray microcomputed tomography (μCT) has been increasingly used for the non-destructive visualization and mineral quantification of geological samples in three dimensions. Using μCT, it is currently possible to investigate the pore network properties, micro-textures, fractures, and transport properties at spatial resolutions down to and below the micrometer level.

Shale exhibits a strong anisotropic property due to its complex structural characteristics, including cleavage, bedding planes, foliation, schistosity, and natural fractures [16]. These characteristics result in different mechanical properties of shale with varying bedding plane inclinations, including hydraulic properties, permeability, porosity, flow, and transport properties [16], [106]. These properties play a significant role in shale's ability to act as a caprock, as its low permeability makes it an effective barrier to the escape of hydrocarbons or CO_2 from the reservoir.

However, fractured or highly porous shale may not be as effective as a caprock, highlighting the importance of understanding the mechanical properties of shale and the evolution of strain localization and fracture mechanisms. This understanding is crucial for ensuring safe and efficient drilling and for maximizing the potential of hydrocarbon reservoirs and CO_2 storage sites. Therefore, further investigation of shale's mechanical properties is necessary to improve our knowledge of its behavior and to develop effective strategies for the exploration and production of hydrocarbons and the management of CO_2 storage sites.
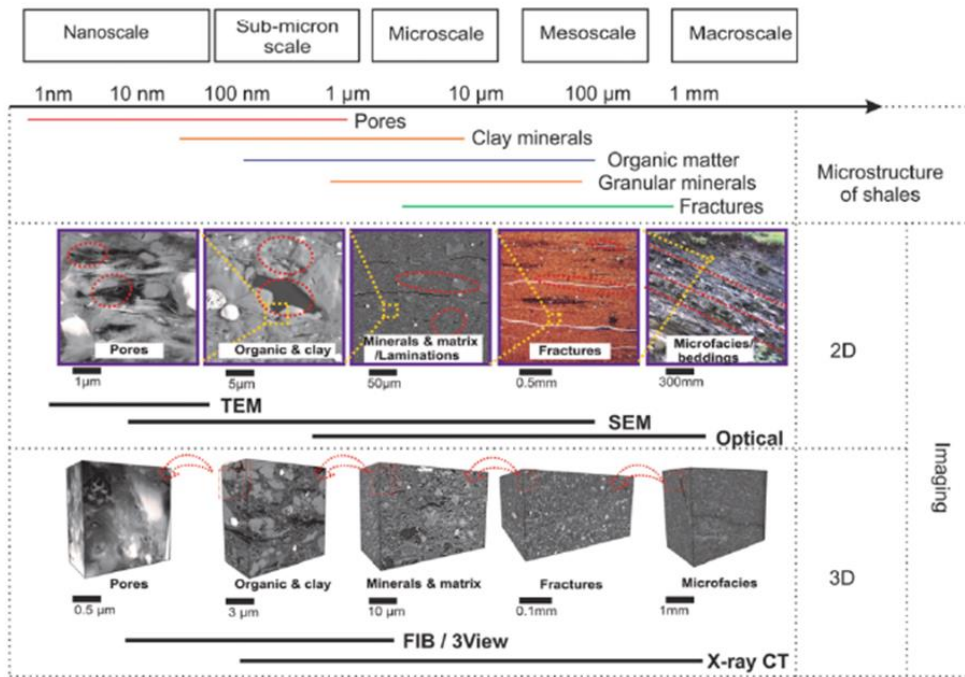
Figure 3.1 The features present in the shales and the different imaging techniques used in the shales are shown here. Figure adapted from [16].

Shales can be targeted as source rocks for oil or gas production, but also serve as caprock and overburden and therefore are encountered while drilling towards a reservoir and as containment guarantee for underground storage purposes. Depending upon the deposition environment, there are different types of shale. Black shales are the most commonly available type of shale on the earth. These black shales are the source of most oil and gas reservoirs. The rocks are black in color due to organic matter's presence in them. Grey-colored shales are due to calcium or clay minerals in them [114]. The presence of hematite gives the shale's red color, while the shales containing goethite are yellow/brown colored [115].

3.1.1 Shale structure

Shales have complex mineralogy and structure, with the majority of them consisting primarily of clay minerals (~ 60%) and other minerals (~ 40%) (such as quartz, chert and feldspar) [116]. It is typical for shales to consist of various minerals, including carbonates such as calcite and dolomite, tectosilicates such as quartz and feldspar, and phyllosilicates like illite, smectite, and kaolinite. Additionally, shales may also contain interlayers of illite and smectite, as well as sulfides, oxides, and phosphates [106], [108]. Studies have shown that the mineral composition of shales is influenced by various factors, including diagenesis processes and the environmental conditions during deposition and maturation [117], [118].

Clay minerals, naturally occurring materials composed of silica, alumina, and water, as well as iron, magnesium, sodium, and potassium, are standard components of shales [119]. The mineralogical composition of the clay phase varies widely depending on the shale type. Illite, smectite, and kaolinite are shale clay minerals occurring most frequently. Illite is an alumino-silicate mineral, muscovite is the end product of illite at high temperatures, and glauconite is a specific type of iron-rich illite. Kaolinite is a layered silicate mineral formed through weathering in tropical and subtropical regions with abundant rainfall, proper drainage, and acidic water conditions, and it is typically white. Shale clay minerals typically contain fine micropores and a significant surface area, contributing to the internal structure required for methane adsorption [120], [121]. Shales with high clay content have higher porosity and permeability than those with higher silica content [122].

The porosity and pore structure of shales play an essential role in their potential as hydrocarbon reservoirs or as reservoir seals, and their geomechanical properties. The pore sizes, structures, and distribution in shales are not entirely understood. According to Bustin et al. (2008) [123], shale gas reservoirs mainly contain natural gas stored within their pore structure and porosity system. The voids within the shale formations are of two types: interparticle porosity and intra-particle porosity [124]. The pore size category groups can be classified into macropores (pores with diameter $\geq$50nm), mesopores (between 2 nm and 50 nm), and nanopores ($<$ 2 nm) [124]. The shale consists of a matrix and fractures. In addition to the classification mentioned above, IUPAC further classifies the micropores into super-micropores (1.4–2.0nm), micropores (0.7–1.4 nm), and ultra-micropores (<0.7nm) [125]. As depicted in Figure 3.2, micropores can take on various shapes,

such as closed pores, blind pores, bottleneck pores, and cross-linked pores. During gas production from shale reservoirs, fractures and the different pore systems make the pathway for gas flow.

Various techniques such as optical microscopy, SEM, TEM, X-ray scattering, and X-ray CT have been used to study the microstructure in shales [15], [16], [126]. X-ray CT has been used recently for non-invasive imaging of internal structures with high spatial resolution. The 3D volume renderings using X-ray CT have been used to study the bedding orientation of shales [15], [16], [126]. Some studies have also demonstrated that using X-ray CT has visualized connectivity and heterogeneity of fractures as well as the different mineral distributions on shales. Using X-ray microtomography and nanotomography, silt-sized minerals and silt-sized organic matter can be imaged in 3D in shales. Three phases including pyrites, minerals, and micropores (and fractures and kerogen) in a shale were quantified using X-ray microtomography [15], [127]–[129]. Minerals, matrix, and organic matter were selected for the pore model in a different shale sample using X-ray nanotomography [15], [106].
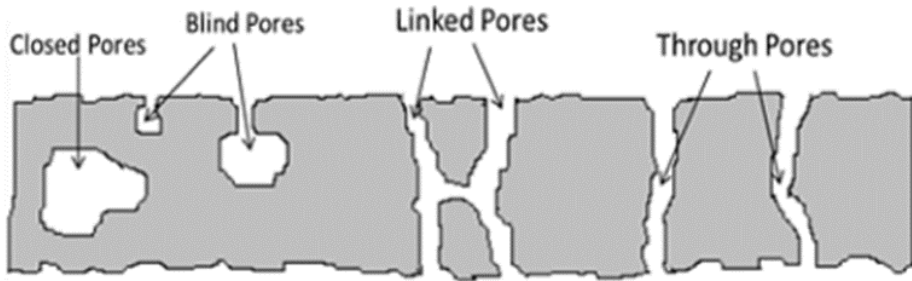

Figure 3.2 The different types of shale pore shapes are depicted here. The figure is used with permission from S Rani et al., 2019 [106].

3.1.2 Mechanical testing of shales.

Understanding the mechanical properties of shale is crucial as they can significantly impact the rock's behavior in various applications, such as oil and gas drilling, mining, and building construction. The mechanical properties of shale are complex and dependent on multiple factors, such as mineralogy, texture, and porosity, as it is a sedimentary rock. The laminated structure and the bedding orientation of the shale sample have a strong influence on the mechanical properties. The mechanical properties of shale are typically evaluated through laboratory testing. These tests involve applying a controlled load or stress to a shale sample and measuring the resulting deformation or failure behavior. Shale's important mechanical properties include its strength, stiffness, ductility, and fracture toughness. These properties help to determine how shale will respond to external loads or stresses and how it will behave under different geological conditions.

Laboratory testing is a crucial component in examining rock characteristics and performance in various circumstances, and it is an essential component of geotechnical exploration and investigation. There are multiple laboratory testing techniques for evaluating the mechanical properties of rock masses, and they are generally divided into two types: (a) Index and indirect strength testing and (b) direct strength testing [130]. In index testing, the fundamental properties of the sample are not evaluated. Common index tests used for studying shales are the point-load index test, Slake's durability test, and Brazilian tensile strength test. Such tests are simple and mostly do not require detailed sample preparations, and certain tests are non-destructive as they do not involve sample failure [131]–[134]. The details of any of these are beyond the scope of the thesis.

Direct strength measurements are used to explore the fundamental properties of the shales. Some of the commonly used direct measurement tests are permeability tests, modulus of deformation – elastic modulus (E) & Poisson ratio (ν), and Uniaxial and triaxial compressive strength tests. Uniaxial compressive test (UCT) can be conducted to measure vertical & horizontal strain response to the applied load, rock properties like uniaxial compressive strength, strain at failure, Young's modulus & Poisson's ratio, and the degree of hardness & brittleness [130]. The triaxial compression test is utilized to assess the strength of rocks under confinement, such as rock samples obtained from deep-seated rock masses; it also allows one to acquire needed input parameters for failure envelope models. When confined, rocks exhibit greater strength, and their deformation

behavior becomes more ductile or strain hardening. This test is used to evaluate the load-bearing capacity of rocks at a depth of 2000 m below the earth's surface [135].

The combination of laboratory experiments, numerical approaches, and field data has provided insights into the macroscopic failure that occurs through the interaction and coalescence of fractures, when a shale or other rock is submitted to shear or tensile stresses [136]–[143]. Researchers have further studied the fatigue response of shales, and efforts have been made to understand the influence of the bedding orientation fatigue behavior of shales [144]. Advances in the time-resolved 3D X-ray CT [26], [41], [74], [75], [145] techniques, and DVC [31] (as mentioned in the previous chapter) have enabled the in-situ investigation of the deformation process. Studies have shown that a combination of X-ray CT, DVC, and triaxial testing can be used to reveal the orientation and distribution of mechanical weaknesses that influence strain localization preceding macroscopic shear failure [146], [147]. The details of the different types of shales studied in this thesis are mentioned in the following section.

3.2 Draupne shale

The Draupne shale is a significant caprock of the North Sea and is vital in assessing potential CO_2 storage sites. The Draupne shales used in this thesis were collected from the Ling depression in the central part of the North Sea [148]–[150]. The Draupne formation is an organic-rich shale formation located within the Viking Group, part of the Upper Jurassic [149]. It comprises several hundred meters of thick source rocks. The Draupne Formation primarily comprises dark grey-brown to black, non-calcareous claystone that can sometimes be fissile [151]. According to the Norwegian Petroleum Directorate (NPD 2021), the mineral composition of the formation is mainly comprised of clays and organic matter [151].

The samples in this thesis were from the section between 2574.86 and 2574.99 m depth (13 cm height), as sketched in Figure 3.3 a, from a nine-meter-long core donated courtesy of Equinor to NGI and SINTEF for use in research projects. With a porosity of around 12 %, its permeability is less than 3.2×10^{-22} m^2 (3.2 nDarcy), and the critical pore throat from mercury intrusion porosimetry is around 9 nm. The material is also characterized by a water content of 6.9 % and has a salt content in the pore fluid of 37g NaCl/l [149].

The mineralogy of the Draupne shale has been evaluated using X-ray diffraction (XRD) in several studies. Multiple studies have reported that the Draupne Formation has an average clay content of $66 \pm 4\%$, while the average quartz and feldspar content is $21 \pm 5\%$, and carbonate and pyrite content is $13 \pm 1\%$ [148]–[150], [152]–[157]. The thickness of the Draupne Formation ranges from 0 to 550 meters, with a total depth range of ~500 to 6500 meters from penetrated wells in the Norwegian North Sea (NPD, 2021) [151]. The TOC content (total organic carbon) in the formation can range from 2 to 15 wt%, although it can reach as high as 20 wt% in some cases [158]. The hydrogen index (HI) of the Draupne Formation can vary significantly due to differences in depth, TOC richness, and maturity [156]. In some areas of the North Sea, the formation also contains sporadic debris flows or turbidites that have led to intermittent quartz-rich sandstone sections within the otherwise clay-rich layers [159], [160]. The mineralogy of the Draupne shales is summarized in table 3.1.
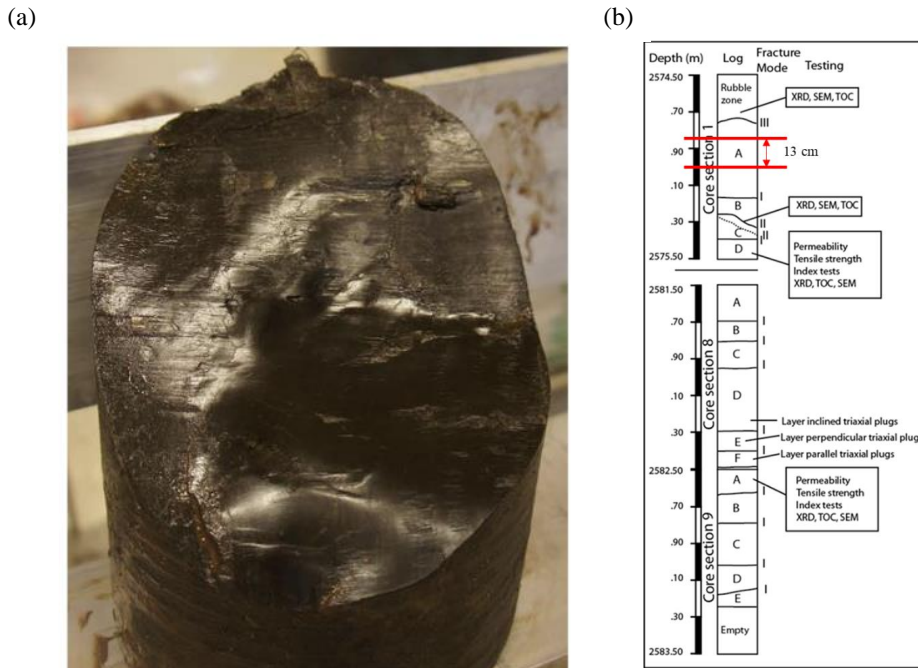
(a)
(b)

Figure 3.3 (a) The cross-section of mechanically tested Draupne shales used with permission from Skurtveit et al. 2015 [149]. (b) The logged core sections showing the location of sampling sites for various tests are included, and the red line indicates the region between which the samples used in this thesis were obtained.

The Draupne shale is a critical caprock in the North Sea and plays a significant role in evaluating potential CO_2 storage locations in the region [149]. Recent studies have examined specific mechanical properties of the Draupne shale using the same core material as in this thesis [148]–[150], [152]–[154]. It was first mentioned by Skurtveit et al. in 2015 [149]. Undrained triaxial tests with different bedding orientations were made and it was reported that the Draupne has an anisotropic undrained strength behavior[153]. Mondol et al. in 2019 reported that the Draupne shales exhibit anisotropy of strength, and it is related to the layering or the bedding planes, as has been observed in many similar shales from the North Sea [152]. When the orientation of the bedding planes is appropriate, they tend to fail before intrinsic failure occurs, as the bedding represents weak planes [150]. Studies have established a correlation between the brittleness of

organic-rich shale and its maturation, indicating a relationship between geomechanical properties and maturation [161], [162]. The effect variation of total organic carbon was studied, and we noted that the results are conflicting [163]–[165]. Using a direct shear box, the study investigated the mechanical properties, specifically the strength, and friction, of a naturally occurring mode II fracture with slickensides. The researchers also utilized various techniques, including photogrammetry and Scanning Electron Microscopy (SEM), to analyze and characterize the fracture before and after testing, as reported by Smith et al. in 2019 [166].

Properties	Values	Units
Water content	6.40	%
Porosity	12.5	%
Grain density	2.51	g/cm^3
Salt content in pore fluid	37	G NaCl/l
Cation exchange capacity	24	Meq/100g
Specific surface area	11	m^2/g
Critical pore throat	9	Nm
Permeability (// bedding)	1.2×10^{-7}	mD
Permeability (bedding)	3.2×10^{-7}	mD
Tensile strength (// bedding)	0.2-1.5	Mpa
Tensile strength (bedding)	4.8-5.5	Mpa
Total organic content (TOC)	6-8	%

Table 3.1 Some of the properties of the Draupne shale are summarized here [149].

Bohloli et al. in 2020 presented the results of an experimental study on Draupne shales [167]. They investigated the laboratory test procedure to simulate the slip of fractures and faults under realistic stress conditions for North Sea CO_2 storage sites. The frictional properties of the fractures were measured during shearing, and the results showed that the friction coefficient increased when the shear velocity was increased, indicating a velocity-strengthening behavior. This suggests that slip-on fractures and faults within these formations may be less prone to producing detectable seismicity during a slip event. The article highlights the implications of these findings for

monitoring reservoir and caprock integrity at CO_2 storage sites [153]. Recent research mainly focuses on the effect of CO_2 injection on the rock's mechanical properties, including strength and stiffness, and examines the potential for fault reactivation using a fault reactivation criterion [135], [168]–[170]. Upon further investigation of the literature, I found that there is not much research understanding the fundamental mechanical properties of the Draupne shales. The conventional approach to testing is usually a blind test, without providing any insights into the process occurring inside the samples during the different ways of mechanical testing. In this thesis, we provided a combination of X-ray computed tomography and digital volume correlation to give the evolution of fracture and strains. The details are shown in the articles and previous chapters.

3.3   Pierre shale

A marine shale from the Upper Cretaceous epoch, the Pierre shale is typically found in the northwest of the United States [171]. Its discovery by Meek and Hayden in 1862 led to its naming, given the area it was found close to Fort Pierre on the Missouri River in South Dakota [172]. According to Meek and Hayden, the shale is dark gray in hue and includes gypsum veins, seams, and fossils [173]. The Pierre shale is often not profoundly buried, making its recovery in large amounts very simple. Its mineralogy is comparable to other shales found during deep borehole drilling, making it the perfect shale for laboratory research. The mineralogical composition of Pierre shales, collected from the Colorado quarry, is chlorite, siderite, pyrite, illite, smectite, and quartz [1], [174]. Details of the mineralogy are given in Table 3.2.
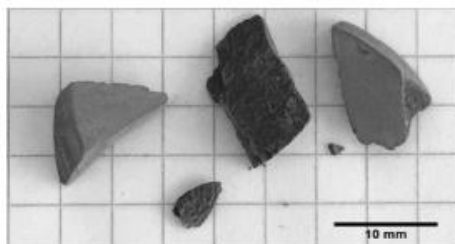
Figure 3.4 Fragments of Pierre shale I sample collected from a Colorado quarry.

Mineral	%	Reactivity
Quartz	16.00	None
Plagioclase	8.55	Slight
Chlorite	29.50	Dissolves
Illite	19.90	May dissolve
Smectite	19.80	Swells in fresh water
Calcite	1.54	Dissolves
Siderite	1.44	Slight
Dolomite/ Ankerite	2.63	Slight
Pyrite	0.64	Slight

Table 4.1 The mineralogy of the Pierre shale is summarized here [1].

There has been some research on the orientation of minerals in Pierre Shale, particularly regarding the preferred orientation of clay minerals within the rock formation [175]. One study published in the journal Clays and Clay Minerals in 1994 investigated the preferred orientation of illite clay minerals in Pierre Shale samples from the Western Interior Seaway in the United States [176]. The researchers used X-ray diffraction (XRD) to analyze the orientation of the clay minerals. They found that the illite crystals exhibited a preferred orientation parallel to the bedding planes of the shale [176]. The authors suggested that this orientation was likely the result of sedimentary processes during the Pierre shale formation. The researchers used X-ray computed tomography (CT) to analyze the spatial distribution of the clay minerals [126][164]. They found that illite and smectite clay minerals were preferentially oriented parallel to the bedding planes of the shale. The authors suggested that this orientation was likely related to the compaction and deformation of the shale during burial and tectonic processes [126].

Overall, while the orientation of minerals in Pierre Shale can be complex and varied, these studies suggest that clay minerals within the shale may exhibit preferred orientations related to the area's geological history and processes. In this thesis, we have used XRDTT and XRD-CT to study scattering from clay minerals and high-density inclusions of Pierre shale, which showed a strong global preferred orientation. More details are given in the attached article.

4. Summary of the Papers in this Thesis

In this chapter, I present the summary of the main results obtained from the articles on which the thesis is based. As the full articles are given in chapter 6, I will not detail the results.

4.1 Time-Resolved in Situ Imaging of Strain Localization in Draupne Shale Under Triaxial Compression

Summary: In this article, we try to provide insights into the mechanical behavior of Draupne shales, as it is crucial in subsurface activities. The study aims to provide an improved understanding of the mechanical behavior of these rocks that have been extensively evaluated for their potential for the permanent storage of carbon dioxide. Using a novel experimental technique of triaxial deformation, axial compressive stress was applied to the shale sample with constant confining stress and pore pressure. The experiment was designed to replicate the conditions similar to ~ 2.6 km depth in the seabed. The evolution of microstructure in Draupne shale under triaxial compression is captured using in-situ time-resolved X-ray micro-tomography with micrometer resolution. The incremental strain field is computed from digital volume correlation analysis.

Perhaps the most crucial observation is that the linear stress-strain curve hides a series of intermittent irreversible destructive events at random locations within the specimen. The macroscopic stress-strain plot of the shale made during the experiment revealed a pseudo-linear behavior (see Fig 4.1 (a)) up to an axial stress of 39 ± 2 MPa and then followed by an increasing ductility when approaching the peak stress. Using a linear fit, the mechanical properties estimated from the linear part of the pseudo-linear portion of the stress-strain curve suggest Young's modulus of $E = 3.6 \pm 0.2$ GPa, which correlates with the reported values. The linearity of the curve was observed to deviate at around 70% of the maximum axial stress, and the fracture point was observed at about 97 ± 2% of the maximum differential stress.

During the experiment, we observed the closing of pre-existing fractures at different locations on the sample. But tracking the evolution of the strain localizations, we observed intermittent event bursts at various locations in the sample. The visualized 3-dimensional displacement field vectors aided in understanding the relative movements occurring inside the sample. Tracking the evolution of the 3D incremental displacement field in the sample, we observed early nonhomogeneous deformations, including intermittent strain clustering at apparently random locations. On examining the time steps, the deformation fields start with a homogeneous state. This initially uniform deformation field, however, undergoes a transition over time, evolving into a rotation-rich state and finally growing into a highly complicated state, which is interpreted as a sign of sample fracture. A sliding block mechanism was noted in the sample post-failure. A clear shear zone with displacements in opposite directions was observed across the fracture just after failure. The local deformations within the sample were noted to be homogeneous thus indicating the rigid nature of the block. There was a noticeable presence of rotating strain just before failure. This form of strain, which occurs around an axis perpendicular to the applied force, is a well-known process in linear elastic fracture mechanics. However, we are not aware of any previously published comparably clear microscopic 3D evidence demonstrating this impact in rocks.
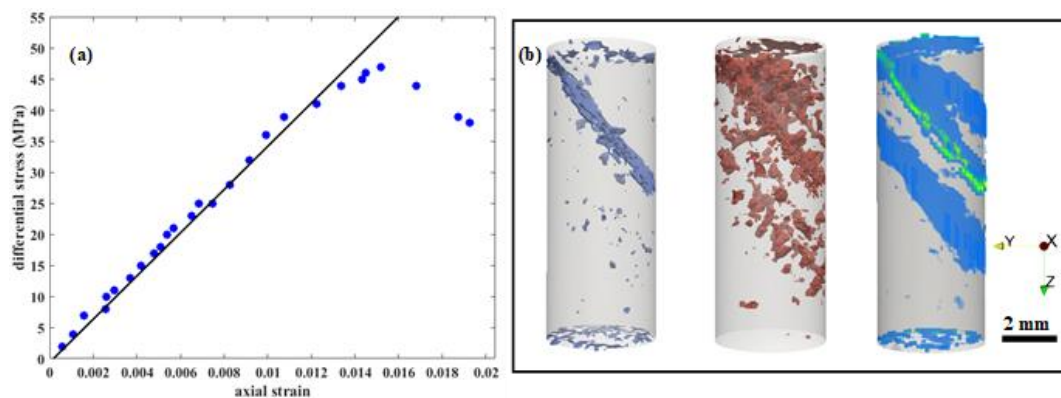

Figure 4.1. Results of mechanical testing with Draupne shale at ID19 (a) Axial strain versus differential stress (b) Evolution of the spatial distribution of high incremental strains. Locations of rock experiencing contraction, dilation, and von Mises strain are plotted in order.

The von Mises and the volumetric strains were calculated from the strain tensor. Motivated by CO_2 and H_2 storage prospects in abandoned oil and gas reservoirs in the North Sea, the experiment reported here contains several exciting results. The evolving distribution of the incremental strain quantified by DVC revealed that high magnitudes of compaction, dilation, and von Mises strain localized along the fracture (Figure 4.1 (b)). The von Mises strain indicates the presence of deviatoric strain accumulation. The time series also demonstrated non-persistent strain localizations over numerous timesteps appearing at different positions across the sample, to our knowledge has not been previously reported. The study also reveals a gradual development of localized strain within the specimen, both incrementally and preceding the macroscopic fault formation. The investigation shows a steady buildup of localized strain inside the material, both incrementally and prior to the creation of a macroscopic defect. In addition, the study also unknown secondary fracture networks linked to the system-spanning fault. These secondary fractures stabilized and finally localized along the major fracture. The experimental and analysis techniques presented in this article reveal the local mechanics in the Draupne shales and can further be applied to understand the stability of these rocks for applications like CO_2 sequestration.

4.2 Deformation characteristics of cement and shale admixtures under triaxial cyclic loading.

Summary: Experimentally evaluating the fatigue evolution of admixtures for soil stabilization can contribute to a better understanding of repetitive and cyclic loads. This article considers the potential of using shale wastes and Portland G cement composite as admixtures to stabilize soils for civil developments. We investigated the effect of cyclic loading and unloading on these admixtures to represent the exposed multi-levels of cyclic loading and unloading during their lifetimes. These effects may not appear immediately and can last for some time. So, it becomes essential to understand the long-term response of these samples under repetitive stress.

Mechanical sieving was used to crush and sort the Draupne shale based on size. Two sets of shale samples were created: A1 with 1-2 mm diameter shale particles and A2 with shale particles larger than 2 mm in diameter. This shale was used with Portland G cement. A third sample, B, was prepared using only 1-3 mm diameter Draupne shale particles compressed within the experiment's rubber sleeve. Microstructure evolution in the shale-Portland G cement admixture under time-

dependent triaxial compression is captured using in-situ dynamic X-ray tomography. The incremental strain field is computed from digital volume correlation analysis. Three samples were tested, each with three cyclic loading and unloading loop levels. The samples are categorized according to the size of Draupne shales, and one of the three samples contained only fragments of pure compacted Draupne shale. The damage and fatigue in the samples are quantitively described from the DVC investigation.

The experimental loading pattern for samples A1, A2, and B is shown in figure 4.2. The LVDT measurements of A1 and A2 exhibited similar response patterns. During cycle I, all samples showed yielding but exhibited stress fluctuations that were too small to discern LVDT oscillations. Cycle II showed a more noticeable LVDT increase, indicating sample fatigue. Samples A1 and A2 showed considerable weakening and higher LVDT readings during cycle III, indicating plastic behavior with increasing permanent deformation throughout loading cycles. Sample B, which was made up of weakly compacted shale particles, hit the LVDT's translation limit, causing the experiment to be terminated during the fourth loop of cycle II. The relationship between irreversible axial strain and unloading strain for samples A1 and A2 is studied, and a linear relationship was noted from the regression analysis.

The displacement fields for sample A2 at different stages of the cyclic loading test tell a detailed study of the mechanical response. From the four steps of the cycle I loop 3, the axial stress was sufficiently low that the displacement field was observed to exhibit a certain degree of localization to the regions containing shale fragments. There was a trend where displacement was most noticeable under the highest stress (loading) and least stress (unloading). Subsequent loops showed similar patterns. Cycle II showed similar patterns, with the displacement field showing localized shifts as stress increased. As stress was reversed, fracture closure was seen, demonstrating partially irreversible elastic-plasto damages. In cycle III, the displacement vectors revealed active deformation of the cement phase under increased load, suggesting significant damage. The pattern of displacement fields in loop 7 of cycle III suggested permanent irreparable damage. This sequence of findings indicates the presence of fatigue and accumulated irreparable damage in the sample.

The volumetric, and von Mises shear strains indicated that the coarse shale particles in the cement matrix influence the strain evolution. Minor volumetric strain was found in cycles I and II,

49

primarily in shale particle areas. In contrast, cycle III exhibited distinct behavior as axial stress increased. As the axial stress was increased from 65-75 MPa low magnitude localized dilation bands with low magnitude were observed. By increasing the axial stress to 70-75 MPa, very localized and strong inclined dilation zones appeared near shale areas. When the axial stress was reduced from 75 to 70 MPa, the magnitude of the dilation bands decreased but remained comparable. Unloading to 65 MPa produced a pattern similar to the loop's early stages, with dilatation and compaction occurring in the same locations.
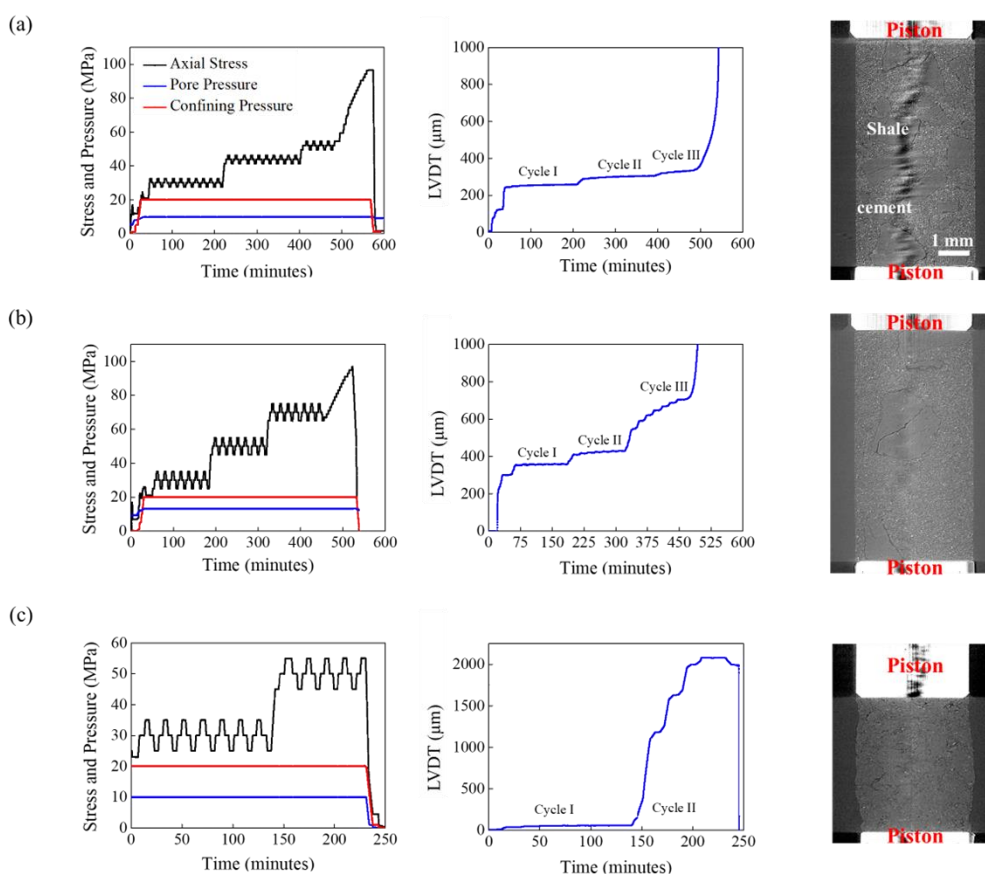

Figure 4.2 The experimental stress (left column) and strain (middle column) history of the samples. a) Sample A1: cement with 1-2 mm shale particles. b) Sample A2: cement with >2 mm shale

particles. C) Sample B: Draupne shale fragments. The right column shows central vertical tomographic cross sections. Natural fractures existed within the shales embedded in the cement matrix before the start of the experiment. The black vertical stripes that are seen across sample A1 are reconstruction artifacts.

The incremental von Mises shear strain in sample A2 during cycle III showcased localized strain development primarily within shale-rich regions. For cycles I and II a rather homogeneous distribution of the von Mises equivalent strain across the shale-rich regions was observed Notably, an early and highly defined deformation event occurred during cycle I, seemingly at the interface between a shale particle and the cement matrix. According to the findings of this investigation, the concentration of larger von Mises strains in shale particle regions could be related to the continuous deformation of these relatively soft materials during loading and unloading. Thus, through this article, we show that the continuous imaging of the sample facilitates a much-improved understanding of the deformation mechanisms in composite materials containing both a brittle (cement) and ductile (clayey shale) component phase.

4.3 Nanoscale imaging of shale fragments with coherent X-ray diffraction

Summary: In paper III, Coherent X-ray diffraction Imaging (CXDI) was used to study the internal structure of microscopic Pierre shale I fragments for the first time. The wide-angle scattering (WAXD) was performed together with the CXDI to study the mineralogy of these shale microparticles. Three samples were studied here, these fragments with size of 2-5 µm were obtained by scratching the sample surface with a scalpel. These microparticles were dispersed on a silicon nitride membrane. From the speckle patterns obtained from the experiments, the electron density maps were reconstructed using an iterative phase-retrieval algorithm. 3D tomograms were reconstructed with a resolution of 26 nm. From the 3D tomograms, it was possible to identify pyrite nanocrystals as inclusions in the quartz-clay matrix and the nanoscale pore structure. The combined CXDI-WAXD analysis enabled the establishment of a correlation between sample morphology and crystallite shape and size.
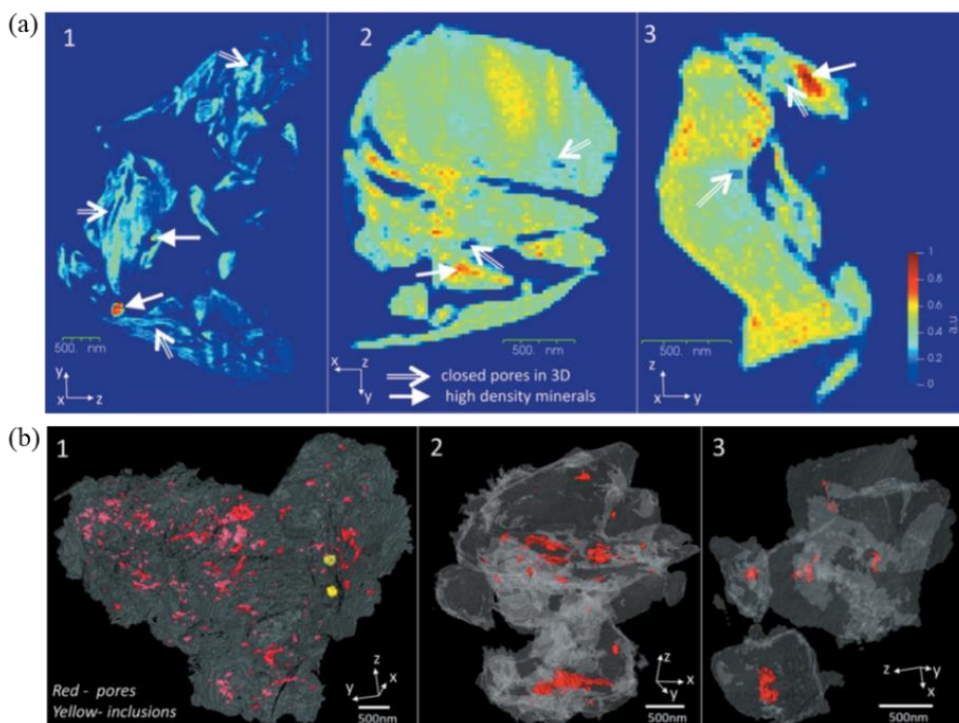
Figure 4.3. (a) Electron density of cross sections through samples 1–3, where the arrows highlight the high-density regions and closed pores. (b) Three-dimensional iso-surface renderings of samples 1–3, the high-density inclusions visible only in sample 1 indicated in yellow. The closed pores are indicated in red. Adapted from [169].

From the 2D electron density maps of the samples, the high-density regions and *closed pores* can be identified. In one of the samples, two spheroidal inclusions, both with a diameter of ~ 200 nm. It should be emphasized that the classification of pores as closed pores here is limited by the resolution of the 3D reconstruction. The electron density of the inclusions is about twice that of the rest of the sample and was ascertained from the WAXD data. In samples 2 and 3, areas with higher density and pore spaces can also be observed. Spheroidal pyrite crystals, as in sample 1, were not observed in samples 2 and 3. The hierarchical structure, complexity, and presence of multiple minerals in Pierre shale even in small samples were supported by the findings of CXDI.

In order to estimate the mineralogy of the shale microparticles a Rietveld refinement of the powder XRD pattern from bulk samples was also carried out. The refinement plots showed several Bragg peaks overlap, giving considerable uncertainty in the concentration estimate for the low-concentration minerals. The quantitative phase analyses revealed that the most dominant mineral present in the sample is quartz, along with clays and feldspar. The clay minerals can be identified as illite, kaolinite, clinochlore, and montmorillonite, while the feldspar group is represented by albite and orthoclase. Minor amounts of pyrite and dolomite were also identified. The results from Paper III highlight the potential of the combined CXDI-WAXD approach as an upcoming imaging modality for 3D nanoscale studies of shales and other geological formations via serial measurements of microscopic fragments, including cuttings from drillings.

4.4 Orientational mapping of minerals in Pierre shale using X-ray diffraction tensor tomography

Summary: The complex mineralogy of the shales has features ranging from several length scales which makes it difficult to investigate. Shales have several clay mineral phases, mixed with silt-sized particles of other minerals, commonly quartz and calcite. The oriented clay phases exhibit preferred orientations relative to the bedding planes which is the reason for the anisotropic scattering in both the small- and wide-angle regimes. The aim of the article is to understand the distribution of the minerals and the 3D orientation of the clay minerals. XRD-CT has been used to non-destructively study the mineral distributions in a sample of Pierre shale which has been correlated with the laboratory attenuation contrast computed tomography. In addition, using XRDTT we studied the nanostructure orientation of the clay mineral clinochlore in Pierre shale using a tomography setup with a single sample rotation axis. The scattering from the high-density large-grain minerals present in the sample was also studied.

The measured scattering features of the XRD-CT diffraction patterns have a total of 141 Debye–Scherrer rings in the range $\mathbf{q} = 0.22$–6.1 Å^{-1}. The high-intensity peaks were observed which correspond to a combination of heavier minerals and/or better-oriented crystallites within the scattering volume. The diffraction signals from clay minerals were observed to have a well-defined preferred orientation across the projections. We observed the quartz particles spread across the sample and randomly oriented with abrupt changes in orientation, we also noted that these mineral

grains are disconnected and of sub-voxel size. Similar observations were noted for the pyrite signal as well, across the sample the grains were randomly oriented grains. Pyrite tended to be localized to certain regions and the intensity distribution suggests a density correlation over longer distances.

The XRDTT method was utilized to study the scattering from the clay minerals and pyrites in the sample. 3 D orientation of the clinochlore crystals was reconstructed for the 001 and 002 scattering peaks. We were able to extract the orientation of the clay minerals and a strong global preferred orientation of the clays was noted along the c-axis parallel to the tomography axis.

5.   Conclusions and Outlook

The thesis aims to provide a better understanding of shales due to their importance in different subsurface applications like the petroleum industry, CO_2 storage, and H_2 storage. This thesis focuses on using non-destructive X-ray computed tomography as the primary tool for the investigation. The mechanical properties of the shales and shale-cement composites are studied using the novel experimental technique of triaxial deformation coupled with X-ray microtomography, while the hierarchical structure of shales is studied at different scales using novel X-ray diffraction computed tomography, X-ray tensor tomography, and coherent X-ray diffraction tomography. In the absence of undamaged field cores, researchers employ analogues from onshore quarries to analyze the mechanical properties of shale layers. Outcrops from the same formation can be discovered in Norway, the United Kingdom, or other areas with similar petrophysical qualities and mineralogies. Because of its identical clay content and porosity values, the Pierre I shale, for example, acts as a proxy for typical North Sea overburden shales. The few field shale cores available serve as calibration points for mechanical tests on outcrop equivalents such as the Pierre I shale. Due to the low availability of core samples owing to the extraction costs, shale *cuttings* readily available during drilling are used. Both outcrop samples and cuttings were used in this thesis depending on their availability.

Firstly, the mechanical properties of Draupne shales from the North Sea are investigated using time-resolved in situ imaging with a triaxial rig, yielding a quantitative description of the caprock sample's behavior under reservoir conditions, leading to failure. From the experiment on the Draupne shale sample, an almost linear behavior of the stress-strain during the loading process is noted. Analysis of the tomography datasets using digital volume correlation (DVC) allowed 3D mapping of the evolving strain tensor fields, providing insights into strain localization accompanying the fracturing process. This investigation revealed that although the deformation plot is linear initially, a detailed analysis using DVC on the dataset suggests that it may be erroneous to use linear elasticity to characterize even this part of the shale deformation. Tracking the evolution of the 3D-displacement fields and comparing the time-steps, an initially

homogeneous deformation fields that undergoes transition over time into a rotation-rich state was observed. Finally, the displacement field grows into a highly complicated state which denotes the sample fracture. The highly rotating strain condition found in 3D immediately prior to collapse had not previously been recorded in microscopic rock investigations, although it has been intuitively and conceptually well defined. A sliding-block mechanism was observed after fracture. Creep observed on the fault suggested that the slow deformations in the shale might be because of the surface slip and not only to bulk creep. Temporary localization of strains prior to the macroscopic fault was noted by following the evolution of the volumetric and von Mises strains. The study also revealed the presence of secondary fracture networks to the fault that spans the system in the sample during the various stages of the experiment. These features have not been reported previously and are important for understanding the failure of shales. The combination of time-resolved 3D microtomography imaging with 3D DVC analysis [26], [74], [75], [145]–[147], enabled in-situ investigations of deformation processes via quantification of shear and volumetric strains within the sample.

The occurrence of irreversible behavior in the early stages of the compression test holds significant implications for understanding fatigue. Typically, when the linear phase is considered elastic, the expectation is that after the load is removed (e.g., dissipation of pore pressure in the underlying reservoir), the shale reverts to its original, intact state. However, if subjected to a new load, assuming a false safety factor might be misleading. The issue of assuming a false safety factor after removing a load becomes clearer in fatigue tests. This is clearly made visible in the fatigue tests in the second study, and the effect is amplified by the heterogeneity of the shale-cement mix.

Next, the potential of using the triaxial rig with X-ray CT together with DVC to understand the time-dependent mechanical behavior of the Draupne shale cement composites under cyclic loading is explored. Previous research has studied sandstone's deformation and fatigue behavior when subjected to cyclic load [177]. The damage evolution and accumulation mode by cyclic loading under different confining pressures based on the sandstone load-unload response ratio were analyzed [178]. Studies on the mechanical behavior of shale rock under cyclic loading and unloading investigated instantaneous strain as well as the different levels of creep [179]. However, there is a lack of studies in triaxial experiments and theory to better understand underground rocks' cycle load mechanical behavior. Here, the experiment was designed to investigate the shale-

cement composite's fatigue evolution and track the evolution of the different strain fields in them. It was interesting to note the evolution of the displacement fields throughout samples with changes in the axial stress. The volumetric strains and the von Mises strain were calculated from image sequences to track the non-homogeneous deformations and the fatigue development in the sample. This investigation also revealed that the inclination and location of the von Mises shear strain and the dilatational and compaction bands formed are highly influenced by the presence of the coarse shale fragments. The investigational fatigue methods and the analysis techniques presented here uncover the local in-situ mechanics in the shale fragments mixed with cement admixture. They can further be applied to understand the long-term stability of these materials for different civil projects such as buildings, roads, and dams.

Pierre Shale I was studied in papers 3 and 4, first with high-resolution coherent X-ray diffractive imaging (CXDI) of several µm sized shale Pierre particles. CXDI and WAXD were used together to analyze the morphology, internal structure, and mineralogy of Pierre Shale I in this paper. Pyrite nanocrystals were directly localized as inclusions in the quartz-clay matrix. The volume percentage of closed pores was calculated to be 0.3-0.4%, which agrees with the stated porosity statistics for shales [94]. We were able to establish a correlation between sample morphology and crystallite form and size using the combined CXDI-WAXD analysis. The suggested methodology allows for quantitative geological and petrophysical investigations on small samples such as drill cuttings, eliminating the requirement for large cores, which are rarely taken from caprock shales.

In paper 4, Pierre shale I was studied again with XRD-CT and XRDTT. The same minerals were identified for the micrometer-sized particles in paper 3 but at a much larger scale. Whereas the complete Field of view (FoV) was 4µm for CXDI in paper 3, each voxel had the size of 50 µm in XRD-CT, and all regions of the sample were found to give rise to similar diffraction patterns. Scattering from clay minerals and high-density inclusions in Pierre shale was investigated using the XRDTT. The generated clay mineral orientation maps demonstrate that texture information may be retrieved using a single tomography axis, as in conventional CT. The presence of numerous clay minerals in shales revealed a significant global preferred orientation, and XRDTT enabled tiny deviations to be mapped in 3D. The mineralogy of chosen locations could be detected by routinely applying sinograms that combine attenuation-contrast and diffraction-contrast data.

Multi-grained pyrite or clinochlore crystallites were discovered in inclusions. Thus, XRD-CT and XRDTT are promising ways to understand shale hierarchical features.

The thesis has shown how the combination of time-resolved *in situ* X-ray CT with digital volume correlation can be used in a novel way to understand the mechanical properties of geological samples. It has been shown that such a combination can acquire fracture evolution during a stress-controlled experiment designed to track damage accumulation and shear localization toward macroscopic failure. In addition, the potential of such a method to track the fatigue evolution during cyclic loading and unloading triaxial tests is also demonstrated. The results of this thesis could lead to follow-up studies. For instance, further theoretical and experimental work and geophysical data analysis are required to characterize the fracture at the geological scale better. Theoretical models of mechanical properties of rock systems with microscale complexity and heterogeneity can be refined using the insights obtained from the investigations. It could also be possible to test and validate different theoretical models that describe the failure mechanism of different rock types. Finite element modeling can also be used to investigate the effects of confining pressure and displacement rate on the mechanical behavior of the different rocks. Further experiments with a range of confining pressures on rock systems can be made to provide a detailed insight into the underlying mechanism of strain localization in porous rocks which is strongly influenced by the applied confinement.

Triaxial mechanical tests are traditionally applied to full-size (40 mm diameter x 80 mm length) cores to characterize the mechanical properties of rocks. The HADES triaxial rig used in our study can only handle samples 5 mm in diameter and 10 mm in length. The size of the geological sample used for triaxial testing is crucial because it can affect the accuracy and representativeness of the results obtained from the test. A larger sample size can provide more reliable results by reducing the effects of heterogeneity, and anisotropy. However, new rigs need to be developed that are capable of handling large samples. The advantage of using the EBS (extremely brilliant source) upgrade at the ESRF is the drastically reduced measurement times. 3-dimensional scans using home laboratory CT take more time than the synchrotron. Hence conducting triaxial compression experiments using a home laboratory CT may cause additional deformation or creep as the sample is maintained at the constant stress during the measurement. With further developments and innovations, hopefully, new advanced home laboratory setups with low measurement time and

sources with high flux will be developed that enable us to conduct experiments in home laboratories much more efficiently.

To conclude, the deformation characterization of geological samples is an active research topic. The experimental and analysis techniques presented in this thesis have been demonstrated as versatile tools that will help to reveal the local mechanics in geological samples and can further be applied to understand the stability of these rocks for subsurface applications.

Bibliography

[1]   P. Cerasi *et al.*, "Shale Creep as Leakage Healing Mechanism in CO_2 Sequestration," *Energy Procedia*, vol. 114, pp. 3096–3112, Jul. 2017, doi: 10.1016/J.EGYPRO.2017.03.1439.

[2]   T. A. Torp and J. Gale, "Demonstrating storage of CO_2 in geological reservoirs: The Sleipner and SACS projects," *Energy*, vol. 29, no. 9–10, pp. 1361–1369, Jul. 2004, doi: 10.1016/j.energy.2004.03.104.

[3]   Z. Li, M. Dong, S. Li, and S. Huang, "CO_2 sequestration in depleted oil and gas reservoirs—caprock characterization and storage capacity," *Energy Convers Manag*, vol. 47, no. 11–12, pp. 1372–1382, Jul. 2006, doi: 10.1016/j.enconman.2005.08.023.

[4]   S. M. Benson and D. R. Cole, "CO_2 Sequestration in Deep Sedimentary Formations," *Elements*, vol. 4, no. 5, pp. 325–331, Oct. 2008, doi: 10.2113/gselements.4.5.325.

[5]   S. M. . M. Kang, E. . Fathi, R. J. . J. Ambrose, I. Y. . Y. Akkutlu, and R. F. . F. Sigal, "Carbon Dioxide Storage Capacity of Organic-Rich Shales," *SPE Journal*, vol. 16, no. 04, pp. 842–855, Dec. 2011, doi: 10.2118/134583-PA.

[6]   L. Ma *et al.*, "Correlative multi-scale imaging of shales: a review and future perspectives," *Geological Society, London, Special Publications*, vol. 454, no. 1, pp. 175–199, Jan. 2017, doi: 10.1144/SP454.11.

[7]   L. M. Anovitz and D. R. Cole, "Characterization and Analysis of Porosity and Pore Structures," *Rev Mineral Geochem*, vol. 80, no. 1, pp. 61–164, 2015, doi: 10.2138/rmg.2015.80.04.

[8]   M. Arif, M. Mahmoud, Y. Zhang, S. I.-I. J. of Coal, and undefined 2021, "X-ray tomography imaging of shale microstructures: A review in the context of multiscale correlative imaging," *Int J Coal Geol*, vol. 233, p. 103641, 2021, doi: 10.1016/j.coal.2020.103641.

[9]   A. Ougier-Simonin, F. Renard, C. Boehm, and S. Vidal-Gilbert, "Microfracturing and microporosity in shales," *Earth Sci Rev*, vol. 162, pp. 198–226, Nov. 2016, doi: 10.1016/j.earscirev.2016.09.006.

[10]   T. A. Saleh, "Advanced trends of shale inhibitors for enhanced properties of water-based drilling fluid," *Upstream Oil and Gas Technology*, vol. 8, p. 100069, Feb. 2022, doi: 10.1016/j.upstre.2022.100069.

[11]   Q. Wang, X. Chen, A. Jha, H. R.-R. and S. Energy, and undefined 2014, "Natural gas from shale formation–the evolution, evidences and challenges of shale gas revolution in United States," *Renewable and Sustainable Energy Reviews*, vol. 30, pp. 1–28, 2014, doi: 10.1016/J.RSER.2013.08.065.

[12]   J. F. W. Gale, S. E. Laubach, J. E. Olson, P. Eichhuble, and A. Fall, "Natural Fractures in shale: A review and new observations," *Am Assoc Pet Geol Bull*, vol. 98, no. 11, pp. 2165–2216, Nov. 2014, doi: 10.1306/08121413151.

Bibliography

[13]   S. Kelly, H. El-Sobky, C. Torres-Verdín, and M. T. Balhoff, "Assessing the utility of FIB-SEM images for shale digital rock physics," *Adv Water Resour*, vol. 95, pp. 302–316, Sep. 2016, doi: 10.1016/j.advwatres.2015.06.010.

[14]   N. Ural, "The significance of scanning electron microscopy (SEM) analysis on the microstructure of improved clay: An overview," *Open Geosciences*, vol. 13, no. 1, pp. 197–218, Feb. 2021, doi: 10.1515/geo-2020-0145.

[15]   L. Ma, "Multi-scale 3D imaging of the microstructure in organic-rich shales," The University of Manchester, United Kingdom, 2016.

[16]   L. Ma *et al.*, "Correlative multi-scale imaging of shales: A review and future perspectives," *Geol Soc Spec Publ*, vol. 454, no. 1, pp. 175–199, 2017, doi: 10.1144/SP454.11.

[17]   J. Als-Nielsen and D. McMorrow, *Elements of modern X-ray physics*. 2011. doi: 10.1002/9781119998365.

[18]   A. C. Kak, M. Slaney, and G. Wang, *Principles of Computerized Tomographic Imaging*, vol. 29, no. 1. Society of Industrial and Applied Mathematics, 2002. doi: 10.1118/1.1455742.

[19]   D. Wildenschild and A. P. Sheppard, "X-ray imaging and analysis techniques for quantifying pore-scale structure and processes in subsurface porous medium systems," *Adv Water Resour*, vol. 51, pp. 217–246, Jan. 2013, doi: 10.1016/j.advwatres.2012.07.018.

[20]   F. K. Mürer *et al.*, "3D Maps of Mineral Composition and Hydroxyapatite Orientation in Fossil Bone Samples Obtained by X-ray Diffraction Computed Tomography," *Sci Rep*, vol. 8, no. 1, p. 10052, Jul. 2018, doi: 10.1038/s41598-018-28269-1.

[21]   F. K. Mürer *et al.*, "Quantifying the hydroxyapatite orientation near the ossification front in a piglet femoral condyle using X-ray diffraction tensor tomography," *Sci Rep*, vol. 11, no. 1, p. 2144, Jan. 2021, doi: 10.1038/s41598-020-80615-4.

[22]   M. Esmaeili *et al.*, "Ptychographic X-ray tomography of silk fiber hydration," *ACS Publications*, vol. 46, no. 2, pp. 434–439, Jan. 2013, doi: 10.1021/ma3021163.

[23]   G. Artioli *et al.*, "X-ray diffraction microtomography (XRD-CT), a novel tool for non-invasive mapping of phase development in cement materials," *Anal Bioanal Chem*, vol. 397, no. 6, pp. 2131–2136, Jul. 2010, doi: 10.1007/S00216-010-3649-0.

[24]   E. Tudisco *et al.*, "Fast 4-D Imaging of Fluid Flow in Rock by High-Speed Neutron Tomography," *J Geophys Res Solid Earth*, vol. 124, no. 4, pp. 3557–3569, Apr. 2019, doi: 10.1029/2018JB016522.

[25]   E. A. Chavez Panduro *et al.*, "Real Time 3D Observations of Portland Cement Carbonation at CO_2 Storage Conditions," *Environ Sci Technol*, vol. 54, no. 13, pp. 8323–8332, Jul. 2020, doi: 10.1021/acs.est.0c00578.

[26]   F. Renard *et al.*, "Dynamic In Situ Three-Dimensional Imaging and Digital Volume Correlation Analysis to Quantify Strain Localization and Fracture Coalescence in Sandstone," *Pure Appl Geophys*, vol. 176, no. 3, pp. 1083–1115, Mar. 2019, doi: 10.1007/S00024-018-2003-X/FIGURES/12.

[27]   N. Lenoir, M. Bornert, J. Desrues, P. Bésuelle, G. V.- Strain, and undefined 2007, "Volumetric digital image correlation applied to X-ray microtomography images from triaxial compression tests

on argillaceous rock," *Wiley Online Library*, vol. 43, no. 3, pp. 193–205, Aug. 2007, doi: 10.1111/j.1475-1305.2007.00348.x.

[28]   S. Raynaud, G. Vasseur, and R. Soliva, "In vivo CT X-ray observations of porosity evolution during triaxial deformation of a calcarenite," *International Journal of Rock Mechanics and Mining Sciences*, vol. 56, pp. 161–170, Dec. 2012, doi: 10.1016/j.ijrmms.2012.07.020.

[29]   F. Renard, J. McBeck, N. Kandula, B. Cordonnier, P. Meakin, and Y. Ben-Zion, "Volumetric and shear processes in crystalline rock approaching faulting," *Proceedings of the National Academy of Sciences*, vol. 116, no. 33, pp. 16234–16239, Aug. 2019, doi: 10.1073/pnas.1902994116.

[30]   J. A. McBeck, B. Cordonnier, S. Vinciguerra, F. R.-G. Research, and undefined 2019, "Volumetric and Shear Strain Localization in Mt. Etna Basalt," *Geophys Res Lett*, vol. 46, no. 5, pp. 2425–2433, Mar. 2019, doi: 10.1029/2018GL081299.

[31]   E. Tudisco, E. Andò, R. Cailletaud, and S. A. Hall, "TomoWarp2: A local digital volume correlation code," *SoftwareX*, vol. 6, pp. 267–270, 2017, doi: 10.1016/j.softx.2017.10.002.

[32]   J. D. Arthur, B. Bohm, and D. Cornue, "Environmental Considerations of Modern Shale Gas Development," in *All Days*, SPE, Oct. 2009. doi: 10.2118/122931-MS.

[33]   M. Eriksson, J. F. van der Veen, and C. Quitmann, "Diffraction-limited storage rings – a window to the science of tomorrow," *J Synchrotron Radiat*, vol. 21, no. 5, pp. 837–842, Sep. 2014, doi: 10.1107/S1600577514019286.

[34]   W. C. Röntgen, "Ueber eine neue Art von Strahlen," *Phys.-med. Gesellschaft*, pp. 1–20, 1985.

[35]   K.-D. Liss, A. Bartels, A. Schreyer, and H. Clemens, "High-Energy X-Rays: A tool for Advanced Bulk Investigations in Materials Science and Physics," *Textures and Microstructures*, vol. 35, no. 3–4, pp. 219–252, Jan. 2003, doi: 10.1080/07303300310001634952.

[36]   R. Cierniak, "Introduction," *X-Ray Computed Tomography in Biomedical Engineering*, pp. 1–5, 2011, doi: 10.1007/978-0-85729-027-4_1.

[37]   L. Romans, *Computed Tomography for Technologists: A comprehensive text*. Lippincott Williams & Wilkins, 2018.

[38]   Z. Du, Y. Hu, N. A. Buttar, A. M.-F. science & nutrition, and undefined 2019, "X-ray computed tomography for quality inspection of agricultural products: A review," *Wiley Online LibraryZ Du, Y Hu, N Ali Buttar, A MahmoodFood science & nutrition, 2019•Wiley Online Library*, vol. 7, no. 10, pp. 3146–3160, Oct. 2019, doi: 10.1002/fsn3.1179.

[39]   H. Jung, "Basic physical principles and clinical applications of computed tomography," *Progress in Medical Physics*, vol. 32, no. 1, pp. 1–17, 2021, doi: 10.14316/pmp.2021.32.1.1.

[40]   V. Petrik, V. Apok, J. A. Britton, B. A. Bell, and M. C. Papadopoulos, "Godfrey Hounsfield and the dawn of computed tomography," *Neurosurgery*, vol. 58, no. 4, pp. 780–786, Apr. 2006, doi: 10.1227/01.NEU.0000204309.91666.06.

[41]   F. Renard, J. McBeck, N. Kandula, B. Cordonnier, P. Meakin, and Y. Ben-Zion, "Volumetric and shear processes in crystalline rock approaching faulting," *Proc Natl Acad Sci U S A*, vol. 116, no. 33, pp. 16234–16239, Aug. 2019, doi: 10.1073/PNAS.1902994116.

[42] J. Radon, "Uber die Bestimmung von Funktionen durch ihre Integralwerte langs gewissez Mannigfaltigheiten, Ber," *Verh. Sachs. Akad. Wiss. Leipzig, Math Phys Klass*, vol. 69, 1917.

[43] A. Faridani, "Introduction to the mathematics of computed tomography," *Inside Out: Inverse Problems and Applications*, vol. 47, no. 1–46, p. 12, 2003.

[44] F. Natterer, *The mathematics of computerized tomography*. SIAM, 2001.

[45] A. Rieder and A. Faridani, "The Semidiscrete Filtered Backprojection Algorithm Is Optimal for Tomographic Inversion," *SIAM J Numer Anal*, vol. 41, no. 3, pp. 869–892, Jul. 2006, doi: 10.1137/S0036142902405643.

[46] J. Beatty, "The Radon Transform and the Mathematics of Medical Imaging," 2012.

[47] D. Qiu and E. Seeram, "Does Iterative Reconstruction Improve Image Quality and Reduce Dose in Computed Tomography?," *Radiol Open J*, vol. 1, no. 2, pp. 42–54, Sep. 2016, doi: 10.17140/ROJ-1-108.

[48] K. Srinivasan, M. Mohammadi, and J. Shepherd, "Investigation of effect of reconstruction filters on cone-beam computed tomography image quality," *Australas Phys Eng Sci Med*, vol. 37, no. 3, pp. 607–614, Sep. 2014, doi: 10.1007/S13246-014-0291-8/FIGURES/6.

[49] M. E. Birkbak, H. Leemreize, S. Frølich, S. R. Stock, and H. Birkedal, "Diffraction scattering computed tomography: a window into the structures of complex nanomaterials," *Nanoscale*, vol. 7, no. 44, pp. 18402–18410, Nov. 2015, doi: 10.1039/C5NR04385A.

[50] G. Artioli *et al.*, "X-ray diffraction microtomography (XRD-CT), a novel tool for non-invasive mapping of phase development in cement materials," *Anal Bioanal Chem*, vol. 397, no. 6, pp. 2131–2136, Jul. 2010, doi: 10.1007/S00216-010-3649-0/FIGURES/3.

[51] G. Harding, J. Kosanetzky, and U. Neitzel, "X-ray diffraction computed tomography," *Med Phys*, vol. 14, no. 4, pp. 515–525, Jul. 1987, doi: 10.1118/1.596063.

[52] P. Bleuet, E. Welcomme, E. Dooryhée, J. Susini, J. L. Hodeau, and P. Walter, "Probing the structure of heterogeneous diluted materials by diffraction tomography," *Nature Materials 2008 7:6*, vol. 7, no. 6, pp. 468–472, Apr. 2008, doi: 10.1038/nmat2168.

[53] V. Middelkoop *et al.*, "3D printed Ni/Al2O3 based catalysts for CO_2 methanation - a comparative and operando XRD-CT study," *Journal of CO_2 Utilization*, vol. 33, pp. 478–487, Oct. 2019, doi: 10.1016/J.JCOU.2019.07.013.

[54] S. W. T. Price *et al.*, "Unravelling the spatial dependency of the complex solid-state chemistry of Pb in a paint micro-sample from Rembrandt's Homer using XRD-CT," *Chemical Communications*, vol. 55, no. 13, pp. 1931–1934, Feb. 2019, doi: 10.1039/C8CC09705D.

[55] M. Eriksson, J. F. Van Der Veen, and C. Quitmann, "Diffraction-limited storage rings – a window to the science of tomorrow," *urn:issn:1600-5775*, vol. 21, no. 5, pp. 837–842, Aug. 2014, doi: 10.1107/S1600577514019286.

[56] S. R. Stock, F. De Carlo, and J. D. Almer, "High energy X-ray scattering tomography applied to bone," *J Struct Biol*, vol. 161, no. 2, pp. 144–150, Feb. 2008, doi: 10.1016/J.JSB.2007.10.001.

Bibliography

[57] U. Kleuker, P. Suortti, W. Weyrich, and P. Spanne, "Feasibility study of x-ray diffraction computed tomography for medical imaging," *Phys Med Biol*, vol. 43, no. 10, p. 2911, Oct. 1998, doi: 10.1088/0031-9155/43/10/017.

[58] Z. Zhu, A. Katsevich, A. J. Kapadia, J. A. Greenberg, and S. Pang, "X-ray diffraction tomography with limited projection information," *Scientific Reports 2018 8:1*, vol. 8, no. 1, pp. 1–6, Jan. 2018, doi: 10.1038/s41598-017-19089-w.

[59] A. M. Beale, S. D. M. Jacques, E. K. Gibson, and M. Di Michiel, "Progress towards five dimensional diffraction imaging of functional materials under process conditions," *Coord Chem Rev*, vol. 277–278, pp. 208–223, Oct. 2014, doi: 10.1016/J.CCR.2014.05.008.

[60] A. Vamvakeros *et al.*, "5D operando tomographic diffraction imaging of a catalyst bed," *Nature Communications 2018 9:1*, vol. 9, no. 1, pp. 1–11, Nov. 2018, doi: 10.1038/s41467-018-07046-8.

[61] J. Palle *et al.*, "Nanobeam X-ray fluorescence and diffraction computed tomography on human bone with a resolution better than 120 nm," *J Struct Biol*, vol. 212, no. 3, p. 107631, Dec. 2020, doi: 10.1016/J.JSB.2020.107631.

[62] T. Beuvier *et al.*, "X-ray nanotomography of coccolithophores reveals that coccolith mass and segment number correlate with grid size," *Nature Communications 2019 10:1*, vol. 10, no. 1, pp. 1–8, Feb. 2019, doi: 10.1038/s41467-019-08635-x.

[63] E. T. B. Skjønsfjell *et al.*, "High-resolution coherent x-ray diffraction imaging of metal-coated polymer microspheres," *Journal of the Optical Society of America A*, vol. 35, no. 1, p. A7, 2018, doi: 10.1364/josaa.35.0000a7.

[64] E. T. B. Skjønsfjell, Y. Chushkin, F. Zontone, and D. W. Breiby, "In situ coherent X-ray diffraction imaging of radiation-induced mass loss in metal–polymer composite spheres," *urn:issn:1600-5775*, vol. 25, no. 4, pp. 1162–1171, May 2018, doi: 10.1107/S160057751800588X.

[65] O. Cherkas, T. Beuvier, D. W. Breiby, Y. Chushkin, F. Zontone, and A. Gibaud, "Direct Observation of Microparticle Porosity Changes in Solid-State Vaterite to Calcite Transformation by Coherent X-ray Diffraction Imaging," *Cryst Growth Des*, vol. 17, no. 8, pp. 4183–4188, Aug. 2017, doi: 10.1021/acs.cgd.7b00476.

[66] Y. Chushkin, F. Zontone, O. Cherkas, and A. Gibaud, "Quantitative nanotomography of amorphous and polycrystalline samples using coherent X-ray diffraction," *J Appl Crystallogr*, vol. 52, no. 3, pp. 571–578, Jun. 2019, doi: 10.1107/S1600576719004394.

[67] J. Miao, P. Charalambous, J. Kirz, and D. Sayre, "Extending the methodology of X-ray crystallography to allow imaging of micrometre-sized non-crystalline specimens," *Nature 1999 400:6742*, vol. 400, no. 6742, pp. 342–344, Jul. 1999, doi: 10.1038/22498.

[68] J. Miao, T. Ishikawa, I. K. Robinson, and M. M. Murnane, "Beyond crystallography: Diffractive imaging using coherent X-ray light sources," *Science (1979)*, vol. 348, no. 6234, pp. 530–535, May 2015, doi: 10.1126/SCIENCE.AAA1394.

[69] H. N. Chapman and K. A. Nugent, "Coherent lensless X-ray imaging," *Nature Photonics 2010 4:12*, vol. 4, no. 12, pp. 833–839, Nov. 2010, doi: 10.1038/nphoton.2010.240.

[70] C. Ponchut, J. M. Rigal, J. Clément, E. Papillon, A. Homs, and S. Petitdemange, "MAXIPIX, a fast readout photon-counting X-ray area detector for synchrotron applications," *Journal of Instrumentation*, vol. 6, no. 01, p. C01069, Jan. 2011, doi: 10.1088/1748-0221/6/01/C01069.

[71] J. R. Fienup, "Phase retrieval algorithms: a comparison," *Applied Optics, Vol. 21, Issue 15, pp. 2758-2769*, vol. 21, no. 15, pp. 2758–2769, Aug. 1982, doi: 10.1364/AO.21.002758.

[72] J. Desrues, R. Chambon, M. Mokni, and F. Mazerolle, "Void ratio evolution inside shear bands in triaxial sand specimens studied by computed tomography," *Geotechnique*, vol. 46, no. 3, pp. 529–546, May 1996, doi: 10.1680/GEOT.1996.46.3.529.

[73] P. Bésuelle, J. Desrues, and S. Raynaud, "Experimental characterisation of the localisation phenomenon inside a Vosges sandstone in a triaxial cell," *International Journal of Rock Mechanics and Mining Sciences*, vol. 37, no. 8, pp. 1223–1237, Dec. 2000, doi: 10.1016/S1365-1609(00)00057-5.

[74] F. Renard, D. Bernard, X. Thibault, and E. Boller, "Synchrotron 3D microtomography of halite aggregates during experimental pressure solution creep and evolution of the permeability," *Geophys Res Lett*, vol. 31, no. 7, Apr. 2004, doi: 10.1029/2004GL019605.

[75] F. Renard, D. Bernard, J. Desrues, and A. Ougier-Simonin, "3D imaging of fracture propagation using synchrotron X-ray microtomography," *Earth Planet Sci Lett*, vol. 286, no. 1–2, pp. 285–291, Aug. 2009, doi: 10.1016/J.EPSL.2009.06.040.

[76] F. Renard, B. Cordonnier, D. K. Dysthe, E. Boller, P. Tafforeau, and A. Rack, "A deformation rig for synchrotron microtomography studies of geomaterials under conditions down to 10 km depth in the Earth," *J Synchrotron Radiat*, vol. 23, no. 4, pp. 1030–1034, Jun. 2016, doi: 10.1107/S1600577516008730.

[77] F. Renard, J. McBeck, N. Kandula, B. Cordonnier, P. Meakin, and Y. Ben-Zion, "Volumetric and shear processes in crystalline rock approaching faulting," *Proc Natl Acad Sci U S A*, vol. 116, no. 33, pp. 16234–16239, Aug. 2019, doi: 10.1073/PNAS.1902994116.

[78] W. R. Crum, T. Hartkens, and D. L. G. Hill, "Non-rigid image registration: theory and practice," *Br J Radiol*, vol. 77, no. suppl_2, pp. S140–S153, Jan. 2004, doi: 10.1259/BJR/25329214.

[79] S. Oh and S. Kim, "Deformable image registration in radiation therapy," *Radiat Oncol J*, vol. 35, no. 2, p. 101, 2017, doi: 10.3857/ROJ.2017.00325.

[80] B. K. Bay, T. S. Smith, D. P. Fyhrie, and M. Saad, "Digital volume correlation: Three-dimensional strain mapping using x-ray tomography," *Exp Mech*, vol. 39, no. 3, pp. 217–226, 1999, doi: 10.1007/BF02323555/METRICS.

[81] H. Toda, E. Maire, Y. Aoki, and M. Kobayashi, "Three-dimensional strain mapping using in situ X-ray synchrotron microtomography," *J Strain Anal Eng Des*, vol. 46, no. 7, pp. 549–561, Jul. 2011, doi: 10.1177/0309324711408975.

[82] A. Buljac *et al.*, "Digital Volume Correlation: Review of Progress and Challenges," *Exp Mech*, vol. 58, no. 5, pp. 661–708, Jun. 2018, doi: 10.1007/S11340-018-0390-7/FIGURES/25.

[83] I. Jandejsek, O. Jiroušek, and D. Vavřík, "Precise strain measurement in complex materials using Digital Volumetric Correlation and time lapse micro-CT data," *Procedia Eng*, vol. 10, pp. 1730–1735, Jan. 2011, doi: 10.1016/J.PROENG.2011.04.288.

[84] L. Huang, R. K. Korhonen, M. J. Turunen, and M. A. J. Finnilä, "Experimental mechanical strain measurement of tissues," *PeerJ*, vol. 2019, no. 3, p. e6545, Mar. 2019, doi: 10.7717/PEERJ.6545/TABLE-2.

[85] J. Adam, M. Klinkmüller, G. Schreurs, and B. Wieneke, "Quantitative 3D strain analysis in analogue experiments simulating tectonic deformation: Integration of X-ray computed tomography and digital volume correlation techniques," *J Struct Geol*, vol. 55, pp. 127–149, Oct. 2013, doi: 10.1016/J.JSG.2013.07.011.

[86] B. Pan, K. Qian, H. Xie, and A. Asundi, "Two-dimensional digital image correlation for in-plane displacement and strain measurement: a review," *Meas Sci Technol*, vol. 20, no. 6, p. 062001, Apr. 2009, doi: 10.1088/0957-0233/20/6/062001.

[87] M. Sutton, W. Wolters, W. Peters, W. Ranson, and S. McNeill, "Determination of displacements using an improved digital correlation method," *Image Vis Comput*, vol. 1, no. 3, pp. 133–139, Aug. 1983, doi: 10.1016/0262-8856(83)90064-1.

[88] E. Tudisco, S. A. Hall, E. M. Charalampidou, N. Kardjilov, A. Hilger, and H. Sone, "Full-field Measurements of Strain Localisation in Sandstone by Neutron Tomography and 3D-Volumetric Digital Image Correlation," *Phys Procedia*, vol. 69, pp. 509–515, Jan. 2015, doi: 10.1016/J.PHPRO.2015.07.072.

[89] S. A. Hall, "A methodology for 7D warping and deformation monitoring using time-lapse seismic data," *Geophysics*, vol. 71, no. 4, pp. O21–O31, Jul. 2006, doi: 10.1190/1.2212227.

[90] S. A. Hall *et al.*, "Discrete and continuum analysis of localised deformation in sand using X-ray μCT and volumetric digital image correlation," *Geotechnique*, vol. 60, no. 5, pp. 315–322, May 2010, doi: 10.1680/GEOT.2010.60.5.315.

[91] W. F. Chen and D. J. Han, "Plasticity for Structural Engineers." Springer-Verlag, p. 310, 1988.

[92] S. Shrivastava, C. Ghosh, and J. J. Jonas, "A comparison of the von Mises and Hencky equivalent strains for use in simple shear experiments," *Philosophical Magazine*, vol. 92, no. 7, pp. 779–786, Mar. 2012, doi: 10.1080/14786435.2011.634848.

[93] B. Metz, O. Davidson, H. De Coninck, M. Loos, and L. Meyer, *IPCC special report on carbon dioxide capture and storage*. 2005.

[94] T. Ajayi, J. S. Gomes, and A. Bera, "A review of CO 2 storage in geological formations emphasizing modeling, monitoring and capacity estimation approaches," *Pet Sci*, vol. 16, pp. 1028–1063, 2019.

[95] E. Lindeberg and P. Bergmo, "The long-term fate of CO_2 injected into an aquifer," *Greenhouse gas control technologies*, vol. 1, pp. 489–494, 2003.

[96] P. Crockford and K. Telmer, "Exploring the fate of CO_2 at British Columbia's planned Fort Nelson Carbon Capture and Storage Project," *Geoscience Reports MEMPR BC*, 2009.

[97] Y.-S. Jun, D. E. Giammar, and C. J. Werth, "Impacts of geochemical reactions on geologic carbon sequestration." ACS Publications, 2013.

[98] N. Koukouzas, Z. Kypritidou, G. Purser, C. A. Rochelle, C. Vasilatos, and N. Tsoukalas, "Assessment of the impact of CO_2 storage in sandstone formations by experimental studies and geochemical modeling: The case of the Mesohellenic Trough, NW Greece," *International Journal of Greenhouse Gas Control*, vol. 71, pp. 116–132, 2018.

[99] U. Berge *et al.*, "Carbon capture and storage." Zero Emission Resource Organization. , 2011.

[100] C. D. Hawkes, P. J. Mclellan, and S. Bachu, "Geomechanical Factors Affecting Geological Storage of CO_2 in Depleted Oil and Gas Reservoirs," *Journal of Canadian Petroleum Technology*, vol. 44, no. 10, pp. 52–61, Oct. 2005, doi: 10.2118/05-10-05/32223.

[101] B. Orlic, "Geomechanical effects of CO_2 storage in depleted gas reservoirs in the Netherlands: Inferences from feasibility studies and comparison with aquifer storage," *Journal of Rock Mechanics and Geotechnical Engineering*, vol. 8, no. 6, pp. 846–859, Dec. 2016, doi: 10.1016/J.JRMGE.2016.07.003.

[102] T. A. Torp and J. Gale, "Demonstrating storage of CO_2 in geological reservoirs: the Sleipner and SACS projects," *Energy*, vol. 29, no. 9–10, pp. 1361–1369, 2004, doi: 10.1016/j.energy.2004.03.104.

[103] R. J. Arts, A. Chadwick, O. Eiken, S. Thibeau, and S. Nooner, "Ten years' experience of monitoring CO_2 injection in the Utsira Sand at Sleipner, offshore Norway," *First break*, vol. 26, no. 1, 2008.

[104] T. A. Torp and K. R. Brown, "CO_2 underground storage costs as experienced at Sleipner and Weyburn," in *Greenhouse Gas Control Technologies 7*, Elsevier, 2005, pp. 531–538. doi: 10.1007/s11440-013-0229-4.

[105] G. Protti, "Win-Win: Enhanced Oil Recovery and CO_2 Storage at EnCana's Weyburn Oilfield," in *World Petroleum Congress*, WPC, 2005, p. WPC-18.

[106] S. Rani, E. Padmanabhan, and B. K. Prusty, "Review of gas adsorption in shales for enhanced methane recovery and CO_2 storage," *J Pet Sci Eng*, vol. 175, pp. 634–643, Apr. 2019, doi: 10.1016/J.PETROL.2018.12.081.

[107] Y. Gensterblum *et al.*, "Gas transport and storage capacity in shale gas reservoirs – A review. Part A: Transport processes," *Journal of Unconventional Oil and Gas Resources*, vol. 12, pp. 87–122, Dec. 2015, doi: 10.1016/J.JUOGR.2015.08.001.

[108] D. J. K. Ross and R. M. Bustin, "Characterizing the shale gas resource potential of Devonian–Mississippian strata in the Western Canada sedimentary basin: Application of an integrated formation evaluation," *Am Assoc Pet Geol Bull*, vol. 92, no. 1, pp. 87–125, Jan. 2008, doi: 10.1306/09040707048.

[109] C. H. Sondergeld, R. J. Ambrose, C. S. Rai, and J. . Moncrieff, "Micro-Structural Studies of Gas Shales," Feb. 2010, doi: 10.2118/131771-MS.

[110] R. M. Slatt and N. R. O'Brien, "Pore types in the Barnett and Woodford gas shales: Contribution to understanding gas storage and migration pathways in fine-grained rocks," *Am Assoc Pet Geol Bull*, vol. 95, no. 12, pp. 2017–2030, Dec. 2011, doi: 10.1306/03301110145.

Bibliography

[111] T. Saif *et al.*, "4D in situ synchrotron X-ray tomographic microscopy and laser-based heating study of oil shale pyrolysis," *Appl Energy*, vol. 235, pp. 1468–1475, Feb. 2019, doi: 10.1016/j.apenergy.2018.11.044.

[112] H. Panahi, M. Kobchenko, and F. Renard, "A 4D Synchrotron X-Ray-Tomography Study of the Formation of Hydrocarbon- Migration Pathways in Heated Organic-Rich Shale," vol. 00000, no. March 2011, pp. 1–12, 2012, doi: 10.2118/162939-PA.

[113] L. Ma *et al.*, "Correlative multi-scale imaging of shales: A review and future perspectives," *Geol Soc Spec Publ*, vol. 454, no. 1, pp. 175–199, 2017, doi: 10.1144/SP454.11.

[114] Harvey. Blatt, R. J. Tracy, and E. G. Ehlers, *Petrology : igneous, sedimentary, and metamorphic.* Macmillan, 2006.

[115] C. W. Tomlinson, "The Origin of Red Beds: A Study of the Conditions of Origin of the Permo-Carboniferous and Triassic Red Beds of the Western United States," *J Geol*, vol. 24, no. 2, pp. 153–179, Feb. 1916, doi: 10.1086/622316.

[116] D. H. Yaalon, "Mineral composition of the average shale: Clay Minerals Bull., v. 5," 1962.

[117] R. Bennett, W. Bryant, and M. Hulbert, *Microstructure of fine-grained sediments: From mud to shale*. Springer Science & Business Media, 1991.

[118] P. Potter, J. Maynard, and W. Pryor, *Sedimentology of shale: study guide and reference source*. Springer Science & Business Media, 2012.

[119] L. Chen, L. Zhang, Q. Kang, H. S. Viswanathan, J. Yao, and W. Tao, "Nanoscale simulation of shale transport properties using the lattice Boltzmann method: permeability and diffusivity," *Scientific Reports 2015 5:1*, vol. 5, no. 1, pp. 1–8, Jan. 2015, doi: 10.1038/srep08089.

[120] C. Volzone, J. O. Rinaldi, and J. Ortiga, "N2 and CO_2 Adsorption by TMA- and HDP-Montmorillonites," *Materials Research*, vol. 5, no. 4, pp. 475–479, Oct. 2002, doi: 10.1590/S1516-14392002000400013.

[121] M. Vandenbroucke and C. Largeau, "Kerogen origin, evolution and structure," *Org Geochem*, vol. 38, no. 5, pp. 719–833, May 2007, doi: 10.1016/J.ORGGEOCHEM.2007.01.001.

[122] B. Venkat Suryanarayana Murthy Pathi, "Factors affecting the permeability of gas shales," University of British Columbia, Vancouver, 2008. doi: 10.14288/1.0052381.

[123] R. M. Bustin, A. M. M. Bustin, X. Cui, D. J. K. Ross, and V. S. M. Pathi, "Impact of Shale Properties on Pore Structure and Storage Characteristics," *Society of Petroleum Engineers - Shale Gas Production Conference 2008*, pp. 32–59, Nov. 2008, doi: 10.2118/119892-MS.

[124] R. G. Loucks, R. M. Reed, S. C. Ruppel, and D. M. Jarvie, "Morphology, Genesis, and Distribution of Nanometer-Scale Pores in Siliceous Mudstones of the Mississippian Barnett Shale," *Journal of Sedimentary Research*, vol. 79, no. 12, pp. 848–861, Dec. 2009, doi: 10.2110/JSR.2009.092.

[125] J. Rouquerol *et al.*, "Recommendations for the characterization of porous solids (Technical Report)," *Pure and Applied Chemistry*, vol. 66, no. 8, pp. 1739–1758, Jan. 1994, doi: 10.1351/PAC199466081739/MACHINEREADABLECITATION/RIS.

[126] M. Josh, L. Esteban, C. Delle Piane, J. Sarout, D. N. Dewhurst, and M. B. Clennell, "Laboratory characterisation of shale properties," *J Pet Sci Eng*, vol. 88–89, pp. 107–124, Jun. 2012, doi: 10.1016/J.PETROL.2012.01.023.

[127] W. Kanitpanyacharoen, F. B. Kets, H. R. Wenk, and R. Wirth, "Mineral preferred orientation and microstructure in the posidonia shale in relation to different degrees of thermal maturity," *Clays Clay Miner*, vol. 60, no. 3, pp. 315–329, Jun. 2012, doi: 10.1346/CCMN.2012.0600308.

[128] S. Zhang, R. Klimentidis, P. B. the S. of C. Analysts, and undefined 2012, "Micron to millimeter upscaling of shale rock properties based on 3D imaging and modeling," *International Symposium of the Society of Core Analysts*, vol. 27, p. 30, 2012.

[129] B. Vega, C. M. Ross, and A. R. Kovscek, "Imaging-Based Characterization of Calcite-Filled Fractures and Porosity in Shales," *SPE Journal*, vol. 20, no. 04, pp. 810–823, Aug. 2015, doi: 10.2118/2014-1922521-PA.

[130] E. Fjaer, R. Holt, P. Horsrud, and A. Raaen, *Petroleum related rock mechanics*. Elsevier, 2008.

[131] J. A. Hudson, S. L. Crouch, and C. Fairhurst, "Soft, stiff and servo-controlled testing machines: a review with reference to rock failure," *Eng Geol*, vol. 6, no. 3, pp. 155–189, Oct. 1972, doi: 10.1016/0013-7952(72)90001-4.

[132] Q. Z. Wang and L. Xing, "Determination of fracture toughness KIC by using the flattened Brazilian disk specimen for rocks," *Eng Fract Mech*, vol. 64, no. 2, pp. 193–201, Sep. 1999, doi: 10.1016/S0013-7944(99)00065-X.

[133] J. J. Swab, J. Yu, R. Gamble, and S. Kilczewski, "Analysis of the diametral compression method for determining the tensile strength of transparent magnesium aluminate spinel," *Int J Fract*, vol. 172, no. 2, pp. 187–192, Dec. 2011, doi: 10.1007/S10704-011-9655-1/METRICS.

[134] N. Erarslan and D. J. Williams, "Experimental, numerical and analytical studies on tensile strength of rocks," *International Journal of Rock Mechanics and Mining Sciences*, vol. 49, pp. 21–30, Jan. 2012, doi: 10.1016/J.IJRMMS.2011.11.007.

[135] N. Agofack, P. Cerasi, A. Stroisz, and S. Rørheim, "Sorption of CO_2 and Integrity of a Caprock Shale," *53rd U.S. Rock Mechanics/Geomechanics Symposium*, vol. ARMA-2019-1753, 2019.

[136] C. H. Park and A. Bobet, "Crack coalescence in specimens with open and closed flaws: A comparison," *International Journal of Rock Mechanics and Mining Sciences*, vol. 46, no. 5, pp. 819–829, Jul. 2009, doi: 10.1016/J.IJRMMS.2009.02.006.

[137] M. Sagong and A. Bobet, "Coalescence of multiple flaws in a rock-model material in uniaxial compression," *International Journal of Rock Mechanics and Mining Sciences*, vol. 39, no. 2, pp. 229–241, Feb. 2002, doi: 10.1016/S1365-1609(02)00027-8.

[138] Baotang Shen, O. Stephansson, H. H. Einstein, and B. Ghahreman, "Coalescence of fractures under shear stresses in experiments," *J Geophys Res Solid Earth*, vol. 100, no. B4, pp. 5975–5990, Apr. 1995, doi: 10.1029/95JB00040.

[139] L. Ngai, Y. Wong, H. H. Einstein, L. N. Y. Wong, and H. H. Einstein, "Using high speed video imaging in the study of cracking processes in rock," *Geotechnical Testing Journal*, vol. 32, no. 2, p. 1, 2009, doi: 10.1520/GTJ101631.

[140] H. Lee and S. Jeon, "An experimental and numerical study of fracture coalescence in pre-cracked specimens under uniaxial compression," *Int J Solids Struct*, vol. 48, no. 6, pp. 979–999, Mar. 2011, doi: 10.1016/J.IJSOLSTR.2010.12.001.

[141] E. H. Madden, M. L. Cooke, and J. McBeck, "Energy budget and propagation of faults via shearing and opening using work optimization," *J Geophys Res Solid Earth*, vol. 122, no. 8, pp. 6757–6772, Aug. 2017, doi: 10.1002/2017JB014237.

[142] C. A. Tang, P. Lin, R. H. C. Wong, and K. T. Chau, "Analysis of crack coalescence in rock-like materials containing three flaws—Part II: numerical approach," *International Journal of Rock Mechanics and Mining Sciences*, vol. 38, no. 7, pp. 925–939, Oct. 2001, doi: 10.1016/S1365-1609(01)00065-X.

[143] T. Wong, P. Baud, and E. Klein, "Localized failure modes in a compactant porous rock," *Geophys Res Lett*, vol. 28, no. 13, pp. 2521–2524, 2001.

[144] C. Li, C. Gao, H. Xie, and N. Li, "Experimental investigation of anisotropic fatigue characteristics of shale under uniaxial cyclic loading," *International Journal of Rock Mechanics and Mining Sciences*, vol. 130, p. 104314, Jun. 2020, doi: 10.1016/J.IJRMMS.2020.104314.

[145] F. Renard, B. Cordonnier, D. K. Dysthe, E. Boller, P. Tafforeau, and A. Rack, "A deformation rig for synchrotron microtomography studies of geomaterials under conditions down to 10 km depth in the Earth," *J Synchrotron Radiat*, vol. 23, no. 4, pp. 1030–1034, Jul. 2016, doi: 10.1107/S1600577516008730.

[146] J. Mcbeck *et al.*, "Investigating the onset of strain localization within anisotropic shale using digital volume correlation of time-resolved X-ray microtomography images," *J Geophys Res Solid Earth*, vol. 123, no. 9, pp. 7509–7528, Sep. 2018, doi: 10.1029/2018JB015676.

[147] J. McBeck, Y. Ben-Zion, and F. Renard, "Volumetric and shear strain localization throughout triaxial compression experiments on rocks," *Tectonophysics*, vol. 822, p. 229181, Jan. 2022, doi: 10.1016/J.TECTO.2021.229181.

[148] E. Skurtveit *et al.*, "Mechanical testing and sealing capacity of the upper jurassic draupne formation, north sea," *ARMA US Rock Mechanics/Geomechanics Symposium*, vol. ARMA, 2015.

[149] E. Skurtveit, J. C. Choi, M. Soldal, L. Grande, R. Maurer, and P. Horsrud, "Mechanical anisotropy characterization of the draupne formation, North Sea," *4th International Conference on Fault and Top Seals 2015: Art or Science?*, pp. 170–174, Sep. 2015, doi: 10.3997/2214-4609.201414078.

[150] N. H. Mondol, "Geomechanical and seismic behaviors of draupne shale: A case study from the central North Sea," *81st EAGE Conference and Exhibition 2019*, vol. 2019, no. 1, pp. 1–5, Jun. 2019, doi: 10.3997/2214-4609.201901599.

[151] N. P. Directorate, "Act relating to mineral activities on the continental shelf (Seabed Minerals Act)." 2021.

[152] M. Kalani, J. Jahren, N. H. Mondol, and J. I. Faleide, "Petrophysical implications of source rock microfracturing," *Int J Coal Geol*, vol. 143, pp. 43–67, Apr. 2015, doi: 10.1016/J.COAL.2015.03.009.

[153] E. Skurtveit, J. C. Choi, J. Osmond, M. Mulrooney, and A. Braathen, "3d Fault Integrity Screening for Smeaheia CO_2 Injection Site," *SSRN Electronic Journal*, Oct. 2020, doi: 10.2139/SSRN.3366335.

[154] M. Nooraiepour, H. Fazeli, R. Miri, and H. Hellevang, "Effect of CO_2 Phase States and Flow Rate on Salt Precipitation in Shale Caprocks - A Microfluidic Study," *Environ Sci Technol*, vol. 52, no. 10, pp. 6050–6060, May 2018, doi: 10.1021/ACS.EST.8B00251.

[155] M. K. Zadeh, N. H. Mondol, and J. Jahren, "Velocity anisotropy of Upper Jurassic organic-rich shales, Norwegian Continental Shelf," *Geophysics*, vol. 82, no. 2, pp. C61–C75, Mar. 2017, doi: 10.1190/GEO2016-0035.1.

[156] J. A. Hansen, N. H. Mondol, F. Tsikalas, and J. I. Faleide, "Caprock characterization of Upper Jurassic organic-rich shales using acoustic properties, Norwegian Continental Shelf," *Mar Pet Geol*, vol. 121, p. 104603, Nov. 2020, doi: 10.1016/J.MARPETGEO.2020.104603.

[157] J. Johnson, F. Renard, NH Mondol, and N. G. Institute, "Salt remobilization timing and its impact on two Norwegian Continental Shelf organic-rich shale formations," *Proceedings of the GeoConvention, Virtual*, 2021.

[158] H. Løseth, L. Wensaas, M. Gading, K. Duffaut, and M. Springer, "Can hydrocarbon source rocks be identified on seismic data?," *Geology*, vol. 39, no. 12, pp. 1167–1170, Dec. 2011, doi: 10.1130/G32328.1.

[159] T. Bugge, B. Tveiten, and S. Bäckström, "The depositional history of the cretaceous in the northeastern North Sea," *Norwegian Petroleum Society Special Publications*, vol. 10, no. C, pp. 279–291, Jan. 2001, doi: 10.1016/S0928-8937(01)80018-7.

[160] G. H. Isaksen and H. I. Ledje, "Source Rock Quality and Hydrocarbon Migration Pathways within the Greater Utsira High Area, Viking Graben, Norwegian North Sea," *Am Assoc Pet Geol Bull*, vol. 85, no. 5, pp. 861–883, May 2001, doi: 10.1306/8626CA23-173B-11D7-8645000102C1865D.

[161] M. Prasad, K. C. Mba, T. E. McEvoy, and M. L. Batzle, "Maturity and impedance analysis or organic-rich shales: Society of Petroleum Engineers Reservoir Evaluation Engineering," 2011.

[162] S. Zargari, T. M. Wilkinson, C. E. Packard, and M. Prasad, "Effect of thermal maturity on elastic properties of kerogen," *Geophysics*, vol. 81, no. 2, pp. M1–M6, Mar. 2016, doi: 10.1190/GEO2015-0194.1.

[163] B. Grieser and J. Bray, "Identification of Production Potential in Unconventional Reservoirs," Mar. 2007, doi: 10.2118/106623-MS.

[164] M. P. Wilson, F. Worrall, R. J. Davies, and A. Hart, "Shallow Aquifer Vulnerability From Subsurface Fluid Injection at a Proposed Shale Gas Hydraulic Fracturing Site," *Water Resour Res*, vol. 53, no. 11, pp. 9922–9940, Nov. 2017, doi: 10.1002/2017WR021234.

[165] N. H. Mondol, "Seal quality prediction using E-Poisson's ratio rock physics templet-A case study from the Norwegian Barents Sea," in *Proceedings of the Ge o Convention. May*, 2018, pp. 7–11.

[166] L. B. Smith, J. Schieber, and R. D. Wilson, "Shallow-water onlap model for the deposition of Devonian black shales in New York, USA," *Geology*, vol. 47, no. 3, pp. 279–283, Mar. 2019, doi: 10.1130/G45569.1.

Bibliography

[167] B. Bohloli, M. Soldal, H. Smith, E. Skurtveit, J. C. Choi, and G. Sauvin, "Frictional properties and seismogenic potential of caprock shales," *Energies (Basel)*, vol. 13, no. 23, p. 6275, 2020.

[168] M. Soldal, E. Skurtveit, J. C. Choi, J. Martinez-Frias, and E. S. No, "Laboratory Evaluation of Mechanical Properties of Draupne Shale Relevant for CO_2 Seal Integrity," *Geosciences 2021, Vol. 11, Page 244*, vol. 11, no. 6, p. 244, Jun. 2021, doi: 10.3390/GEOSCIENCES11060244.

[169] M. J. Rahman, M. Fawad, J. Jahren, and N. H. Mondol, "Top seal assessment of Drake Formation shales for CO_2 storage in the Horda Platform area, offshore Norway," *International Journal of Greenhouse Gas Control*, vol. 119, p. 103700, Sep. 2022, doi: 10.1016/J.IJGGC.2022.103700.

[170] M. Fawad, M. J. Rahman, and N. H. Mondol, "Seismic-derived geomechanical properties of potential CO_2 storage reservoir and cap rock in Smeaheia area, northern North Sea," *The Leading Edge*, vol. 40, no. 4, pp. 254–260, Apr. 2021, doi: 10.1190/TLE40040254.1.

[171] J. C. Fooks and M. B. Dusseault, "Strength of Pierre I Shale As Function of Moisture Content," in *ISRM EUROCK*, OnePetro, Sep. 1996.

[172] J. E. Martin, J. L. Bertog, and D. C. Parris, "Revised lithostratigraphy of the lower Pierre Shale Group (Campanian) of central South Dakota, including newly designated members," *Special Paper of the Geological Society of America*, vol. 427, pp. 9–21, 2007, doi: 10.1130/2007.2427(02).

[173] L. G. Schultz and H. W. Menard, "Mixed-layer clay in the Pierre Shale and equivalent rocks, northern Great Plains region," *Professional Paper*, 1978, doi: 10.3133/PP1064A.

[174] H. A. Tourtelot and T. B. Nolan, *Preliminary investigation of the geologic setting and chemical composition of the Pierre Shale, Great Plains region*. 1962.

[175] H. R. Wenk, W. Kanitpanyacharoen, and M. Voltolini, "Preferred orientation of phyllosilicates: Comparison of fault gouge, shale and schist," *J Struct Geol*, vol. 32, no. 4, pp. 478–489, Apr. 2010, doi: 10.1016/J.JSG.2010.02.003.

[176] D. R. Setterholm, *along the eastern margin of the Western Interior Seaway*, vol. 287. Geological Society of America, 1994.

[177] P. Cerasi and L. E. Walle, "Investigation of Potential Loss of Injectivity and Formation Integrity Due to Pressure Cycling," *Energy Procedia*, vol. 86, pp. 420–431, Jan. 2016, doi: 10.1016/J.EGYPRO.2016.01.043.

[178] B. Sun, Z. Zhu, C. Shi, and Z. Luo, "Dynamic mechanical behavior and fatigue damage evolution of sandstone under cyclic loading," *International Journal of Rock Mechanics and Mining Sciences*, vol. 94, pp. 82–89, Apr. 2017, doi: 10.1016/J.IJRMMS.2017.03.003.

[179] B. Zhao, D. Liu, Z. Li, W. Huang, and Q. Dong, "Mechanical behavior of shale rock under uniaxial cyclic loading and unloading condition," *Advances in Civil Engineering*, vol. 2018, 2018, doi: 10.1155/2018/9750480.

Papers

Paper 1

Time-Resolved *In Situ* Imaging of Strain Localization in Draupne Shale under Triaxial Compression

Aldritt Scaria Madathiparambil[1], Kim Robert Tekseth,[1] Fredrik K. Mürer,[1,2] Benoît Cordonnier,[3,4]
Nicolaine Agofack,[5] Jessica McBeck,[3] Pierre Cerasi,[5] François Renard[3,6] Basab Chattopadhyay,[1]
and Dag W. Breiby[1,7,*]

[1] *Department of Physics, Norwegian University of Science and Technology (NTNU), Høgskoleringen 5,
7491 Trondheim, Norway*

[2] *SINTEF Helgeland AS, Halvor Heyerdahls vei 33, 8626 Mo i Rana, Norway*

[3] *The Njord Centre, Departments of Geosciences and Physics, University of Oslo, Oslo, Norway*

[4] *ESRF − The European Synchrotron, CS40220, Grenoble 38043, France*

[5] *SINTEF Industry, Applied Geoscience Department, 7465 Trondheim, Norway*

[6] *ISTerre, University Grenoble Alpes, Grenoble INP, CNRS, IRD, University Gustave Eiffel, Grenoble, France*

[7] *Department of Microsystems, University of South-Eastern Norway (USN), 3184 Borre, Norway*

Understanding the mechanical behavior of rocks is crucial in subsurface activities, including storage of carbon dioxide and hydrogen gases, which both rely on shale caprocks as potential sealing barriers. Several current large-scale initiatives focus on potential carbon storage in North Sea aquifers. The Draupne Formation contains a series of shale layers interbedded with sandstone layers, the overall thickness of which varies in the range from tens to hundreds of meters. Injection of carbon dioxide into the underlying sandstone reservoirs leads to changes in the surrounding stress field, which can result in fault reactivation or the creation of microfractures, and thus, alter the performance of the shale caprock. Time-resolved microcomputed tomography (4D μCT) has, in recent years, become a powerful technique for studying the mechanical properties of rocks under stress conditions similar to those prevailing in geological reservoirs. Here, we present results from experiments performed on Draupne shale using a triaxial rig combined with 4D μCT based on synchrotron radiation. Detailed mechanical analysis of the tomography datasets by digital volume correlation reveals the three-dimensional pattern of the temporally evolving deformation field. Intermittent bursts of deformation at different locations within the specimen are observed, which eventually evolve into a major fracture plane extending laterally across the whole sample. This study suggests that the pseudolinear-elastic-appearing behavior in the macroscopic stress-strain relationship previously reported for Draupne shale samples could consist of a series of irreversible processes occurring at various weak points within the sample. The combination of 4D μCT imaging with strain analysis enables *in situ* investigations of deformation processes via quantification of shear and volumetric strains within the sample, thus providing an improved understanding of the fracture dynamics of shales.

I. INTRODUCTION

The geomechanical response of organic-rich shales to external stress is important knowledge because these materials play a crucial role in a range of environmentally and industrially important processes, including the petroleum industry, CO_2 storage, and H_2 storage. Shale caprocks are exposed to significant loading due to both natural geological stresses, such as thermal stresses and high fluid pressure, and industrial stresses like drilling, fracturing, and fluid injection. The microscale mechanical response of stressed shale greatly affects the stability of the formations, also at much longer length scales of kilometers. Shale rocks may contain multiple fractures that coalesce under stress, causing a transition from stable-to-unstable fracture growth [1,2]. Understanding these processes of fracture formation, eventually leading to macroscopic failure, is critical for a wide range of applications. The influence of fracture development within shales on the permeability of fluids during CO_2 injection and storage remains poorly understood. This lack of knowledge can largely be ascribed to the microscale complexity and heterogeneity of shales [2–5]. Recent studies have focused on the potential for the storage of CO_2 in saline aquifers, coal seams, and

*dag.breiby@ntnu.no

depleted oil and gas reservoirs [6–8]. Geological formations containing porous sandstone reservoirs capped with low-porosity low-permeability caprocks are excellent candidates for CO_2 storage [6]. Shale formations that are around a hundred meters thick act as the caprock for most of these reservoirs. Studies have shown that shale-capped formations tend to adsorb CO_2 and have the potential to inject and store CO_2 [9]. Current academic studies and several full-scale industrial efforts are focusing on evaluating the potential for the storage of CO_2 in the seabed of the North Sea and elsewhere [10,11].

Triaxial mechanical testing, sometimes applied to full-size (12 inch) cores, remains the workhorse for characterizing the mechanical properties of rocks. However, to refine the theoretical models of mechanical behavior for rock systems with highly differing properties, microscopic insights that cannot be gained from macroscopic testing alone are increasingly desired [12]. Imaging techniques like scanning electron microscopy (SEM), sometimes combined with focused-ion-beam milling, can be used to acquire high-resolution images and chemical information through spectroscopy [13]. X-ray diffraction (XRD) is also extensively used for mineral identification. During the last decade, x-ray microcomputed tomography (μCT) has been increasingly used for the nondestructive visualization and mineral quantification of geological samples in three dimensions [14,15]. Using μCT, it is possible to investigate the pore-network properties, microtextures, fractures, and transport properties at spatial resolutions down to, and below, the micrometer level [16]. Recently, time-resolved x-ray microtomography (4D μCT) has opened the possibility of monitoring dynamic processes like mechanical responses and fluid penetration of geomaterials [17,18]. The advent of triaxial test cells compatible with μCT has facilitated investigating the stress- and time-dependent deformation of rock samples [19–22]. We note that neutron-computed tomography is also increasingly used to this end [23,24]. Additional μCT techniques have recently been introduced to the rock-physics community, e.g., those with diffraction contrast [25] and based on coherent imaging [26,27].

In situ three-dimensional (3D) time-resolved x-ray imaging in combination with digital volume-correlation (DVC) analysis [28,29] is demonstrated to provide detailed information about the evolution of microscopic and macroscopic strain fields at micrometer-scale spatial resolution [17,18,23]. DVC algorithms find the displacement field that best maps each small subvolume (e.g., $10 \times 10 \times 10$ voxels) within a 3D μCT dataset recorded at one time step onto another μCT dataset recorded at a later time step [29]. This is achieved by identifying similar density patterns within those subvolumes and finding the local minute translations, rotations, and dilations that maximize the correlation between pairs of sequential tomograms. DVC is able to capture small systematic movements within the

sample that are practically impossible to detect by just observing the tomographic images. Maps showing the 3D displacement and/or strain fields give insights into the mechanical properties of rock samples [30]. Quantitative studies of grain adjustments and rotations at the microscale and the shear-strain distribution in rock samples have been reported. The combination of μCT monitoring and mechanical testing can assist in predicting reservoir properties of the rocks by analyzing the response of porosity and permeability to mechanical stress [30,31].

Stress and strain localization proceeds by destructive microevents that tend to concentrate in weak areas of the specimen [30]. In clay-rich rocks like shales, the dominant micromechanisms leading to strain localization inside shear bands are known to be rotation and decohesion at the grain scale [30]. Also, in rocks, the development of well-defined cracks occurs due to local micromechanical events and the coalescence of microcracks. Strain localization is commonly observed in clayey specimens and can form either a single failure plane or multiple parallel failure planes, depending on the uniformity of the specimen's initial density, the tendency to dilate or to contract, and the boundary conditions [32]. Dilation and compaction are directly linked to the overconsolidation ratio of the clay specimen, that is, the highest overburden (here, axial) stress previously exposed to the sample divided by the current overburden stress.

The present study aims to investigate the mechanical properties of Draupne shale from the North Sea, a caprock recently receiving extensive attention because of its potential for permanent storage of the greenhouse gas CO_2 in the underlying porous sandstone [5,32]. Time-resolved synchrotron μCT combined with DVC analysis is used to estimate the 3D strain distribution throughout a centimeter-sized core of Draupne shale under jacketed triaxial loading. We apply increasing axial compressive stress, oriented perpendicular to the lamination bedding planes, combined with constant confining (lateral) stress to replicate the conditions at a depth of about 2.6 km in the seabed where the samples were obtained. Using DVC analysis, the 3D local strain-displacement field is obtained from the *in situ* CT data. Based mainly on the calculated volumetric strain and the von Mises equivalent strain, we discuss, in detail, the dynamics of strain localization in the Draupne shale as the sample undergoes brittle failure.

II. MATERIALS AND METHODS

A. Shale sample

The sample used in this study was collected at a depth of 2575 m from a borehole in the Draupne Formation. Draupne shale is a caprock that is a low-permeable, homogeneous, and anisotropic black shale with a porosity of about 12% [5,33]. The total organic content of the sample core is reported to be 6–8%, and the permeability is

estimated to be less than 3.2×10^{-22} m^2 (3.2 nDarcy) with a critical pore throat size of 9 nm [4,5]. The very same sample core has been characterized using SEM, XRD, mechanical tests, and permeability measurements [2,3,34]. XRD studies have indicated the presence of more than 60% clay [4]. To prevent damage and drying in contact with air, the core was kept submerged in Marcol™ oil during all stages of sample preparation. An electric drill was used to prepare the 5-mm-diameter cylindrical sample, with its bedding planes perpendicular to the symmetry axis of the cylinder. The cylinder end surfaces were polished to obtain a specimen with a length of 10 mm and right angles for stable mechanical contact.

B. HADES triaxial rig

The shale core sample was deformed *in situ* under triaxial-loading conditions using the HADES rig, cf. Figure 1, installed at beamline ID19 at the European Synchrotron Radiation Facility (ESRF) [20]. This apparatus has a low x-ray attenuation for photon energies >60 keV and can apply stresses both axially (up to 200 MPa) and radially (up to 100 MPa) at temperatures up to 200 °C, while the external fluid ("pore") pressure can be varied from 0.1 to 100 MPa. The body of the rig is constructed from a single piece of titanium with a wall thickness of about 5 mm at the sample location. The sample was saturated with brine (3.6-wt% NaCl) at the same NaCl concentration as that of the native pore fluid prior to loading. The pore fluid pressure in the HADES apparatus was controlled by two hydraulic pumps, one for the pore fluid inlet and the other for the outlet, which could be used in either constant-pressure or constant-flow-rate modes with predefined ramps. The sample was installed between two stainless-steel pistons, with the axial loading imposed by the movable upper piston. Two independent pumps controlled the confining pressure and the axial load. A Viton™ fluoropolymer elastomer encased the rock sample, and the confining pressure was applied on this jacket using silicone oil.

The chosen coordinate system was with the z axis parallel to the cylinder axis, coinciding with the direction of the axial stress, σ_{ax}, and with the x-y plane perpendicular to σ_{ax}. The differential stress, σ_{zz}, was calculated as

$$\sigma_{zz} = \sigma_{\mathrm{ax}} - (\sigma_{\mathrm{conf}} + \sigma_{\mathrm{pore}}) - \sigma_{\mathrm{friction}}. \qquad (1)$$

Here, σ_{ax}, σ_{conf}, and σ_{pore} denote the applied axial stress, confining pressure, and pore pressure, respectively. The frictional stress, $\sigma_{\mathrm{friction}}$, is caused by the mechanics of the HADES setup and is determined from a range of previous experiments to equal approximately (18.1 ± 0.1) MPa. A linear variable differential transformer (LVDT) incorporated into the HADES rig was used to measure axial shortening, and thus, the axial strain, ε_{zz}, of the sample.

The time-resolved axial strain, ε_{zz}, was also obtained from the 3D x-ray images by measuring the shortening of the rock core between the two pistons.

C. Time-lapse microcomputed tomography acquisition

Measurements were performed using the "white" x-ray beam option at ESRF ID19, with a rectangular cross section (5×10 mm^2, defined by slits upstream of the experimental hutch) to image the entire sample inside the HADES rig. A PCO EDGE 5.5 RS detector was used to acquire the projections. Due to x-ray adsorption by the walls of the rig, the equivalent x-ray energy crossing the sample was close to 70 keV. To monitor sample deformation, the stress was increased stepwise and x-ray CT data were acquired while the stress was kept constant. This quasistatic approach was used to reduce the problem of sample movements during the scan, potentially blurring the 3D images. After each stress-step increment, the apparatus was rotated by 180° about a vertical axis, while acquiring 2500 radiographic x-ray projections with a total scan time of about 65 s, giving an effective reconstructed voxel size of $(6.5 \; \mu m)^3$. Every 2 min, a new tomographic scan was started to obtain effectively 4D (i.e., time-resolved 3D) images as the sample was mechanically stressed and deformed. In total, 90 full tomograms were recorded, and the full experiment including stress and pressure ramps lasted nearly 16 h. The experiment was performed at ambient temperature (24 °C). The tomograms were reconstructed using the software PyHST2 [35], involving filtered back-projection coupled with Paganin's propagation-based phase-contrast algorithm [34]. The grayscale value of each voxel in the tomogram was proportional to the x-ray attenuation coefficient, which was a function of density and atomic number. Bright gray levels in the tomogram corresponded to highly attenuating high-density regions, dark gray values were lightly attenuating minerals, and intermediate gray levels corresponded to voxels containing intermediate and/or a subresolution mixture of high- and low-attenuation minerals.

The experimental loading path is displayed in Fig. 1(a); see also Table S1 within the Supplemental Material [36]. The experiment was stress controlled and designed to track damage accumulation and shear localization towards macroscopic failure. The experiment may naturally be divided into the following three parts, as visualized in Fig. 1: stage O, with the initial loading; stage A, in which σ_{zz} was increased up to fracturing; and stage B, in which σ_{zz} was kept constant. An unload-load and a load-unload loop were incorporated in stage O [Fig. 1(a)] to assess the elastic properties of the sample; the first loop should, in principle, provide the bulk modulus and the second loop the Young's modulus; however, these measurements could not be reliably interpreted because, at this early stage of the experiment, the sample was not yet fully settled
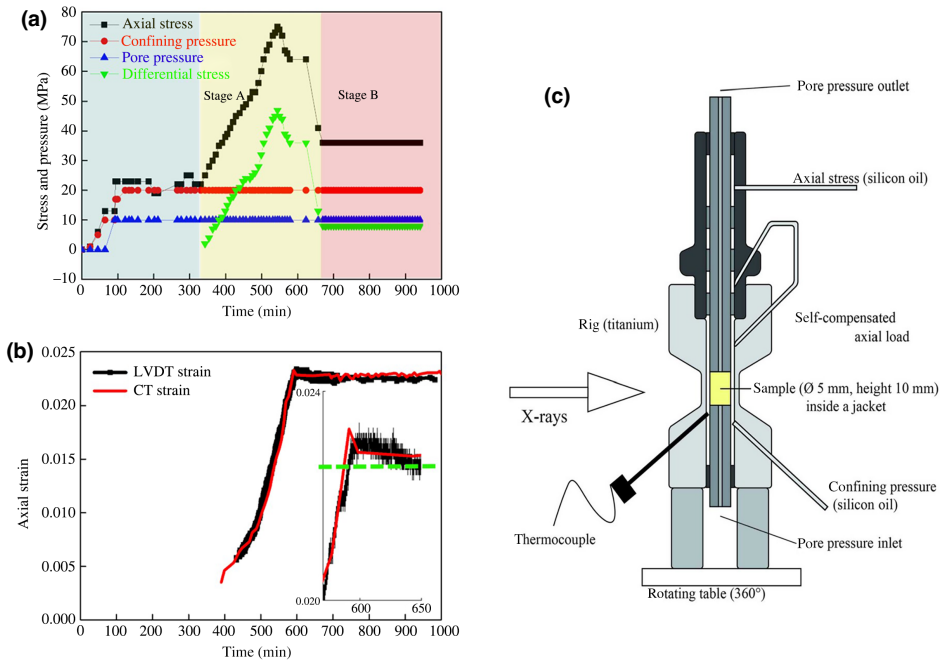
FIG. 1. Overview of the experiment. (a) Axial stress, σ_{ax}; confining pressure, σ_{conf}; pore pressure, σ_{pore}; and differential stress, σ_{zz}, are plotted as function of time during the experiment. Stage O (consolidation) is shaded in light gray, stage A (axial stress increase) is shaded in yellow, and stage B (constant stress) in light red. Peak axial stress precedes the brittle failure of the core sample. (b) Axial strain, ε_{zz}, as function of time obtained from CT data (red) and from the LVDT measurement (black). Data points for times <400 min are not reliable, owing to minor sample shifts. Inset highlights strain evolution around the fracture event, revealing that the sample expands just after fracturing. Here, axial compression strain is plotted as being positive. Green dashed line indicates the long-term asymptote of axial strain. (c) Sketch of the HADES cell (reproduced from Ref. [20] with permission from IUCr).

in the rig and shifted a little between subsequent stress increments.

During stage O, the pore pressure, confining pressure, and axial stress were increased up to 10, 20, and 22 MPa, respectively. After reaching these values, the confining and pore pressures were kept constant, while the differential stress was stepwise further increased to a maximum of $\sigma_{zz} \sim 48$ MPa (for σ_{ax} of about 75 MPa) and the sample deformed with an average axial strain rate of $(2.1 \pm 0.1) \times 10^{-6}$ s^{-1} [Fig. 1(b)]. This strain rate was chosen to fit the desired stress path with expected peak stress into the time allotted at the synchrotron. Upon reaching peak stress, the material was no longer able to support the applied stress and underwent brittle failure. The axial stress was subsequently reduced to 36 MPa; this was a differential stress level that the shale could sustain without further large deformations for the remainder of the experiment. Because of the rather high axial loading rate, combined with the extremely low permeability of the Draupne shale, it should be noted that, even though the

externally controlled confining pressure and liquid pressure were kept constant, the actual pore pressure inside the rock sample was likely to have increased during the experiment. Experimental data suggesting a Skempton A value of around 0.3 [37] are provided in the Supplemental Material (Text S4) [36]. These considerations imply that, at failure, the effective confining pressure was probably lower than the values provided by the pore-pressure transducers.

D. Digital volume-correlation analysis

DVC was performed using the open-source software Tomowarp2 [29], which, through interpolation methods, returned the incremental 3D displacement field, $\mathbf{u}(\mathbf{r},t)$, between subsequent pairs of tomograms. For most of the DVC calculations, the chosen region of interest was fully contained within the rock sample to suppress disturbing features from the jacket (rubber sleeve) and irregularities on the surface of the sample. An example of DVC

analysis performed for the full field of view is provided in the Supplemental Material [36]; the displacement fields of both the shale sample and the polymer sleeve are visualized in Fig. S4.

The DVC spatial resolution is necessarily inferior to the CT's raw-data resolution, depending on the chosen node spacing. Technically, both the node spacing and the correlation window size are known to strongly influence the magnitude of the strain estimated by the DVC algorithm [28]. The local correlation between the two datasets is quantified with a *correlation coefficient* ranging from 0 (no correlation) to 1 (full correlation) [29]. We used a node spacing of 20 voxels (130 μm) with a cubic correlation window of 10 voxels in size length [volume of (65 μm)^3]. These parameters were kept fixed for all the calculations and were selected following tests to investigate their influence on the resolution; see the Supplemental Material (Text S3) [36]. An outcome of these tests is that we consider, consistent with previous reports [31,38], the obtained displacement and strain fields to be quantitatively reliable only for comparisons between different regions and times within the sample, while the absolute strain values are much more uncertain.

From the series of 3D displacement fields, the incremental second-rank three-dimensional strain-tensor field, $\varepsilon(\mathbf{r},t)$, was calculated, revealing the changes that occurred within the time interval between the acquisitions of the pair of tomograms used in the calculation. The tomograms used for the DVC calculations were chosen at regular intervals of the macroscopic axial strain, specifically about 0.002, which corresponded to an LVDT increment of about 20 μm. We denoted a DVC time point as, for example, ix(44,45), which signified that the ninth pair of tomograms used in the DVC calculation were acquired with the first at a differential stress of 44 MPa and the second at 45 MPa. The enumerated pairs of tomograms used for the DVC analysis can be read from Fig. 2 and Table S1 within the Supplemental Material [36].

III. RESULTS

A. Macroscopic stress and strain

The macroscopic stress-strain behavior in stage A of the shale sample is shown in Fig. 2. As indicated by the straight line, we observed essentially linear behavior during loading up to $\sigma_{zz} = (39 \pm 2)$ MPa, followed by an increasing ductility when approaching the peak stress. After the peak stress was reached, the stress dropped rapidly, and the curve became nearly horizontal. Because shales are highly anisotropic, their mechanical properties will vary with the orientation of the shale bedding planes relative to the core axis [39,40]. Prior to the linear regime of the stress-strain plot, i.e., in stage O, we observed an initial nonlinear response (not shown in Fig. 2), which
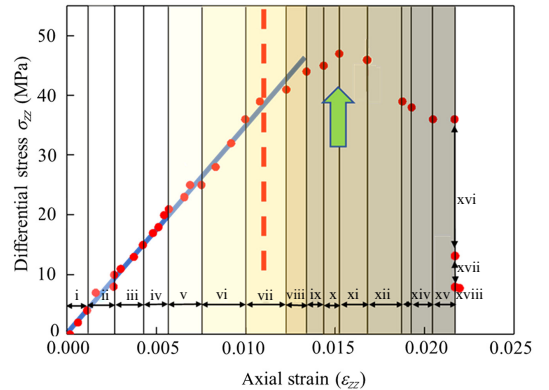
FIG. 2. Differential compressive stress, σ_{zz}, plotted as a function of axial strain, ε_{zz}, during the experiment. Superposed straight gray line suggests an almost linear stress-strain relationship for axial strain levels <0.01. Vertical dashed red line gives the approximate yielding point, and green arrow indicates the peak stress at failure. Roman numerals give the DVC time-step intervals, with i–xv corresponding to stage A in Fig. 1.

could be ascribed to fine adjustments or shifts of the specimen in the rig and the closing of preexisting cracks and pores in the sample under increasing stress. The ostensible interpretation of the stress-strain data in Fig. 2 is that the shale rock exhibits linear elastic behavior. The maximum axial strain, ε_{zz}, consistent with such pseudoelastic behavior, as judged from the macroscopic stress-strain curve in Fig. 2, would be about 0.011 ± 0.001. Estimating the mechanical properties of the sample from the pseudolinear portion of the stress-strain curve, using a linear fit, suggests a Young's modulus of $E = (3.6 \pm 0.2)$ GPa. While this estimate correlates well with reported values obtained for uniaxial compression tests on Draupne shales [40], we demonstrate in the following analysis that this apparently elastic behavior arises despite a series of small, perhaps irreversible, deformation events.

The yield point, defined as where the stress-strain curve starts to deviate from the linear fit, was at a stress level of about 70% of the maximum σ_{zz} (Fig. 2). Beyond this point, the common interpretation [15,17,30,41,42] is that permanent and irreversible deformation and cracks develop in the sample, initially located at soft spots or other defects. These intermittent deformations are generally thought to localize and to grow stably as additional stress is added to reach the overall failure of the sample. Note that, with the resolution of this μCT experiment, these microscopic deformations cannot be seen directly, as they are smaller than the voxel size. The approximate onset of the unstable crack growth in the sample is indicated by the green arrow in Fig. 2, occurring within $97\% \pm 2\%$ of the maximum differential stress.

B. Direct μ-CT observations

Selected views of the sample, before and after the development of the macroscopic primary fracture across the sample, are provided in Fig. 3. This large macroscopic fracture extending laterally throughout the whole sample developed near the upper piston and was aligned predominantly along a plane with an inclination angle of $38° ± 3°$ with respect to the direction of maximum compressive stress, σ_{zz} (i.e., the cylinder axis z). Cross sections of the reconstructed tomograms reveal the presence of natural fractures in the shale sample at low axial stress [Figs. 3(a1) and 3(b1)]. The majority of microcracks and pores in Draupne shales are at the submicron scale [5], and consequently, below the spatial resolution of these images. Natural fractures were found at several locations in the sample. The same location in different scans was chosen for comparison [Figs. 3(a1)–3(d1)], carefully correcting for the length of the sample gradually being shortened during the experiment. With increasing σ_{zz}, natural fractures initially present at different positions in the sample were observed to close, in agreement with reported observations of stress-induced closing of preexisting cracks and pores in shales and other sedimentary rock systems [40].

Preceding stage B, the sample fractured, and the two portions of rock were observed to behave as two rigid bodies sliding on top of each other [Figs. 3(c2)–3(d2)]. The differential stress was then maintained at 8 MPa until the

end of the experiment. Close inspection of Fig. 1(b) also reveals that the specimen, in fact, expands in the axial direction (ε_{zz} decreases) slightly during the first minutes after failure, which is a hallmark of (semi)brittle failure [43]. The sample expansion was also observed in the DVC analysis (data not shown). During the later parts of stage B, the (small) strain events present are located mainly along the fracture plane and at the top and bottom regions of the sample.

C. Microscopic displacement field

To study the microscopic deformation processes towards sample failure, the incremental displacement vector field, $\mathbf{u}(\mathbf{r}, t)$, was obtained by DVC, and is visualized in Fig. 4. The 3D displacement field, $\mathbf{u}(\mathbf{r}, t)$, gives a microscopic view of deformations within the sample. Upon comparing the time steps from v(21,25) up to x(45,47), the initially homogenous deformation field develops via a rotation-rich state into a highly complex state, signifying sample fracture. It is clear from Fig. 4(a) that nonhomogenous deformations are present at least from ix(44,45), and a sliding block is seen for xvii(13,8) onwards, similar to that reported for other rocks like sandstone [43]. Note the clear shear zone seen across the fracture in Fig. 4(b), with displacements in opposite directions. The local deformation field is homogeneous within the blocks, revealing their rigid nature. The displacement field, $\mathbf{u}(\mathbf{r}, t)$, both in 3D and
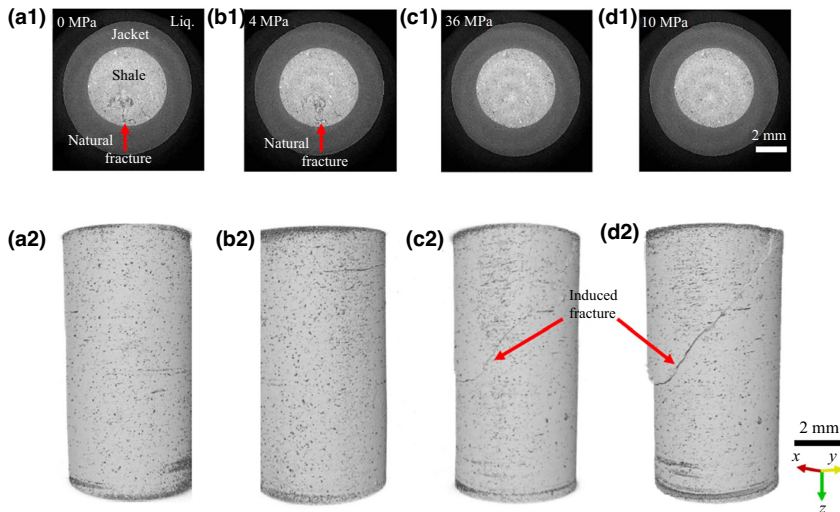
FIG. 3.   Selected μCT tomograms of the shale sample (a),(b) before (stage A) and (c),(d) after (stage B) sample failure with the formation of an induced primary fracture spanning across the sample. Top row shows cross sections perpendicular to the core-sample axis; all are obtained at the same axial location at 1.6 mm from the bottom of the sample, showing the closing of preexisting natural fractures upon increasing differential stress, σ_{zz}. Natural fractures seen in the sample (here), as indicated by the red arrows in (a1),(b1) have closed at the higher stress states in (c),(d). Bottom row gives 3D perspective views of the specimen at the same states as in (a1)−(d1), clearly revealing the induced macroscopic primary fracture after failure.

for central 2D axial cross sections, for all the time steps, are shown in Figs. S5 and S6 within the Supplemental Material [36].

Immediately before failure, a pronounced rotational strain state was observed, cf. xiii(39,38). Rotational strain about an axis perpendicular to the applied stress is a known mechanism associated with linear elastic fracture mechanics [30,44], but we are not aware of earlier reported similarly clear microscopic 3D data showing this effect in rocks. To better appreciate this rotational feature, a magnified view is provided in Fig. 5 and a series of cross sections are provided in Fig. S9 within the Supplemental Material [36].

D. Irreversibility in the initial linear phase and strain localization near failure

The von Mises equivalent strain, ε_{eq}, was calculated from the displacement field, $\mathbf{u}(\mathbf{r}, t)$, obtained from DVC (Supplemental Material, Text S1 [36]). The von Mises strain indicates the presence of deviatoric strain. The time series provided in Fig. 6 clearly demonstrates nonpersistent strain localizations appearing at disparate positions across the sample, but these have not been previously reported from experimental observations over numerous time steps, as seen here. We observe the progressive development of incremental strain localization within the specimen and localization of the strain before the formation of the macroscopic specimen-spanning fault.

The primary shear band that localized along the fracture plane was consistent with reported observations of shear banding and localization in clays and other granular materials [30,45,46]. Besides this primary shear band, we also observed local shear strain that was concentrated along less-pronounced secondary shear bands. These secondary shear bands are temporary nonpersistent modes of localization, that is, localized high-strain regions, which form and eventually disappear, as observed in the specimen during the early loading stage of the test.

The first images in the top row of Fig. 6 show the influence of intermittent deformation events on the von Mises incremental strain field. This behavior is consistent with stress-induced stabilization of the specimen and the closing of preexisting fractures, as previously mentioned. The evolved structure of the von Mises strain distribution after point xiv qualitatively matches the major fracture directly observed in the tomograms, cf. Fig. 3. Figure 6(b) highlights the presence of secondary fractures in the sample. The presence of von Mises strain [Fig. 6(b)] surrounding the major fracture can be attributed to the slipping of the top section of the sample over the bottom section after fracturing.

The incremental volumetric strain field, $\varepsilon_V = \Delta V/V$, was calculated from the incremental strain tensor as described in the Supplemental Material (Text S1 [36]). This field

reveals the magnitude of local dilatancy (positive values; $\Delta V/V > 0$) and compaction (negative values) in the sample. The evolving distribution of the incremental strain quantified by DVC revealed that high magnitudes of compaction, dilation, and von Mises strain were localized along the fracture (Figs. 6 and 7). In Fig. 7, a series of selected states of the time evolution of the ε_V field in the sample are shown. We observed the presence of intermittent compaction events throughout the sample that eventually localized to form the major fracture and a similar localization pattern was seen for the local dilation. These intermittent density changes are understood to be caused by the presence of weak zones in the sample and are also likely to be related to the closing of preexisting fractures or voids, as exemplified in Fig. 3. DVC analysis also identified secondary fractures that were difficult to discern directly in the tomograms, see, e.g., xv(36,36) in Fig. 7. These secondary fractures were observed to stabilize and eventually localize along the major fracture. The significant strain seen near the upper and lower ends of the sample was caused by direct contact with the pistons. Analysis of the strain evolution in the shale demonstrates that the deformations were occurring in the sample throughout the apparently linear-elastic loading stage, while strain localization was only observed in the last few time steps before macroscopic failure. Judging from Fig. 7, strain localization took place around time steps x–xii, i.e., slightly preceding or coinciding with the peak stress.

The spatially averaged volumetric strain and von Mises strain are plotted as a function of time in Fig. 8, thus providing a link between the microscopic and macroscopic behavior of the sample. Point 1 represents the minimum value for the mean volumetric strain, defined as the dilation-initiation point, with a stress, σ_{zz}, of 18 MPa, about 40% of the failure stress. This point indicates compaction of the sample, as the volumetric strain is negative, which we interpret as the closing of preexisting microcracks and collapse of pores throughout the specimen. This interpretation is supported by the results of Fig. 3 where closing of the preexisting natural fractures can be directly observed in the CT images. After point 1, the mean volumetric strain increased rapidly. In the time between points 1 and 2, small deformations dominated by rather localized dilational strains, as observed with the DVC analysis, took place. These deformations could be due to natural heterogeneity, whereas sample shifts are excluded, as they would have been readily observed in the experimental data. The fact that the loading curve resumes its steep upward trend, and that no substantial localization happens until after xi(47,46), emphasize that these are small-strain ($\ll 0.01$) events. We interpret these localized strain dilations as small inelastic (destructive) events. While time constraints during the experiment barred the performance of unload-reload cycles, such testing has been done on other samples of the same shale material (cf. Fig. S10
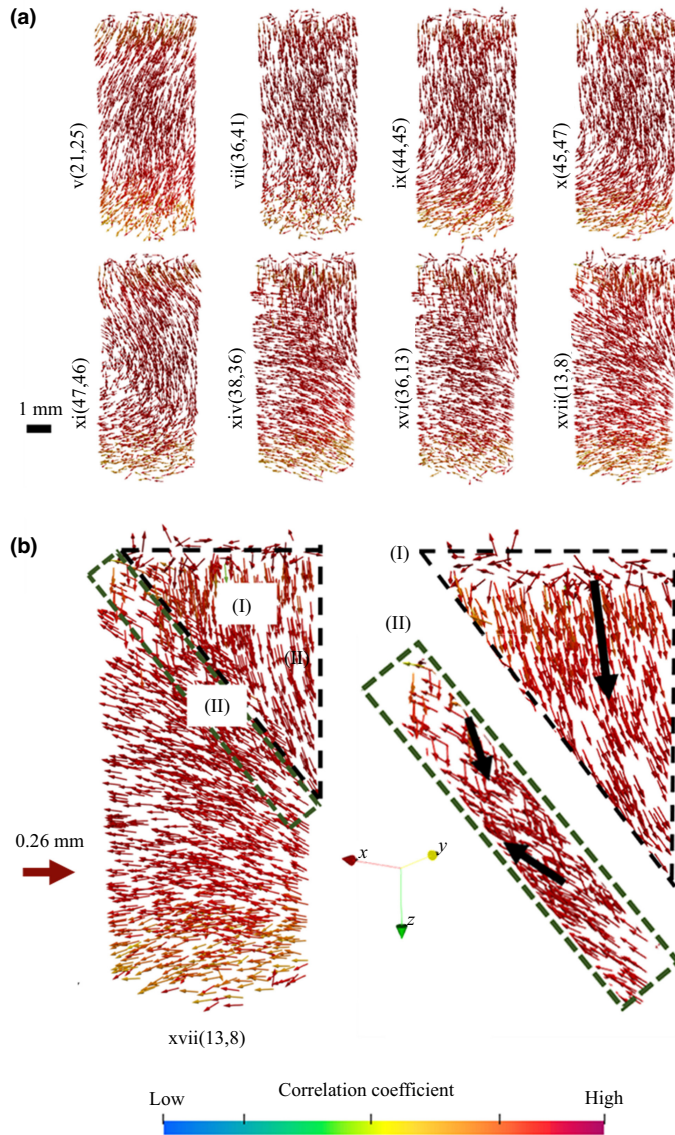
FIG. 4.   Incremental displacement vector field, **u**(**r**, *t*). (a) Cross-section view of **u**(**r**, *t*) for selected time steps. (b) Enlarged view of xvii(13,8). Bold black arrows are guides to the eye that represent the overall movement in the sample. Color coding represents the correlation coefficient of the DVC analysis, with the prevailing red representing high correlation, indicating a reliable analysis.

within the Supplemental Material [36]), showing stress-strain behavior consistent with inelastic deformation. Note also that, while inelastic deformations would generally be expected to weaken the sample, in the compression test reported here, such weakening might be hard to detect; in

other words, the stress-strain curve might still stay close to linear, as observed, after minor local compaction events. For stage B, we observe that the partitioning of strain between dilation and compaction remains almost constant with time.
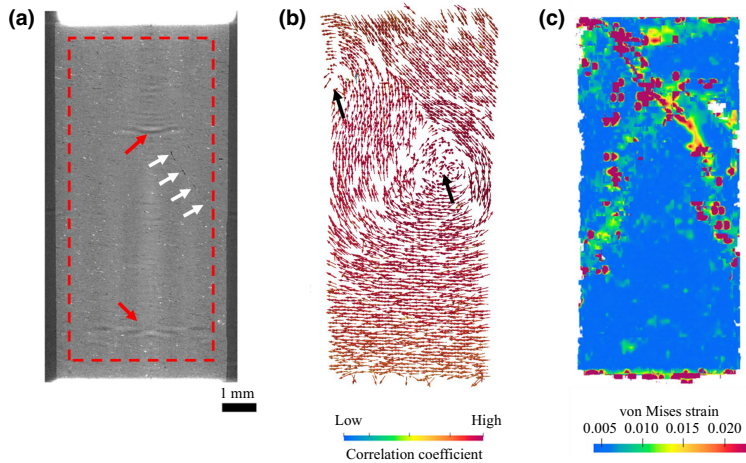
FIG. 5.   Axial cross sections showing the state of the sample immediately prior to failure, at $\sigma_{zz} = 39$ MPa. (a) CT raw-data cross section. Some ring artefacts from the CT reconstruction can be seen (red arrows), and the nascent fracture is indicated by white arrows. Rectangle indicates the region of interest used for the DVC analysis. (b) Displacement field obtained from DVC interval xiii(39,38). Note the rotational nature of the displacement field, as highlighted by the two black arrows pointing to two centers of rotation on the footwall side of the inclined fault. (c) Corresponding von Mises equivalent strain. Viewing angle is specifically chosen to highlight the circular strain state in (b).

Fracture coalescence likely produces the increasing dilation observed at point 2. This point occurred at a differential stress, σ_{zz}, of 28 MPa, which was about 61% of the failure stress. Once the volumetric strain crossed zero to positive values, the volumetric strain continued to rise, perhaps due to the release and redistribution of the strain energy. It is reasonable to assert that, at this stage, the microcracks grow rapidly and eventually coalesce into a larger fracture. We observe two time steps with averaged millistrain values of >0.5, as indicated by points 3 and 4 in Fig. 8, following major drops in the axial stress.

IV. DISCUSSION

Motivated by the prospect of CO_2 and H_2 storage in abandoned oil and gas reservoirs in the North Sea, the experiment reported here contains several results that are of particular interest. Until recently, CO_2 has mainly been stored in saline aquifers, which are large layers of permeable sandstone filled with brine. The resident brine is displaced by CO_2 during injection. The extent of these reservoirs helps maintain the final fluid pore pressure at a level not too high compared to what it was before injection. To maximize the injected mass, CO_2 is preferably kept in its supercritical phase. Consequently, for the temperature expected after compression and given some heating at the well head, the reservoirs considered should be deeper than 700 m. For depleted (abandoned) oil and gas reservoirs, the depth is typically more than 2 km below the seafloor, which roughly corresponds to a pore pressure of >20 MPa and vertical stress of >40 MPa for the reservoir, considering an average material density of >2000 kg/m^3. H_2 storage will be in gaseous form and will rely mostly on abandoned fields, with smaller volumes needed compared to CO_2. Consequently, there is no particular depth requirement, except that several caprock and overburden barriers should be present to prevent leakage. Since most North Sea production fields are 2–5 km below the seabed, H_2 will be stored at these depths with the same pressure and stress values as noted above.

Since we are discussing the overlying shale caprock in this article, the stress values could be slightly lower (the Draupne core was obtained from around 1970 m depth). Additionally, for the experiments reported here, we had to consider the admissible pressure ranges of the HADES cell and the precision in maintaining the pressure at different levels. Relevance for natural climate solutions was our primary concern in these tests, and we tried to mimic pressure conditions, while, at the same time, working within the time limits of the allotted time slot at the synchrotron, which dictated the maximum permissible peak stress and the minimum strain rate for reaching peak stress. These constraints enforced some compromises, as ideally one would prefer the pore pressure not to increase too quickly during the stress changes for these low-permeability rocks.
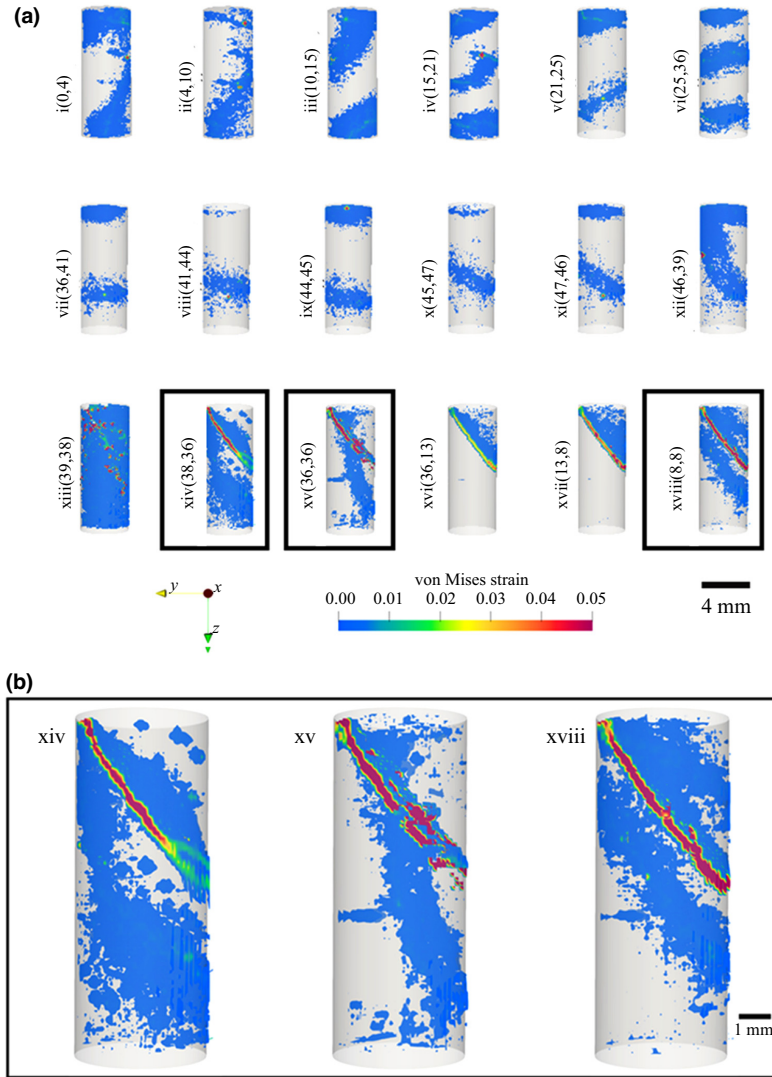
FIG. 6. Perspective view of the von Mises equivalent incremental strain, ε_{eq}, for stage A. (a) In about the first 10 time steps, strain distribution varies apparently randomly from one time step to the next. Strain appears to localize at about time step x, and the sample ruptures near xiii. (b) Enlarged views of strain states xiv, xv, and xviii. Primary shear band has $\varepsilon_{\text{eq}} > 0.05$ (red in the figure), and secondary features with significantly lower strain (blue) are also seen. Note that ε_{eq} values of zero are rendered as transparent.

From knowledge of the permeability, the pressure diffusion time can be estimated, assuming an incompressible pore fluid [47]. In designing such triaxial tests, one can adopt two paths: either (i) use the net stress principle, i.e., that failure occurs in the rock when the stress-pore pressure exceeds the strength limit, and thus, one can lower

the applied pore pressure relative to the *in situ* value; or (ii) try to operate as close to *in situ* conditions as possible. We chose the second approach, moderated by the above constraints.

A conceivably critical observation in our study is that the apparently linear stress-strain curve in fact contains
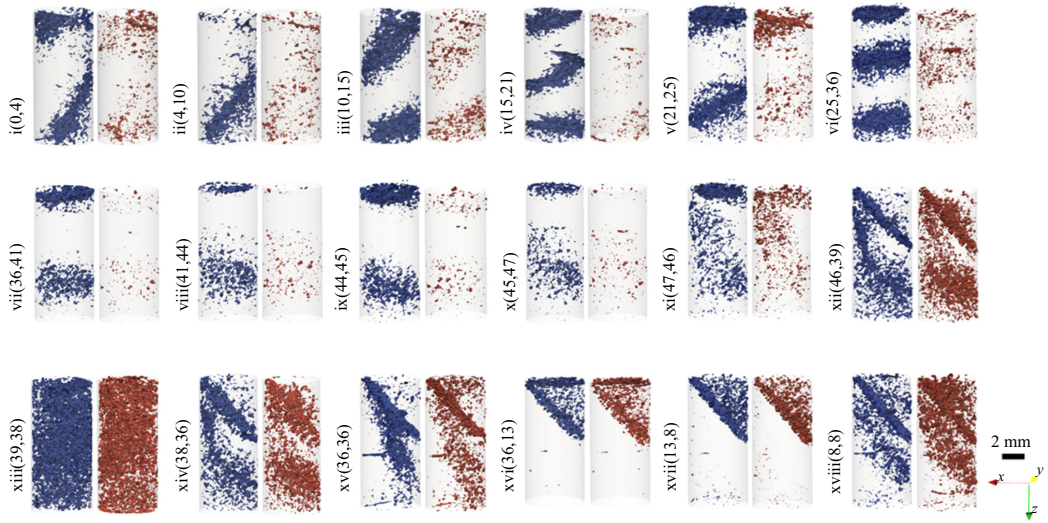
FIG. 7.   Perspective visualizations of the volumetric strain evolution in stage A. Images are split into pairs to show the spatial distribution of compaction, $\varepsilon_V < 0$ (left, blue), and dilation, $\varepsilon_V > 0$ (right, red). Blue isosurfaces represent incremental compaction ε_V in the range $(-0.6, -0.005)$, and red isosurfaces are dilative incremental ε_V in the range $(0.005, 0.6)$, with ranges chosen to highlight the dynamics. Gray shaded cylinder outline is an idealized (truncated) representation of the region of interest used for the DVC analysis.

a series of intermittent minor strain events taking place at random locations within the specimen. As elaborated below, we have reason to believe that these strain events are irreversible and destructive. Arguably, the Young's modulus could thus be somewhat higher than that prescribed by the straight line in Fig. 2, perhaps by a factor of 2–5, as suggested by the smaller irregularities of the curve. It is widely known that shales are highly brittle, and the yielding point indicated in Fig. 2 could be an unrealistically high stress value. Specifically, the value of (39 ± 2) MPa should not be interpreted as the maximum stress the Draupne shale sample can endure elastically. Furthermore, the apparently random locations of the intermittent events observed in the strain evolution indicated that the specimen was highly uniform; otherwise, one might expect the strain localization and subsequent failure to be confined to the weakest region of the sample.

Supported by the experiments, we argue that, despite the linear stress-strain curve up to semibrittle failure, irreversible damage occurs in the rock, and we cannot qualify this behavior under initial loading as being linear elastic. This quite intriguing observation can be addressed if we compare the strains incurred in the sporadic events shifting location to expectations given the known smallest elastic moduli of the mineral constituents of grains and grain cement, as well as clay stacks, as a function of stress increments over the time lapse for DVC. We

have also seen this linear behavior in other shales, where, invariably, if unload-reload loops are incorporated into the triaxial test, the unload slope is steeper than the master load slope (see also Fig. S10 within the Supplemental Material [36]). We note, of course, that this response is very different from that of a typical metal-bar elongation test, which exhibits a plastic yield point, then work hardening or softening until peak stress-associated failure. The observed behavior is indicative of two related phenomena: (1) the presence of a mixture of recoverable (elastic) and irreversible (plastic, damage) deformation upon loading, where unloading reveals plastic deformation; and (2) the master loading curve is characterized by "fresh" grain-bond destruction events that are self-similar in the sense that new small regions of intact rock get damaged as the axial stress is increased, and therefore, the same straight slope is observed.

The highly rotational strain state observed in 3D immediately prior to failure was not previously reported in microscopic rock studies but has been well described intuitively and theoretically [44]. Our study gives detailed and important insights into the failure of a comparably minute piece of shale from the Draupne formation, triggering the questions of representativity and upscaling. This consequence of limited synchrotron access is likely to be reduced in the future, as experiments that are feasible in university laboratories keep evolving at a rapid pace.
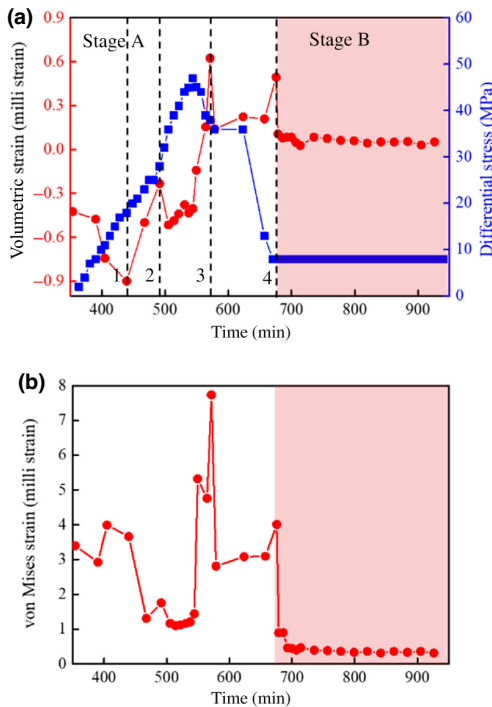
FIG. 8. Strain evolution spatially averaged over the entire sample. (a) Volumetric strain (red circles) and axial stress (blue squares) plotted as a function of elapsed time. Point 1 marks the initiation of dilation, point 2 is the initiation of microcracks, and points 3 and 4 indicate large incremental volumetric-strain-drop events. (b) von Mises equivalent strain.

V. CONCLUSION

Here, we studied how a shale caprock sample was brought to failure under reservoir conditions. Specifically, a Draupne shale sample was investigated through triaxial testing monitored by synchrotron-based microcomputed tomography and digital volume-correlation analysis. We described quantitatively the sample evolution towards failure. Most importantly, we provided data indicating that the initial linear stress-strain phase contained irreversible deformations. The onset of failure occurred by an increase of dilation and a pronounced high-shear state, as previously reported for Green River shale [31]. Tracking the evolution of the 3D incremental displacement field in the sample (Fig. 4), we observed early nonhomogenous deformations, including intermittent strain clustering at apparently random locations. After fracture, a sliding-block mechanism was observed. By following the evolution of the volumetric and von Mises strains, the temporary localization that occurred in the sample prior to the formation of

the macroscopic fault was revealed. The creep observed on this macroscopic fault indicated that the slow deformations in the shale could be related to the slip on the surface and not only to bulk creep. This study also revealed the presence of the secondary fracture networks that connected to the system-spanning fault in the sample at different stages of the experiment; these features are important to understand the failure of shales and have not previously been reported. The experimental and analysis techniques presented herein reveal the local mechanics in the Draupne shales and can further be applied to understand the stability of these rocks for applications like CO_2 sequestration.

[1] M. F. Ashby and S. D. Hallam, The failure of brittle solids containing small cracks under compressive stress states, Acta Metall. **34**, 497 (1986).

[2] J. F. W. Gale, S. E. Laubach, J. E. Olson, P. Eichhubl, and A. Fall, Natural fractures in shale: A review and new observations, AAPG Bull. **98**, 2165 (2014).

[3] B. L. Alemu, P. Aagaard, I. A. Munz, and E. Skurtveit, Caprock interaction with CO_2: A laboratory study of reactivity of shale with supercritical CO_2 and brine, Appl. Geochem. **26**, 1975 (2011).

[4] N. Agofack, P. Cerasi, E. Sonstebo, and J. Stenebraten, Thermo-poromechanical properties of Pierre II shale, Rock Mech. Rock Eng. **55**, 6703 (2022).

[5] E. Skurtveit, E. Aker, M. Soldal, M. Angeli, and Z. Wang, Experimental investigation of CO_2 breakthrough and flow mechanisms in shale, Pet. Geosci. **18**, 3 (2012).

[6] Z. H. Zhang and D. Huisingh, Carbon dioxide storage schemes: Technology, assessment and deployment, J. Cleaner Prod. **142**, 1055 (2017).

[7] G. P. D. De Silva, P. G. Ranjith, and M. S. A. Perera, Geochemical aspects of CO_2 sequestration in deep saline aquifers: A review, Fuel **155**, 128 (2015).

[8] C. M. White, B. R. Strazisar, E. J. Granite, J. S. Hoffman, and H. W. Pennline, Separation and capture of CO_2 from large stationary sources and sequestration in geological formations - coalbeds and deep saline aquifers, J. Air Waste Manage. Assoc. **53**, 645 (2003).

[9] B. Jia, Z. Chen, and C. Xian, Investigations of CO_2 storage capacity and flow behavior in shale formation, J. Pet. Sci. Eng. **208,** 109659 (2022).

[10] M. Bui, C. S. Adjiman, A. Bardow, E. J. Anthony, A. Boston, S. Brown, P. S. Fennell, S. Fuss, A. Galindo, L. A. Hackett, *et al.*, Carbon capture and storage (CCS): The way forward, Energy Environ. Sci. **11,** 1062 (2018).

[11] E. K. Halland, F. Riis, C. Magnus, W. T. Johansen, I. M. Tappel, I. T. Gjeldvik, T. Solbakk, and V. T. H. Pham, CO_2 storage atlas of the Norwegian part of the North Sea, Energy Procedia **37,** 4919 (2013).

[12] M. Josh, L. Esteban, C. Delle Piane, J. Sarout, D. N. Dewhurst, and M. B. Clennell, Laboratory characterisation of shale properties, J. Pet. Sci. Eng. **88-89,** 107 (2012).

[13] S. Kelly, H. El-Sobky, C. Torres-Verdin, and M. T. Balhoff, Assessing the utility of FIB-SEM images for shale digital rock physics, Adv. Water Resour. **95,** 302 (2016).

[14] V. Cnudde and M. N. Boone, High-resolution x-ray computed tomography in geosciences: A review of the current technology and applications, Earth-Sci. Rev. **123,** 1 (2013).

[15] F. Renard, J. McBeck, B. Cordonnier, X. J. Zheng, N. Kandula, J. R. Sanchez, M. Kobchenko, C. Noiriel, W. L. Zhu, P. Meakin, *et al.*, Dynamic *in situ* three-dimensional imaging and digital volume correlation analysis to quantify strain localization and fracture coalescence in sandstone, Pure Appl. Geophys. **176,** 1083 (2019).

[16] M. J. Blunt, B. Bijeljic, H. Dong, O. Gharbi, S. Iglauer, P. Mostaghimi, A. Paluszny, and C. Pentland, Pore-scale imaging and modelling, Adv. Water Resour. **51,** 197 (2013).

[17] F. Renard, J. McBeck, N. Kandula, B. Cordonnier, P. Meakin, and Y. Ben-Zion, Volumetric and shear processes in crystalline rock approaching faulting, Proc. Natl. Acad. Sci. U. S. A. **116,** 16234 (2019).

[18] E. A. Chavez Panduro, B. Cordonnier, K. Gawel, I. Børve, J. Iyer, S. A. Carroll, L. Michels, M. Rogowska, J. A. McBeck, H. O. Sørensen, *et al.*, Real time 3D observations of Portland cement carbonation at CO_2 storage conditions, Environ. Sci. Technol. **54,** 8323 (2020).

[19] Y. Geraud, F. Mazerolle, S. Raynaud, and P. Lebon, Crack location in granitic samples submitted to heating, low confining pressure and axial loading, Geophys. J. Int. **133,** 553 (1998).

[20] F. Renard, B. Cordonnier, D. K. Dysthe, E. Boller, P. Tafforeau, and A. Rack, A deformation rig for synchrotron microtomography studies of geomaterials under conditions down to 10 km depth in the Earth, J. Synchrotron Radiat. **23,** 1030 (2016).

[21] S. Raynaud, G. Vasseur, B. Celerier, D. Loggia, M. Ghoreychi, M. H. Mathon, and F. Mazerolle, Experimental study of the relation between the permeability of kaolinite and its deformation at micro and macro scale, Int. J. Rock Mech. Min. Sci. **47,** 559 (2010).

[22] E. M. Charalampidou, S. A. Hall, S. Stanchits, H. Lewis, and G. Viggiani, Characterization of shear and compaction bands in a porous sandstone deformed under triaxial compression, Tectonophysics **503,** 8 (2011).

[23] E. Tudisco, M. Etxegarai, S. A. Hall, E. M. Charalampidou, G. D. Couples, H. Lewis, A. Tengattini, and N. Kardjilov, Fast 4-D imaging of fluid flow in rock by high-speed neutron tomography, J. Geophys. Res.-Solid Earth **124,** 3557 (2019).

[24] E. Tudisco, S. A. Hall, E. M. Charalampidou, N. Kardjilov, A. Hilger, and H. Sone, in *10th World Conference on Neutron Radiography (WCNR)* (Elsevier Science Bv, Grindelwald, Switzerland, 2014), pp. 509.

[25] F. K. Murer, A. S. Madathiparambil, K. R. Tekseth, M. Di Michiel, P. Cerasi, B. Chattopadhyay, and D. W. Breiby, Orientational mapping of minerals in Pierre shale using x-ray diffraction tensor tomography, IUCrJ **8,** 747 (2021).

[26] W. De Boever, A. Diaz, H. Derluyn, T. De Kock, J. Van Stappen, J. Dewanckele, T. Bultreys, M. Boone, T. De Schryver, E. T. B. Skjonsfjell, *et al.*, Characterization of composition and structure of clay minerals in sandstone with ptychographic x-ray nanotomography, Appl. Clay Sci. **118,** 258 (2015).

[27] B. Chattopadhyay, A. S. Madathiparambil, F. K. Murer, P. Cerasi, Y. Chushkin, F. Zontone, A. Gibaud, and D. W. Breiby, Nanoscale imaging of shale fragments with coherent x-ray diffraction, J. Appl. Crystallogr. **53,** 1562 (2020).

[28] B. K. Bay, T. S. Smith, D. P. Fyhrie, and M. Saad, Digital volume correlation: Three-dimensional strain mapping using x-ray tomography, Exp. Mech. **39,** 217 (1999).

[29] E. Tudisco, E. Ando, R. Cailletaud, and S. A. Hall, TomoWarp2: A local digital volume correlation code, SoftwareX **6,** 267 (2017).

[30] E. Fjær, R. M. Holt, P. Horsrud, and A. M. Raaen, *Petroleum related rock mechanics*, 2nd ed. (Elsevier, Amsterdam, 2008).

[31] J. McBeck, M. Kobchenko, S. A. Hall, E. Tudisco, B. Cordonnier, P. Meakin, and F. Renard, Investigating the onset of strain localization within anisotropic shale using digital volume correlation of time-resolved x-ray microtomography images, J. Geophys. Res.-Solid Earth **123,** 7509 (2018).

[32] J. Rahman, M. Fawad, and N. H. Mondol, Organic-rich shale caprock properties of potential CO_2 storage sites in the northern North Sea, offshore Norway, Mar. Pet. Geol. **122,** 104665 (2020).

[33] J. A. Hansen, N. H. Mondol, and M. Fawad, Organic content and maturation effects on elastic properties of source rock shales in the central North Sea, Interpretation **7,** T477 (2019).

[34] D. Paganin, S. C. Mayo, T. E. Gureyev, P. R. Miller, and S. W. Wilkins, Simultaneous phase and amplitude extraction from a single defocused image of a homogeneous object, J. Microsc. **206,** 33 (2002).

[35] A. Mirone, E. Brun, E. Gouillart, P. Tafforeau, and J. Kieffer, The PyHST2 hybrid distributed code for high speed tomographic reconstruction with iterative reconstruction and a priori knowledge capabilities, Nucl. Instrum. Methods Phys. Res., Sect. B **324,** 41 (2014).

[36] See the Supplemental Material at http://link.aps.org/supplemental/10.1103/PhysRevApplied.20.034046 for details on the strain calculation, principal component analysis, effect of node spacing, and Skempton A coefficient.

[37] N. Agofack, P. Cerasi, A. Stroisz, and S. Rørheim, in *53rd U.S. Rock Mechanics/Geomechanics Symposium* (2019).

[38] M. J. Turunen, S. Le Cann, E. Tudisco, G. Lovric, A. Patera, S. A. Hall, and H. Isaksson, Sub-trabecular strain

evolution in human trabecular bone, Sci. Rep. **10**, 13788 (2020).

[39] S. Heng, X. Z. Li, X. Liu, and Y. Chen, Experimental study on the mechanical properties of bedding planes in shale, J. Nat. Gas Sci. Eng. **76**, 103161 (2020).

[40] M. Soldal, E. Skurtveit, and J. C. Choi, Laboratory evaluation of mechanical properties of Draupne shale relevant for CO_2 seal integrity, Geosciences **11**, 244 (2021).

[41] F. Renard, B. Cordonnier, M. Kobchenko, N. Kandula, J. Weiss, and W. L. Zhu, Microscale characterization of rupture nucleation unravels precursors to faulting in rocks, Earth Planet. Sci. Lett. **476**, 69 (2017).

[42] W. F. Chen and D. J. Han, *Plasticity for Structural Engineers* (Springer, New York, 2011).

[43] P. Bésuelle, J. Desrues, and S. Raynaud, Experimental characterisation of the localisation phenomenon inside a Vosges sandstone in a triaxial cell, Int. J. Rock Mech. Min. Sci. **37**, 1223 (2000).

[44] D. D. Pollard and P. Segall, in *Fracture Mechanics of Rock*, edited by B.K. Atkinson (Academic Press, London, 1987), p. 277.

[45] A. Aydin, R. I. Borja, and P. Eichhubl, Geological and mathematical framework for failure modes in granular rock, J. Struct. Geol. **28**, 83 (2006).

[46] J. Desrues and G. Viggiani, Strain localization in sand: An overview of the experimental results obtained in Grenoble using stereophotogrammetry, Int. J. Numer. Anal. Methods Geomech. **28**, 279 (2004).

[47] P. Cerasi, E. Lund, M. L. Kleiven, A. Stroisz, S. Pradhan, C. Kjøller, P. Frykman, and E. Fjær, Shale creep as leakage healing mechanism in CO_2 sequestration, Energy Procedia **114**, 3096 (2017).

Supplementary Information:

Time-Resolved in Situ Imaging of Strain Localization in Draupne Shale Under Triaxial Compression

Aldritt Scaria Madathiparambil, Kim Robert Tekseth, Fredrik K. Mürer,
Benoît Cordonnier, Nicolaine Agofack, Jessica McBeck, Pierre Cerasi, François Renard,
Basab Chattopadhyay, Dag W. Breiby[*]

The Supplementary Information contains:

- One table (Table S1)
    - o *Table S1. Experimental details and steps used for digital volume correlation (DVC) calculations.*

- Four text sections (Texts S1 to S4)
    - o *Text S1. Incremental Strain Calculation*
    - o *Text S2. Principal Strain Analysis*
    - o *Text S3. Effect of Node Spacing on the Calculated Incremental Strain Magnitudes*
    - o *Text S4. Skempton A Coefficient*

- Ten figures (S1 to S10)

Table S1. Experimental details and steps used for digital volume correlation (DVC) calculations.

No.	Stage	Time (min)		Differential stress (MPa)		Axial strain	
		Initial	final	Initial	final	Initial	final
i	A	342	364	0	4	0	1.12
ii	A	364	390	4	10	1.12	2.64
iii	A	390	412	10	15	2.64	4.24
iv	A	412	440	15	21	4.24	5.7
v	A	440	474	21	25	5.7	7.52
vi	A	474	506	25	36	7.52	9.97
vii	A	506	522	36	41	9.97	10.79
viii	A	522	530	41	44	10.79	12.27
ix	A	530	537	44	45	12.27	13.4
x	A	537	544	45	47	13.4	14.36
xi	A	544	550	47	46	14.36	15.23
(Peak stress)							
xii	A	550	564	46	39	15.23	16.85
xiii	A	564	571	39	38	16.85	19.28
xiv	A	571	578	38	36	19.28	20.48
xv	A	578	623	36	36	20.48	21.68
xvi	B	623	657	36	13	21.68	21.23
xvii	B	657	670	13	8	21.20	21.16
xviii	B	670	676	8	8	21.16	21.25

Text S1. Incremental Strain Calculation

To characterize the evolving incremental strain in the sample, the displacement fields **u(r)** obtained from DVC were used. We calculated the changes in the local volumetric and shear strain with the following standard formalism of incremental strain theory [1].

The displacement gradient tensor is defined as $\nabla \mathbf{u} = \partial u_i / \partial x_j$ and can be reformulated as

$$\nabla \mathbf{u} = \frac{\partial u_i}{\partial x_j} = \frac{1}{2}(\frac{\partial u_i}{\partial x_j} + \frac{\partial u_j}{\partial x_i}) + \frac{1}{2}(\frac{\partial u_i}{\partial x_j} - \frac{\partial u_j}{\partial x_i}) = \varepsilon_{ij} + \omega_{ij}. \tag{1}$$

The incremental strain tensor ε_{ij} represents the symmetric part of $\nabla \mathbf{u}$, which thus has six independent components:

$$\varepsilon_{ij} \equiv \frac{1}{2}(\frac{\partial u_i}{\partial x_j} + \frac{\partial u_j}{\partial x_i}) = \begin{pmatrix} \varepsilon_{11} & \varepsilon_{12} & \varepsilon_{13} \\ \varepsilon_{12} & \varepsilon_{22} & \varepsilon_{23} \\ \varepsilon_{13} & \varepsilon_{23} & \varepsilon_{33} \end{pmatrix}. \tag{2}$$

The antisymmetric tensor ω_{ij} accounts for the rotational part of $\nabla \mathbf{u}$ and has three independent components:

$$\omega_{ij} \equiv \frac{1}{2}(\frac{\partial u_i}{\partial x_j} - \frac{\partial u_j}{\partial x_i}) = \begin{pmatrix} \omega_{11} & 0 & 0 \\ 0 & \omega_{22} & 0 \\ 0 & 0 & \omega_{33} \end{pmatrix}. \tag{3}$$

The incremental strain tensor $\boldsymbol{\varepsilon}$ can additionally be decomposed into a deviatoric part **e** and an isotropic volumetric part, as $\mathbf{e} = \boldsymbol{\varepsilon} - 1/3 \cdot \mathrm{tr}(\boldsymbol{\varepsilon})\mathbf{I}$ or, in tensor notation, $e_{ij} = \varepsilon_{ij} - (\varepsilon_{11} + \varepsilon_{22} + \varepsilon_{33})\delta_{ij}/3$. The infinitesimal strain tensor $\boldsymbol{\varepsilon}$ is real and symmetric and, therefore, has three real eigenvalues or principal strains ε_1, ε_2, and ε_3, with corresponding orthogonal eigenvectors. The principal strain directions are those where there is no shear strain. The eigenvalues ε_1, ε_2 and ε_3 denote the principal strains and give the elongations in the principal directions. The algebraically largest, middle and smallest eigenvalues are called the major, intermediate, and minor principal strains, respectively [1]. The volumetric strain ε_V is the relative incremental change in volume, i.e., the change in the volume divided by the original volume, defined as

$$\varepsilon_V = (V_f - V_i)/V_i = \mathrm{tr}(\boldsymbol{\varepsilon}) = \varepsilon_{11} + \varepsilon_{22} + \varepsilon_{33} = \varepsilon_1 + \varepsilon_2 + \varepsilon_3, \tag{4}$$

where V_i and V_f denote the initial and final volumes, respectively.
To describe the evolution of incremental deviatoric strain, we chose to use the von Mises equivalent strain, defined as

$$\varepsilon_{eq} = \sqrt{\frac{2}{3}\mathbf{e} : \mathbf{e}} = \sqrt{\frac{4}{3}Y_2}, \tag{5}$$

$$Y_2 = \frac{1}{2}(e_{11}^2 + e_{22}^2 + e_{33}^2 + 2e_{12}^2 + 2e_{23}^2 + 2e_{13}^2). \tag{6}$$

Text S2. Principal Strain Analysis
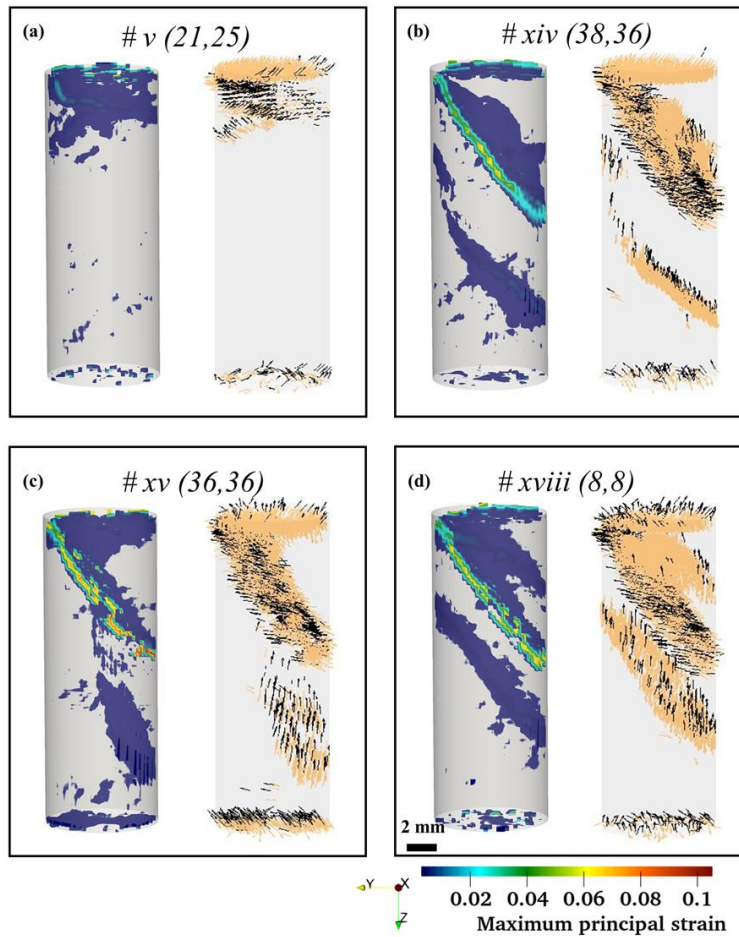
FIG. S1. Principal strain analysis. Distribution of the magnitude of the major principal strain and the corresponding vector directions obtained from the DVC analysis at different loading steps. The maximum principal strain vectors oriented upwards along the *z*-axis are shown in black and vectors pointing downwards are shown in orange. Time steps: (a) Stage A #*v*(21,25), (b) Stage B #*xiv*(39,38), (c) Stage B #*xv*(38,36), and (d) Stage B #*xvii*(13,8).

The principal strain is a useful quantity for extracting the key features from the strain field, readily extracted by eigenvalue analysis (see text S1). In Fig. S1, we visualize the projection of the maximum principal strain vectors onto the *z*-axis to reveal the direction of the dominant strain component in the sample. At the beginning of the compression test, high strain values were observed near the upper end of the specimen, with a majority of the principal strain vectors pointing downwards, caused by the pressure exerted by the upper piston on the sample. For time steps closer to the peak stress, the maximum principal strain distribution localizes along the fractures. A closer look at the directions of the principal strain vectors reveals the relative slipping of the parts for both the main and secondary fractures.

Text S3. Effect of Node Spacing on the Calculated Incremental Strain Magnitudes

To study quantitatively the effect of the node spacing on the calculated incremental strain magnitude, DVC analysis was also performed for a set of finer node spacings. We selected a range of node spacing from 4 voxels to 24 voxels and the correlations windows were also changed so that there was no overlap between the adjacent correlation windows, cf. Fig. S2.
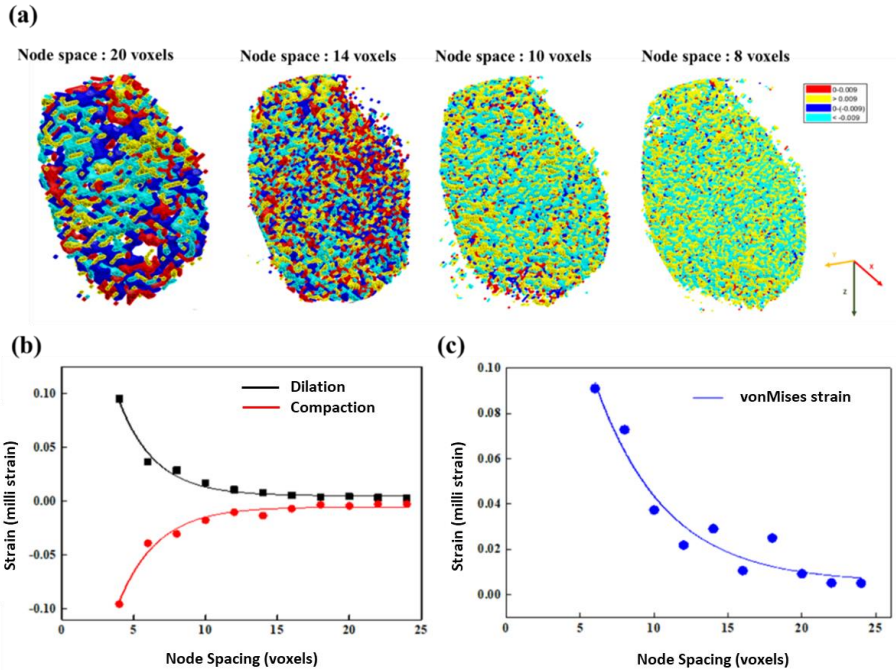
FIG. S2. Influence of the node spacing on the DVC strain for time step #*xvii*(36,13). (a) The spatial distribution of ε_V across the fracture plane. The dilational strains are plotted in red for values (0,0.009) and yellow ($\varepsilon_V > 0.009$). The compactional strains are shown in blue for values (0, -0.009) and cyan ($\varepsilon_V < -0.009$). (b) The change in the ε_V strain values averaged over the sample as function of node spacing. (c) von Mises equivalent strain ε_{eq} as function of node spacing. The solid lines in (b) and (c) are guides to the eye.

The results indicate that the strains are dependent on the node spacing used for the DVC calculation. Based on this study, we conclude that only higher local strains are detectable using small enough node spacings. The strain magnitudes are seen to increase rapidly with a decrease in the node spacing. The physical interpretation of this behavior is that for larger node spacings, lower strains are expected because rapidly varying shorter-ranged strain values tend to cancel when averaged over larger volumes. Similar consistent observations have been reported for other sedimentary rocks and for bone related studies [2,3]. If the ambiguity in selecting the node spacing renders the absolute values of the strain fields imprecise, we have chosen a node spacing of 20 voxels for which slightly larger (25 voxels) or smaller (15 voxels) windows would give similar results.

Text S4. Skempton A Coefficient

Triaxial experiments on other samples from the same borehole core where the sample for the μCT triaxial test was taken are shown in Agofack *et al*. [4]. Mohr cycles at failure are given in Figure S3, displaying the shear stress as function of the effective normal stress. Each half-cycle has a diameter equal to $\sigma_{ax}{}' - \sigma_{conf}{}'$ and is centered at $(\sigma_{ax}{}' + \sigma_{conf}{}')/2$ (indicated with dots on the 1st -axis of the figure with the sample color). $\sigma_{ax}{}' \equiv \sigma_{ax} - \sigma_{pore}$ and $\sigma_{conf}{}' \equiv \sigma_{conf} - \sigma_{pore}$ are effective axial stress and effective confining pressure. σ_{conf} is the confining pressure, σ_{ax} and σ_{pore} are the axial stress and pore pressure at failure, respectively. The maximum shear stress is $\sigma_{ax}{}' \equiv (\sigma_{ax} - \sigma_{conf})/2$. The dashed line indicates a likely failure envelope. The diameter of the cycle represents the maximum of the deviatoric stress for a giving effective confining pressure.
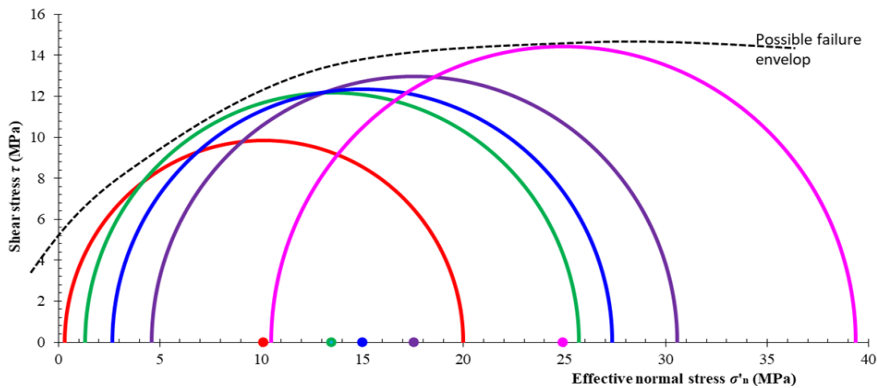
FIG. S3. Mohr cycles from triaxial experiments on Draupne shale samples from the same core where the sample deformed in the present study was extracted. Adapted from experiments presented in [4].

During the deviatoric phase (where the confining pressure is kept constant and the axial stress is increased), the pore pressure changes. This variation of the pore pressure with the deviatoric stress is related to a coefficient called *Skempton A*, defined by $\Delta\sigma_{pore} \equiv A \times \Delta(\sigma_{ax} - \sigma_{conf})$. From the experiments presented above, this coefficient is in the range (0.29, 0.48) [4].
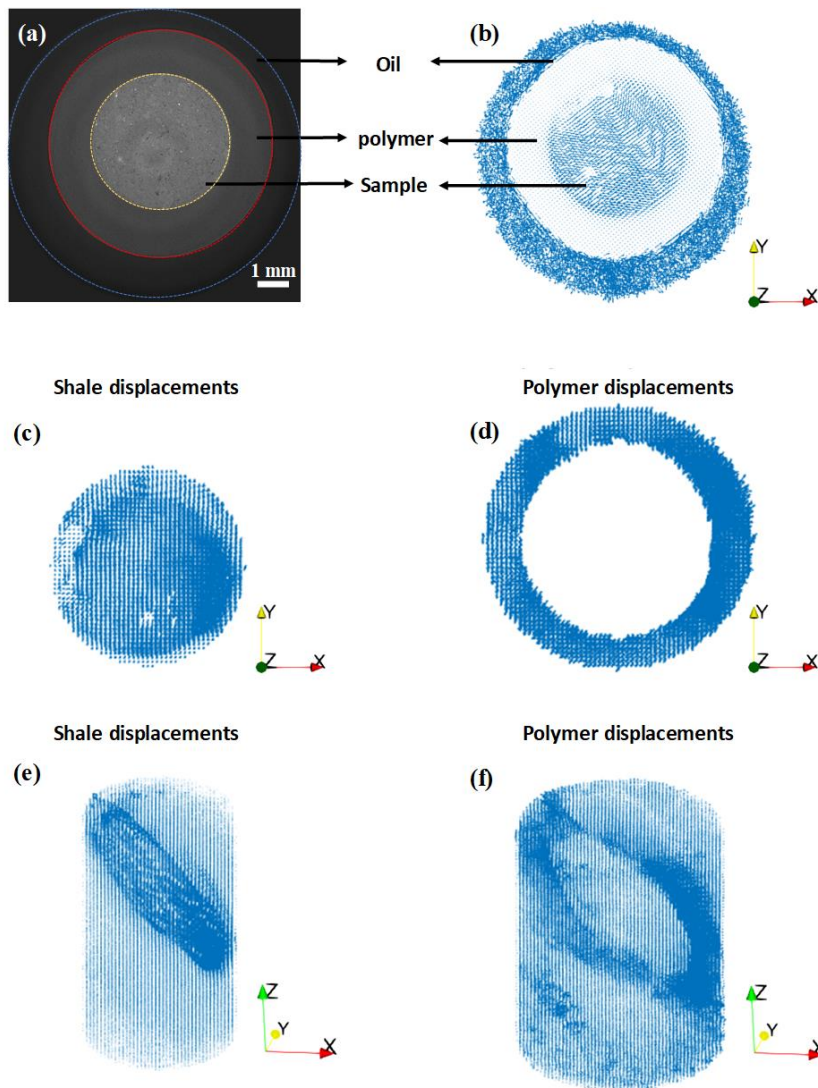
FIG. S4. DVC displacement fields for the full measured field of view, for DVC step #*xviii*(8,8), during which some slip occurred on the main fault. (a) Representative tomogram lateral cross section, where the region inside the yellow dotted circle contains the shale sample, the region between yellow and red lines the rubber Viton® sleeve, and the region between blue and red lines contains the oil providing the confining pressure in the cell. (b)-(f) The displacement fields from DVC calculations.
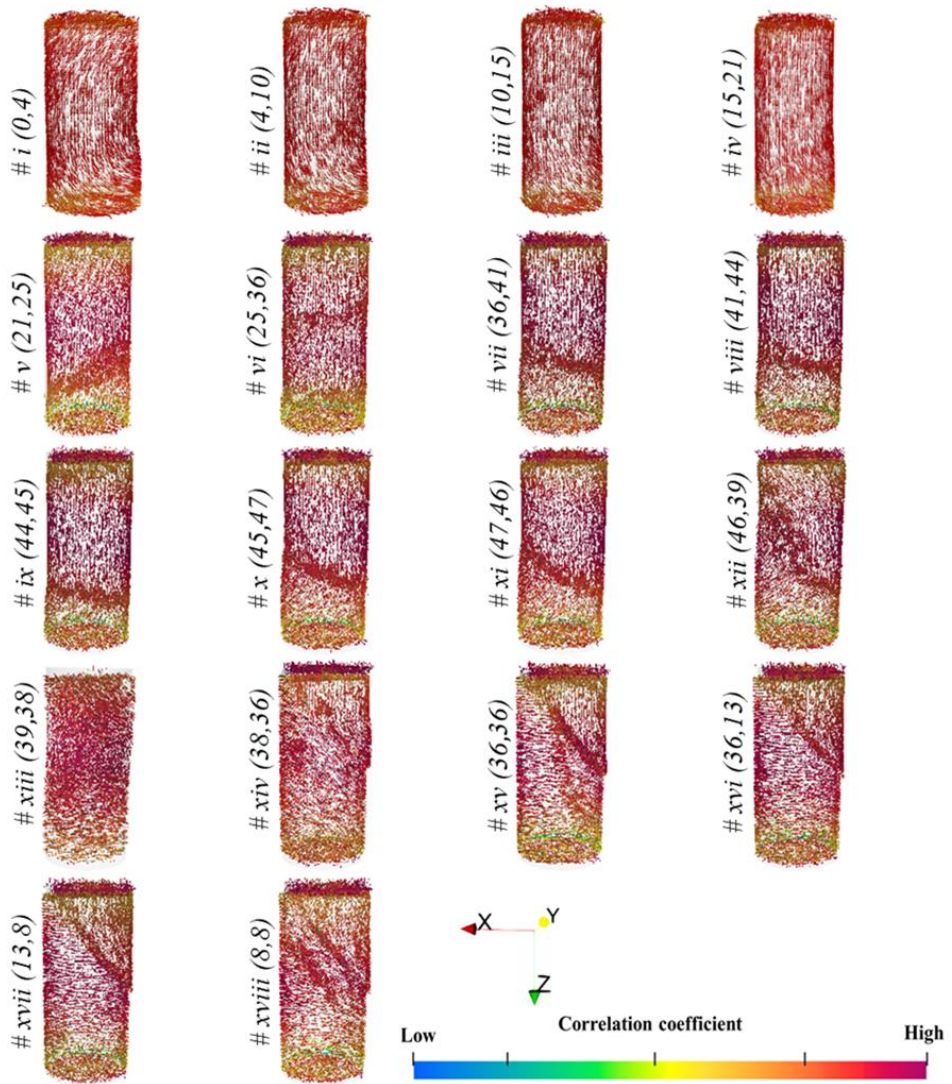
FIG. S5. Perspective visualization of the 3D displacement field **u**(**r**,*t*) for all DVC time steps #*i* - #*xviii* for the full sample. Note the significant deformation of the sample in #*xiii*(39,38) just before failure. The correlation coefficient indicates the reliability of the DVC result.
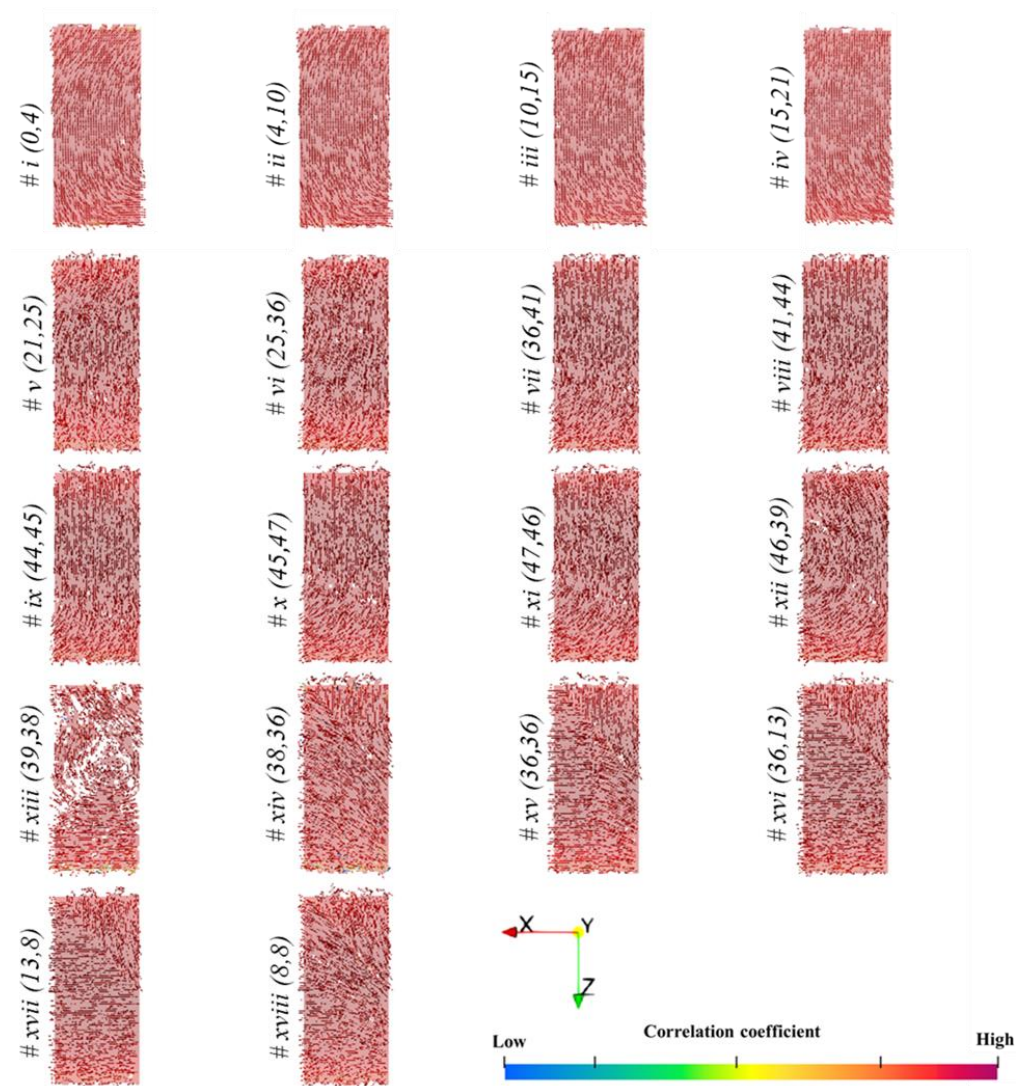
FIG. S6. Central axial slice of the displacement field **u**(**r**,*t*) for all the DVC steps.
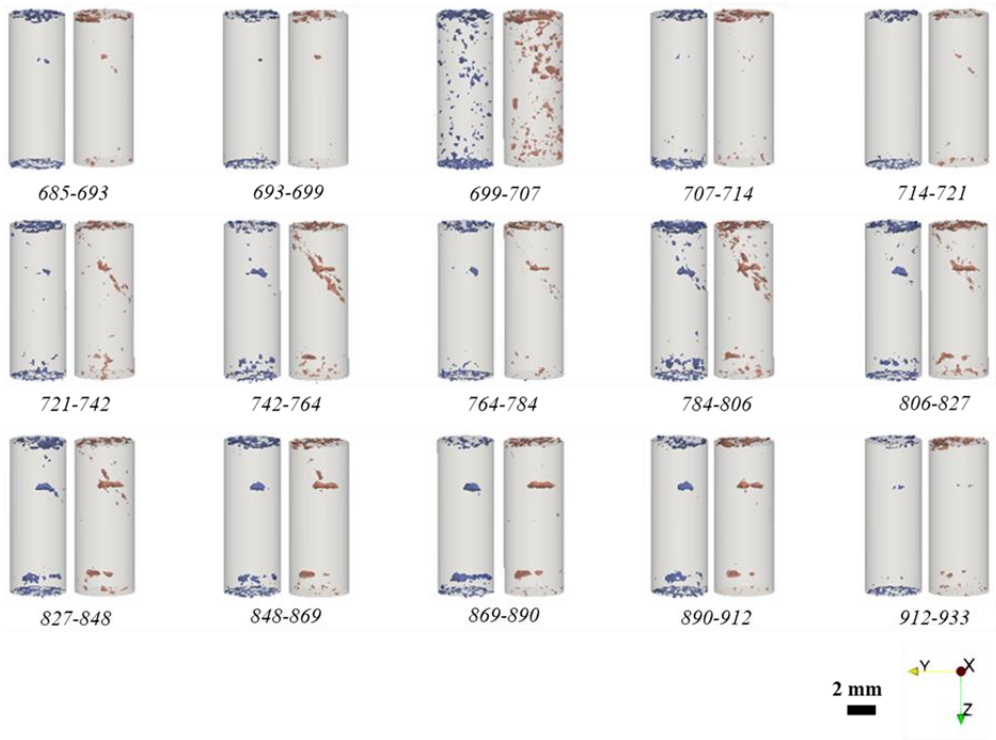
FIG. S7. Time evolution of the compaction (blue) and dilation (brown) during stage B, where the differential stress σ_{zz} was maintained constant. The blue isosurfaces represent incremental compaction ε_V in the range (-0.6, -0.005) and the red isosurfaces are dilative incremental ε_V in the range (0.005, 0.6). The evolutions of the compaction and the dilation for stage B occur between 675 and 940 minutes (Figure 1).
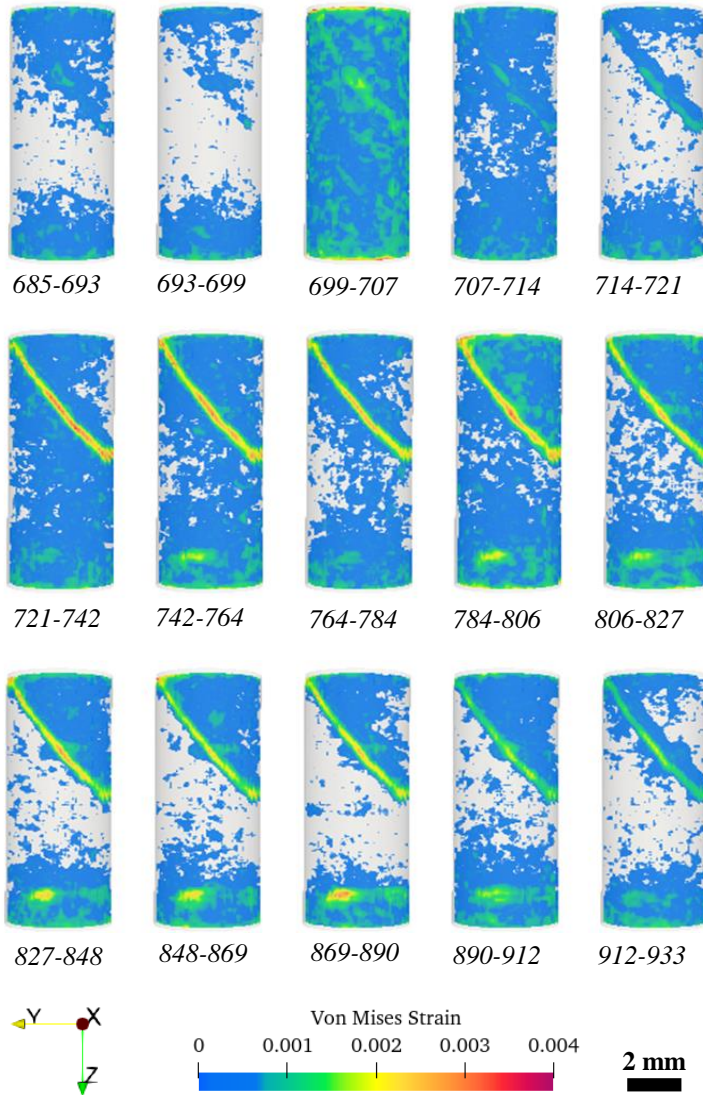
FIG. S8. Time evolution of the von Mises strain during stage B. The von Mises strain concentrates predominantly along the fracture plane of the sample and is essentially constant and low to the end of the experiment. The evolutions of the shear band for stage B occurred in the time intervals (in minutes) indicated for each subfigure. Note that ε_{eq} values of zero are rendered as transparent.
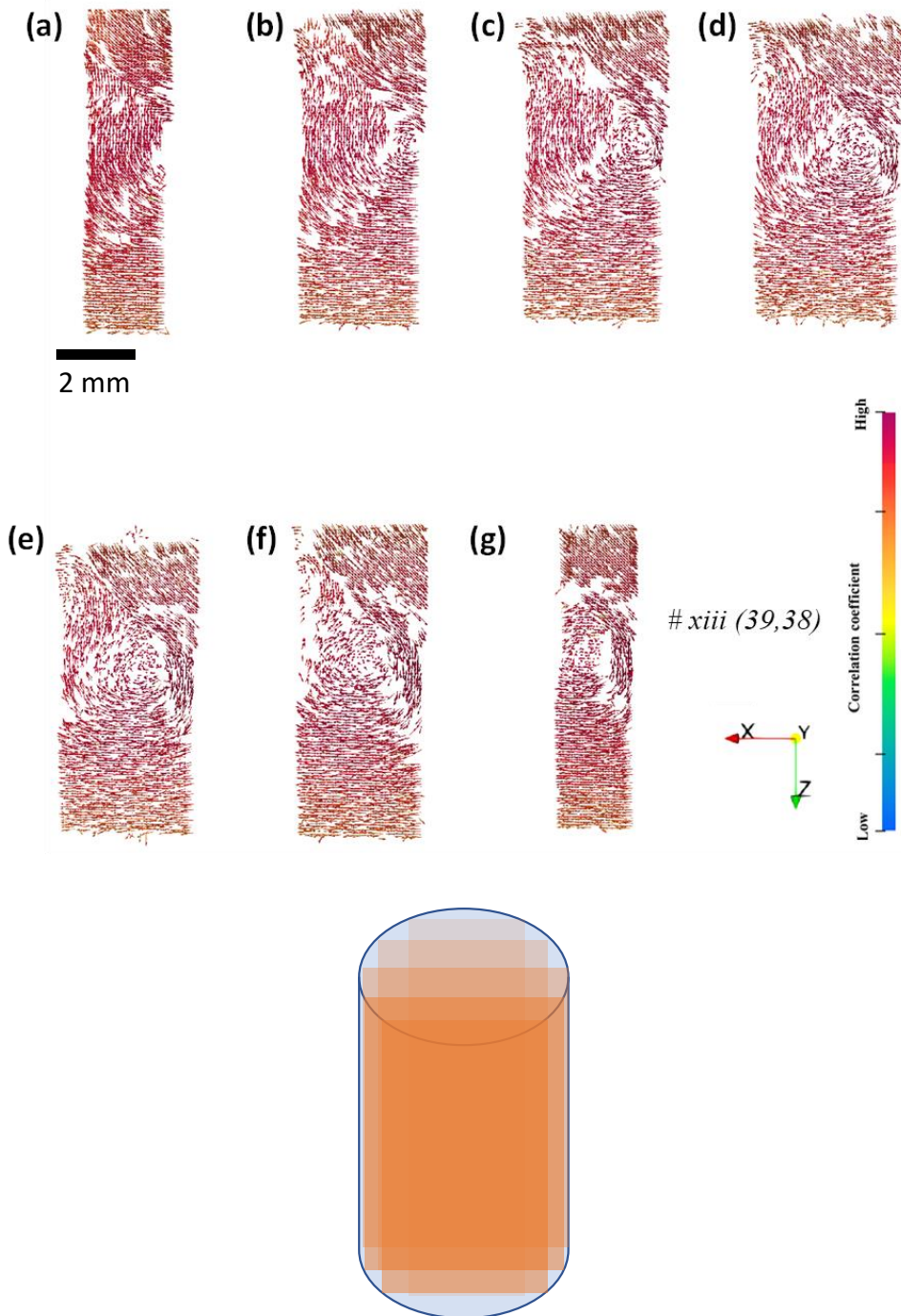
FIG. S9. Multi-slice view of the displacement field obtained for DVC time step #*xiii*(39,38). Parallel axial slices with a separation of 0.8 mm as sketched in the bottom figure are presented. Note that the rotational strain state extends through the entire sample.
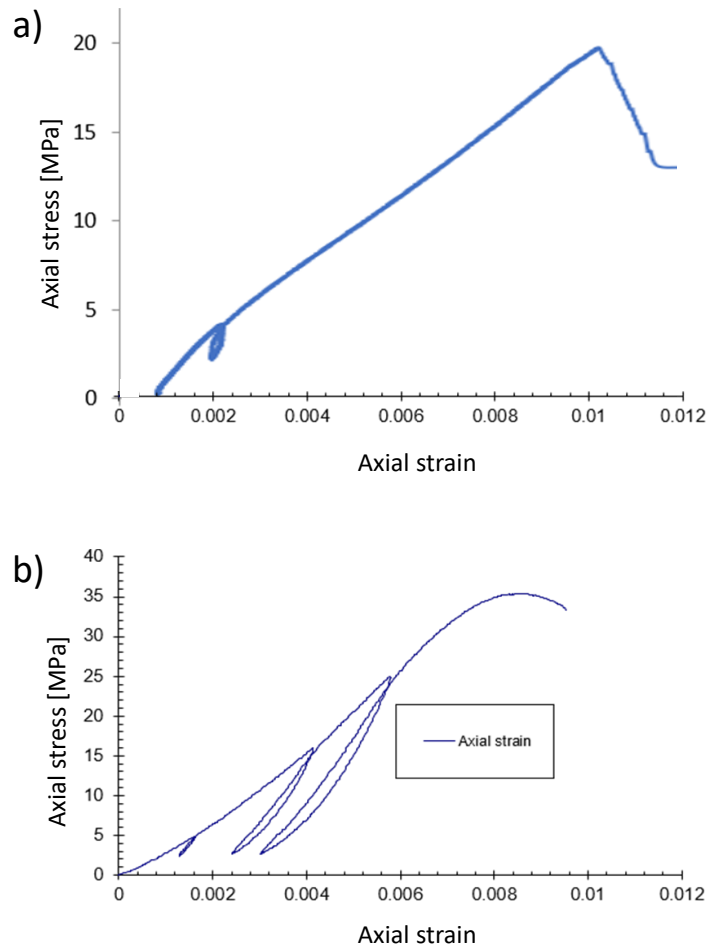
FIG. S10. Complementary triaxial tests. a) Draupne shale with a single unload-reload loop, showing a steeper slope in the axial stress-strain domain. b) Castlegate sandstone at 2 MPa confining stress incorporating three unload-reload loops, showing steeper slope in the axial stress-strain domain. Note the hysteresis seen in both cases.

References

[1] W. F. Chen and D. J. Han, Plasticity for Structural Engineers, J. Ross Publishing, 2007.

[2] J. McBeck, M. Kobchenko, S. A. Hall, E. Tudisco, B. Cordonnier, P. Meakin, and F. Renard, Investigating the Onset of Strain Localization Within Anisotropic Shale Using Digital Volume Correlation of Time-Resolved X-Ray Microtomography Images, J. Geophys. Res. Solid Earth 123, 7509 (2018).

[3] M. J. Turunen, S. Le Cann, E. Tudisco, G. Lovric, A. Patera, S. A. Hall, and H. Isaksson, Sub-trabecular strain evolution in human trabecular bone, Sci. Rep., 10 (2020).

[4] N. Agofack, P. Cerasi, A. Stroisz, and S. Rørheim, Sorption of CO_2 and Integrity of a Caprock Shale, 53rd U.S. Rock Mech. Symp. (2019).

Paper 2

Madathiparambil, Aldritt Scaria; Mirzaei, Fazel; Tekseth, Kim Robert Bjørk;
Cordonnier, Benoit; Agofack, Nicolaine; Cerasi, Pierre; Renard, Francois;
Chattopadhyay, Basab; Breiby, Dag Werner.
Mechanical response of cement 1 and shale admixtures under cyclic triaxial loading
monitored by in-situ synchrotron micro-computed tomography.

This paper is submitted for publication and is therefore not included.

Paper 3

Nanoscale imaging of shale fragments with coherent X-ray diffraction

Basab Chattopadhyay,[a]* Aldritt S. Madathiparambil,[a] Fredrik K. Mürer,[a] Pierre Cerasi,[b] Yuriy Chushkin,[c] Federico Zontone,[c] Alain Gibaud[d] and Dag W. Breiby[a,e]*

[a]PoreLab, Department of Physics, Norwegian University of Science and Technology (NTNU), Høgskoleringen 5, Trondheim, 7491, Norway, [b]Petroleum Department, SINTEF Industry, Trondheim, 7465, Norway, [c]ESRF – The European Synchrotron, 71 Avenue des Martyrs, Grenoble, 38000, France, [d]LUNAM, IMMM, UMR 6283 CNRS, Faculté des Sciences, Le Mans, 72085, France, and [e]Department of Microsystems, University of South-Eastern Norway, Campus Vestfold, Borre, 3182, Norway. *Correspondence e-mail: basab.chattopadhyay@ntnu.no, dag.breiby@ntnu.no

Despite the abundance of shales in the Earth's crust and their industrial and environmental importance, their microscale physical properties are poorly understood, owing to the presence of many structurally related mineral phases and a porous network structure spanning several length scales. Here, the use of coherent X-ray diffraction imaging (CXDI) to study the internal structure of microscopic shale fragments is demonstrated. Simultaneous wide-angle X-ray diffraction (WAXD) measurement facilitated the study of the mineralogy of the shale microparticles. It was possible to identify pyrite nanocrystals as inclusions in the quartz–clay matrix and the volume of closed unconnected pores was estimated. The combined CXDI–WAXD analysis enabled the establishment of a correlation between sample morphology and crystallite shape and size. The results highlight the potential of the combined CXDI–WAXD approach as an upcoming imaging modality for 3D nanoscale studies of shales and other geological formations via serial measurements of microscopic fragments.

1. Introduction

Shales, the most abundant sedimentary rocks in the Earth's crust, are typically made up of clay microparticles and silt-size mineral grains. Characterized by extremely low permeability in the range of tens of nanodarcys (10^{-21} m^2), shales act as sealing caprock for oil and gas reservoirs over geological times (Neuzil, 2019; Vialle *et al.*, 2019). As such, shales are utilized in carbon capture and storage (CCS) (Bourg, 2015), groundwater remediation (Ingebritsen *et al.*, 2006) and storage of nuclear waste (Neuzil, 2013). As pointed out by Bourg (2015), these technologies which rely on shales can potentially contribute up to 70% of the global CO_2 reduction efforts required to limit atmospheric CO_2 in coming decades (Pacala & Socolow, 2004). The characterization of morphology and the porous structure of shales is a challenging task because of the inherent structural heterogeneity and complex mineralogy (Ma, Fauchille *et al.*, 2017). Although studied for many years, the structure–property relationship for shales remains elusive (Bourg, 2015; Dayal, 2017; Leu *et al.*, 2016; Schultz *et al.*, 1980), which poses serious engineering problems, *e.g.* for their use as a source rock or as a low-permeability barrier material.

The physical properties of shales are dependent on the grain size, mineralogy, porosity and permeability. Knowledge of the internal structure is essential to the understanding of fluid transport and storage mechanisms in shales. The presence of hydrocarbons in the subsurface is a direct consequence of the low permeability of shales over the reservoirs,
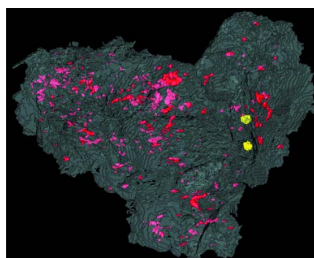
trapping the hydrocarbons there despite the buoyancy forces tending to make them migrate to shallower layers. The low permeability of shales is sought after for containment of CO_2 (Vialle *et al.*, 2019) or nuclear waste sequestration (Neuzil, 2013). However, many shales have a total porosity above 30%, comparable to permeable sandstones (Horsrud, 2001). It follows that pore connectivity and pore-size distribution are important for the macroscopic permeability properties. The transport properties must therefore be determined by considering the pore structure at the smallest scale, in the clay-rich areas where nanometre-scale pores are present (Chen *et al.*, 2013; Javadpour, 2009). Investigating shales at the shortest scale is likely to be an important step towards improving predictive models but it is expensive to obtain correctly preserved core samples from shale layers. However, the drilling process produces rock fragments called cuttings, which need to be evacuated from the well and therefore can provide valuable information on the various geological layers (Bradbury *et al.*, 2007). Recently, the interest in using cuttings from drilling campaigns for obtaining geological information has seen a revival (Carugo *et al.*, 2013; Klimova *et al.*, 2019; Stuckman *et al.*, 2019). Some index tests may be performed at the drill site, when the cuttings are 'fresh', meaning that desiccation has not had time to occur and thus induce cracks. These tests may include density and porosity estimations, together with more advanced tests such as continuous wave technology measurements (Nes *et al.*, 1998) to estimate the compressive strength of the geological formations.

Pores in shales can vary over length scales from nanometres to several micrometres and they are distributed heterogeneously (Leu *et al.*, 2016). Pores have been reported to be present in the vicinity of clay minerals or in contact areas between crystallites of non-clay minerals such as pyrite crystals. The distribution of pores in the shale matrix is related to mineral orientation (Leu *et al.*, 2016; Zhao *et al.*, 2019). The anisotropic pore structure in shales leads to anisotropy in flow and transport properties (Ma *et al.*, 2018). However, the complex structure of shale with respect to the size, orientation and location of the minerals and pores at different length scales makes their precise characterization a challenging task. Multiscale imaging techniques are often used to study and assess shale pore structure (Ma, Fauchille *et al.*, 2017). For example, transmission electron microscopy provides atomic-scale spatial resolution but with a limited field of view of several nanometres, while X-ray micro-computed tomography provides a large field of view (cm) but with a comparatively poor resolution (µm) (Ma *et al.*, 2018).

Coherent X-ray diffraction imaging (CXDI) is an imaging approach based on computationally reconstructing images of the object from far-field (Fraunhofer) diffraction patterns obtained with a highly coherent X-ray beam (Chapman & Nugent, 2010). The key advantage of CXDI is that 3D electron-density maps of the sample can be obtained with a high spatial resolution as good as 5 nm (Chapman & Nugent, 2010; Miao *et al.*, 2015; Sandberg *et al.*, 2013). CXDI does not require a vacuum environment, as is the case in electron microscopy, and hence reduces the challenges with the sample

degradation. Over the past decade, the CXDI technique has matured, and it is currently increasingly applied for solving challenges related to environmental, biological and materials sciences. For example, structural aspects of coccolithophores (Beuvier *et al.*, 2019), polymer microcomposites (Skjønsfjell, Kleiven *et al.*, 2018; Skjønsfjell, Chushkin *et al.*, 2018), vaterite-to-calcite phase transitions in microparticles (Cherkas *et al.*, 2017) and 3D phase distribution in an olivine–iron–sulfur sample (Jiang *et al.*, 2013) have recently been reported. The recent advances in CXDI so far remain unexploited in research on shale or other geological formations. A notable exception is the structural study of sandstones where ptychographic CXDI was utilized (De Boever *et al.*, 2015).

In this article, we demonstrate the use of CXDI to study the internal structure and morphology of shale fragments. To the best of our knowledge, this study is the first application of CXDI for imaging shales. The mineralogy of the crystalline shale microparticles was studied simultaneously using wide-angle X-ray diffraction (WAXD). The combined CXDI–WAXD methodology has been demonstrated recently using single-component materials (Chushkin *et al.*, 2019). We explore the feasibility of the combined CXDI–WAXD approach as a powerful 3D imaging modality for the study of multicomponent samples. The use of CXDI, as discussed in the following, necessitates that the sample sizes are sufficiently small for successful phase retrieval. This limitation presents challenges with respect to the general representativity of the shale samples, but the reported study demonstrates the applicability of the methodology for understanding the finer structures expected to be found in shales, related to clay content and nanoscale features. We propose the combined CXDI–WAXD methodology as a promising approach to study environmentally important geological materials at the smallest scale.

2. Experimental

2.1. Sample

The sample rock used in this study is Pierre Shale I (PS1), extracted from an outcrop in Colorado, USA (Cerasi *et al.*, 2017). The main objective of studying PS1 was to understand its microstructure as part of our ongoing research into its potential as an analogue for typical North Sea caprock for CCS operations (Cerasi *et al.*, 2017). Fragments of PS1 with a size of 2–5 µm were obtained from a core sample by scratching the sample surface with a scalpel. The microparticles were then dispersed on the surface of an X-ray transparent Si_3N_4 membrane (Silson Ltd, 100 nm thickness) under ambient conditions for the CXDI measurements. Isolated particles on the membrane surface were selected using an in-line optical microscope integrated in the beamline. The selected particles (three in total) were positioned in the centre of the coherent beam and measured sequentially.

2.2. CXDI–WAXD measurements

The CXDI–WAXD experiments were performed at the coherent scattering station of the ID10 beamline 'ID10CS' at
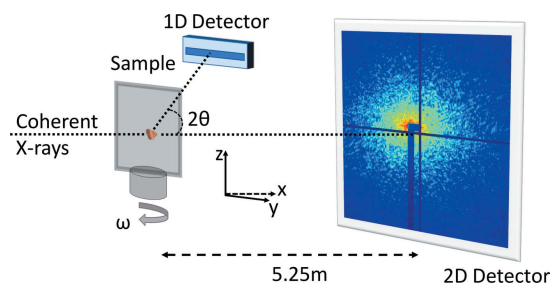
Figure 1
The experimental setup for simultaneous CXDI–WAXD measurements.

the ESRF – The European Synchrotron in Grenoble, France (Chushkin *et al.*, 2014). A monochromatic 8.1 keV (λ = 1.53 Å) collimated ('pencil shaped') X-ray beam from a three-undulator source was used (Skjønsfjell *et al.*, 2016). The coherent primary beam from an Si(111) monochromator was selected to 10 × 10 μm (horizontal × vertical, full width at half-maximum) by rollerblade slits 50 cm upstream of the sample. Two-dimensional scattering patterns were collected using a Maxipix detector (516 × 516 pixels) (Ponchut *et al.*, 2011) with a 55 × 55 μm pixel size placed 5.25 m downstream from the sample. Correspondingly, the voxel size in real-space reconstructions is 26.1 × 26.1 × 26.1 nm. The intense direct beam was blocked by a beamstop which covered the 24 × 24 central pixels, to prevent damage to the detector. A sketch of the experimental setup is shown in Fig. 1. The scattering measurements were carried out at projection angles ω ranging from ∼−80 to 80° in steps of 0.25° with respect to the normal of the membrane surface. At each projection angle, a small-angle scattering pattern was collected on the 2D detector using an exposure time of 2.0 s. The WAXD patterns were acquired simultaneously as outlined in previous work (Chushkin *et al.*, 2019; Wallander & Wallentin, 2017) using a Mython 1K 1D detector. The WAXD detector was placed ∼45 mm behind the sample and offset ∼40 mm from the direct beam trajectory, allowing the small-angle scattered X-rays to propagate undisturbed to the Maxipix 2D detector. The Mython 1D detector has an active area of 50 μm × 8 mm divided into 1028 channels. The detector covered an angular range of 15–61° in 2θ. For analyses of the WAXD data, the background was subtracted and the channel number was converted to scattering angle 2θ using the known Bragg peak positions of a calibration standard Si powder. The angular resolution was 0.067 and 0.016° at 15 and 61° 2θ angles, respectively. During the tomographic ω scan, the membrane shadowed the diffracted beam near orientation angles of $\omega = 2\theta - 90°$, creating a blind range ('missing wedge') of ∼5° in the WAXD data. Powder diffraction data of a bulk PS1 sample were collected at the ID15A beamline at ESRF (wavelength λ = 0.248 Å).

2.3. CXDI reconstruction

In CXDI an isolated microscopic object is illuminated by a plane wave with a transverse coherence length larger than the

object; this results in a speckled diffraction pattern which is recorded by the detector. The recorded far-field diffraction intensity (see Fig. S1 in the supporting information for an example of the diffraction pattern for the studied samples) is proportional to the square of the modulus of the Fourier transform (FT) of the electron density of the scattering object $\rho(\mathbf{r})$, *i.e.* $I(\mathbf{q}) \propto |F(\mathbf{q})|^2$. Here, $F(\mathbf{q}) = |F(\mathbf{q})| \exp[-i\varphi(\mathbf{q})] = \text{FT}[\rho(\mathbf{r})]$, and $\mathbf{q}$ is the scattering vector. Knowledge of the phase, $\varphi(\mathbf{q})$, at the detector plane is necessary for retrieving the real-space image, but the phase information is lost in diffraction experiments because only intensities can be measured. However, for coherent radiation, the phase of the scattered field can be reconstructed using iterative numerical algorithms relying on appropriate constraints (Miao *et al.*, 2015, 1999). In reciprocal space, the calculated scattering amplitude is constrained to equal the square root of the measured intensity. In real space, a support defines regions containing nonzero electron density, outside of which the density is forced to be zero. The initial loose support is refined using the shrink-wrap algorithm (Marchesini *et al.*, 2003). This computational phase-retrieval process can be solved by several known algorithms; in this article, the hybrid input–output with error reduction algorithm was used (Chushkin *et al.*, 2014; Fienup, 1982; Miao *et al.*, 2015). The underlying fundamental principle that allows the phase-retrieval algorithm to converge is that the phase of a 2D or 3D object is uniquely coded in coherent diffraction patterns that are sampled at least twice finer than the Nyquist frequency, known as the oversampling criterion (Miao *et al.*, 1999, 2015; Sayre, 1991). In practice, it requires that the detector pixel size p is about three times smaller than the size of speckles in the diffraction pattern. Consequently, to fulfil the oversampling condition, the sample size, s, is given by $s \leq D\lambda/3p$, where D is the sample-to-detector distance and λ is the X-ray photon wavelength. Hence, in our experimental setup (D = 5.25 m, λ = 1.53 Å and p = 55 μm), samples smaller than ∼5 μm fulfil the condition for oversampling by giving speckles in the diffraction pattern that extend over several detector pixels (representative diffraction patterns of the three samples are shown in Fig. S1).

Convergence of the iterative algorithm was reached after ∼1000 iterations, and 20 3D reconstructions were averaged to reduce noise and smooth random high-frequency variations. The spatial resolution of the final images was estimated using the phase-retrieval transfer function (PRTF) (Chapman *et al.*, 2006) shown in Fig. S2. A PRTF value of 0.5 was used as a criterion to estimate the spatial resolution. Accordingly, we found 29.6, 36.3 and 55.2 nm resolutions for samples 1, 2 and 3, respectively. The variation in the resolution is a direct consequence of the variation in the size of the samples. The smaller the sample the weaker the scattered signal (Fig. S1) and hence the poorer the resolution. In our study, sample 1 was the largest and sample 3 was the smallest. The size of the sample also had an impact on the low-frequency density variations (see Fig. 2). In the reconstructed CXDI images, artefacts in the form of over- or underestimation of the electron densities are present. These artefacts can at least partially
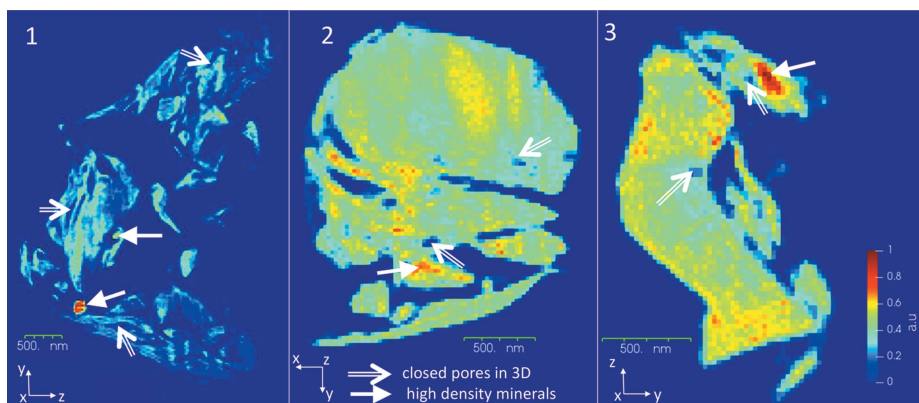
Figure 2
Electron-density cross sections through samples 1–3, highlighting the high-density regions and closed pores. Numerous larger pores connected to the particle exterior are easily seen.

be attributed to the fact that the scattered intensities near the direct beam, corresponding to the lowest spatial frequencies, were not measured in our CXDI experiment (Skjønsfjell, Kleiven *et al.*, 2018; Thibault *et al.*, 2006). We estimated that 10, 4 and 1 central speckles were missing for samples 1, 2 and 3, respectively. The reconstructed images were processed by subtracting background noise and setting all negative density values to zero. Image processing and analyses were carried out using *Tomviz* (Hanwell *et al.*, 2019) and *Avizo* (2018). Representative scanning electron microscopy (SEM) images and corresponding energy-dispersive X-ray spectroscopy (EDS) spectra are shown in Figs. S3 and S4. SEM shows the surface morphology and does not allow characterization of the internal porosity and crystalline phase determination. Hence correlation between CXDI and the SEM images is difficult and comparison with SEM images does not provide additional information. CXDI is a reliable imaging modality and has been demonstrated to be accurate in numerous studies during the past two decades (Chapman & Nugent, 2010; Chushkin *et al.*, 2019).

3. Results and discussion

CXDI allows studying the surface morphology of the samples in addition to their internal porous structure. The 2D electron-density maps of samples 1–3 depicted in Fig. 2 show the high-density regions and closed pores (see the white arrows). The most distinctive feature in sample 1 is the presence of two spheroidal inclusions, both with a diameter of ∼200 nm. The relative electron density corresponding to these inclusions is about twice that of the rest of the sample, consistent with the presence of pyrite (FeS_2) as the inclusion mineral. Similarly, in samples 2 and 3, one can identify high-density regions and pore spaces. Spheroidal pyrite crystals, as in sample 1, were not observed in samples 2 and 3 but the presence of pyrite can be ascertained from the WAXD data discussed later. From Fig. 2 one can also conclude the presence of lower-density

minerals, notably clay minerals and/or organic content in sample 1. Conversely, in samples 2 and 3, the electron-density distribution is rather uniform throughout the entire sample, consistent with the reported presence of quartz, illite, albite or orthoclase. (See Movies S1–S3 in the supporting information.)

Three-dimensional isosurface renderings (see also Movies S1–S3) highlighting the pore structures of all the samples are depicted in Fig. 3. The closed pore volumes are estimated to be 0.31 (5), 0.43 (4) and 0.39 (7) vol.% in samples 1, 2 and 3, respectively. By 'closed pores' we refer to porous structures enclosed within the 3D structure and thus not connected to the external sample surface. The spatial distribution of the closed pores is non-uniform, as the pores are observed to be localized to certain regions of the sample and they do not display a connected pore network (Fig. 3). The characteristic diameter of the observed closed pores, as estimated from the 3D CXDI data sets, varied from 50 to 200 nm.

In shales the presence of closed pores has been observed in the vicinity of high-density minerals like pyrite, as seen in sample 2, or within the clay matrix, as in sample 1 (*cf*. Fig. 2) (Ma, Fauchille *et al.*, 2017). The pore structure observed here can be classified as the inter-mineral pores that appear at the grain boundaries between mineral phases and/or intra-mineral pores, which are present in agglomerates of minerals such as pyrite and dolomite (Ma *et al.*, 2016, 2018). However, it is difficult to classify the pore structure conclusively owing to challenges in preparing the small and brittle samples, the inherent inability of CXDI imaging to distinguish between different mineral phases of similar density, and insufficient resolution of the data sets.

In order to estimate the mineralogy of the PS1 sample, a Rietveld refinement (Rietveld, 1969) of the powder diffraction pattern from bulk samples was carried out using the *GSAS-II* software package (Toby & Von Dreele, 2013). The corresponding refinement plot is given in Fig. S5. As seen from Fig. S5, several Bragg peaks overlap, giving a considerable uncertainty in the concentration estimate for the low-
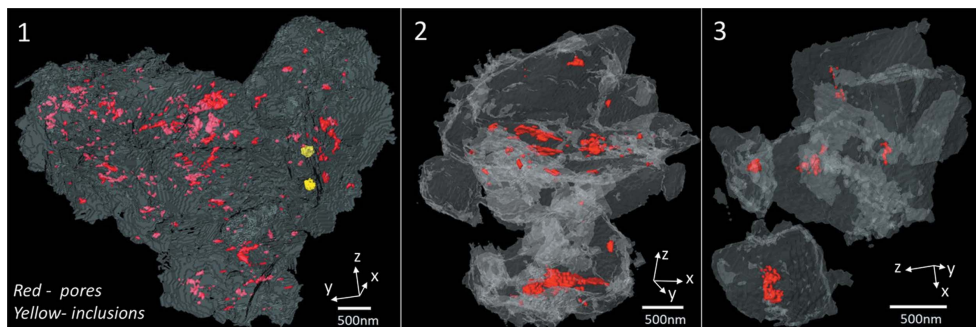
Figure 3
3D iso-surface renderings of samples 1–3 with the high-density inclusions (only visible in sample 1) and 3D closed pores shown.

concentration minerals. The quantitative phase analyses revealed that the most dominant mineral present in the sample is quartz, along with clays and feldspar, which is consistent with previous reports (Kuila & Prasad, 2013; Schultz *et al.*, 1980). The clay minerals can be identified as illite, kaolinite, clinochlore and montmorillonite, while the feldspar group is represented by albite and orthoclase. Minor amounts of pyrite and dolomite were also identified.

The simultaneously recorded WAXD measurements provide valuable insights into the minerals present in the microparticles studied here. Figs. 4(*a*)–4(*c*) show polar diffraction maps with the diffracted intensity plotted as a function of the 2θ angle (radius) and the sample rotation angle ω (azimuth). Figs. 4(*d*)–4(*f*) depict the corresponding 1D diffraction profiles obtained by averaging over ω. Indexing of the Bragg peaks was carried out using these 1D diffraction profiles. The presence of the quartz 100 diffraction ring is apparent in samples 1 and 2, as seen in Figs. 4(*a*) and 4(*b*). In sample 1, a coincidentally in-plane wide orientation (with respect to the Si_3N_4 membrane) of the (100) plane of quartz is observed, whereas in sample 2 the corresponding orientation is uniform but grainier. Other peaks in the diffraction patterns can be attributed to the clay or feldspar minerals present in the shale structure. The 111 peak of pyrite can be indexed in all three diffractograms, confirming the presence of pyrite in PS1. Although present in trace amounts, the pyrite contained in the samples can be distinguished by its characteristic spheroidal geometry (Er *et al.*, 2016; Scott *et al.*, 2009), as seen in Figs. 2 and 3. The presence of pyrite in the form of clusters of small crystallites has been reported in other shale specimens using electron microscopy (Ma, Fauchille *et al.*, 2017; Rodriguez *et al.*, 2014). Figs. 4(*g*)–4(*i*) show the corresponding 3D iso-surface renderings of the three samples (see Movies S1–S3).

Distinct relations between the sample morphology and the 1D diffraction patterns were observed. Sample 1 is composed of numerous small crystallites with sizes less than 1 μm and this is manifested in the 1D diffraction pattern as broad peaks. The broad 100 quartz peak implies the presence of small quartz crystallites of size ∼11 nm (as estimated using the Scherrer formula, Fig. S7) in both samples 1 and 2. The

absence of the characteristic quartz 100 diffraction peak in sample 3 can be attributed to either (i) the absence of quartz in the sample or (ii) the presence of only one or a few quartz crystallites oriented such that no diffraction peaks were recorded. In samples 2 and 3, the Bragg peaks corresponding to other mineral phases are sharper owing to the presence of larger crystallites. In sample 3, large crystallites with sharp facets are evident in the CXDI reconstruction [*cf.* Fig. 4(*i*)].

The complementary information obtained from the 3D CXDI images and the corresponding WAXD data could be utilized to study phase information in multiphase objects, and crystal shape and orientation information. With the current experimental setup, only a limited quantitative analysis of the WAXD data could be carried out as the 1D detector covers only a small solid angle. Moreover, the step size of 0.25° in the scanned projection angle ω is large compared with the intrinsic width of the crystallite Bragg peaks. Future experimental setups will be improved to facilitate correlation between the 3D CXDI images and shape/orientation information of the constituent crystallites.

The size of the sample in this combined CXDI–WAXD approach is dictated by the oversampling condition that must be satisfied for the phase-retrieval algorithm to converge. Larger samples will give smaller speckles, covering fewer detector pixels (see Fig. S1). Oversampling can be improved by increasing the sample-to-detector distance, but the spatial resolution of the reconstruction will then degrade owing to the reduced numerical aperture (finite detector size). The achievable resolution is thus dependent on the sample-to-detector distance. The recently finished upgrade of the ESRF (extremely brilliant source, EBS) (ESRFnews, 2017), together with new large-array pixelated 2D detectors, is expected to improve these aspects by providing a higher resolution in three dimensions (<5 nm), a larger field of view (10–15 μm) and the possibility of time-resolved studies.

It is instructive to compare CXDI with X-ray phase nano-computed tomography (nanoCT), which also relies on a highly coherent X-ray beam and offers higher sensitivity than conventional X-ray computed tomography (Cloetens *et al.*, 1999; Mokso *et al.*, 2007). While CXDI as described is based on reconstructing a real-space image from Fraunhofer diffraction

patterns, phase nanoCT relies on propagation-based phase contrast in the Fresnel regime (Cloetens *et al.*, 1999). For the latter technique, one or more raw images at different focus-to-sample distances are analysed to numerically retrieve one optimal image through the Paganin method (Paganin *et al.*, 2002). NanoCT enables imaging of larger samples of ∼100 µm, albeit with a lower resolution of ∼50–100 nm, as dictated by the depth-of-field limitation (Tsai *et al.*, 2016), and arguably with quantitatively less accurate phase contrast as Paganin's approach is based on homogeneous single-component samples (Häggmark *et al.*, 2017; Hehn *et al.*, 2018). For 3D CXDI, the depth of field is not a concern, because the resolution is governed by the maximum scattering angle. For samples with high angles of scattering, the size of the detector limits the maximum scattering angle and hence the resolution. Moreover, in CXDI sample vibration does not affect the resolution as the probe is a plane wave. In contrast to nanoCT, CXDI is more suited for high-resolution imaging of small (<6 µm)

samples where the sample size is limited by the available sample-to-detector distance.

Another concern is to what extent the samples are representative of the larger core sample or, ultimately, of the entire geological formation. This question includes the arbitrariness in the sample preparation and selection. Clearly, sample preparation by focused-ion-beam milling (Trtik *et al.*, 2013) should be attempted to achieve well defined sample geometries at selected regions of interest. The upcoming larger field of view (ESRFNews, 2017) will also reduce the current ambiguities relating to whether the extracted micrometre-scale samples are in fact grains that are comparatively hard with respect to the surrounding matrix, and also whether the pores observed here as 'open' are in fact part of larger 'closed' pores that represent a weak zone through the material.

With the mentioned upcoming experimental improvements relating to the EBS source, we envision a measurement scheme where a large number of rock fragments (say, 10^1–10^4)
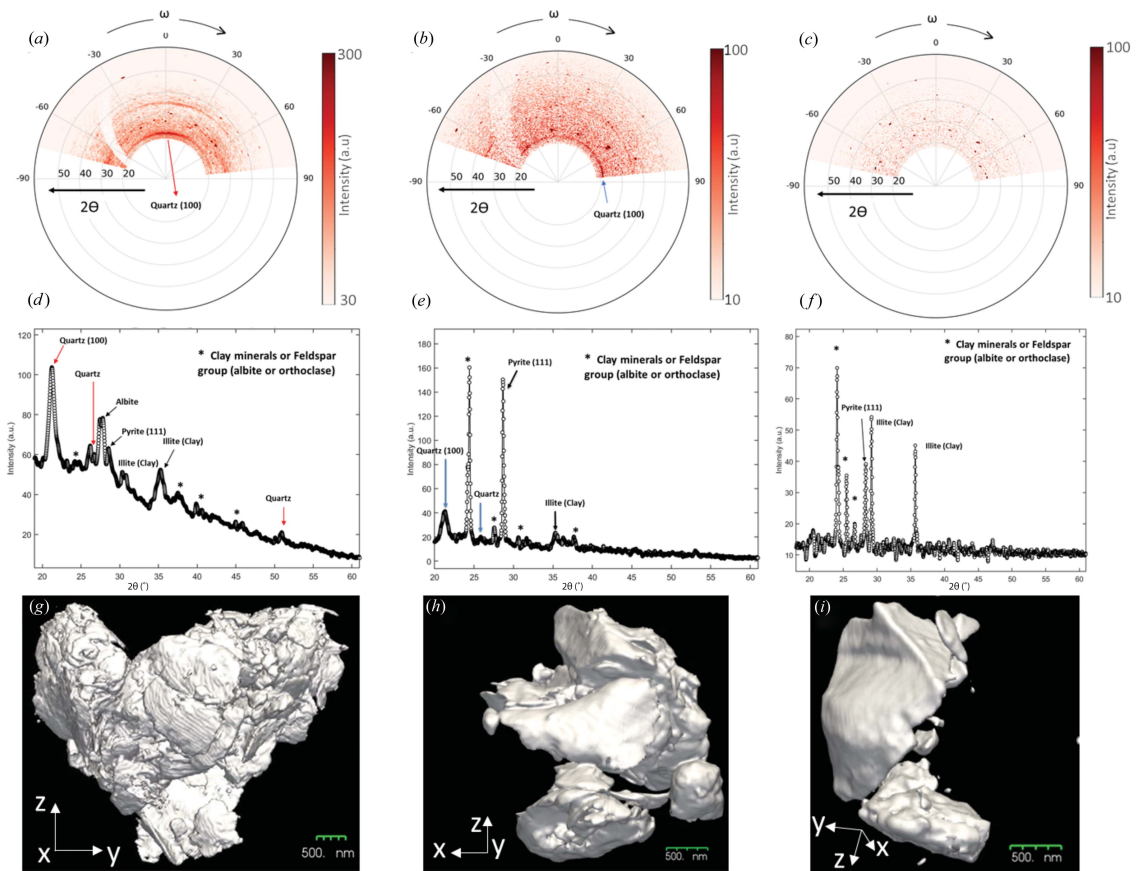
Figure 4
(*a*)–(*c*) Polar maps of diffraction data with the diffracted intensity plotted as a function of the 2θ angle (radius) and the sample rotation angle ω for samples 1, 2 and 3, respectively. (*d*)–(*f*) Corresponding 1D diffraction data obtained by integrating over ω. (*g*)–(*i*) 3D iso-surface renderings of the CXDI reconstruction for samples 1, 2 and 3, respectively.

are sequentially imaged by CXDI in a fully automated fashion along with precise corresponding WAXD measurements. With this approach, the different advantages of CXDI and X-ray diffraction microscopy (Mürer *et al.*, 2018; Poulsen, 2012) will work together, giving high-resolution imaging with mineral specificity besides providing information about crystal orientation and interlayer spacing. With these considerations in mind, we advocate the combined CXDI–WAXD approach as a promising imaging modality for the nanoscale study of shales and other complex geological structures.

4. Conclusions

In this article, we have demonstrated the combined use of CXDI and WAXD to study the morphology, internal structure and mineralogy of Pierre Shale I. It was possible to directly localize pyrite nanocrystals as inclusions in the quartz–clay matrix. The volume percentage of closed pores was estimated to be in the range of 0.3–0.4%, which corroborates the reported porosity data for shales (Ma, Taylor *et al.*, 2017). The combined CXDI–WAXD analysis enabled us to establish a correlation between sample morphology and crystallite shape and size. The methodology proposed here opens possibilities for quantitative geological and petrophysical analyses on small samples such as drill cuttings, removing the need for large cores which are seldom taken from caprock shales.

The experimental and the reconstructed data for samples 1–3 are available freely through the UNINETT Sigma2 repository – https://doi.org/10.11582/2019.00044.

References

Avizo (2018). *Avizo 9*, https://www.fei.com/software/amira-avizo/.
Beuvier, T., Probert, I., Beaufort, L., Suchéras-Marx, B., Chushkin, Y., Zontone, F. & Gibaud, A. (2019). *Nat. Commun.* **10**, 751.
Bourg, I. C. (2015). *Environ. Sci. Technol. Lett.* **2**, 255–259.
Bradbury, K. K., Barton, D. C., Solum, J. G., Draper, S. D. & Evans, J. P. (2007). *Geosphere*, **3**, 299–318.
Carugo, C., Malossi, A., Balossino, P., Galimberti, R., Gioacchini, L., Rivolta, F., Previde Massara, E. & Pingitore, F. (2013). International Petroleum Technology Conference, 26–28 March 2013, Bejing, China. https://doi.org/10.2523/IPTC-17186-MS.
Cerasi, P., Lund, E., Kleiven, M. L., Stroisz, A., Pradhan, S., Kjøller, C., Frykman, P. & Fjaer, E. (2017). *Energy Proc.* **114**, 3096–3112.
Chapman, H. N., Barty, A., Marchesini, S., Noy, A., Hau-Riege, S. P., Cui, C., Howells, M. R., Rosen, R., He, H., Spence, J. C. H., Weierstall, U., Beetz, T., Jacobsen, C. & Shapiro, D. (2006). *J. Opt. Soc. Am. A*, **23**, 1179.
Chapman, H. N. & Nugent, K. A. (2010). *Nat. Photon.* **4**, 833–839.
Chen, C., Hu, D., Westacott, D. & Loveless, D. (2013). *Geochem. Geophys. Geosyst.* **14**, 4066–4075.
Cherkas, O., Beuvier, T., Breiby, D. W., Chushkin, Y., Zontone, F. & Gibaud, A. (2017). *Cryst. Growth Des.* **17**, 4183–4188.
Chushkin, Y., Zontone, F., Cherkas, O. & Gibaud, A. (2019). *J. Appl. Cryst.* **52**, 571–578.
Chushkin, Y., Zontone, F., Lima, E., De Caro, L., Guardia, P., Manna, L. & Giannini, C. (2014). *J. Synchrotron Rad.* **21**, 594–599.
Cloetens, P., Ludwig, W., Baruchel, J., Van Dyck, D., Van Landuyt, J., Guigay, J. P. & Schlenker, M. (1999). *Appl. Phys. Lett.* **75**, 2912–2914.
Dayal, A. M. (2017). *Shale Gas: Exploration and Environmental and Economic Impacts*, ch. 1. New York: Elsevier Inc.
De Boever, W., Diaz, A., Derluyn, H., De Kock, T., Van Stappen, J., Dewanckele, J., Bultreys, T., Boone, M., De Schryver, T., Skjønsfjell, E. T. B., Holler, M., Breiby, D. W. & Cnudde, V. (2015). *Appl. Clay Sci.* **118**, 258–264.
Er, C., Li, Y., Zhao, J., Wang, R., Bai, Z. & Han, Q. (2016). *J. Nat. Gas Geosci.* **1**, 435–444.
ESRFnews (2017). No. 77, December 2017, http://cdn.pagelizard.co.uk/Datastore/iop/ESRFnews/mags/1712.pdf.
Fienup, J. R. (1982). *Appl. Opt.* **21**, 2758.
Häggmark, I., Vågberg, W., Hertz, H. M. & Burvall, A. (2017). *Opt. Express*, **25**, 33543.
Hanwell, M. D., Harris, C. J., Genova, A., Schwartz, J., Jiang, Y. & Hovden, R. (2019). *Microsc. Microanal.* **25**, 408–409.
Hehn, L., Morgan, K., Bidola, P., Noichl, W., Gradl, R., Dierolf, M., Noël, P. B. & Pfeiffer, F. (2018). *APL Bioeng.* **2**, 016105.
Horsrud, P. (2001). *SPE Drilling Completion*, **16**, 68–73.
Ingebritsen, S. E., Sanford, W. E. & Neuzil, C. E. (2006). *Groundwater in Geologic Processes*, 2nd ed. Cambridge University Press.
Javadpour, F. (2009). *J. Can. Pet. Technol.* **48**, 16–21.
Jiang, H., Xu, R., Chen, C. C., Yang, W., Fan, J., Tao, X., Song, C., Kohmura, Y., Xiao, T., Wang, Y., Fei, Y., Ishikawa, T., Mao, W. L. & Miao, J. (2013). *Phys. Rev. Lett.* **110**, 205501.
Klimova, A. A., Azarova, S. V., Yazikov, E. G. & Matveenko, A. (2019). *IOP Conf. Ser. Earth Environ. Sci.* **272**, 022004.
Kuila, U. & Prasad, M. (2013). *Geophys. Prospect.* **61**, 341–362.
Leu, L., Georgiadis, A., Blunt, M. J., Busch, A., Bertier, P., Schweinar, K., Liebi, M., Menzel, A. & Ott, H. (2016). *Energy Fuels*, **30**, 10282–10297.
Ma, L., Fauchille, A. L., Dowey, P. J., Pilz, F. F., Courtois, L., Taylor, K. G. & Lee, P. D. (2017). *Geomechanical and Petrophysical Properties of Mudrocks*, edited by E. H. Rutter, J. Mecklenburgh & K. Taylor, Vol. 454, pp. 175–199. Geological Society of London.
Ma, L., Slater, T., Dowey, P. J., Yue, S., Rutter, E. H., Taylor, K. G. & Lee, P. D. (2018). *Sci. Rep.* **8**, 11683.
Ma, L., Taylor, K. G., Dowey, P. J., Courtois, L., Gholinia, A. & Lee, P. D. (2017). *Int. J. Coal Geol.* **180**, 100–112.
Ma, L., Taylor, K. G., Lee, P. D., Dobson, K. J., Dowey, P. J. & Courtois, L. (2016). *Mar. Petrol. Geol.* **72**, 193–205.
Marchesini, S., He, H., Chapman, N., Hau-Riege, P., Noy, A., Howells, R., Weierstall, U. & Spence, J. C. H. (2003). *Phys. Rev. B*, **68**, 140101.
Miao, J., Charalambous, P., Kirz, J. & Sayre, D. (1999). *Nature*, **400**, 342–344.
Miao, J., Ishikawa, T., Robinson, I. K. & Murnane, M. M. (2015). *Science*, **348**, 530–535.
Mokso, R., Cloetens, P., Maire, E., Ludwig, W. & Buffière, J. (2007). *Appl. Phys. Lett.* **90**, 144104.
Mürer, F. K., Sanchez, S., Álvarez-Murga, M., Di Michiel, M., Pfeiffer, F., Bech, M. & Breiby, D. W. (2018). *Sci. Rep.* **8**, 10052.

Nes, O. M., Horsrud, P., Sønstebø, E. F., Holt, R. M., Ese, A. M., Økland, D. & Kjørholt, H. (1998). *SPE Reservoir Eval. Eng.* **1**, 282–287.

Neuzil, C. E. (2013). *Eos Trans. AGU*, **94**, 261–262.

Neuzil, C. E. (2019). *Annu. Rev. Earth Planet. Sci.* **47**, 247–273.

Pacala, S. & Socolow, R. (2004). *Science*, **305**, 968–972.

Paganin, D., Mayo, S. C., Gureyev, T. E., Miller, P. R. & Wilkins, S. W. (2002). *J. Microsc.* **206**, 33–40.

Ponchut, C., Rigal, J. M., Clément, J., Papillon, E., Homs, A. & Petitdemange, S. (2011). *J. Instrum.* **6**, C01069.

Poulsen, H. F. (2012). *J. Appl. Cryst.* **45**, 1084–1097.

Rietveld, H. M. (1969). *J. Appl. Cryst.* **2**, 65–71.

Rodriguez, R., Crandall, D., Song, X., Verba, C. & Soeder, D. (2014). NETL-TRS-6-2014, 40, NETL Technical Report Series, US Department of Energy, National Energy Technology Laboratory, Morgantown, West Virginia, USA.

Sandberg, R. L., Huang, Z., Xu, R., Rodriguez, J. A. & Miao, J. (2013). *JOM*, **65**, 1208–1220.

Sayre, D. (1991). *Direct Methods of Solving Crystal Structures*, edited by H. Schenk, NATO ASI Series, Vol. 274, pp. 353–356. Boston: Springer.

Schultz, L. G., Tourtelot, H. A., Gill, J. R. & Boerngen, J. G. (1980). Geological Survey Professional Paper 1064-B, p. 114, https://pubs.usgs.gov/pp/1064b/report.pdf.

Scott, R. J., Meffre, S., Woodhead, J., Gilbert, S. E., Berry, R. F. & Emsbo, P. (2009). *Econ. Geol.* **104**, 1143–1168.

Skjønsfjell, E. T. B., Chushkin, Y., Zontone, F. & Breiby, D. W. (2018). *J. Synchrotron Rad.* **25**, 1162–1171.

Skjønsfjell, E. T. B., Chushkin, Y., Zontone, F., Patil, N., Gibaud, A. & Breiby, D. W. (2016). *Opt. Express*, **24**, 10710.

Skjønsfjell, E. T. B., Kleiven, D., Patil, N., Chushkin, Y., Zontone, F., Gibaud, A. & Breiby, D. W. (2018). *J. Opt. Soc. Am. A*, **35**, A7.

Stuckman, M. Y., Lopano, C. L., Berry, S. M. & Hakala, J. A. (2019). *J. Nat. Gas Sci. Eng.* **68**, 102922.

Thibault, P., Elser, V., Jacobsen, C., Shapiro, D. & Sayre, D. (2006). *Acta Cryst.* A**62**, 248–261.

Toby, B. H. & Von Dreele, R. B. (2013). *J. Appl. Cryst.* **46**, 544–549.

Trtik, P., Diaz, A., Guizar-Sicairos, M., Menzel, A. & Bunk, O. (2013). *Cem. Concr. Compos.* **36**, 71–77.

Tsai, E. H. R., Usov, I., Diaz, A., Menzel, A. & Guizar-Sicairos, M. (2016). *Opt. Express*, **24**, 29089.

Vialle, S., Ajo-Franklin, J. & Carey, J. W. (2019). Editors. *Geological Carbon Storage: Subsurface Seals and Caprock Integrity*, 1st ed. New York: John Wiley & Sons.

Wallander, H. & Wallentin, J. (2017). *J. Synchrotron Rad.* **24**, 925–933.

Zhao, Y., Peng, L., Liu, S., Cao, B., Sun, Y. & Hou, B. (2019). *Mar. Petrol. Geol.* **102**, 116–125.

Supporting information for article:

Nanoscale imaging of shale fragments with coherent X-ray diffraction

Basab Chattopadhyay, Aldritt S. Madathiparambil, Fredrik K. Mürer, Pierre Cerasi, Yuriy Chushkin, Federico Zontone, Alain Gibaud and Dag W. Breiby
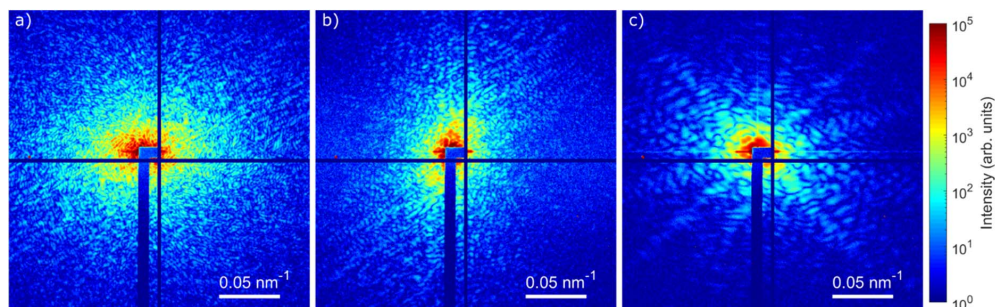
Figure S1 Representative far-field diffraction patterns for : (a) sample 1 corresponding to sample size of ~5μm, (b) sample 2 with size of ~3μm and (c) sample 3 with a size of ~2μm. Sample 1 has the strongest scattering signal and smallest speckle size while in sample 3 the scattered signal is weak and the speckle sizes are biggest.
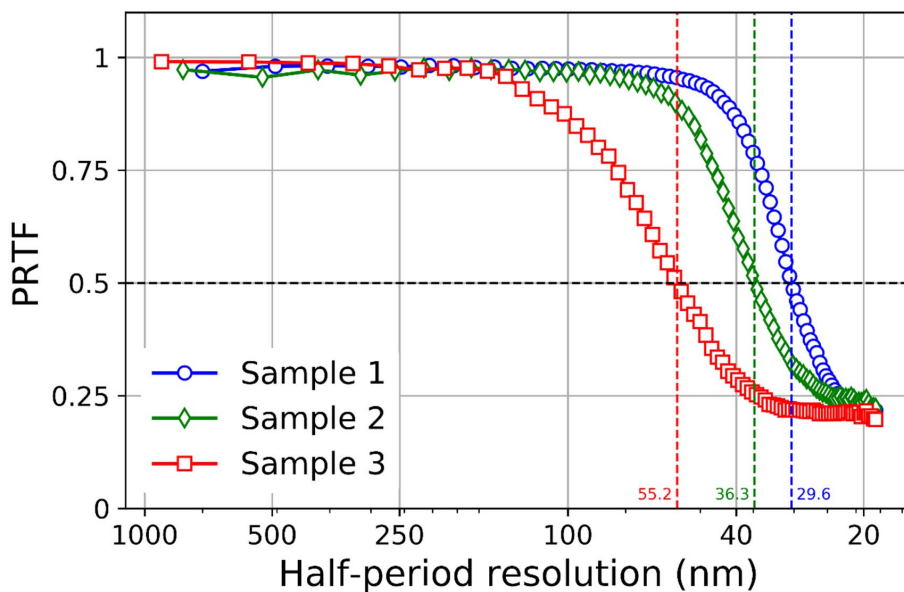
Figure S2 PRTF evaluated from the iterative phase retrieval process for samples 1-3. The positions used to estimate the spatial resolution are shown with dotted lines.
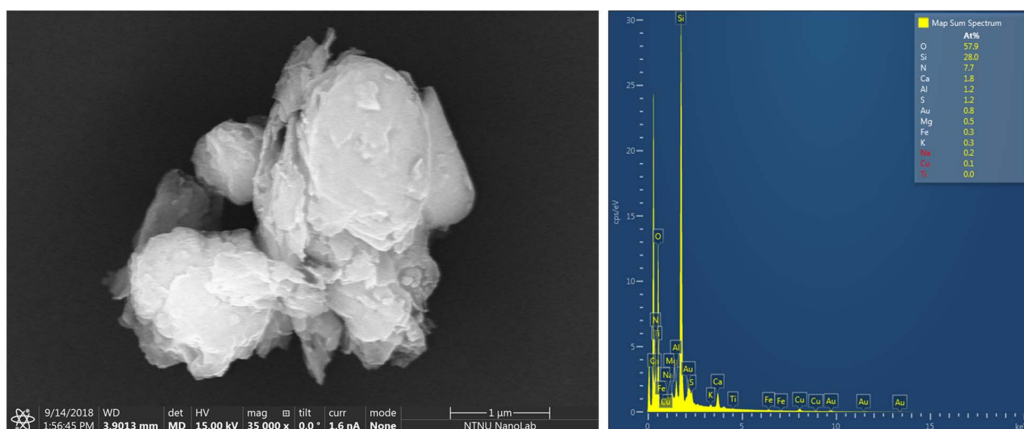
Figure S3 SEM image and the corresponding EDS spectrum for a ~4μm shale fragment.
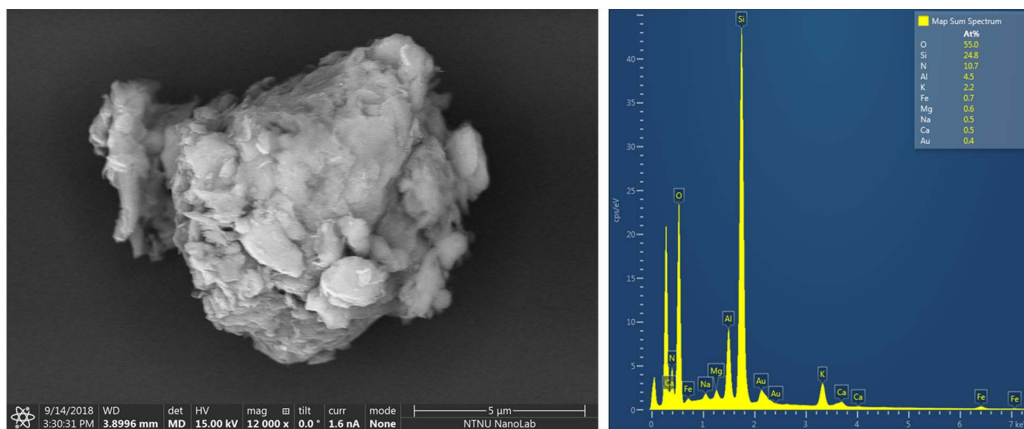
Figure S4 SEM image and the corresponding EDS spectrum for a ~10μm shale fragment.
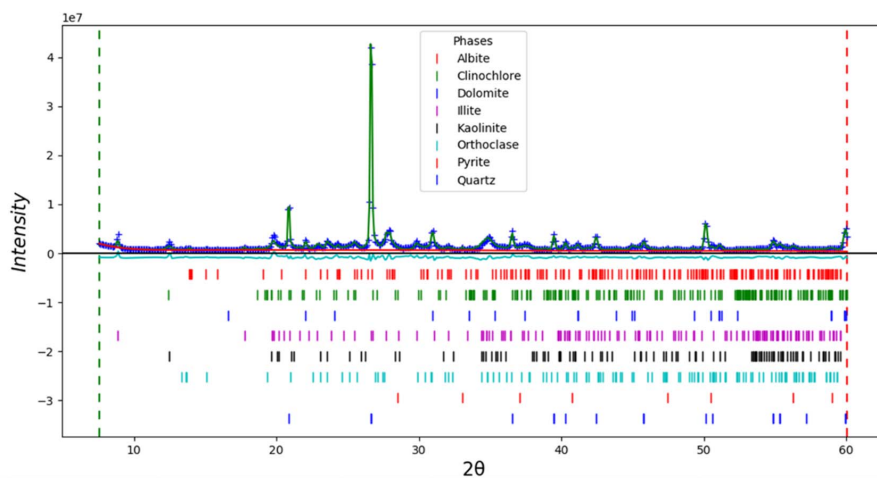
Mineral class	Mineral	Wt %	Chemical Formula	Mass Density (g/cm³)
	Quartz	34(1)	SiO_2	2.65
Clay	Illite	30(1)	$K\,Al_4Si_2O_{12}$	2.78
	Kaolinite	5(1)	$Al_2Si_2O_9H_4$	2.59
	Montmorillonite	Traces	$Al_2\,Si_4\,O_{12}\,Ca_{.5}$	1.80
	Clinochlore	6 (1)	$Mg_{4.5}\,Fe_{0.5}Al_{1.84}\,Si_{3.16}\,O_{18}H_8$	2.71
Feldspar	Albite	12(1)	$NaAlSi_3O_8$	2.62
	Orthoclase	7(1)	$KAlSi_3O_8$	2.56
Carbonate	Dolomite	5(1)	$CaMgC_2O_6$	2.84
	Pyrite	1(1)	FeS_2	5.01

Figure S5 Rietveld refinement plot (top) and the corresponding phase analyses for a bulk sample of PS1. The powder diffraction data was collected at the ESRF ID15A beamline.
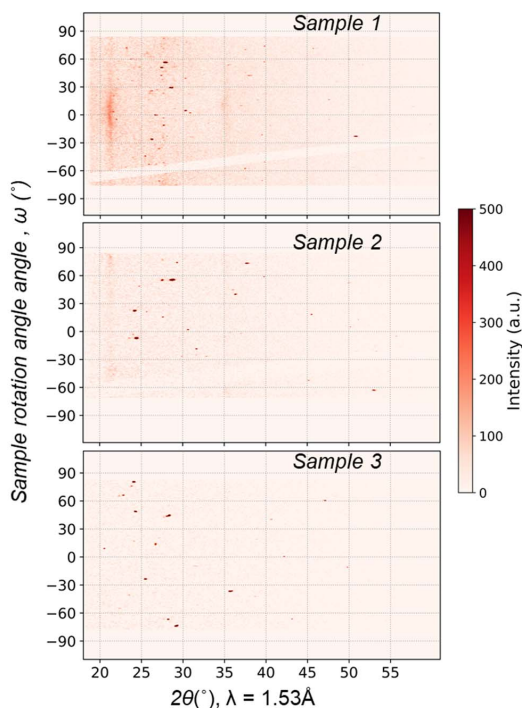
Figure S6 WAXD datasets for samples 1-3 with the sample rotation angle ω (˚) plotted as function of 2θ (˚).
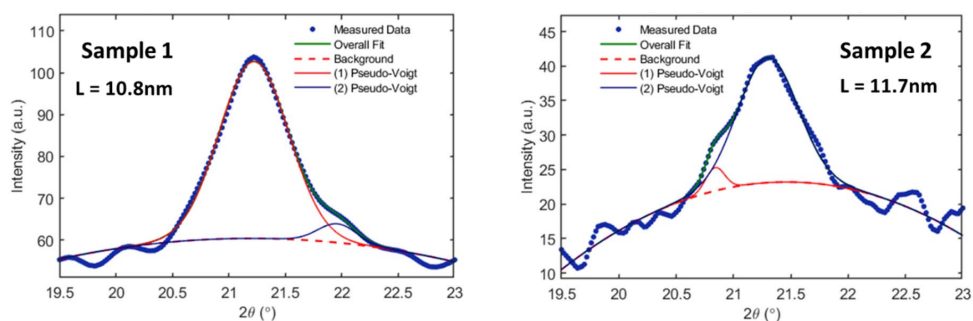
Figure S7 Crystallite size (L) corresponding to the quartz *100* peak at $2\theta \approx 21.19$˚. Fitting of the peak was done in LIPRAS (Web Page: https://github.com/SneakySnail/LIPRAS) using a pseudo-Voigt peak profile. Peak position and FWHM obtained from the fitting were used in the Scherrer formula to estimate the crystal size.

Movie S1-S3 3D isosurface view for samples 1-3 respectively with the high-density regions (pyrite minerals) shown in yellow within the transparent quartz-clay matrix.

Paper 4

IUCrJ

Orientational mapping of minerals in Pierre shale using X-ray diffraction tensor tomography

Fredrik K. Mürer,[a] Aldritt Scaria Madathiparambil,[a] Kim Robert Tekseth,[a] Marco Di Michiel,[b] Pierre Cerasi,[c] Basab Chattopadhyay[a] and Dag W. Breiby[a,d]*

[a]PoreLab, Department of Physics, Norwegian University of Science and Technology, Høgskoleringen 5, Trondheim 7491, Norway, [b]ESRF, The European Synchrotron, 71 Avenue des Martyrs, Grenoble 38000, France, [c]Petroleum Department, SINTEF Industry, Trondheim 7465, Norway, and [d]Department of Microsystems, University of South-Eastern Norway, Campus Vestfold, Borre 3184, Norway. *Correspondence e-mail: dag.breiby@ntnu.no

Shales have a complex mineralogy with structural features spanning several length scales, making them notoriously difficult to fully understand. Conventional attenuation-based X-ray computed tomography (CT) measures density differences, which, owing to the heterogeneity and sub-resolution features in shales, makes reliable interpretation of shale images a challenging task. CT based on X-ray diffraction (XRD-CT), rather than intensity attenuation, is becoming a well established technique for non-destructive 3D imaging, and is especially suited for heterogeneous and hierarchical materials. XRD patterns contain information about the mineral crystal structure, and crucially also crystallite orientation. Here, we report on the use of orientational imaging using XRD-CT to study crystallite-orientation distributions in a sample of Pierre shale. Diffraction-contrast CT data for a shale sample measured with its bedding-plane normal aligned parallel to a single tomographic axis perpendicular to the incoming X-ray beam are discussed, and the spatial density and orientation distribution of clay minerals in the sample are described. Finally, the scattering properties of highly attenuating inclusions in the shale bulk are studied, which are identified to contain pyrite and clinochlore. A path forward is then outlined for systematically improving the structural description of shales.

1. Introduction

The orientation of nano-crystallites affects the macroscopic physical properties in a wide range of hierarchical materials such as bones (Stock, 2015), polymers (Baer *et al.*, 1987) and shales (Leu *et al.*, 2016). X-ray micro-computed tomography (µCT), based on intensity attenuation of the beam as it propagates through the specimen, has, owing to technical advances during the last decade, become a workhorse for studies of complex natural and manmade material structures, both at home laboratories and at synchrotrons. However, despite its successes, µCT has some important limitations. Using µCT, the structural information provided is usually in the micrometre range and it is difficult to distinguish materials of similar electron density, thus limiting the information obtained about the underlying nature of the material. For example, with unresolved nanoscale porosity, the effective attenuation of a volume element in the specimen can take a wide range of values, making the segmentation and subsequent analysis prone to error. While electron microscopies can give superior structural resolution for certain samples, the field of view is vanishingly small, with the associated risk of rendering the analysis of little macroscale relevance. For all these reasons, it is of high importance to develop new methods that can be used at different length scales and inherently contain structural information arising at the nanoscale.

 747
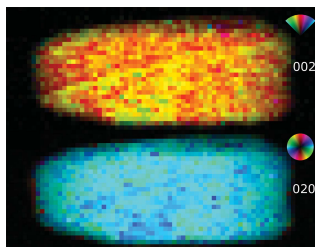
Wide-angle X-ray diffraction (XRD) is a firmly established technique for crystallographic studies, giving conclusive information about the atomic scale arrangements. Owing to recent technical advances, perhaps most notably fast-readout area detectors (Vaughan *et al.*, 2020), various scanning XRD techniques have been developed, including hierarchical orientational mapping (Paris, 2008), whereby the averaged orientation properties of molecular structures at the Ångström length scale are probed over larger length scales ranging from micrometres to several millimetres. For fine-grained isotropic materials, X-ray diffraction computed tomography (XRD-CT) (Harding *et al.*, 1987; Kleuker *et al.*, 1998; Stock *et al.*, 2008; Mürer *et al.*, 2018; Grünewald *et al.*, 2020) currently allows 3D non-destructive determination of material composition, particle size, shape and crystal lattice parameters of millimetre-sized samples with spatial resolution typically in the 10^{-1}–10^2 micrometre range (Birkbak *et al.*, 2015; Palle *et al.*, 2020). Reconstructed diffractograms can be combined with Rietveld refinement (Rietveld, 1969; Frølich *et al.*, 2016) or Williamson–Hall analysis (Williamson & Hall, 1953; Mürer *et al.*, 2021) for accurate determination of material volume fractions, and hence be used to obtain accurate spatially resolved maps of sample composition, crystallite size and strain. XRD-CT normally requires that the specimen materials are fine grained and isotropic, ensuring that the scattering signal from each sample voxel is rotationally invariant (Feldkamp *et al.*, 2009). Qualitative material-distinguishing XRD-CT can still be performed if the materials are only weakly anisotropic by suppressing the orientation information contained in the diffraction patterns during the tomographic reconstruction (Stock *et al.*, 2008; Mürer *et al.*, 2018). Moreover, scattering approximately parallel to the rotation axis is readily seen to be invariant with respect to sample rotation, allowing moderately complex orientation arrangements to be reconstructed (Egan *et al.*, 2013; Gürsoy *et al.*, 2015; Mürer *et al.*, 2018) using *e.g.* the standard filtered backprojection (FBP) algorithm. Small-angle X-ray scattering CT (Schroer *et al.*, 2006; Feldkamp *et al.*, 2009) utilizes similar working principles as XRD-CT and is used to probe larger structural features in the tens of nanometres range.

Whereas XRD has been used for sample-averaged texture measurements for decades, small-angle scattering and X-ray diffraction tensor tomography (SASTT, XRDTT) have been recently introduced (Skjønsfjell *et al.*, 2016; Liebi *et al.*, 2015, 2018) as techniques to retrieve the spatially resolved 3D nanostructure *orientation* distributions across millimetre-sized samples. SASTT and XRDTT utilize a similar experimental setup as XRD-CT, however the sample is rotated about two orthogonal axes during the experiment to allow sufficient sampling of the direction-dependent scattering. Orientation information can also be retrieved with XRDTT by using a single tomography axis if the measured scattering is predominantly in the direction of the tomography axis. A model function based on spherical harmonics (Roe & Krigbaum, 1964) can be used to describe the orientational distribution function for each sample voxel, typically of size $(1–100\ \mu m)^3$, and this model function is fitted to the measured data using *e.g.* a conjugated gradient optimization routine. While traditional pole figure (texture) analysis aims to describe the averaged orientation distribution function valid for a presumably uniform sample (Bunge, 1969; Breiby & Samuelsen, 2003), tensor tomography can reconstruct 3D maps of the variations of the texture in heterogeneous non-uniform samples. SASTT and XRDTT have recently been demonstrated on bone (Liebi *et al.*, 2015, 2018; Guizar-Sicairos *et al.*, 2020; Mürer *et al.*, 2021), polymers (Skjønsfjell *et al.*, 2016) and brain tissue (Gao *et al.*, 2019). While SASTT/XRDTT have facilitated 3D orientational X-ray imaging, the experiments are time consuming because many (typically >10^6) diffraction patterns have to be collected to adequately probe the sample. Previous studies report measurement times of >24 h when the sampled volume is ~50^3 voxels. In addition to being time consuming, the tensor-tomography experiments expose the samples to high radiation doses, potentially causing radiation damage. Therefore, ways of reducing the measurement time and dose in tensor-tomography experiments need to be further investigated.

Shales are fine-grained sedimentary rocks and exist in a variety of types with varying chemical composition (Shaw & Weaver, 1965). Shales contain several clay mineral phases, mixed with silt-sized particles of other minerals, commonly quartz and calcite. The oriented clay phases, consisting typically of flake-shaped grains exhibiting preferred orientations relative to the bedding planes, give rise to anisotropic scattering in both the small- and wide-angle regimes (Wenk *et al.*, 2010). Shales show pronounced fissility, *i.e.* a tendency of splitting along flat planes parallel to the stratification. Shales typically split into thin laminae of a few millimetres thickness, reflecting the parallel orientation of clay mineral flakes. Sandstones, with their simpler composition and high porosity (10–40%), often exhibit a rather uniform pore-size distribution, and are currently considered well understood in terms of both mechanical properties and fluid permeability (Keelan, 1982). Shales, on the other hand, with numerous mineral phases present, combined with nanoscale porosity and pronounced anisotropy, await scientific breakthroughs with improved imaging methods before a better understanding can be reached (Ma *et al.*, 2017).

In this article, we demonstrate XRDTT of a sample of Pierre shale. First, we present the mineral composition and the observed texture in the diffraction patterns, which can be used to infer the orientation of clay minerals. Thereafter, we discuss the 3D orientation of the clay minerals present in the sample volume and demonstrate the feasibility of using XRDTT for retrieving the sample nanostructure orientation by using a tomography setup with a single sample rotation axis. Finally, we study the scattering from comparably large high-density mineral grains in the shale sample.

2. Experimental

2.1. Sample

The Pierre shale sample was extracted from blocks obtained from a Colorado quarry (Cerasi *et al.*, 2017), and further cored

to make cylindrical plugs from which fragments were detached and stored in air at room temperature. The sample was glued onto a pin and mounted on a goniometer head with its bedding-plane normal essentially co-aligned with the tomographic rotation axis.

2.2. XRD-CT

2.2.1. CT measurements. The very same Pierre shale sample was measured using both home-laboratory attenuation-contrast μCT and synchrotron XRD-CT, see Fig. 1 for sketches of the setups and coordinate conventions. Studying the same sample with both modalities allows the diffraction-contrast 3D tomograms to be co-registered and quantitatively compared with the higher-resolution μCT 3D tomogram.

XRD-CT measurements were performed at the beamline ID15A (Vaughan *et al.*, 2020) at the ESRF, Grenoble, France. A partly coherent beam of photon energy 50.00 keV was used ($\lambda = 0.2480$ Å). The beam was collimated into a pencil-shaped beam of dimensions 50×50 μm by using compound refractive lenses and slits. A Dectris Pilatus3 CdTe 2M detector with a pixel size of 172 μm (Vaughan *et al.*, 2020), placed at a calibrated sample–detector distance of 775 mm, was used to collect the scattered radiation with an exposure time of 30 ms. For each projection angle α about the vertical tomographic y axis, the sample was line scanned along x. The scanning direction was reversed between consecutive line scans to reduce motor-movement time. A total number of 71 steps in x and 61 angular steps of α, with $\alpha \in [0°, 180°]$, were used, giving $\Delta\alpha = 3.0°$. The scan procedure was repeated for 29 steps in y to measure the full 3D volume, giving a total of $74 \times 61 \times 29 \simeq 1.6 \times 10^5$ recorded diffraction patterns. The total measurement time was ~2.0 h, including overhead time for motor movements. The diffraction patterns were radially and azimuthally integrated (Ashiotis *et al.*, 2015) into 2048 radial bins and 64 azimuthal bins to reduce the size of the dataset before further analysis and 3D reconstruction. Prior to the reconstructions, the data were filtered to remove outlier intensities (see Section S11 of the supporting information) and corrected for attenuation. XRD-CT sinograms were generated for each Bragg peak by azimuthally averaging the q-integrated

scattering after background subtraction. Attenuation-contrast CT parallel-beam sinograms were generated with the Radon transform from the reconstructed tomograms, as the measured attenuation-contrast CT projection data were obtained in the cone-beam geometry [Fig. 1(*a*)], preventing a direct comparison with the XRD-CT sinograms.

2.2.2. XRDTT reconstruction. XRDTT reconstruction was carried out using the freely available SASTT software developed by the Coherent X-ray Scattering Group at the Swiss Light Source, Paul Scherrer Institute (Liebi *et al.*, 2015). The main features will be summarized in the following. The orientational distribution function in each sample voxel $\mathbf{r}'$, for a given momentum transfer q, was modelled as the absolute square of a spherical harmonic expansion (Liebi *et al.*, 2018):

$$\hat{R}_q(\mathbf{r}') = \left| \sum_{l,m} a_l^m(\mathbf{r}') Y_l^m[\Theta(\mathbf{r}'), \Phi(\mathbf{r}')] \right|^2, \qquad (1)$$

where $a_l^m(\mathbf{r}')$ are coefficients (here with dimensions of the square root of intensity) for the spherical harmonics $Y_l^m[\Theta(\mathbf{r}'), \Phi(\mathbf{r}')]$ of degree l and order m. This model is strongly related to pole figures describing anisotropy, and spherical harmonics are routinely used for texture analysis (Roe & Krigbaum, 1964). For all XRDTT analysis in this article, $m = 0$, *i.e.* the orientation distributions are assumed to be uniaxial. $\Theta(\mathbf{r}')$ and $\Phi(\mathbf{r}')$ denote the polar and azimuthal angles in the spherical harmonics coordinate system at position $\mathbf{r}'$. The sample coordinates $\mathbf{r}'$ are related to the laboratory coordinate system by

$$\mathbf{r}' = R_n^{\exp}\mathbf{r}, \qquad (2)$$

where

$$R_n^{\exp} = \begin{pmatrix} \sin\alpha & \cos\alpha & 0 \\ -\cos\alpha\sin\beta & \sin\alpha\sin\beta & \cos\beta \\ \cos\alpha\cos\beta & -\sin\alpha\cos\beta & \sin\beta \end{pmatrix}. \qquad (3)$$

The angles α and β refers to the sample rotation angles used during tomography and are indicated in Fig. 1(*b*). If only a single tomography axis is used, as for the Pierre shale sample in this work, $\beta = 0$. Notably, the rotation matrix $R_n^{\exp}$ gives the sample z' axis parallel to the laboratory frame y axis for $\alpha = \beta$
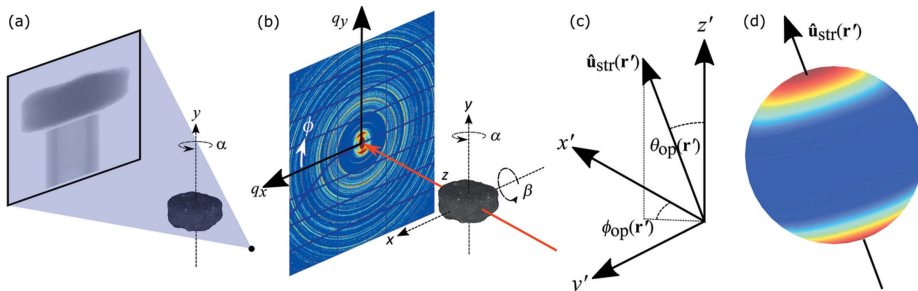

Figure 1
Schematic setups for (*a*) home-laboratory cone-beam attenuation-contrast CT and (*b*) synchrotron parallel-beam XRD-CT. (*c*) A sample coordinate system $\mathbf{r}' = (x', y', z')^{\mathrm{T}}$ defined such that the z' axis is parallel to the laboratory frame y axis. The local preferred orientation for each sample voxel is described by $\hat{\mathbf{u}}_{\mathrm{str}}(\mathbf{r}')$. (*d*) An illustration of a uniaxial scattering intensity distribution for a single sample voxel.

$= 0°$. For each voxel, the parameters $a_0^0(\mathbf{r'})$, $a_2^0(\mathbf{r'})$, $a_4^0(\mathbf{r'})$, $a_6^0(\mathbf{r'})$, $\theta_{op}(\mathbf{r'})$ and $\phi_{op}(\mathbf{r'})$ were fitted using a conjugated gradient method with precalculated analytical expressions for the gradients.

From the reconstructed $a_l^m(\mathbf{r'})$ coefficients, we calculated the uniaxial order parameter, also known as Hermans' orientation parameter $S(\mathbf{r'})$ (Hermans *et al.*, 1946), which gives a measure of the local degree of preferred orientation:

$$S(\mathbf{r'}) = \frac{3}{2}\left[\langle \cos^2\Theta(\mathbf{r'})\rangle - 1\right]. \quad (4)$$

For highly oriented materials, S tends towards one. For isotropic materials, S is zero.

For the clinochlore 002/kaolinite 002 peaks, the reconstructed spatial variation of the local-crystallite-orientation distribution was obtained using XRDTT. To reduce the amount of streak artefacts in the reconstructions, we applied a filter to remove outlier intensities in the azimuthal intensity distributions deviating more than three absolute deviations from the median. Physically, this filtering approach can be considered as suppressing the larger crystallites to better discern the distributions of the quasi-continuous clay matrix. Other groups have recently demonstrated alternative methods for dealing with outlier intensities in diffraction patterns (Vamvakeros *et al.*, 2021).

2.3. Attenuation-contrast CT

Attenuation-contrast μCT of the Pierre shale sample was performed with a home-laboratory cone-beam CT instrument of type Nikon XTH 225, equipped with a PerkinElmer (Waltham, USA) 1620 CN CS detector with 2000 × 2000 pixels. A tungsten reflection target was used with an acceleration voltage of 180 kV. No beam-conditioning filter was used, and 1001 equally angularly spaced projections were obtained with $\alpha \in [0°, 360°]$. The 3D attenuation-coefficient map was reconstructed using the Nikon software *X-TEK CT Pro 3D*, based on the Feldkamp–Davis–Kress algorithm (Feldkamp *et al.*, 1984), giving an isotropic voxel size of 5.0 μm.

3. Results and discussion

3.1. The mineral composition and clay mineral orientation in Pierre shale

Home-laboratory attenuation-contrast μCT of the shale sample is presented in Figs. 2(a) and 2(b). The attenuation was approximately uniform across the whole sample, except for some highly attenuating regions appearing as bright spots in the reconstructed tomograms. Owing to unresolved nanoscale grains and inclusions in the heterogeneous sample, giving strong partial volume effects, these CT data cannot be segmented in a reproducible and meaningful manner. This statement is emphasized by the high-resolution holography cross section presented in Section S3, clearly demonstrating that the typical grain size is much smaller than the chosen XRD-CT voxel size. While it is tempting to claim that the strongly absorbing regions could be electron-rich iron-containing inclusions of pyrite, it is, as we shall demonstrate, perilous to do so without further analysis.

The measured XRD-CT diffraction patterns [Figs. 2(c)–2(f)] consist of (i) quasi-continuous Debye–Scherrer rings originating from the many randomly oriented small-grained polycrystalline minerals, and (ii) numerous interspersed high-intensity Bragg peaks corresponding to larger and/or better-oriented crystallites within the
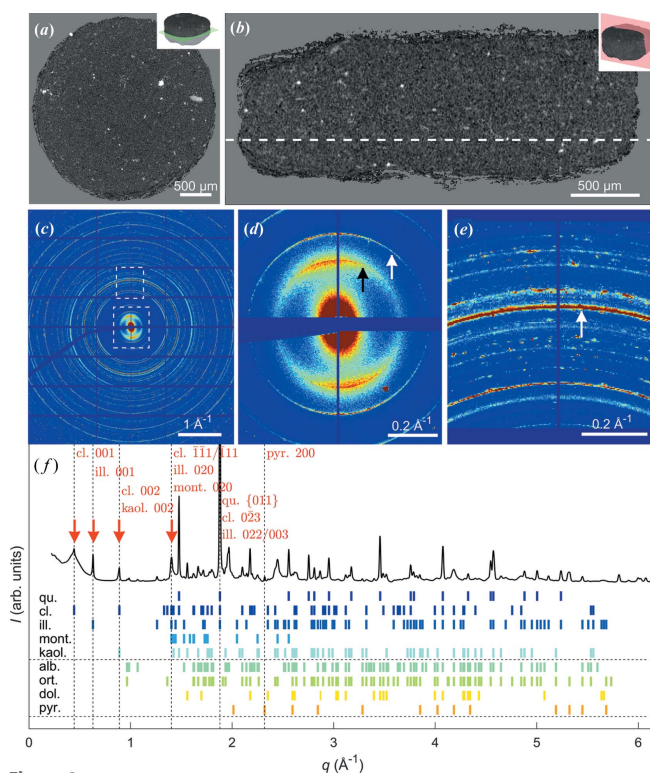

Figure 2
An overview of the Pierre shale sample. (*a*), (*b*) Orthogonal attenuation-contrast CT cross sections. (*c*) A single diffraction pattern obtained from the sample centre with insets shown in (*d*) and (*e*). There is strong texture in the clinochlore 001 and illite 001 peaks, marked with black and white arrows, respectively, in (*d*). The white arrow in (*e*) points to the overlapping Bragg peaks of quartz {011}, clinochlore 0$\bar{2}$3 and illite 022/003. The grid and the missing data are due to detector panel gaps and the beam stop. (*f*) An indexed diffractogram revealing the sample composition. The low-q Bragg peaks marked with red arrows all display pronounced texture. The intense overlapping peaks of quartz {011}, clinochlore 0$\bar{2}$3 and illite 022/003 have been cut in (*f*) for display purposes. Abbreviations: qu., quartz; cl., clinochlore; ill., illite; mont., montmorillonite; kaol., kaolinite; alb., albite; ort., orthoclase; dol., dolomite; and pyr., pyrite.

scattering volume (Wilchinsky, 1951). By averaging all the measured diffraction patterns ($\sim 10^5$) for the sample, a volume-averaged 'master' diffractogram was obtained, which we in a related study (Chattopadhyay *et al.*, 2020) have shown by Rietveld refinement to be consistent with the presence of quartz and illite, with smaller amounts of montmorillonite, kaolinite, clinochlore, albite, orthoclase and pyrite. Indexed peaks based on the volume-averaged diffractogram are shown in Fig. 2(f). A total of 141 Bragg peaks in the measured range $q = 0.22$–6.1 Å^{-1} were identified and compared with tabulated values from the American Mineralogist Crystal Structure Database (http://rruff.geo.arizona.edu/AMS/amcsd.php). Notably, as there were numerous Bragg peaks present giving substantial peak overlap, only clinochlore 001, illite 001, clinochlore 002/kaolinite 002, kaolinite 020/montmorillonite 020, quartz {011} (overlapping with clinochlore and illite) and pyrite {200} were used for further analysis, see Fig. 3.

An example of a single-exposure diffraction pattern obtained with the pencil beam penetrating the sample near its centre is shown in Figs. 2(c)–2(e), where many sharp Debye–Scherrer rings can be observed. Most of the rings are essen-

tially isotropic, with the important exception of the low-q rings originating from the clay phases. The broad clinochlore 001 and illite 001 Bragg peaks exhibit strong texture with dominant scattering in the same direction, understood to originate from the clay crystallites being aligned with the bedding planes (Sander, 1934; Wenk *et al.*, 2010).

As a first step towards quantifying the anisotropic intensity distribution of the clay minerals we used Fourier analysis to retrieve the integrated intensity and dominant scattering direction (Bunk *et al.*, 2009), with selected results presented in Fig. 3. The maps shown are all from the projection with $\alpha = 36°$, yet for different narrow q regions, thus targeting different minerals in the sample. This analysis was carried out without tomographic reconstruction, only quantifying the azimuthal intensity variations (texture) present in the recorded diffraction patterns. The background scattering was subtracted, with the background estimated from averaging the intensity at the peak shoulders, and the intensity was averaged radially (along q) across each Bragg peak. The scattering patterns from the broad clinochlore 001, illite 001, clinochlore 002/kaolinite 002 and kaolinite 020/montmorillonite 020 peaks were found to be
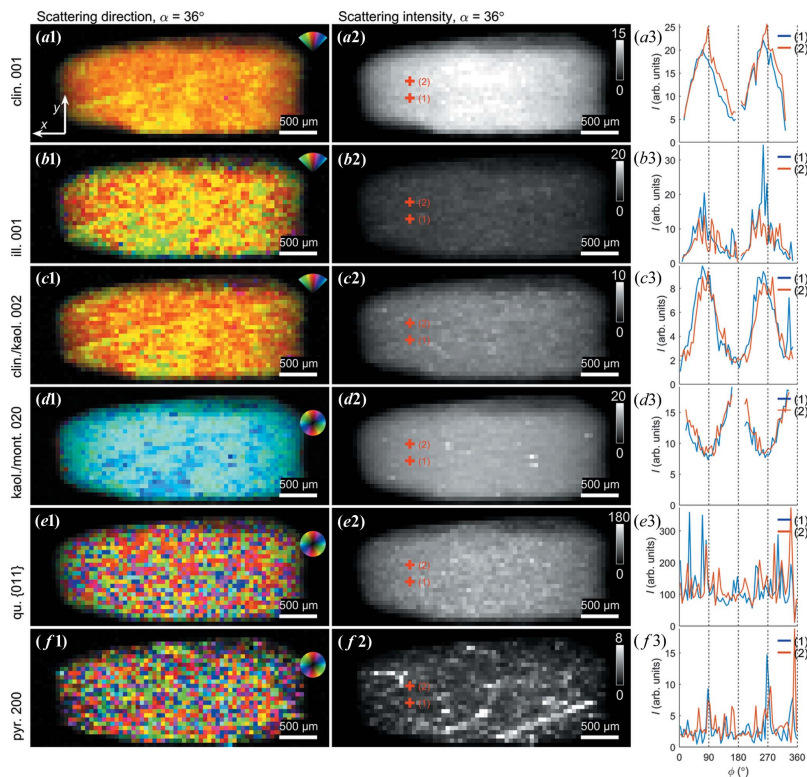

Figure 3
Orientation, intensity and orientation distribution of selected Bragg diffraction peaks, observed for the projection angle $\alpha = 36°$. Note the band-like orientation feature stretching diagonally across the sample. (a1) Dominant scattering direction for the clinochlore 001 Bragg peak, colour coded as shown in the inset. (a2) Azimuthally integrated intensity of the clinochlore Bragg peak. (a3) Azimuthal intensity variations for two points indicated in (a2). (b)–(f) Similarly for the illite 001, clinochlore 002/kaolinite 002, kaolinite 020/montmorillonite 020, quartz {011} (overlapping with clinochlore and illite) and pyrite {200} Bragg peaks, respectively.

highly directional in all sample regions [Figs. 3(a)–3(d)], whereas the scattering from pyrite {200} and quartz {011} was isotropic [Figs. 3(e) and 3(f)]. The azimuthal intensity variations from selected points are shown in the third column. Consistently, the preferred orientation of clinochlore 001, illite 001 and clinochlore 002/kaolinite 002 is seen to be orthogonal to kaolinite 020/montmorillonite 020 [cf. Figs. 3(a1)–3(c1) versus 3(d1)]. The integrated scattering intensity suggests that the clay minerals and quartz were distributed rather evenly across the whole sample volume, as expected from the uniform appearance of the sample, whereas localized regions of pyrite were found. Still, from the spiked azimuthal intensity variations at selected points [e.g. Fig. 3(b3)], it is evident that there were also contributions from larger clay crystallites (see below).

Uniquely for the presented $\alpha = 36°$ projection, a band of variation in the clay signals can be discerned across the sample. This feature stretching diagonally across the sample was observed for the broad peak containing clinochlore 001, illite 001, and clinochlore 002/kaolinite 002 in both preferred orientation and integrated intensity. These slight variations in the scattered intensity could originate from density gradients or be due to large favourably oriented crystallites. The fact that these bands could only be seen for one projection angle suggests that the observed band is in fact a plane across the sample that has a well defined angle with the rotation axis, thus being blurred for all the other projection angles. While tensorially reconstructing the plane proved elusive, the observed plane might be associated with shale fissility.

The clay diffraction signals varied smoothly across the projections with well defined preferred orientation, however the signals from quartz [(Fig. 3(e)] and pyrite [Fig. 3(f)] were qualitatively different. Note that α-quartz (SiO$_2$) is trigonal (space group $P3_221$) and pyrite (FeS$_2$) is simple cubic (space group $Pa\bar{3}$). The many and strong scattering contributions are interpreted to be caused by a combination of heavier elements, larger crystallites, and the Bragg scattering condition being better fulfilled. With the resolution of our experiment, the quartz particles appear to be present across the full sample volume and randomly oriented with abrupt changes in orientation between adjacent exposures, strongly suggesting that these mineral grains are disconnected and of sub-voxel size. The quartz {011} reflections by symmetry have a multiplicity of 12, which must be accounted for if we desire a more quantitative interpretation of the signal. Similar considerations apply to the pyrite {200} signal (multiplicity of six), with randomly oriented grains found across the whole sample. Pyrite tended to be localized to certain regions [Fig. 3(f)] and the intensity distribution suggests a density correlation over longer distances.

3.2. Retrieving the clay mineral orientation by XRDTT

Numerical XRDTT reconstructions, as described in Section 2.2.1, allowed determining the local orientation of the clay crystallites from the measured textured scattering. For XRDTT, multiple tomography axes have previously been used to provide sufficient sampling of the reciprocal space (Liebi et al., 2015, 2018; Schaff et al., 2015). However, it remains debated how much redundancy is needed for faithfully reconstructing preferred orientation distributions in a given sample, a topic that was already raised by Liebi et al. (2018). Intuitively, it appears that for 'well behaved' samples with (i) a global uniaxial orientation and (ii) a broad orientational distribution function associated with each voxel, a single tomographic rotation axis co-linear with the unique axis of the sample is sufficient to reconstruct maps of crystallite preferred orientation. We provide support for this claim using a piglet bone/cartilage sample, measured with multiple tomography axes, by comparing reconstructions based on the full dataset with a single-axis subset, see Section S7. In essence, when the beam energy is high ($E = 50.00$ keV), the Ewald sphere is nearly flat at the Bragg peaks studied here; for clay, $q \simeq 0.6$–1.4 Å^{-1} and $2\theta \simeq 1.4$–3.2°. The Bragg angle θ is thus an order of magnitude smaller than the observed width of the assumedly uniaxial ($m = 0$) orientation distributions. Thus, when scanning the sample 180° around the tomography axis, the uniaxial orientation distributions ('pole figures') of all the low-q diffraction peaks will be measured to good accuracy.

Reconstructed XRDTT cross sections of the clay sample are shown in Fig. 4, exactly matching the µCT cross sections in Fig. 2. In Fig. 4, cross-sectional maps of the overlapping clinochlore 002/kaolinite 002 peak are displayed showing (i) the local isotropic scattering intensity $a_0(\mathbf{r}')$, (ii) the uniaxial (polar) angle $\theta_{op}(\mathbf{r}')$ of the preferred orientation axis with respect to the z' axis [Fig. 1(c)], and (iii) the Hermans' parameter $S(\mathbf{r}')$ describing the degree of orientation. As seen in the reconstructed $a_0(\mathbf{r}')$, the density of clay minerals was approximately uniform, see Figs. 4(a) and 4(d). Despite local variations, the clay mineral orientation was found to be directed mainly in one direction, as expected for a relatively small shale sample [Figs. 4(b) and 4(e)]; however the degree of preferred orientation, described by the Hermans' S parameter, varies [Figs. 4(c) and 4(f)]. Similar XRDTT reconstructions were made for the broad low-q peak which includes clinochlore 001; however the reconstructed preferred orientation directions differed from the clinochlore 002 case (Fig. 4), presumably due to the large amount of Bragg peak overlap, see Section S8. The mean preferred orientation direction of the [001] clay axis was found to be given by the angles $\phi_{op, mean}$ = 80.1° and $\theta_{op, mean} = 6.4°$ by averaging the scattering directions for all voxels in the sample. The reconstructions were robust; different initial values for the XRDTT reconstructions provided similar results. Choosing the sample z' axis to (approximately) coincide with the predominant clay mineral orientation, as governed by equation (3), appears advantageous for numerical reconstruction, as the resulting $\theta_{op}(\mathbf{r}')$ is close to zero, and then $\theta_{op}(\mathbf{r}')$ and $\phi_{op}(\mathbf{r}')$ are far from gimbal lock.

As a plausibility test of the XRDTT results, the forward-simulated scattering from the reconstructed model was calculated and found to be similar to the measured scattering, as shown in Fig. 5. Additionally, to support the finding of the dominant clay orientations in the sample, we simulated the

forward scattering from a numerical phantom of the same size and shape as the measured sample, but with all voxels assigned the same orientation. Setting $\phi_{op} = 90.0°$ and $\theta_{op} = 10.0°$ reproduced the gross features of the measured projection data, *cf.* Fig. 5. By comparing the $\alpha = 0°$ and $\alpha = 180°$ projections, the dominant scattering directions are seen to be symmetrically flipped about the vertical axis for clinochlore 001 (coinciding with illite 001). This observation implies that the reciprocal lattice vector for clinochlore 002/kaolinite 002 was oriented approximately perpendicular to the incoming beam direction for these projections, and thus directly gives an estimate of the tilt of the bedding-plane normal with respect to the tomography axis.

3.3. Identifying clastic inclusions by combining XRD-CT and attenuation-contrast CT

When we introduced the attenuation-contrast CT cross section in Fig. 2(a), we emphasized the fundamental ambi-

guities associated with the mineral identification and segmentation. We shall now demonstrate how this problem can be resolved by combining the two datasets. Fig. 6(a) shows the same attenuation-contrast CT cross section as in Fig. 2(a), with three strongly attenuating inclusions highlighted. Additional cross-sectional views of these three inclusions are provided in Section S2. In the XRD-CT sinograms, several discontinuous traces are present, see Fig. 6(d) and Section S10. These discontinuities are caused by the crystallites rotating in and out of the diffraction condition, and imply that tomograms cannot be straightforwardly reconstructed by adapting methods from conventional CT. Attempting to use *e.g.* FBP (after filtering and averaging) gave substantial streak artefacts, precluding reliable reconstruction and interpretation, see also Figs. S11.1 and S11.2 of the supporting information.

Instead of automated XRDTT analysis, we thus relied on studying the spatial distributions of the minerals in the sample by direct comparison of the XRD-CT sinograms with attenuation-contrast CT sinograms. From the close correspondence between the co-registered sinograms we were able to map specific minerals in the sample, without being affected by streak artefacts in the tomograms. Sinograms derived from diffraction patterns of clinochlore 001, illite 001, clinochlore 002/kaolinite 002 (overlapping with clinochlore and illite), and pyrite {200} are shown in Fig. 6(d). For pyrite {200}, the sinogram curves corresponding to particles marked (1) and (2) have approximately constant intensity for all projection angles α, implying that for every rotation step of the sample, approximately the same number of crystallites must satisfy the Bragg condition. By studying the raw diffraction patterns, we could indeed confirm that these pyrite particles consist of several randomly oriented crystalline grains, see Figs. S4.3 and S4.4. The full diffractograms for the regions (1) and (2) could be reconstructed as
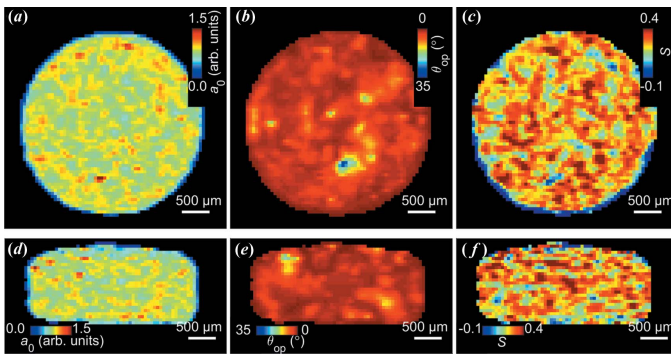

Figure 4
Reconstructed XRDTT orthogonal cross sections of the overlapping clinochlore 002/kaolinite 002 Bragg peaks. (a), (d) Isotropic scattering a_0. (b), (e) Directionality of scattering relative to the tomography axis. (c), (f) The reconstructed Hermans' parameter S, *cf.* equation (4).
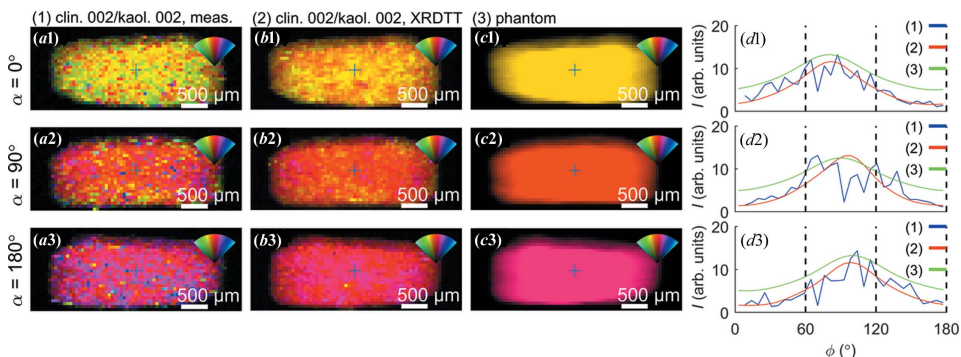

Figure 5
Comparison of the measured directional clay scattering with forward projections of the XRDTT reconstruction and the simple phantom. (a) Measured scattering of clinochlore 002 and kaolinite 002 for 0, 90 and 180°. (b) Forward-projected scattering from XRDTT reconstruction. (c) Forward-projected scattering from the phantom, where all voxels have been assigned the same direction. (d) Azimuthal intensity distributions for points marked with (+).
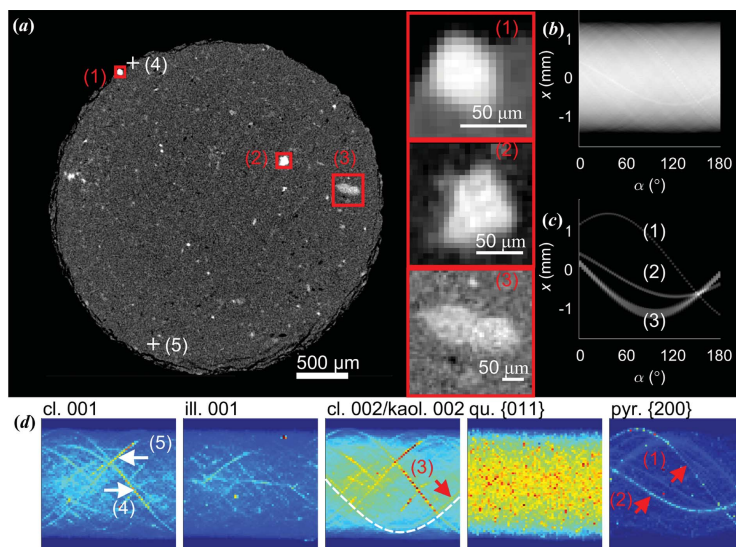
Figure 6
Identification of clastic mineral composition by comparing attenuation- and XRD-contrast sinograms. (a) An attenuation-contrast cross section of the sample. Three inclusions are marked with red rectangles and have been magnified. A sinogram (Radon transform) of the entire cross section in (a). (c) A sinogram made by including only the bright regions indicated by the red rectangles in (a). (d) XRD-CT sinograms based on clinochlore 001, illite 001, clinochlore 002/kaolinite 002, quartz {011} (overlapping with clinochlore and illite), and pyrite {200}. All sinograms are displayed with different intensity scales. The white dashed line is a guide to the eye.

shown in Fig. S12, consistently showing presence of the pyrite Bragg peaks. Region (3) in Fig. 6 matched curves in the clinochlore 002/kaolinite 002 sinograms [Fig. 6(d)], firmly rejecting the idea that these strongly attenuating features are all electron-rich minerals. There were features, exemplified by (4) and (5) in Fig. 6(a), with a strong XRD-CT signal corresponding to clinochlore, that did not give a distinct signal in the attenuation-contrast CT. In addition to the comparison between the attenuation-contrast CT and XRD-CT sinograms made to identify the mineralogy in the selected regions in Fig. 6(a), the correlation between the attenuation-contrast CT sinograms and the XRD-CT sinograms was calculated, see Section S13. This procedure gave similar information as XRD-CT reconstruction (see Sections S11 and S12), however avoiding streak artefacts originating from the CT reconstruction, and is thus suggested as an alternative method for mineral localization in under-sampled measurements.

Other strategies exist to retrieve the spatial and orientational distributions of crystallites that are large compared with the voxel size. Notably, 3DXRD (Poulsen, 2004) allows accurate crystalline mapping, also including orientation, provided that diffraction spots originating from individual grains can be uniquely separated, and the diffraction signal predominantly originates from larger grains, contrary to the case observed in the present work.

Our motivation for this work has been to study the spatial distributions and orientation of minerals in shales to better understand their physicochemical properties. We have inves-

tigated if we could obtain the clay mineral orientation by applying XRDTT, similar to what has previously been carried out on bone by us (Mürer et al., 2021) and others (Liebi et al., 2015, 2018; Grünewald et al., 2020); however, here we used a single tomography axis, thus significantly reducing the experimental complexity and the reconstruction computing time. In tensor tomography, when the solution is found by optimization of a large amount ($\sim 10^6$) of parameters, the use of multiple tomography axes can be beneficial in adding more sampling points to prevent the optimization from stagnating in local minima. Similar orientation patterns (Fig. 4) were found with different initial conditions of the angular optimization, supporting both the validity of the orientational maps and the experimental procedure. We refer again to the study of the bone and cartilage, reported in Section S7, for a detailed comparison of reconstructions with one or two tomographic axes.

Shales contain pores and mineral grains on length scales from nanometres to centimetres (Ma et al., 2017), and in this experiment we were limited by (i) the 50 μm voxel size, defined by the size of the beam in XRD-CT, and (ii) the limited resolution in q due to the placement of the detector far from the sample. We have previously demonstrated that even small fragments (~ 4 μm diameter) of Pierre shale can consist of several mineral phases (Chattopadhyay et al., 2020). However, the large field of view used in this experiment enabled us to nondestructively map out larger (~ 50–100 μm) mineral features within a millimetre-sized volume, a feat that to our knowledge would have been impossible with other chemistry-sensitive techniques used to characterize shale, such as electron backscatter diffraction (Prior et al., 1999). XRD-CT and XRDTT are clearly promising pathways towards a much richer understanding of the micro- and nano-scale features in shales, deserving of the efforts of implementing a fully automated systematic analysis.

4. Conclusions

We have utilized XRDTT to study scattering from clay minerals and high-density inclusions in Pierre shale. Orientation maps of the clay minerals have been obtained, demonstrating that texture information from clay minerals can be extracted in XRDTT by using a single tomography axis as in conventional CT. The abundant clay minerals in shales were demonstrated to exhibit strong global preferred orientation as expected, and with XRDTT also minor variations could be

mapped in 3D. We have demonstrated that a systematic use of sinograms based on combining the attenuation-contrast and diffraction-contrast data allows identification of the mineralogy of selected regions. Inclusions were identified to contain multi-grained pyrite or clinochlore crystallites.

5. Related literature

The following references are cited in the supporting information for this article: van Aarle *et al.* (2016), Hughes *et al.* (1989), Kak & Slaney (1987), Meneghini *et al.* (2003), Vamvakeros *et al.* (2015), Wenk & Heidelbach (1999).

References

Aarle, W. van, Palenstijn, W. J., Cant, J., Janssens, E., Bleichrodt, F., Dabravolski, A., De Beenhouwer, J., Joost Batenburg, K. & Sijbers, J. (2016). *Opt. Express*, **24**, 25129.

Ashiotis, G., Deschildre, A., Nawaz, Z., Wright, J. P., Karkoulis, D., Picca, F. E. & Kieffer, J. (2015). *J. Appl. Cryst.* **48**, 510–519.

Baer, E., Hiltner, A. & Keith, H. D. (1987). *Science*, **235**, 1015–1022.

Birkbak, M. E., Leemreize, H., Frølich, S., Stock, S. R. & Birkedal, H. (2015). *Nanoscale*, **7**, 18402–18410.

Breiby, D. W. & Samuelsen, E. J. (2003). *J. Polym. Sci. B Polym. Phys.* **41**, 2375–2393.

Bunge, H. J. (1969). *Mathematische Methoden Der Texturanalyse*. Berlin: Akademie-Verlag.

Bunk, O., Bech, M., Jensen, T. H., Feidenhans'l, R., Binderup, T., Menzel, A. & Pfeiffer, F. (2009). *New J. Phys.* **11**, 123016.

Cerasi, P., Lund, E., Kleiven, M. L., Stroisz, A., Pradhan, S., Kjøller, C., Frykman, P. & Fjaer, E. (2017). *Energy Procedia*, **114**, 3096–3112.

Chattopadhyay, B., Madathiparambil, A. S., Mürer, F. K., Cerasi, P., Chushkin, Y., Zontone, F., Gibaud, A. & Breiby, D. W. (2020). *J. Appl. Cryst.* **53**, 1562–1569.

Egan, C. K., Jacques, S. D. M., Di Michiel, M., Cai, B., Zandbergen, M. W., Lee, P. D., Beale, A. M. & Cernik, R. J. (2013). *Acta Biomaterialia*, **9**, 8337–8345.

Feldkamp, J. M., Kuhlmann, M., Roth, S. V., Timmann, A., Gehrke, R., Shakhverdova, I., Paufler, P., Filatov, S. K., Bubnova, R. S. & Schroer, C. G. (2009). *Phys. Status Solidi A*, **206**, 1723–1726.

Feldkamp, L. A., Davis, L. C. & Kress, J. W. (1984). *J. Opt. Soc. Am. A*, **1**, 612–619.

Frølich, S., Leemreize, H., Jakus, A., Xiao, X., Shah, R., Birkedal, H., Almer, J. D. & Stock, S. R. (2016). *J. Appl. Cryst.* **49**, 103–109.

Gao, Z., Guizar-Sicairos, M., Lutz-Bueno, V., Schröter, A., Liebi, M., Rudin, M. & Georgiadis, M. (2019). *Acta Cryst.* A**75**, 223–238.

Grünewald, T. A., Liebi, M., Wittig, N. K., Johannes, A., Sikjaer, T., Rejnmark, L., Gao, Z., Rosenthal, M., Guizar-Sicairos, M., Birkedal, H. & Burghammer, M. (2020). *Sci. Adv.* **6**, eaba4171.

Guizar-Sicairos, M., Georgiadis, M. & Liebi, M. (2020). *J. Synchrotron Rad.* **27**, 779–787.

Gürsoy, D., Biçer, T., Almer, J. D., Kettimuthu, R., Stock, S. R. & De Carlo, F. (2015). *Philos. Trans. R. Soc. A*, **373**, 20140392.

Harding, G., Kosanetzky, J. & Neitzel, U. (1987). *Med. Phys.* **14**, 515–525.

Hermans, J. J., Hermans, P. H., Vermaas, D. & Weidinger, A. (1946). *Recl Trav. Chim. Pays Bas*, **65**, 427–447.

Hughes, J. M., Cameron, M. & Crowley, K. D. (1989). *Am. Mineral.* **74**, 870–876.

Kak, A. C. & Slaney, M. (1987). *Principles of Computerized Tomographic Imaging Society for Industrial and Applied Mathematics*. Philadelphia: Society for Industrial and Applied Mathematics.

Keelan, D. K. (1982). *J. Pet. Technol.* **34**, 2483–2491.

Kleuker, U., Suortti, P. W. W., Weyrich, W. & Spanne, P. (1998). *Phys. Med. Biol.* **43**, 2911–2923.

Leu, L., Georgiadis, A., Blunt, M. J., Busch, A., Bertier, P., Schweinar, K., Liebi, M., Menzel, A. & Ott, H. (2016). *Energy Fuels*, **30**, 10282–10297.

Liebi, M., Georgiadis, M., Kohlbrecher, J., Holler, M., Raabe, J., Usov, I., Menzel, A., Schneider, P., Bunk, O. & Guizar-Sicairos, M. (2018). *Acta Cryst.* A**74**, 12–24.

Liebi, M., Georgiadis, M., Menzel, A., Schneider, P., Kohlbrecher, J., Bunk, O. & Guizar-Sicairos, M. (2015). *Nature*, **527**, 349–352.

Ma, L., Fauchille, A. L., Dowey, P. J., Figueroa Pilz, F., Courtois, L., Taylor, K. G. & Lee, P. D. (2017). *Geol. Soc. London, Spec. Publ.* **454**, 175–199.

Meneghini, C., Dalconi, M. C., Nuzzo, S., Mobilio, S. & Wenk, R. H. (2003). *Biophys. J.* **84**, 2021–2029.

Mürer, F. K., Chattopadhyay, B., Madathiparambil, A. S., Tekseth, K. R., Di Michiel, M., Liebi, M., Lilledahl, M. B., Olstad, K. & Breiby, D. W. (2021). *Sci. Rep.* **11**, 1–12.

Mürer, F. K., Sanchez, S., Álvarez-Murga, M., Di Michiel, M., Pfeiffer, F., Bech, M. & Breiby, D. W. (2018). *Sci. Rep.* **8**, 1–13.

Palle, J., Wittig, N. K., Kubec, A., Niese, S., Rosenthal, M., Burghammer, M., Grünewald, T. A. & Birkedal, H. (2020). *J. Struct. Biol.* **212**, 107631.

Paris, O. (2008). *Biointerphases*, **3**, FB16–FB26.

Poulsen, H. F. (2004). *Three-Dimensional X-ray Diffraction Microscopy: Mapping Polycrystals and their Dynamics*. Berlin: Springer.

Prior, D. J., Boyle, A. P., Brenker, F., Cheadle, M. C., Day, A., Lopez, G., Peruzzi, L., Potts, G. J., Reddy, S., Spiess, R., Timms, N. E., Trimby, P., Wheeler, J. & Zetterström, L. (1999). *Am. Mineral.* **84**, 1741–1759.

Rietveld, H. M. (1969). *J. Appl. Cryst.* **2**, 65–71.

Roe, R. J. & Krigbaum, W. R. (1964). *J. Chem. Phys.* **40**, 2608–2615.

Sander, B. (1934). *Z. Für Krist. Mater.* **89**, 97–124.

Schaff, F., Bech, M., Zaslansky, P., Jud, C., Liebi, M., Guizar-Sicairos, M. & Pfeiffer, F. (2015). *Nature*, **527**, 353–356.

Schroer, C. G., Kuhlmann, M., Roth, S. V., Gehrke, R., Stribeck, N., Almendarez-Camarillo, A. & Lengeler, B. (2006). *Appl. Phys. Lett.* **88**, 164102.

Shaw, D. B. & Weaver, C. E. (1965). *J. Sediment. Petrol.* **35**, 213–222.

Skjønsfjell, E. T., Kringeland, T., Granlund, H., Høydalsvik, K., Diaz, A. & Breiby, D. W. (2016). *J. Appl. Cryst.* **49**, 902–908.

Stock, S. R. (2015). *Calcif. Tissue Int.* **97**, 262–280.

Stock, S. R., De Carlo, F. & Almer, J. D. (2008). *J. Struct. Biol.* **161**, 144–150.

Vamvakeros, A., Jacques, S. D. M., Di Michiel, M., Middelkoop, V., Egan, C. K., Cernik, R. J. & Beale, A. M. (2015). *J. Appl. Cryst.* **48**, 1943–1955.

Vamvakeros, A., Matras, D., Jacques, S. D. M., di Michiel, M., Middelkoop, V., Cong, P., Price, S. W. T., Bull, C. L., Senecal, P. & Beale, A. M. (2021). *Catal. Today*, **364**, 242–255.

Vaughan, G. B. M., Baker, R., Barret, R., Bonnefoy, J., Buslaps, T., Checchia, S., Duran, D., Fihman, F., Got, P., Kieffer, J., Kimber, S.

A. J., Martel, K., Morawe, C., Mottin, D., Papillon, E., Petitdemange, S., Vamvakeros, A., Vieux, J.-P. & Di Michiel, M. (2020). *J. Synchrotron Rad.* **27**, 515–528.

Wenk, H. R. & Heidelbach, F. (1999). *Bone*, **24**, 361–369.

Wenk, H. R., Kanitpanyacharoen, W. & Voltolini, M. (2010). *J. Struct. Geol.* **32**, 478–489.

Wilchinsky, Z. W. (1951). *Acta Cryst.* **4**, 1–9.

Williamson, G. K. & Hall, W. H. (1953). *Acta Metall.* **1**, 22–31.

IUCrJ

Volume 8 (2021)

Supporting information for article:

Orientational mapping of minerals in Pierre shale using X-ray diffraction tensor tomography

Fredrik K. Mürer, Aldritt Scaria Madathiparambil, Kim Robert Tekseth, Marco Di Michiel, Pierre Cerasi, Basab Chattopadhyay and Dag W. Breiby

S1. Pierre shale

Figure S1 shows pieces of Pierre shale and the studied sample mounted onto a polymer pin which was attached to the goniometer head. The sample was cut to the shape of a cylinder, with approximate diameter 3.5 mm and height 1.3 mm.
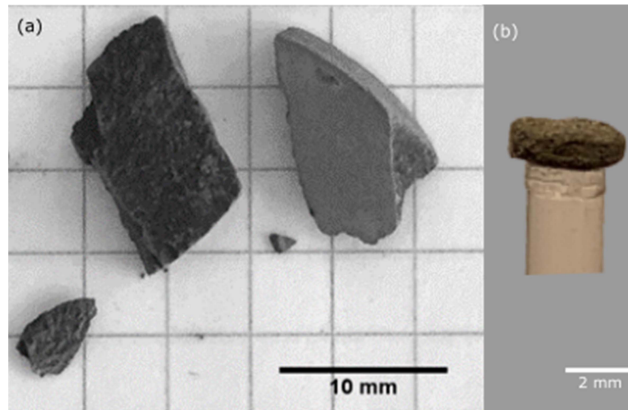
Figure S1 Sample preparation. (a) Pierre shale outcrop. (b) Photograph of the shale sample mounted onto a pin, which was attached to the goniometer head.

S2. Attenuation-contrast cross-sections

Orthogonal views are provided of the high-density inclusions, shown in Figs. 2 and 6 in the main article, see Fig S2.
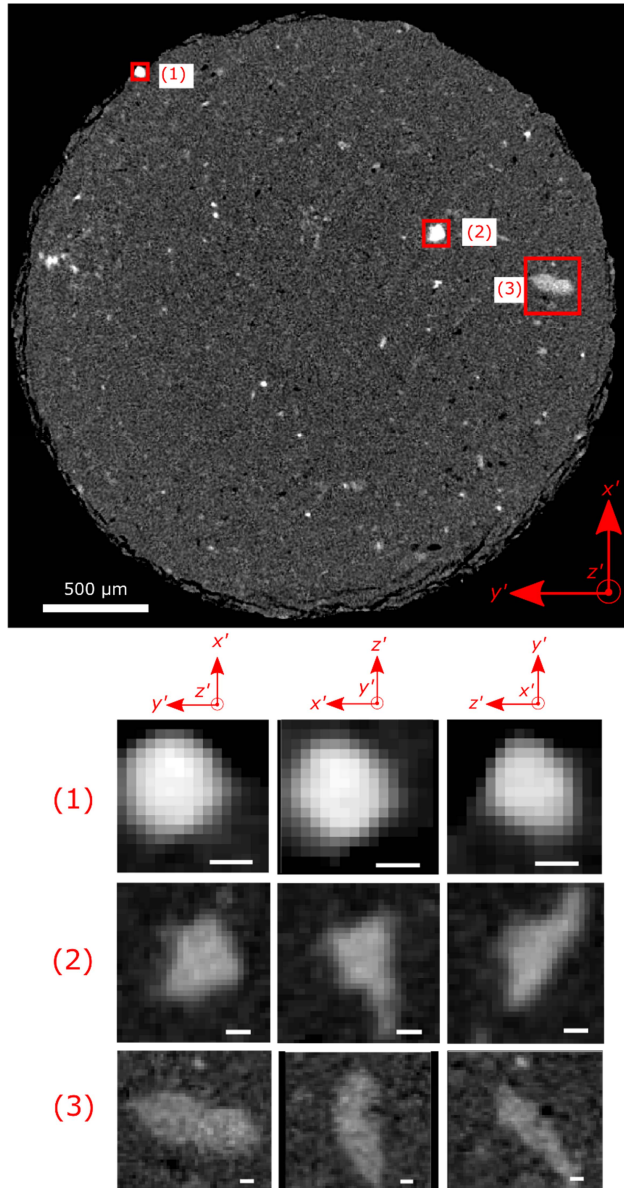
Figure S2 Attenuation-contrast CT cross-sections. a) The cross-section displayed in the article. b-j) Orthogonal cross-sections of the high-density particles marked with rectangles. The scalebars in the insets are 25 µm. Different intensity scaling has been used for the cross-section in (a) and the various insets to enhance the contrast.

S3. High-resolution synchrotron phase-contrast imaging of Pierre shale

To study the local variations in grain sizes in the sample we did phase-contrast local tomography at the beamline ID16 at the ESRF, Grenoble. A cross-section obtained from the exact same Pierre shale sample as measured with XRD-CT and presented in the main article is shown in Fig. S3. The reconstructed voxel size is 60 nm, allowing identification of single grains, however the field-of-view with this method is limited to only cover a small region within the sample centre.
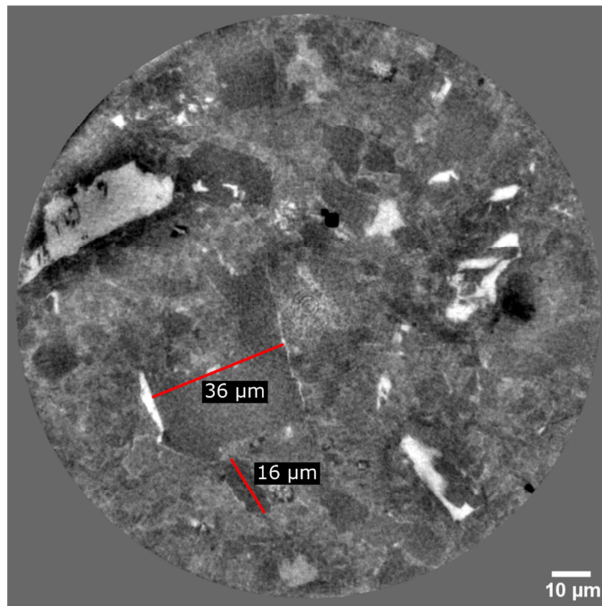
Figure S3 Cross-section of Pierre shale, imaged with high-resolution synchrotron phase-contrast CT. Local tomography propagation phase-contrast CT, measured at ID16, ESRF with a reconstructed voxel size of 60 nm. The exact same sample as measured in the manuscript, but with a smaller field of view. The approximate sizes of larger grains have been indicated.

S4. Oriented scattering from minerals

Figures S4.1 and S4.2 show the directional scattering for the shale sample from 6 different Bragg peaks with the sample orientation for $\alpha = 0°$ and $\alpha = 180°$, respectively, complementary to Fig. 3 in the main article where $\alpha = 36°$ is shown. Each pixel (x,y) corresponds to a single measured diffraction pattern.
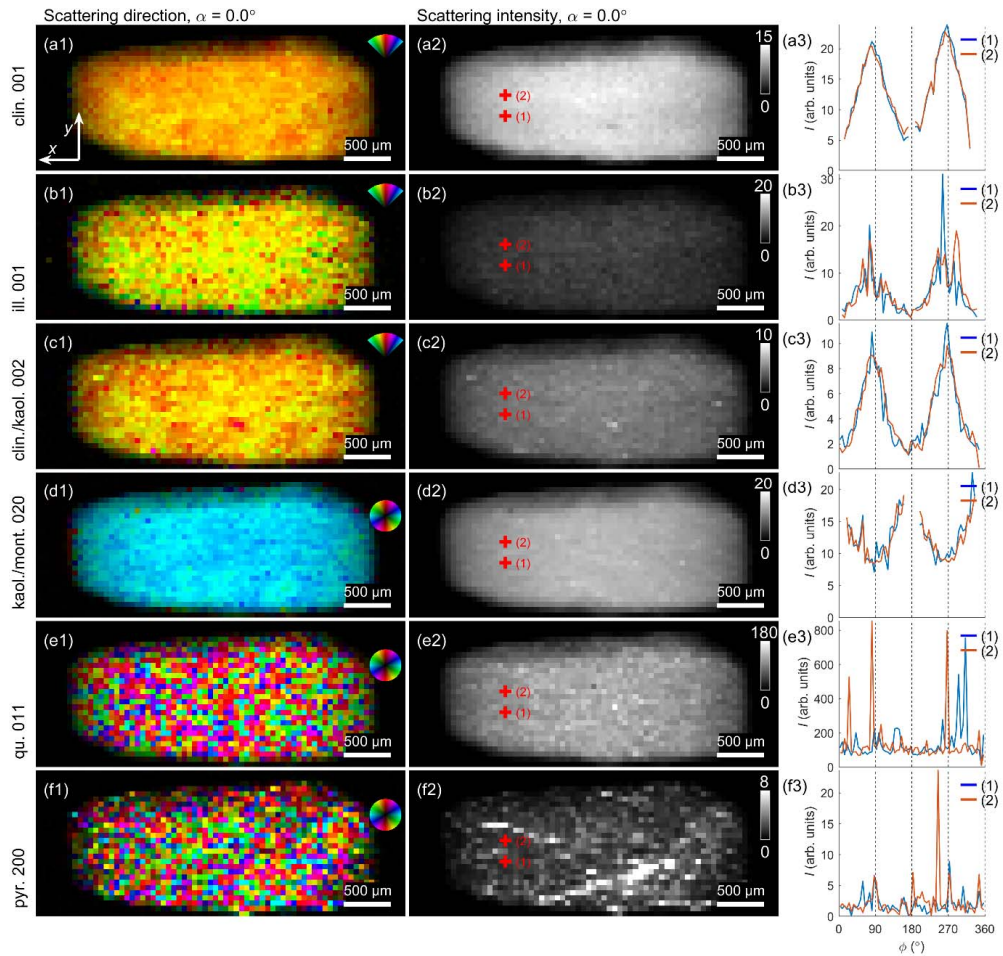
Figure S4.1 Dominant scattering direction and integrated scattered intensity obtained for a single projection with $\alpha = 0°$.
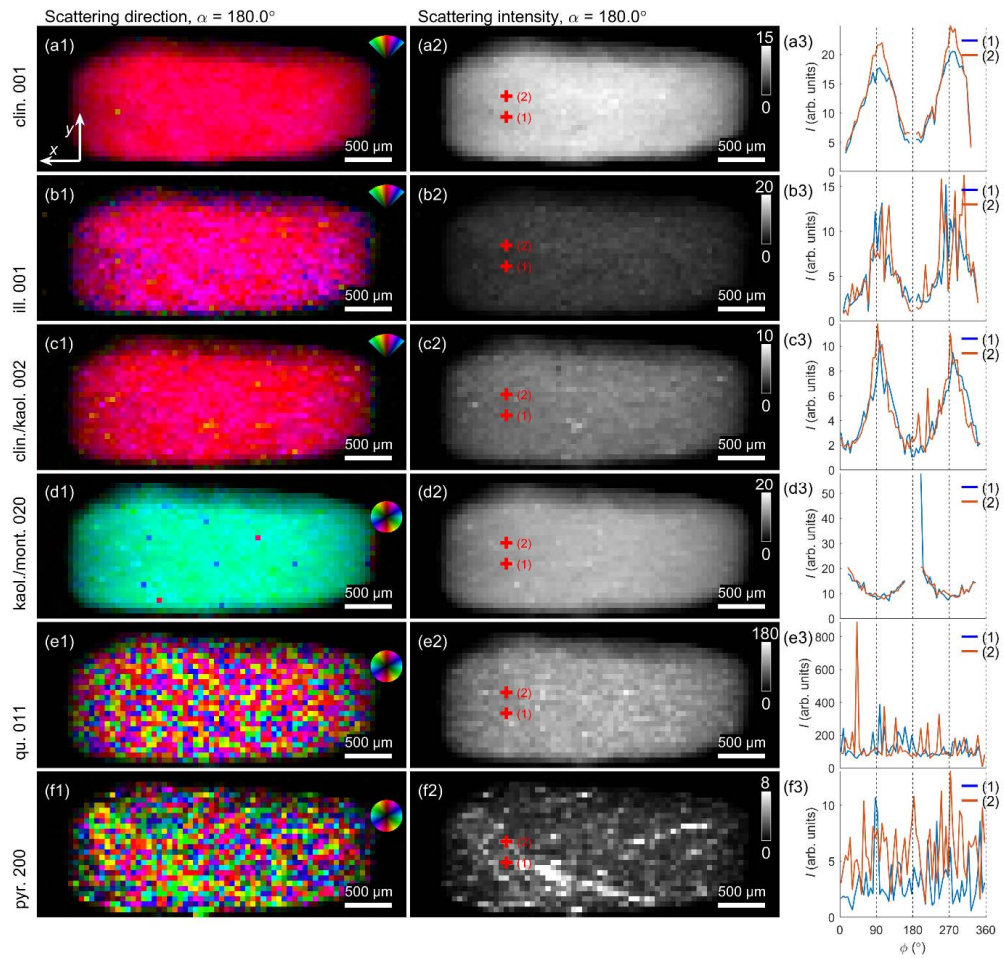
Figure S4.2 Dominant scattering direction and integrated scattered intensity obtained for a single projection with $\alpha = 180°$.
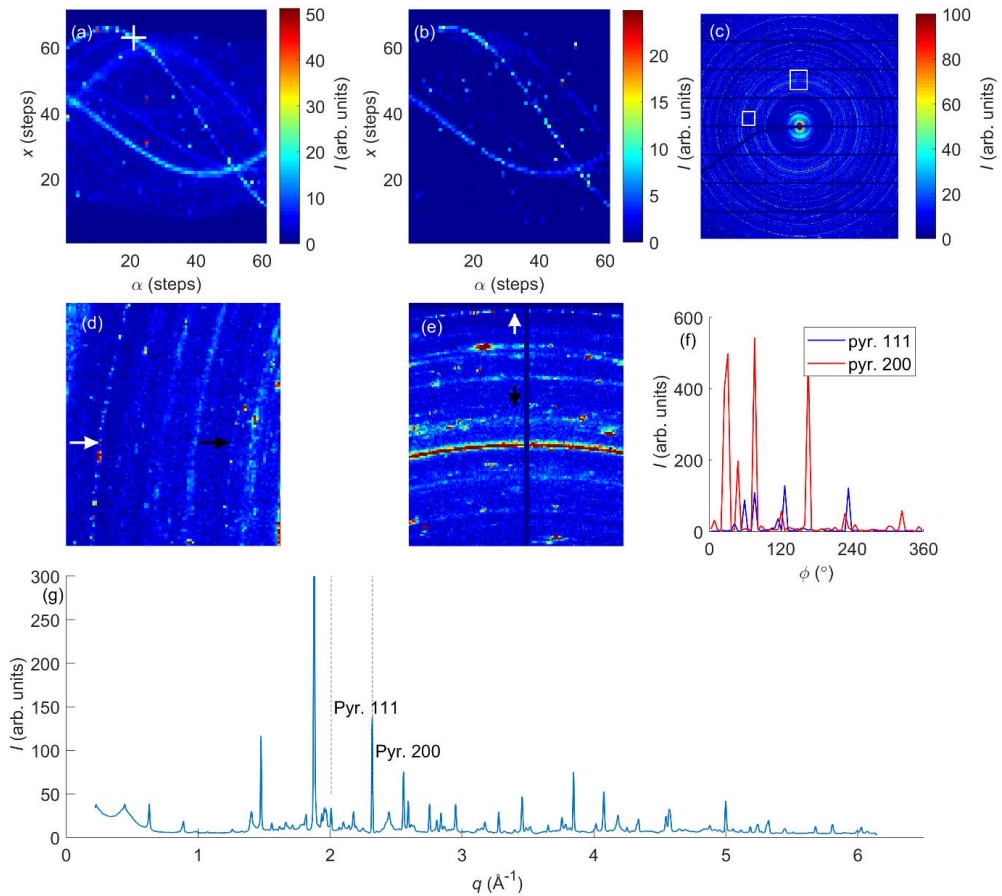
Figure S4.3 Scattering from the pyrite-containing region marked (1) in Figure 6a. (a) Sinogram of pyrite {200}. (b) Unfiltered sinogram of pyrite {111}. (c) Diffraction pattern corresponding to the white (+) in (a). (d-e) Magnified regions from (c). The black and white arrows point to the pyrite {111} and {200} Bragg peaks, respectively. (f) Azimuthal intensity variation of pyrite {111} and {200}. (g) Azimuthal integrated intensity of the diffraction pattern in (c). Steps in x and α are 50 µm and 3.0°, respectively.
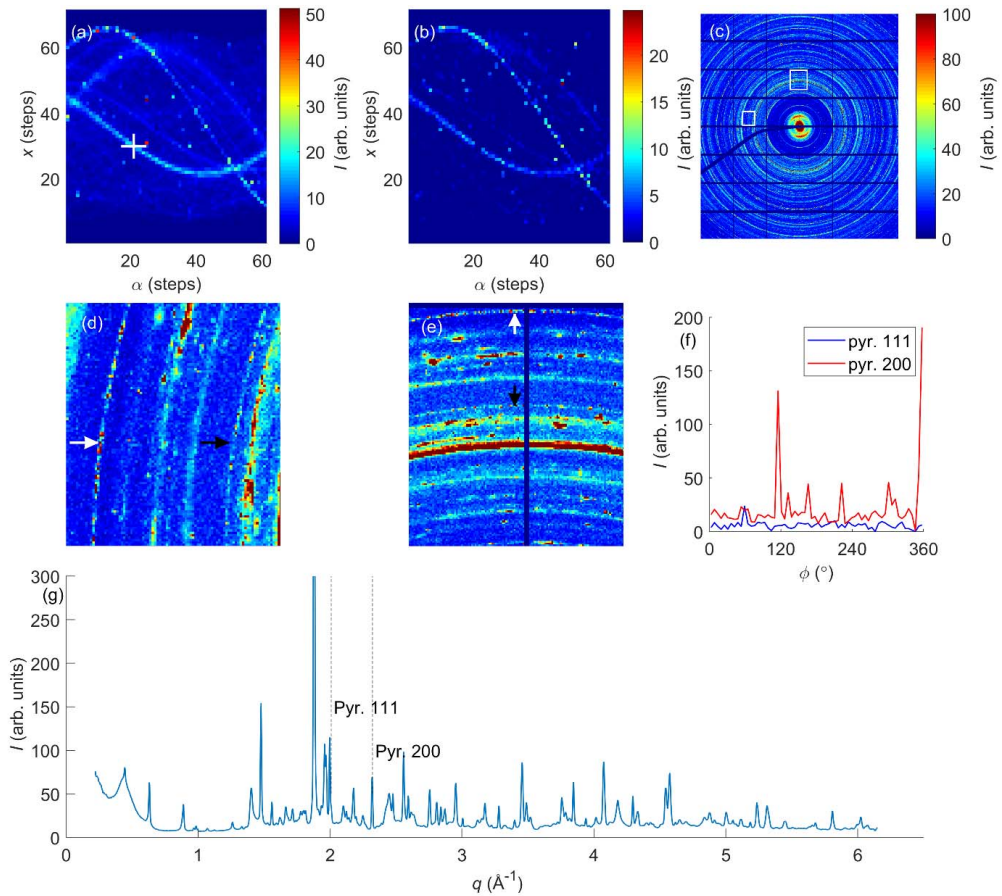
Figure S4.4 Scattering from the pyrite-containing region marked (2) in Figure 6a. (a) Sinogram of pyrite {200}. (b) Unfiltered sinogram of pyrite {111}. (c) Diffraction pattern corresponding to the white (+) in (a). (d-e) Magnified regions from (c). The black and white arrows point to the pyrite {111} and {200} Bragg peaks, respectively. (f) Azimuthal intensity variation of pyrite {111} and {200}. (g) Azimuthal integrated intensity of the diffraction pattern in (c). Steps in x and α are 50 µm and 3.0°, respectively.

S5. Sample attenuation corrections

Beam attenuation artefacts were observed in the reconstructed tomograms in both the isotropic XRD-CT reconstruction and in the orientational XRDTT reconstruction. As no attenuation measurements were done during the experiment, we devised a simple attenuation correction based on the reconstructed cross-sections. The attenuation correction was applied for the reconstruction of all sinograms, except where the diffraction patterns had been filtered before integration. An uncorrected reconstructed cross-section of the illite 001 scattering is shown in Figure S5a. From the line plot in Figure S5c, it is seen that for the uncorrected tomogram (having the attenuation coefficient $\mu = 0$), lower intensities occur close to the sample centre, where the beam is most attenuated upon traversing the sample.

The sample attenuation correction of the sample was done by:

(i)   Performing an initial reconstruction to make a sample mask.
(ii)   Assigning an effective attenuation coefficient μ, constant for the whole sample volume.
(iii) Forward projection of the simulated transmission sinogram.
(iv)   Correcting the sinogram by the simulated transmission sinogram.

The attenuation correction was applied for both isotropic XRD-CT and for XRDTT. Examples are shown in Figure 4.2. The absorption correction in isotropic XRD-CT was applied separately for each q. An attenuation coefficient of $\mu = 0.005$ vox^{-1} was found to mitigate the absorption artefacts, cf. Fig. S5(b) and (c).
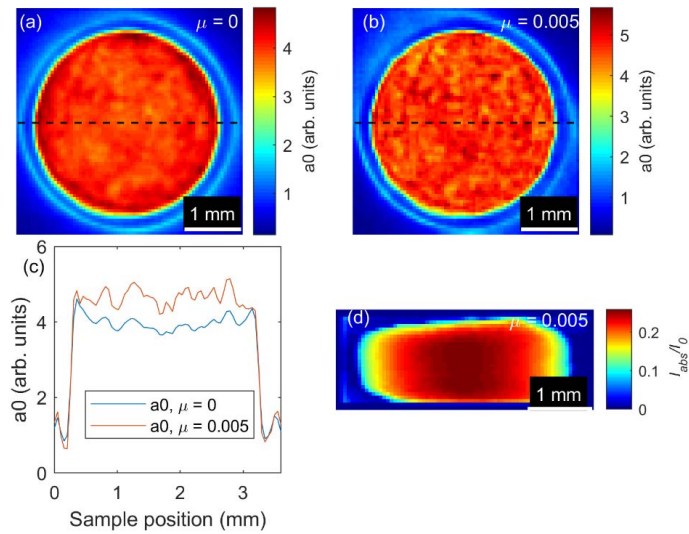
Figure S5 Absorption corrections for the Pierre shale sample. (a) Reconstructed isotropic tomogram of illite 001 using no absorption correction. Higher intensity regions can be observed close to the sample edges. (b) Reconstructed tomogram of illite using an absorption correction of $\mu = 0.005$ vox^{-1}. c) Line plot through cross sections in (a) and (b). Higher constructed intensities can be observed close to the sample edges in the uncorrected reconstruction. (d). Forward simulated azimuthally integrated intensity projection ($\alpha = 0°$), using an absorption coefficient of $\mu = 0.005$ vox^{-1}. The maximum absorption in the projection is estimated to be approximately 20%.

S6. XRDTT reconstruction

XRDTT reconstruction was done by following the approach described by (Liebi *et al.*, 2018) and by using the small-angle scattering tensor tomography (SASTT) package developed by the coherent X-Ray Scattering Group at the Paul Scherrer Institute, Villigen, Switzerland. An additional rotation matrix was used to align the sample z'-axis with the laboratory y-axis, see Fig. 1 and Eqs. 2 and 3. Parameters used for XRDTT reconstruction of the clinochlore 001 and clinochlore 002 peaks are found in Table S4. The parameter names refer to entries in the SASTT MATLAB package.

Table S6 Initial parameters used for XRDTT reconstruction of clinochlore 001 and clinochlore 002 Bragg peaks. Cf. (Liebi *et al.*, 2018) for a full description.

STEP	Parameter	Clinochlore 002/kaolinite 002
Symmetric intensity	regularization	not applicable
	regularization_angle	not applicable
	itmax	20
SH angles	regularization	not applicable
	regularization_angle	not applicable
	itmax	50
	a1_init	1
	a2_init	-20
	a3_init	10000
	l	[0 2 4 6]
	m	[0 0 0 0]
	theta_init	pi/4
	phi_init	pi/4
SH coefficients	regularization	1
	regularization_angle	not applicable
	kernel3D	window3(3,3,3,@hamming)
	itmax	20
	l	[0 2 4 6]
	m	[0 0 0 0]
	a	[0.001 -0.0001 0.001 0.0001]
Combination of all parameters	itmax	50
	regularization	not applicable
	regularization_angle	not applicable
	regularization_angle_coeff	2.00

S7. XRDTT of hydroxyapatite crystallites in bone using a single tomography axis

To further strengthen our assumption of using a single tomography axis for tensor tomography to determine the clay mineral orientation in shale, we demonstrate the approach on a sample of bone, measured using two tomography axes. The primary constituent of bone is the mineralized collagen fibre matrix, where the mineralized phase consists of hydroxyapatite (HA) crystallites (Stock, 2015), located within and outside the collagen fibre bundles. The textured wide-angle X-ray scattering from bone originates primarily from the electron density periodicity within the HA crystallites, and the preferred orientation of the crystallites with respect to the trabecula gives information about the collagen fibre orientation, which is closely tied to the mechanical properties of bone (Wenk & Heidelbach, 1999; Stock, 2015).

We have in a previous study used XRDTT to determine the 3D *c*-axis orientation of bone mineral hydroxyapatite crystallites of the same sample (Mürer *et al.*, 2021). Measurements of the bone and cartilage sample were done by a tensorial tomography measurement scheme utilizing two sample rotation axes (Liebi *et al.*, 2018). α denotes the fast-axis *tomography* rotation and β the tilt axis. $\beta = 0°$ corresponds to single-axis tomography, as was used for the shale sample. For $\beta = 0°$, 61 projections were recorded with $\Delta\alpha = 3.0°$, thus giving $\alpha \epsilon [0°, 180°]$. For $\beta \epsilon [5°, 40°]$, i.e. the additional sample tilts for tensor tomography, $\Delta\alpha = 180° /(60° \cdot \cos(\beta))$ was used with $\alpha \epsilon [0°, 360°]$. The factor $\cos(\beta)$ accounts for the distribution of equally spaced sampling points on a sphere (Liebi *et al.*, 2018). To collect each projection, the sample was raster scanned in (x,y) with 65×67 steps. The scan in (x,y) was repeated for 259 different projections, giving a total number of $65 \times 67 \times 259 \approx 1.1 \cdot 10^6$ recorded diffraction patterns. The exposure time for each diffraction pattern was 50 ms. The total measurement time for the bone-cartilage sample was approximately 26 hours, including overhead time for sample translation and rotation.

The femorotibial bone-cartilage joint sample was cut from a hindlimb femoral condyle of a 60-day-old piglet. No animal was euthanized specifically for this study, and the hindlimb originated from a previous study approved by the Norwegian Animal Research Authority. The whole hindlimb was formalin fixed, stored in a 70 wt.% ethanol/water solution, and the extracted section surrounding the bone-cartilage interface at the medial condyle of dimensions $\sim 2.7 \times 2.1 \times 2.1$ mm^3 was mounted inside a 3 mm polyimide tube, ensuring that he sample stayed immersed in ethanol-water solution, and thus hydrated, both before and during the experiment.
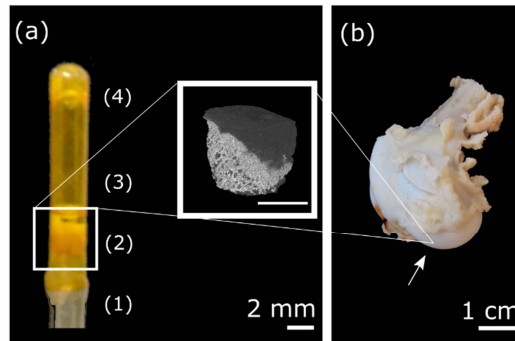
Figure S7.1 Sample preparation of bone and cartilage sample for XRDTT. (a) Sample holder used to keep the sample hydrated during the experiments. (1) Steel rod; (2) Sample mounted on rubber plug; (3) Polyimide ("Kapton") tube; (4) Epoxy droplet. (b) Distal end of a femur (hind-limb) of a young pig. The location where the studied sample was extracted from is marked by a white arrow.

An overview of the bone-cartilage sample is presented in Fig. S7.1. As shown in the PPC-CT tomograms in Fig. S7.2a and S7.2b, the highly scattering and attenuating bone minerals in the sample appear as high intensity (bright) regions. A diffraction pattern obtained with the X-ray beam going through the center of the sample is shown in Fig. S7.2c, with the corresponding azimuthally averaged diffractogram provided in Fig. S7.2d. All observed Bragg peaks in Fig. S7.2d originate from HA (Hughes *et al.*, 1989). The HA002 and HA004 peaks displayed texture, apparent as azimuthal intensity variations in Fig. S7.2e, consistent with a preferred orientation of the HA *c*-axis(Wenk & Heidelbach, 1999). Texture could not be seen in the other Debye-Scherrer rings, because of the many overlapping Bragg peaks, consistent with previous reports from bone (Meneghini *et al.*, 2003). There was no HA scattering originating from the cartilage, with the notable exception of the mineralized cartilage zone close to the bone-cartilage interface. Fig. S7.2f shows the dominant scattering direction of the HA002 peak obtained for a randomly chosen projection with $(\alpha, \beta) = (60º, 0º)$, with each pixel (x,y) in Fig. S7.2f corresponding to a single measured diffraction pattern, all revealing HA002 scattering in approximately the same direction perpendicular to the bone-cartilage interface. The irregularities at the bottom and right edge are due to artefacts introduced by cutting the brittle bone with a surgical blade, as confirmed by comparison with the PPC-CT tomograms.
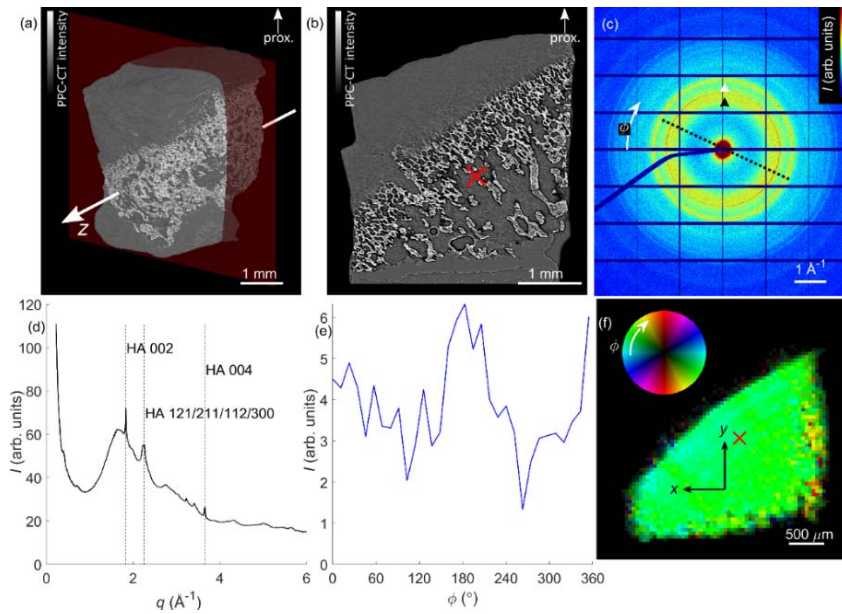
Figure S7.2 Scattering from the bone-cartilage sample. (a) 3D PPC-CT tomogram, with the proximal direction indicated. (b) PPC-CT cross section corresponding to the plane indicated in (a). (c) Representative diffraction pattern (on linear intensity scale) from the bone region of the sample. The black and white arrow heads indicate the HA002 and the overlapping HA121/211/112/300 Bragg peaks, respectively. The dotted line indicates the dominant scattering direction for the HA002 peak. (d) Azimuthal average of the diffraction pattern in (c). (e) Azimuthal intensity variations of the HA002 scattering, revealing a preferred orientation of the HA crystallites, obtained by integrating the measured intensity over $q \in [1.77 \text{ Å}^{-1}, 1.88 \text{ Å}^{-1}]$ and subtracting the background scattering. (f) The dominating HA002 scattering direction. Each pixel corresponds to a single measured diffraction pattern. The location of the obtained diffraction pattern in (c) is indicated by a red cross.

Based on the anisotropy of the HA002 Bragg peak we used XRDTT to reconstruct the HA crystallite *c*-axis orientation in the bone-cartilage sample. The XRDTT reconstructions were based on (i) all 259 measured projections, and (ii) only the 61 projections obtained with $\beta = 0°$, corresponding to the measurement scheme in conventional attenuation-contrast CT (Kak, Avinash C., Slaney, 1987) and single-axis XRD-CT (Harding *et al.*, 1987; Stock *et al.*, 2008; Kleuker *et al.*, 1998). 2D cross-sections of the reconstructed tomograms are shown in Fig. S7.3a and S.7b, demonstrating a close resemblance between the two reconstructions. A quantitative comparison of the reconstructed preferred orientation reconstructed using all tomography axes and only a single tomography axis was done by calculating the angular difference in orientation $\gamma(\mathbf{r'})$ reconstructed from the two datasets, defined as

$$\gamma(\mathbf{r'}) = \arccos\left(\hat{\mathbf{u}}^{n=259}_{HA002}(\mathbf{r'}) \cdot \hat{\mathbf{u}}^{n=61}_{HA002}(\mathbf{r'})\right), \tag{S7.1}$$

where $\hat{\mathbf{u}}(\mathbf{r'})$ are unity vectors indicating the HA crystallite *c*-axis preferred orientation direction in each sample voxel. To compare the reconstructed reciprocal maps, determined by the reconstructed $a_l^m(\mathbf{r'})$, we compared the reconstructed Hermans' parameter $S(\mathbf{r'})$ (cf. Eq. 4 in the main article) obtained from the different reconstructions by

$$\Delta S(\mathbf{r'}) = S^{n=259}_{HA002}(\mathbf{r'}) - S^{n=61}_{HA002}(\mathbf{r'}) \tag{S7.2}$$

From the maps of $\gamma(\mathbf{r'})$ and $\Delta S(\mathbf{r'})$ we observed the difference of the XRDTT tomograms reconstructed from all tomography axes and one tomography axes to be mainly restricted to the sample edges and close to gaps between the trabecula in the sample, cf. Fig. S7.3c and S7.3d. The analysis demonstrates that at least for the present dataset, the local HA *c*-axis orientation can be reliably reconstructed using a single tomography axis.
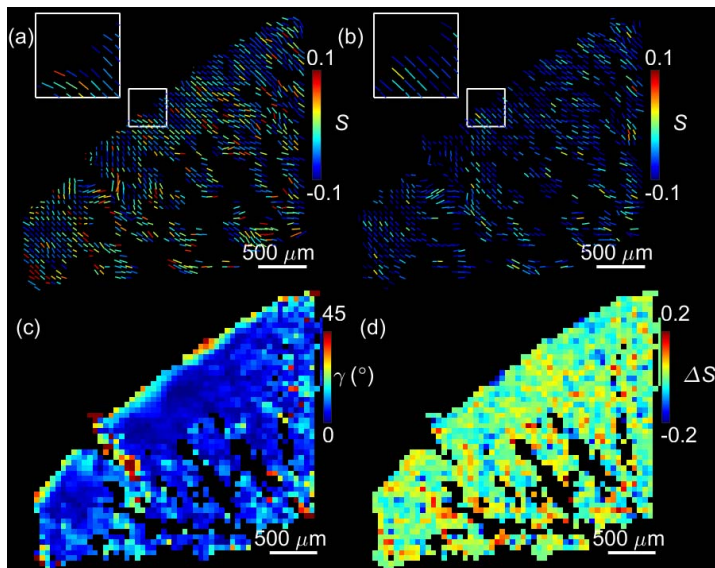
Figure S7.3 Comparison of HA orientation in bone for reconstructions based on 259 or 61 projections. (a) Cross section reconstructed using all 259 projections obtained with two tomography axes. (b) Cross-section reconstructed using only the 61 projections obtained for $\beta = 0°$. The color coding in (a) and (b) indicates the reconstructed Hermans' parameter S, cf. Eq. 4. (c) Angle between reconstructed preferred orientation directions in (a) and (b), cf. Eq. S7.1. (d) The difference in Hermans' parameter between (a) and (b), cf. Eq. S7.2.

S8. XRDTT reconstructions of clinochlore 001

By using the same strategy as for reconstruction of the clinochlore 002/kaolinite 002 Bragg peak as shown in Fig. 4 in the main article, XRDTT maps were generated using the broad clinochlore 001 peak, shown in Fig. S8. Similar orientation features were found as for the clinochlore 002/kaolinite 002 peak, although differing slightly due to Bragg peak overlap.
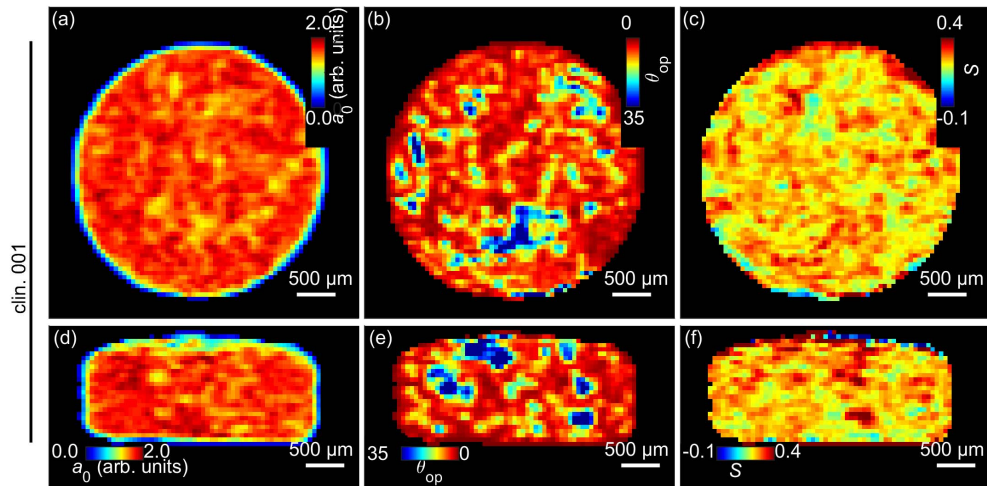
Figure S8 XRDTT reconstructions of clinochlore 001.

S9. Representative orientation distributions for clay minerals

Figure S9 shows the scattering resulting scattering intensity distributions reconstructed for two selected voxels of the sample. The scattering intensities are calculated by using Eq. 1.
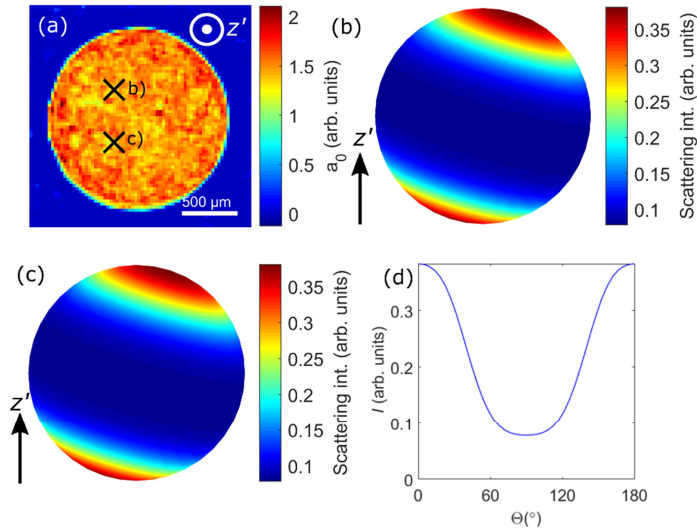
Figure S9 XRDTT cross-section and examples of reconstructed scattering intensity. a) a0 cross-section. b) Scattering distribution map from point marked "b)" in a). The reconstructed spherical coefficients and preferred orientation angles are $a_0^0 = 1.37$, $a_2^0 = 0.39$, $a_4^0 = 0.02$, $a_6^0 = -0.03$, $\theta_{op} = 19.0°$ and $\phi_{op} = 64.4°$. c) Scattering distribution map from point marked "c)" in a). The reconstructed spherical coefficients and preferred orientation angles are $a_0^0 = 1.43$, $a_2^0 = 0.40$, $a_4^0 = -0.09$, $a_6^0 = -0.03$, $\theta_{op} = 5.1°$. $\phi_{op} = 115.9°$. d) Polar intensity distribution corresponding to b).

S10. Sinograms for multiple Bragg peaks

In the sample averaged diffraction patterns, we could identify 114 Bragg peaks between $q \in (0, 6.2)$ Å^{-1}. The generated sinograms for the cross-section corresponding to the cross-section in Fig. 6 are shown in Fig. S10.1-S10.4 for prominent peaks (cf. Fig. 2) for $q \in (0, 3.0)$ Å^{-1}. Peaks with
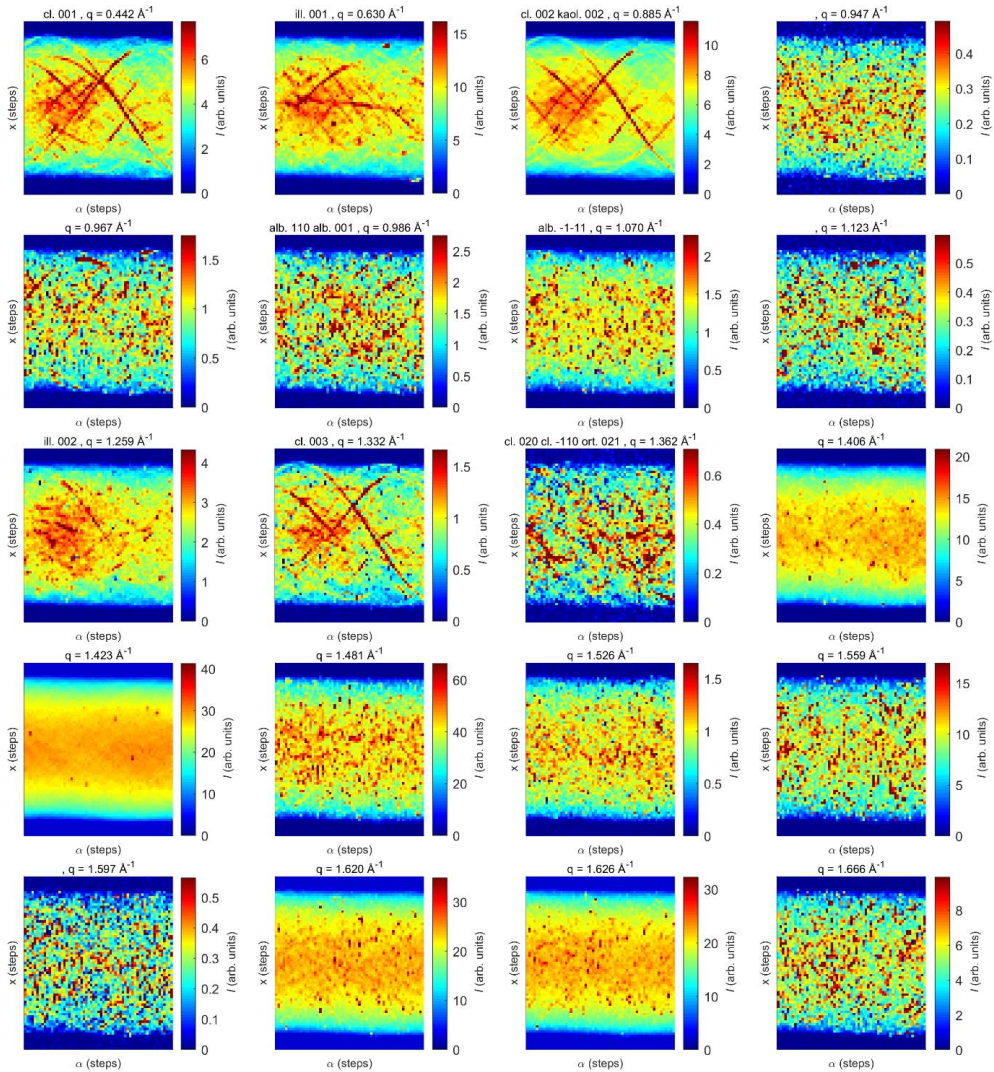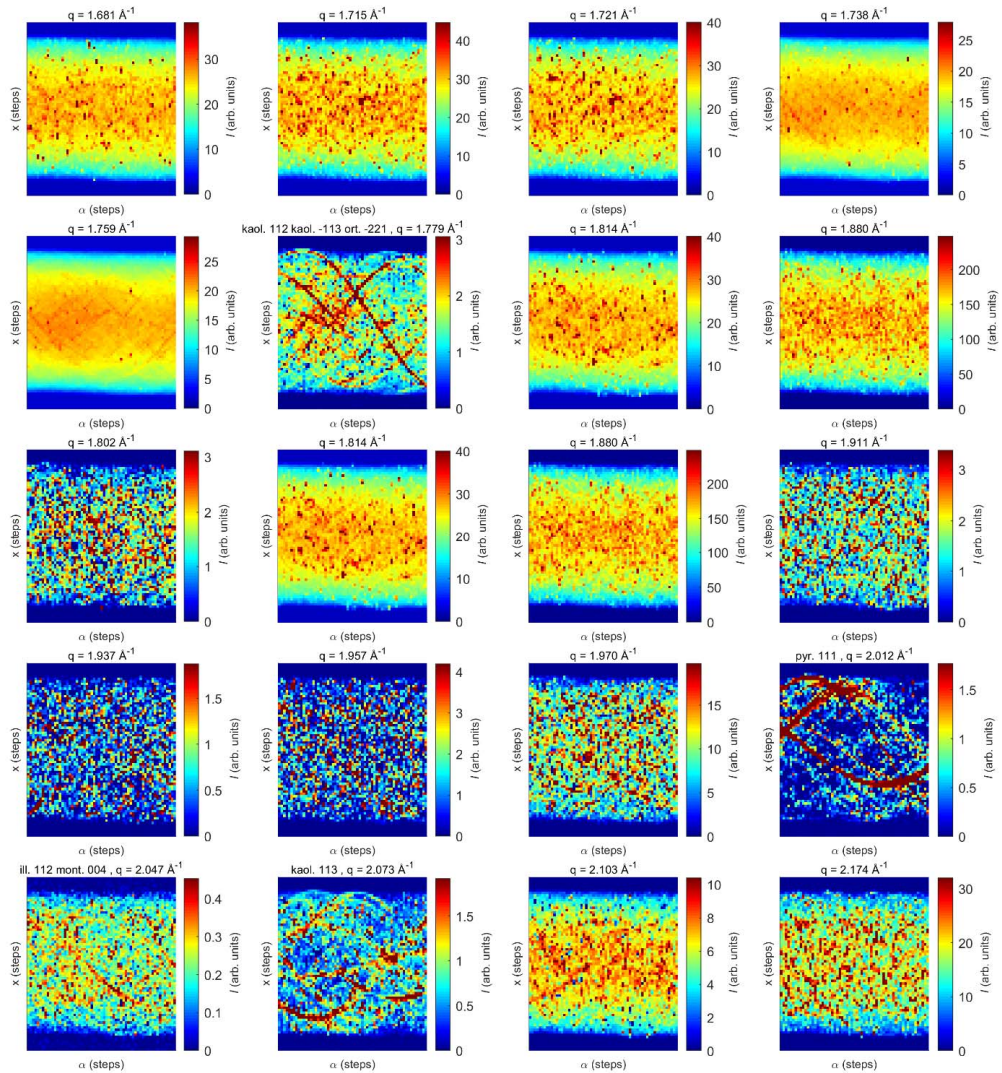

Figure S10.1 Parallel-beam XRD-CT sinograms for Bragg peaks in shale corresponding to a single cross-section. The different panels correspond to different q. Background has been subtracted by averaging the scattering intensity at the peak shoulders.
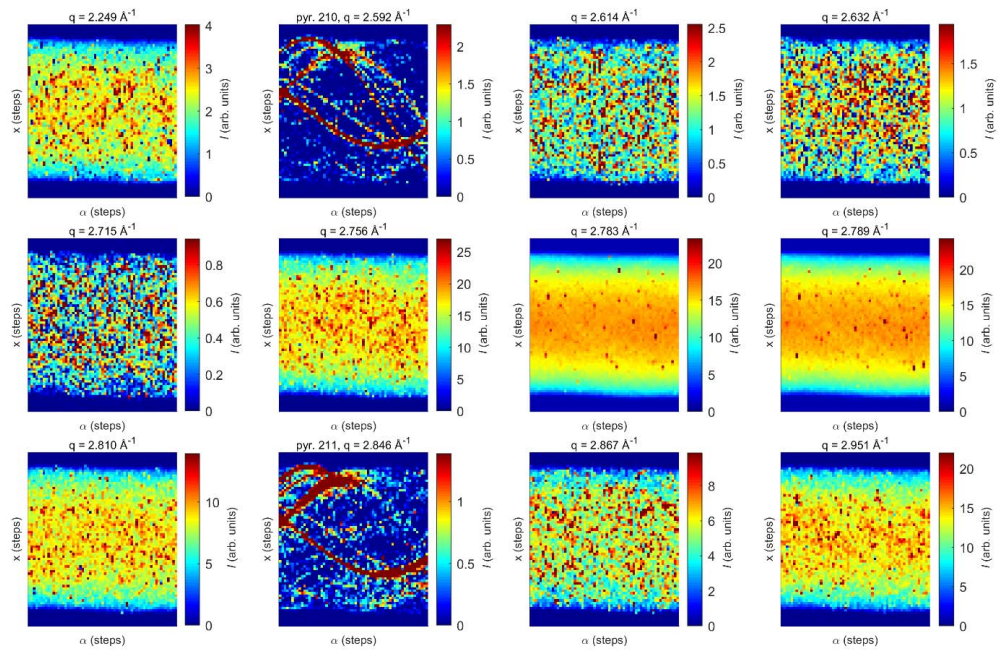
Figure S10.2 Parallel-beam XRD-CT sinograms for Bragg peaks in shale corresponding to a single cross-section. The different panels correspond to different q. Background has been subtracted by averaging the scattering intensity at the peak shoulders.

Figure S10.3 Parallel-beam XRD-CT sinograms for Bragg peaks in shale corresponding to a single cross-section. The different panels correspond to different q. Background has been subtracted by averaging the scattering intensity at the peak shoulders.

S11. Filtered backprojection reconstructed XRD-CT data

Isotropic XRD-CT reconstruction was done on sinograms $I(x,y,\alpha,q)$ separately for the integrated datasets of the shale sample without background subtraction, cf. 2.2. The unfiltered diffraction patterns were 1D median filtered in the azimuthal direction (in ϕ) before azimuthal averaging. XRD-CT reconstruction (Birkbak *et al.*, 2015) was done separately for each q (2048 radial bins). The reconstruction was done using the filtered backprojection (FBP) (Kak, Avinash C., Slaney, 1987) algorithm as implemented in the ASTRA toolbox (van Aarle *et al.*, 2016) in combination with custom-made macros. The reconstructed voxel size in XRD-CT was $(50 \; \mu m)^3$. Several choices of filtering is available for reconstruction in isotropic XRD-CT. Figure S7 shows the comparison between median filtering the projections in φ before creating sinograms, or filtering the diffraction patterns in polar coordinates with an alpha-trimmed-mean filter with varying filter strength, before binning into radial bins, as previously demonstrated by (Vamvakeros *et al.*, 2015).
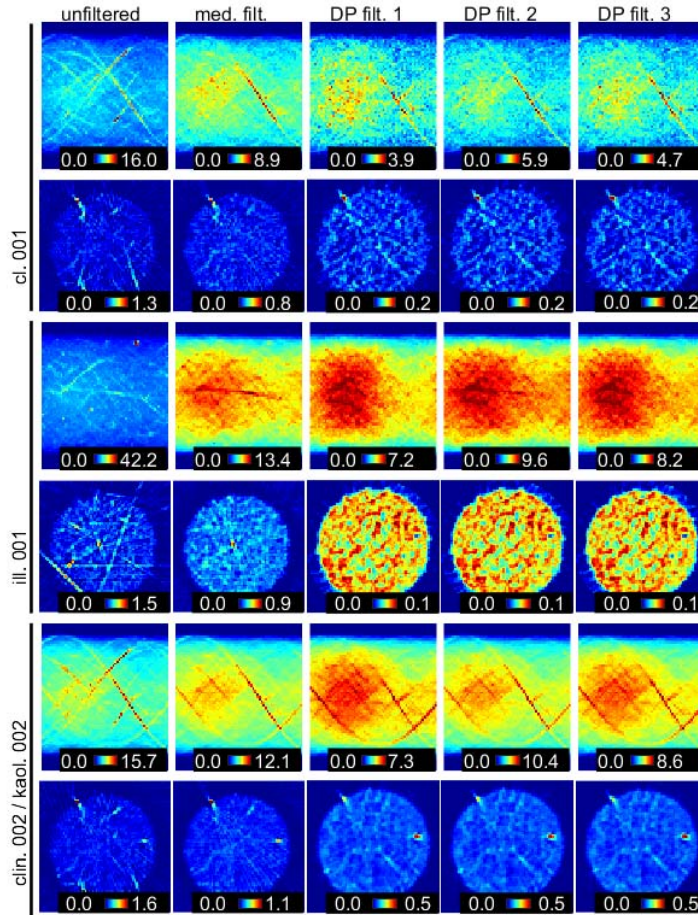
Figure S11.1 Different filtering strategies before XRD-CT reconstruction. "med. filt" denotes filtering of the azimuthal intensity distributions after radial and azimuthal integration, while "DP filt. 1", "DP filt. 2" and "DP filt. 3", are filtering of the diffraction patterns with different filter strengths (1-3) before radial and azimuthal integration.
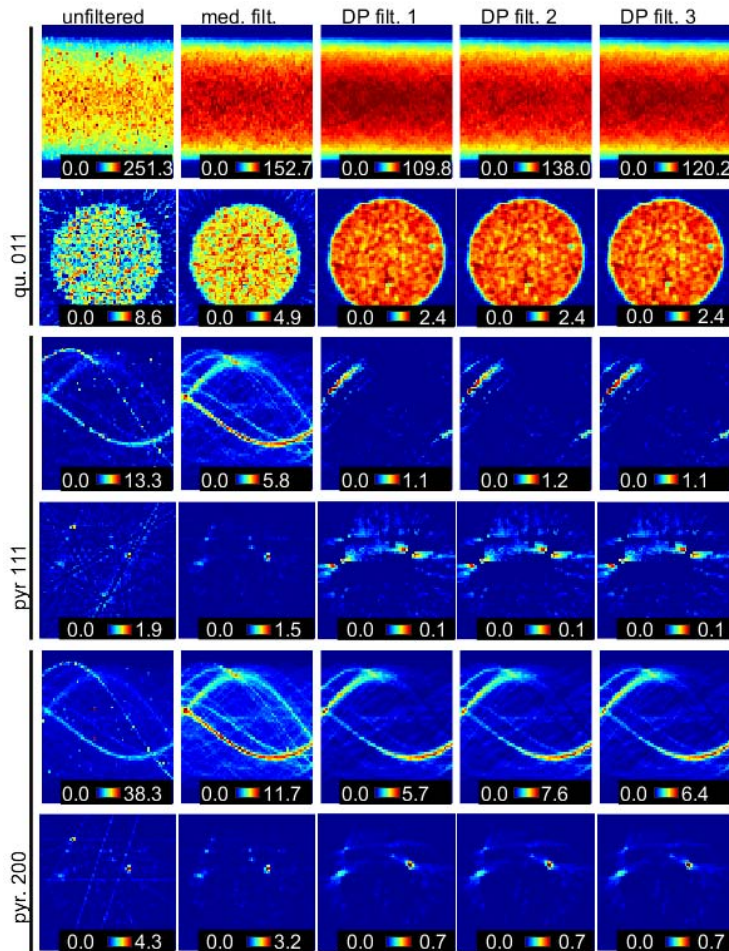
Figure S11.2 Different filtering strategies before XRD-CT reconstruction. "med. filt" denotes filtering of the azimuthal intensity distributions after radial and azimuthal integration, while "DP filt. 1", "DP filt. 2" and "DP filt. 3", are filtering of the diffraction patterns with different filter strengths (1-3) before radial and azimuthal integration.

S12. Reconstructed diffractograms

Figure S12 shows reconstructed diffractogram from the particles marked (1), (2) and (3) in the main article.
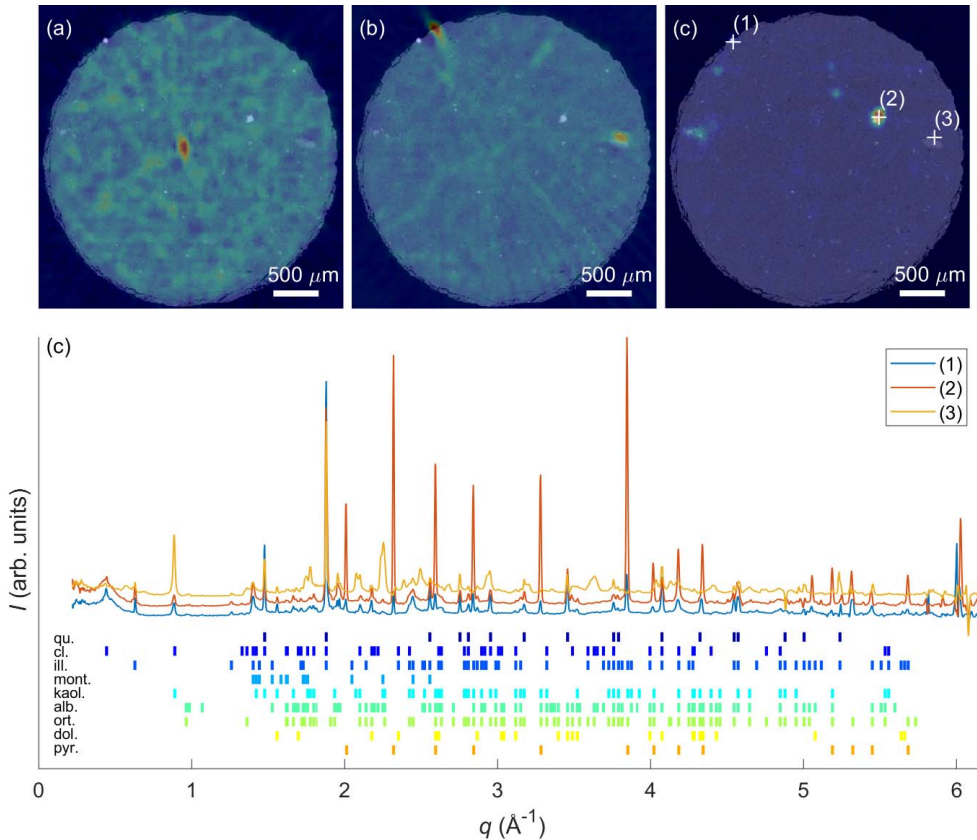

Figure S12 XRD-CT revealing the full diffractograms at localized sample points. (a-c) Overlay of attenuation-contrast cross-section in Fig 6a with (a) illite 002, (b) clinochlore 002/kaolinite 002 and (c) pyrite 200. (c) Reconstructed diffractograms for points (1), (2) and (3) indicated in (c), based on median filtered sinograms.

S13. XRD-CT and attenuation-contrast CT correlation analysis

A quantitative comparison of the attenuation-contrast CT and XRD-CT of Pierre shale was made by calculating the correlation between the attenuation-contrast sinograms and the XRD-CT sinograms for each q. This analysis gives similar information as for XRD-CT reconstruction, where local mineral content can be assigned to the different voxels, however without using XRD-CT reconstruction (see S12), which could lead to artefacts for large crystallites or oriented minerals. The correlation coefficient $r(q)$ is calculated by from the attenuation-contrast and XRD-CT sinograms by

$$r(q) = \frac{\sum_x \sum_\alpha (I_{\text{att.CT}}(x,\alpha) - \bar{I}_{\text{att.CT}})(I_{\text{XRD-CT}}(x,\alpha,q) - \bar{I}_{\text{XRD-CT}}(q))}{\sqrt{\sum_x \sum_\alpha (I_{\text{att.CT}}(x,\alpha) - \bar{I}_{\text{att.CT}})^2}\ \sqrt{\sum_x \sum_\alpha (I_{\text{XRD-CT}}(x,\alpha,q) - \bar{I}_{\text{XRD-CT}}(q))^2}}, \qquad \text{(S12.1)}$$

where

$$\bar{I}_{\text{att.CT}} = \frac{1}{N_x N_\alpha} \sum_x \sum_\alpha I_{\text{att.CT}}(x,\alpha) \qquad \text{(S12.2)}$$

and

$$\bar{I}_{\text{XRD-CT}}(q) = \frac{1}{N_x N_\alpha} \sum_x \sum_\alpha I_{\text{XRD-CT}}(x,\alpha,q). \qquad \text{(S12.3)}$$

The analysis gave high correlation between the attenuation-contrast sinogram curves for particles marked (1) and (2) for q corresponding to pyrite. Low correlation between the clinochlore-containing regions was observed, due to the lower signal to noise ratio of these sinograms.
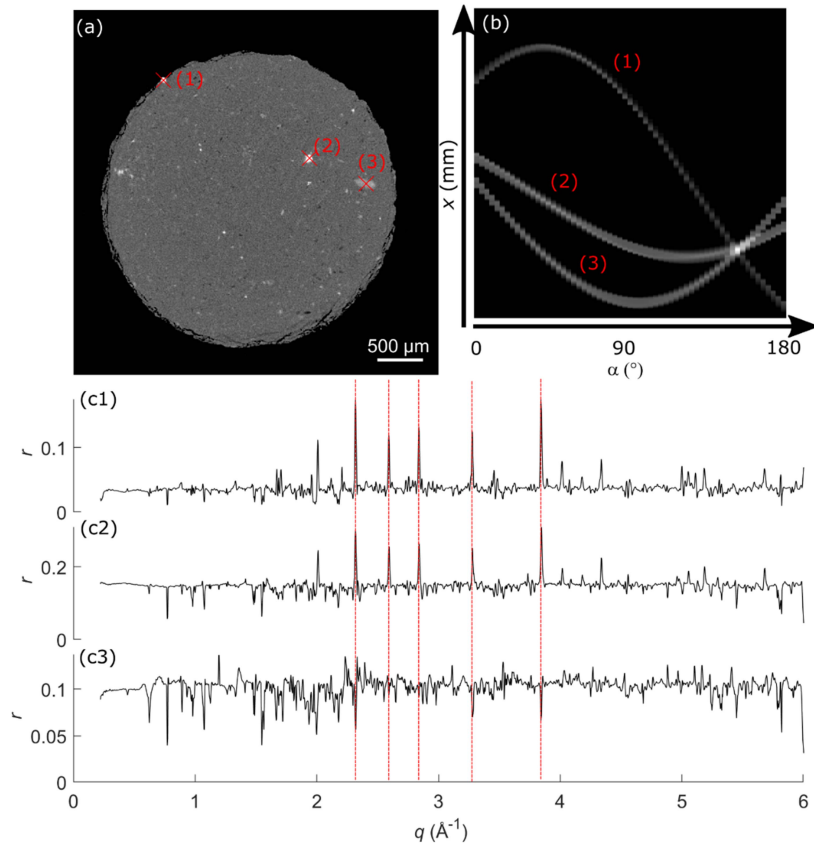
Figure S13 Correlation analysis between attenuation-contrast CT and XRD-CT of Pierre shale. (a) Measured cross-section. Particles are indicated with (1), (2) and (3). (b) Corresponding parallel beam sinogram (Radon transform) of points marked with (X) in (a). (c1-c3) Sinogram correlation between attenuation-contrast CT and XRD-CT. The red vertical lines indicate q corresponding to pyrite Bragg peaks.

References

van Aarle, W., Palenstijn, W. J., Cant, J., Janssens, E., Bleichrodt, F., Dabravolski, A., De Beenhouwer, J., Joost Batenburg, K. & Sijbers, J. (2016). *Opt. Express*. **24**, 25129.

Birkbak, M. E., Leemreize, H., Frølich, S., Stock, S. R. & Birkedal, H. (2015). *Nanoscale*. **7**, 18402–18410.

Harding, G., Kosanetzky, J. & Neitzel, U. (1987). *Med. Phys.* **515**, 515–525.

Hughes, J. M., Cameron, M. & Crowley, K. D. (1989). *Am. Mineral.* **74**, 870–876.

Kak, Avinash C., Slaney, M. (1987). Principles of Computerized Tomographic Imaging Society for Industrial and Applied Mathematics.

Kleuker, U., Suortti, P., W., W. & Spanne, P. (1998). *Phys. Med. Biol.* **43**, 2911–2923.

Liebi, M., Georgiadis, M., Kohlbrecher, J., Holler, M., Raabe, J., Usov, I., Menzel, A., Schneider, P., Bunk, O. & Guizar-Sicairos, M. (2018). *Acta Crystallogr. Sect. A Found. Adv.* **74**, 12–24.

Meneghini, C., Dalconi, M. C., Nuzzo, S., Mobilio, S. & Wenk, R. H. (2003). *Biophys. J.* **84**, 2021–2029.

Mürer, F. K., Chattopadhyay, B., Madathiparambil, A. S., Tekseth, K. R., Di Michiel, M., Liebi, M., Lilledahl, M. B., Olstad, K. & Breiby, D. W. (2021). *Sci. Rep.* **11**, 1–12.

Stock, S. R. (2015). *Calcif. Tissue Int.* **97**, 262–280.

Stock, S. R., De Carlo, F. & Almer, J. D. (2008). *J. Struct. Biol.* **161**, 144–150.

Vamvakeros, A., Jacques, S. D. M., Di Michiel, M., Middelkoop, V., Egan, C. K., Cernik, R. J. & Beale, A. M. (2015). *J. Appl. Crystallogr.* **48**, 1943–1955.

Wenk, H. R. & Heidelbach, F. (1999). *Bone*. **24**, 361–369.

NTNU

Norwegian University of
Science and Technology